UNIVERSITY OF SOUTHAMPTON

System Parameters of X-Ray Binaries

Andrew D. Barnes

Submitted for the degree of Doctor of Philosophy

SCHOOL OF PHYSICS AND ASTRONOMY
FACULTY OF SCIENCE

December 5, 2006

UNIVERSITY OF SOUTHAMPTON

ABSTRACT

FACULTY OF SCIENCE

SCHOOL OF PHYSICS AND ASTRONOMY

Doctor of Philosophy

System Parameters of X-Ray Binaries

by Andrew D. Barnes

In this thesis various aspects of X-ray binaries (XRBs) are investigated, with particular emphasis on the value of high-resolution, phase-resolved optical spectroscopy. Observations of heavily blended nitrogen and carbon emission lines in the low mass X-ray binary (LMXB) system XB 1254–690, utilising the technique of Doppler Tomography, have allowed the motion of the donor star to be traced for the first time. In combination with measurements tracing the motion of the compact object, true dynamical mass constraints for both the compact object and donor star have been derived.

Similar studies of other LMXBs have proved highly successful in unveiling the system kinematics. These sources are presented together here and examined as a cohesive population for the first time. We find evidence suggesting that two systems in particular, Aql X–1 and GX 339–4, are highly evolved. In contrast, GX 9+9 is exceptional in not possessing any evidence for the presence of CNO processing. The remaining seven sources in the sample possess remarkably similar properties, the interpretation of which has important ramifications for current models of binary formation and evolution.

Recent B-band spectroscopy of the bizarre XRB SS 433 has provided tantalising glimpses of absorption features common to early-type supergiant stars. These features have previously been interpreted as a tracer of the donor star. However, comprehensive B- and I-band phase-resolved spectra clearly show that the velocities of these features do not correspond to the expected motion of the mass donor, but rather to a clumpy, accretion-driven outflow.

Acknowledgements

There have been many people who have aided this work either through direct involvement with the science or background encouragement, and as Will Clarkson once said, this section is by no means exhaustive. Jose Luis Galache and Adam Hill both started at the same time as me, and have been a tremendous help in getting me through the last few years. I also have to thank my office mates in Room 4077 over the years, Pablo, Alex and in particular Derek and Andy, for joining me in plentiful X-piloting sessions to work off the frustrations of a morning of astrophysic'ing. I must also thank Essex wideboy and Thundercats fan Ed Pope for not snoring too much in the Alpine foothills (?!?) of Kent.

This work would not have been possible without the support of my thesis advisor Phil Charles, my *in loco Philentis* Christian Knigge and Remon Cornelisse (ik zal u in het Nederlands, een taal met veel interessant lawaai, en oneven vertalingen dankzij Babelfish danken). Simons Clark and Harris, Rob Hynes, Danny Steeghs and Jorge Casares have been invaluable, as was Tariq Shahbaz for introducing me to the wild world of astronomical observation. PPARC have been very kind to fund this work, and send me to all sorts of lovely places around the world. I thank Tom Marsh for the use of MOLLY and various other wonderful pieces of software.

My family, friends (will I beat you Lue?) and in particular Lorna have been very supportive throughout. I should also mention my brew-partner Vincent Jurdic and his peculiar obsession with pickling rare fruits in schnapps. Santé.

Brian May (famous astronomer and part-time rock star) once proclaimed that astronomy is a lot more fun when you are not an astronomer, but I think that is a little unfair. Instead, I prefer to leave the reader with the following thought:

"Its the essential oils that make the difference"

– Original Source Honey & Lemon Moisturising Body Wash, Lush

Contents

List of Figures

List of Tables

Chapter 1

X-Ray Binary Phenomena

In 1962, Giacconi et al. (1962) discovered the first extra-solar X-ray point source during a rocket flight. For this work, Giacconi was subsequently awarded part of the Nobel Prize in Physics in 2002. Subsequent observations of this source, known as Sco X–1, suggested that it was a binary system with a period of 18.9 hours and an optical counterpart of V $\sim$ 12 mag (Gursky et al., 1966; Sandage et al., 1966; Gottlieb et al., 1975). During the period between 1962 and 1966 it was realised that binary systems could emit X-rays, through accretion onto a compact object (Hayakawa & Matsuoka, 1963; Salpeter, 1964; Zel'Dovich, 1964), either a neutron star or black hole.

Since their discovery, accreting compact objects in the Galaxy have offered unique insights into the astrophysics of the end stages of stellar evolution and the physics of matter under extreme physical conditions. New phenomena were discovered and understood, such as the periodic pulsations in the X-ray lightcurve of spinning neutron stars (Giacconi et al., 1971) and the thermonuclear flashes on the surfaces of neutron stars that are detected as powerful X-ray bursts (Grindlay et al., 1976). Moreover, the masses of the compact objects were measured in a number of systems, providing the strongest evidence for the existence of black holes in the universe (Webster & Murdin, 1972; Bolton, 1972; McClintock & Remillard, 1986). Accreting neutron stars and black holes have been monitored in broad spectral bands, from the radio to γ-rays, leading to the discovery of highly relativistic jets (Mirabel & Rodriguez, 1994), to the indirect imaging of the accretion flows (Horne, 1985), and to the possible identification of neutron stars with masses close to the maximum value allowed by general relativity (Barziv et al., 2001).

1.1 X-ray binaries

1.1.1 Classification

Over 90% of the strong Galactic X-ray binary (XRB) sources appear to fall into two distinct groups. These are classified according to the mass of the stellar donor, as this broadly divides the mechanism for mass transfer (see Fig. 1.1 and Table 1.1). The low-mass X-ray binaries (LMXBs) contain a $\lesssim 1M_{\odot}$ donor. Donor types typically range through late-type main sequence stars up to A-type, and F–G-type subgiants. In some very evolved systems, the donor can even be a white dwarf (Liu et al., 2001). A late-type or degenerate star does not generally possess a natural wind strong enough to power the observed X-ray source. Significant mass transfer will only occur if the companion fills its critical gravitational potential lobe (the Roche lobe, see Section 1.2.1). X-ray heating of the accretion disc and the companion star dominates the optical light, and LMXBs appear as faint blue stars (Bradt & McClintock, 1983).

In many X-ray binaries the mass-losing star does not fill its Roche lobe and the compact component must accrete from a wind created by its companion. Wind accretion is an inherently less efficient process than Roche lobe overflow, with mass leaving the star in all directions, not just towards the accretor. In general, only a small fraction of the wind is accreted, in contrast to the Roche lobe case where almost all of the mass may be captured by the accreting component. For this process to result in a compact star that is a bright X-ray source, the companion star has to be massive ($\gtrsim 10M_{\odot}$) in order to drive a strong wind. Typically, the companion is an O- or B-type star, and such systems are classified as high-mass X-ray binaries (HMXBs). The optical luminosity of the donor will be comparable to or greater than that of the X-ray source, with the optical properties of the system dominated by the companion star (Conti, 1978; Petterson, 1978).

The large difference in the companion masses between low- and high-mass X-ray binaries leads to a number of additional differences between these two classes of systems. The lifetimes of HMXBs are determined by the evolution of the high-mass companions and are short ($\sim 10^5 - 10^7$ yr), whereas the lifetimes of the LMXBs are determined by the mass-transfer process and are longer ($\sim 10^7 - 10^9$ yr). Since the neutron stars in HMXBs accrete for a relatively short period of time, their magnetic fields do not evolve away from their high birth values, and hence these neutron stars appear mostly as accretion-powered pulsars. On the other hand, the prolonged phase of accretion onto neutron stars in LMXBs is believed to be responsible for the

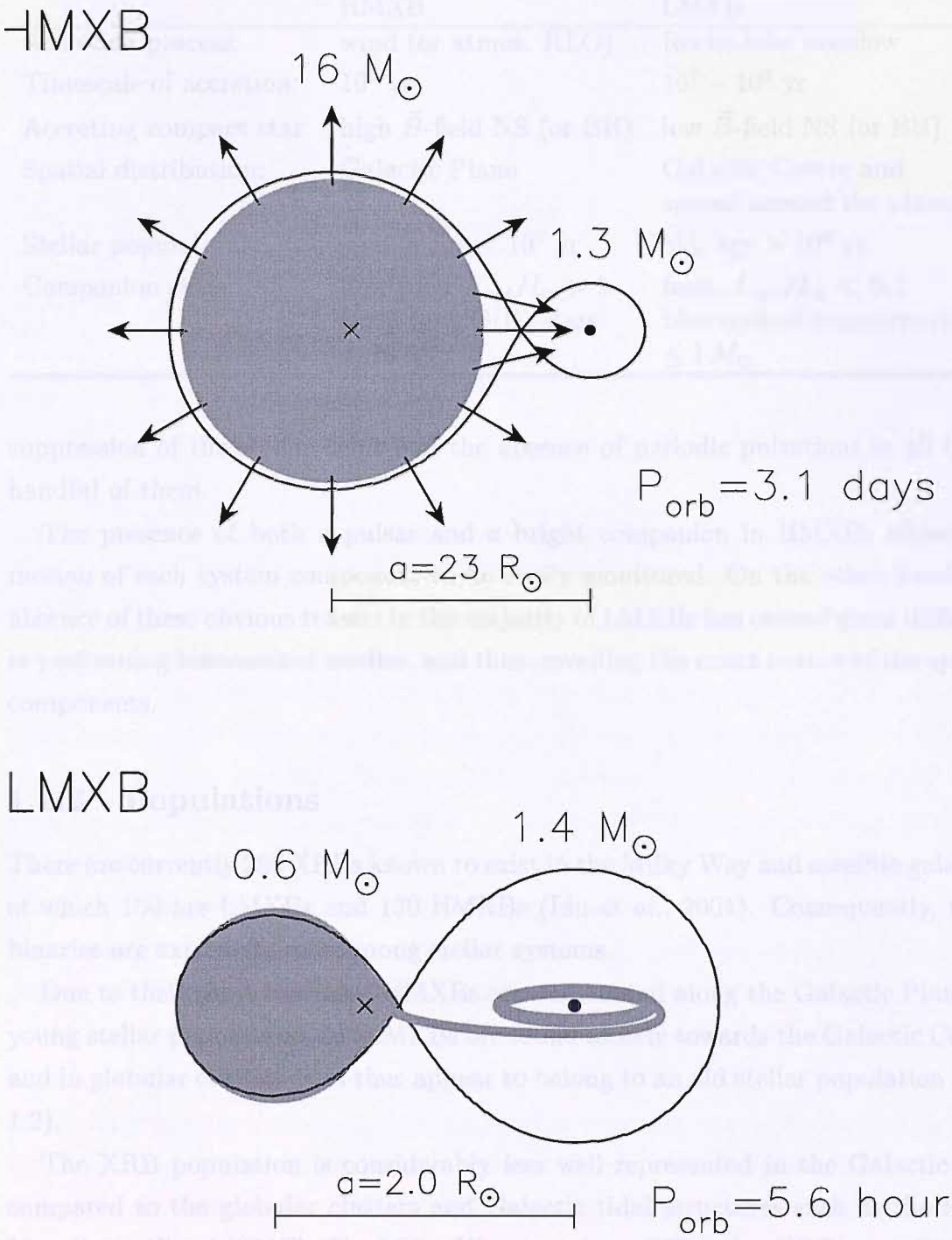

Figure 1.1: Examples of a typical HMXB (top) and LMXB (bottom). The accretor in the HMXB is fed by a strong high-velocity stellar wind and/or by beginning atmospheric Roche-lobe overflow. The compact object in an LMXB is surrounded by an accretion disk which is fed by Roche-lobe overflow. Taken from Tauris & van den Heuvel (2003).

Table 1.1: The two main classes of strong Galactic X-ray sources

	HMXB	LMXB
Accretion process:	wind (or atmos. RLO)	Roche-lobe overflow
Timescale of accretion:	10^5 yr	$10^7 - 10^9$ yr
Accreting compact star:	high $\vec{B}$-field NS (or BH)	low $\vec{B}$-field NS (or BH)
Spatial distribution:	Galactic Plane	Galactic Centre and spread around the plane
Stellar population:	young, age $< 10^7$ yr	old, age $> 10^9$ yr
Companion stars:	luminous, $L_{\rm opt}/L_x > 1$ early-type O(B)-stars $> 10\,M_\odot$	faint, $L_{\rm opt}/L_x \ll 0.1$ blue optical counterparts $\leq 1\,M_\odot$

suppression of the stellar fields and the absence of periodic pulsations in all but a handful of them.

The presence of both a pulsar and a bright companion in HMXBs allows the motion of each system component to be easily monitored. On the other hand, the absence of these obvious tracers in the majority of LMXBs has caused great difficulty in performing kinematical studies, and thus unveiling the exact nature of the system components.

1.1.2 Populations

There are currently 280 XRBs known to exist in the Milky Way and satellite galaxies, of which 150 are LMXBs and 130 HMXBs (Liu et al., 2001). Consequently, these binaries are extremely rare among stellar systems.

Due to their short lifetimes, HMXBs are distributed along the Galactic Plane, as young stellar populations do. LMXBs are found mostly towards the Galactic Centre and in globular clusters, and thus appear to belong to an old stellar population (Fig. 1.2).

The XRB population is considerably less well represented in the Galactic field compared to the globular clusters and Galactic tidal structures such as the Small Magellanic Cloud (SMC). The Milky Way contains ~280 active XRBs out of $\sim 10^{12}$ stars; if we scale by the number of stars in the SMC then we would expect to see perhaps ~3 XRBs in the SMC. In fact, there are now over 60 HMXBs discovered in the SMC with no known LMXBs (Haberl et al., 2000; Liu et al., 2001). The Large Magellanic Cloud (LMC) contains ~30 HMXBs (Haberl & Pietsch, 1999; Kahabka, 2002) and two LMXBs (Liu et al., 2001). The LMC and SMC are thought to have

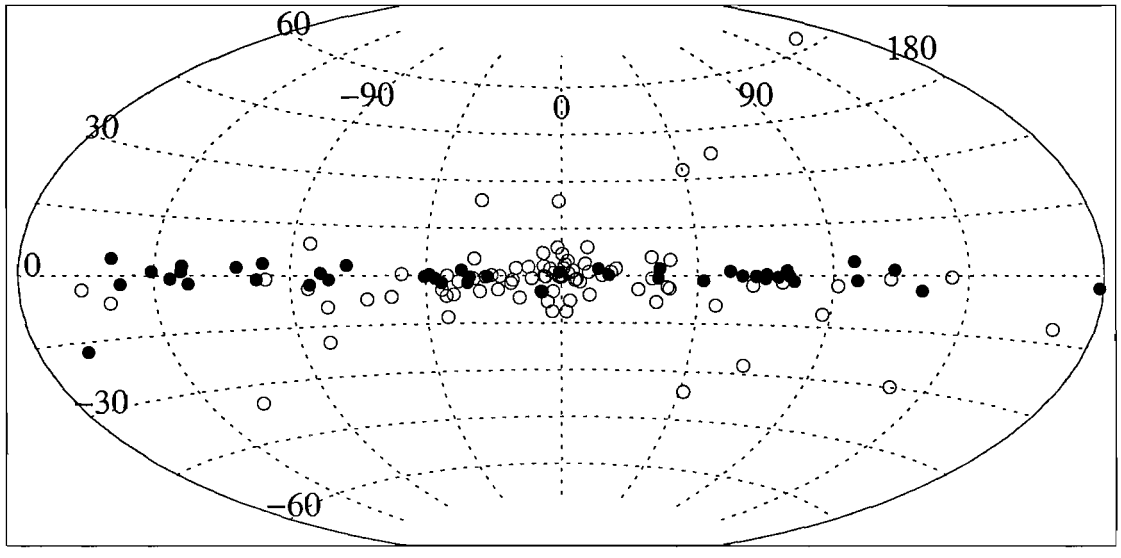

Figure 1.2: Distribution of Low-Mass X-ray Binaries (open symbols) and High-Mass X-ray Binaries (filled symbols) in Galactic coordinates. Taken from Grimm et al. (2002).

undergone tidal interaction ~0.2–0.4 Gyr ago (Gardiner et al., 1994), triggering star formation in both bodies and producing the massive overpopulation of HMXBs compared to the Milky Way. That the SMC possesses a higher population of HMXBs than the LMC supports this model as the smaller of the two interacting bodies will undergo the more severe disruption. However, the star formation rates in the two bodies are rather similar, and so the differences in binary population could perhaps be attributed to more thorough observations of the SMC. Metallicity may also be a parameter (see e.g. Martayan et al., 2006).

The LMXB population in globular clusters is also over-dense compared to the Galactic field by two orders of magnitude (Verbunt & Hut, 1987). This suggests that formation channels are at work in clusters that are not important in the Galactic disc. The obvious candidate is interactions between stellar systems; the collisional timescale for a star in a globular cluster is several orders of magnitude shorter than for the Galactic disc (Binney & Tremaine, 1987). As a result, each XRB may undergo several stellar encounters over the cluster lifetime of $\sim 10^{9-10}$ years. Two- and three-body encounters can thus drive the evolution of close binary systems, for example the capture by an isolated compact object of an encountered star through tidal dissipation (Fabian et al., 1975), or by three-body encounters in which a star may be exchanged for the encountered star (Hut et al., 1992).

1.2 The Physics of Accretion

We introduce here the physics of accretion in close binaries. This section draws heavily on the discussion in the excellent graduate textbook by Frank et al. (2002), which should be referred to for further details.

1.2.1 Accretion and the Roche lobe

The binary separation, a, is given in terms of the fundamental observational quantity, the binary period P, through Kepler's Law:

$$4\pi^2 a^3 = G(M_1 + M_2)P^2 \tag{1.1}$$

where M_1 and M_2 are the masses of the two binary components. For binary periods of the order of hours, a can be conveniently expressed in the form:

$$a = 3.5 \times 10^{10}(M_1 + M_2)^{1/3} P_{hr}^{2/3} \quad cm \tag{1.2}$$

The effective gravitational potential in a binary system is determined by the masses of the stars and the centrifugal force arising from the motion of the two stars around one another. One may write this potential as:

$$\Phi_R = -\frac{GM_1}{r_1} - \frac{GM_2}{r_2} - \frac{\Omega^2 r_3^2}{2} \tag{1.3}$$

where r_1 and r_2 are the distances to the centre of the stars with mass M_1 and M_2, respectively; Ω is the orbital angular velocity; and r_3 is the distance to the rotational axis of the binary. It is assumed that the stars are small with respect to the distance between them and that they revolve in circular orbits. In a binary where tidal forces have circularised the orbit, and brought the two stellar components into synchronised co-rotation, one can define fixed equipotential surfaces in a co-moving frame. The equipotential surface passing through the first Lagrangian point, L_1 defines the 'pear-shaped' *Roche-lobe* at which the force on a test mass is zero (see the cross-section in Fig. 1.3). L_1 is a saddle point in the potential: in the direction along the line connecting the centres of mass (the x-direction in Fig. 1.3) it is a local maximum, whereas in the y-direction it is a minimum. If the initially more massive star (the donor) evolves to fill its Roche lobe the unbalanced pressure at L_1 will initiate mass transfer (Roche lobe overflow) onto its companion star (the accretor). The radius of the donor's Roche lobe, R_L is defined as that of a sphere with the

same volume as the lobe. The complicated form of Φ_R means that we must resort to numerical calculation to find this as a function only of the orbital separation, a and the mass ratio:

$$q \equiv \frac{M_{\rm donor}}{M_{\rm accretor}} = \frac{M_2}{M_1} \tag{1.4}$$

of the binary components. It can be approximated for all values of q as (Eggleton, 1983):

$$\frac{R_L}{a} = \frac{0.49\, q^{2/3}}{0.6\, q^{2/3} + \ln(1 + q^{1/3})} \tag{1.5}$$

The lobe radius of the primary is given by replacing q with q^{-1}. For mass ratios $0.1 \lesssim q \lesssim 0.8$ an alternative form for R_L may be used (Paczynski, 1971):

$$\frac{R_L}{a} = 0.462 \left(\frac{q}{1+q} \right)^{1/3} \tag{1.6}$$

which allows a to be eliminated from Kepler's Third Law, and under the assumption that the Roche lobe-filling low-mass donor has evolved slowly and is thus still on or near the main sequence ($M_2 \simeq R_2$), results in the period-mass relation:

$$M_2 \sim 0.11 P_{hr} \tag{1.7}$$

with M_2 measured in solar masses. Indeed, for low-mass Roche lobe filling X-ray binaries, orbital periods of ~few hours are frequently observed.

The process of mass transfer in a binary will change not only the mass ratio q, but the period P and separation a also due to the redistribution of angular momentum within the system. Taking the orbital angular momentum of the binary to be that of two point masses:

$$J = M_1 M_2 \left(\frac{Ga}{M_1 + M_2} \right)^{1/2} \tag{1.8}$$

Assuming that the mass transfer is conservative (i.e. $\dot{M}_1 + \dot{M}_2 = 0$, $\dot{M}_2 < 0$), the effect of this transfer on the Roche lobe of the donor can then be described by (see e.g. Frank et al., 2002):

$$\frac{\dot{R}_2}{R_2} = \frac{2\dot{J}}{J} + \frac{2(-\dot{M}_2)}{M_2} \left(\frac{5}{6} - q \right) \tag{1.9}$$

Clearly there are two cases, depending on whether q is larger or smaller than 5/6. For $q > 5/6$ the mass transfer results in the Roche lobe shrinking, resulting in further mass transfer and a runaway process. Mass transfer from more massive M_2 to less

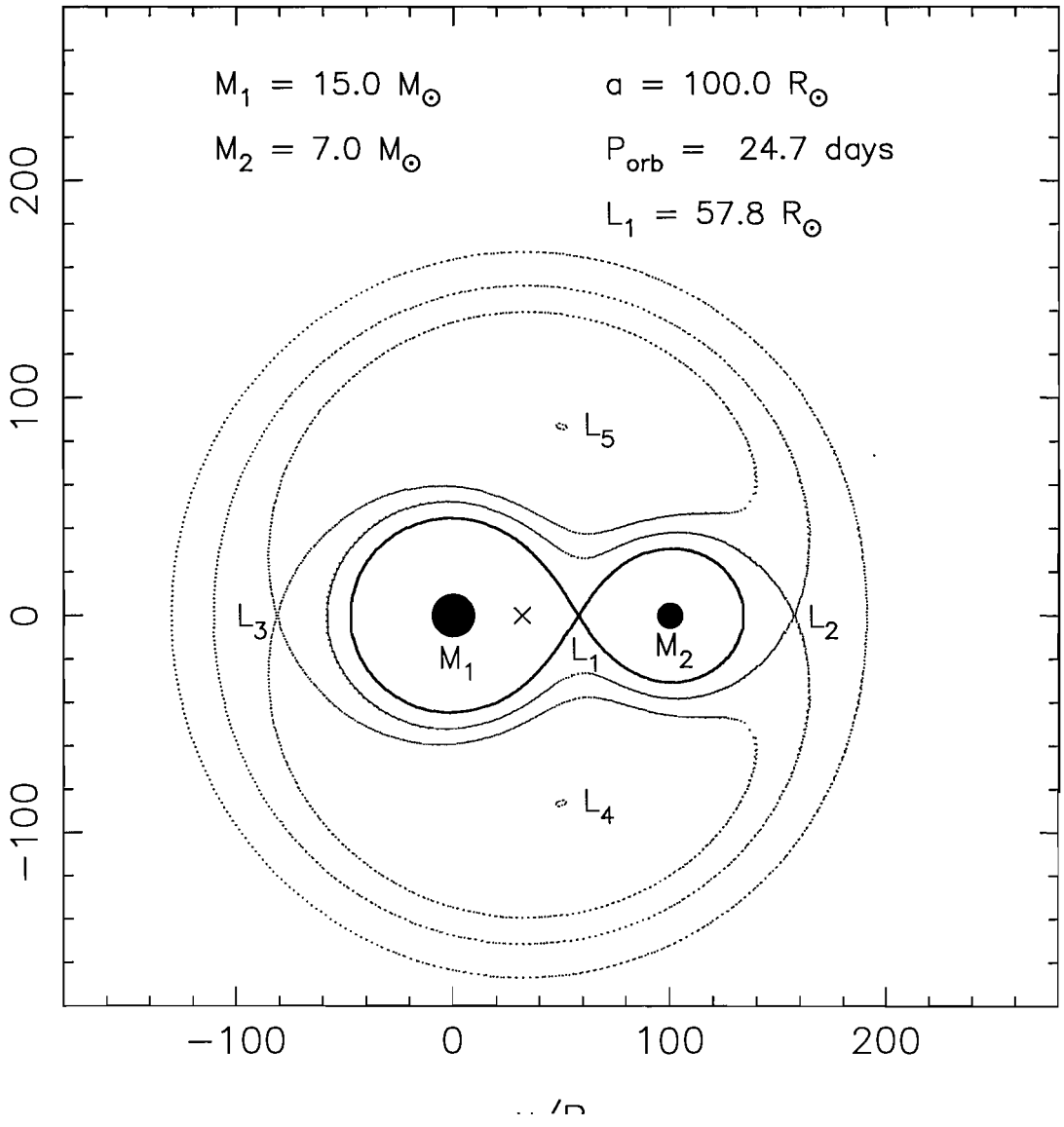

Figure 1.3: A cross-section in the equatorial plane of the critical equipotential surfaces in a binary. The x- and y-axes are plotted in units of $R_\odot$. The thick curve crossing through L_1 is the Roche-lobe. Taken from Tauris & van den Heuvel (2003).

massive M_1 redistributes matter away from the centre of mass, so the remaining mass M_2 moves in to conserve angular momentum; as a result the binary separation decreases along with the runaway increase in accretion rate. This process takes place on the thermal timescale of the donor ($\sim 10^{3-7}$ yr depending on the donor radius), so corresponding systems must be very rare, representing an intermediate step to the final state of the binary. The runaway spin-together is only halted if sufficient mass is transferred to bring the mass ratio beneath the critical value of 5/6 before system coalescence.

For $q \lesssim 5/6$ mass transfer will expand the Roche lobe, which would oppose accretion as the donor will no longer overflow the Roche lobe. Mass transfer therefore only continues if either the star expands or the binary loses angular momentum. In wide ($a \gtrsim$ few $R_\odot$) binaries, post main-sequence donor evolution may cause the donor expansion to keep pace with expansion of the Roche lobe. However, the majority of LMXBs have much more compact orbits than this ($a \sim R_\odot$), so accretion must be driven by angular momentum loss from the system. A variety of effects can give $\dot{J} < 0$. In short period systems gravitational radiation is important, whilst angular momentum loss in a wind magnetically linked to the secondary is a currently favoured possibility (see e.g.. Verbunt (1993) and Frank et al. (2002) for discussion).

1.2.2 Disc Formation

A consequence of Roche lobe overflow is that the transferring material possesses rather high specific angular momentum (J) in many cases. Accreting matter forms a disc when J is too large for it to hit the accreting object directly. The circularisation radius, where the matter would orbit if it lost energy but not angular momentum, is defined as

$$R_{circ} = \frac{J^2}{GM_1} \tag{1.10}$$

The condition for disc formation is typically that R_{circ} should be larger than the effective size of the accretor. This effective size is identical with the radius of a non-magnetic neutron star, but is of order the magnetospheric radius if there is a dynamically significant magnetic field. For the case of a black hole the effective size is the radius of the last stable circular orbit.

Assuming that matter can indeed orbit at R_{circ}, the fundamental assumption of disc theory (that energy is lost more rapidly than angular momentum) means that accretion can only take place through a sequence of circular orbits with gradually

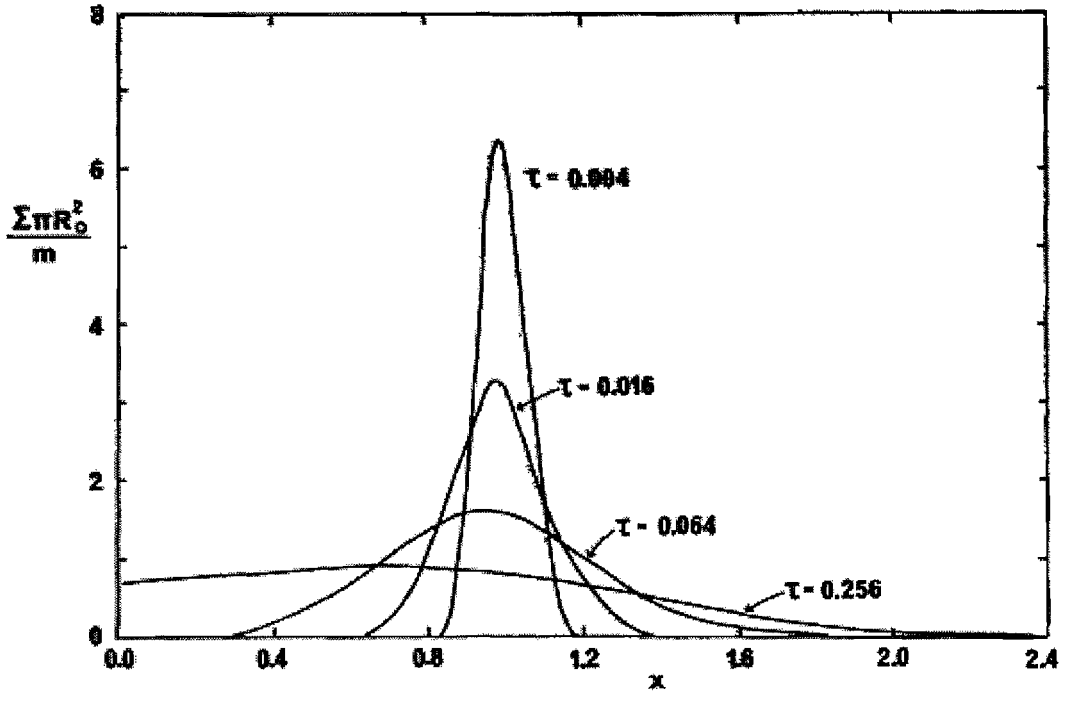

Figure 1.4: The viscous evolution of a ring of matter of mass m. The surface density Σ is shown as a function of dimensionless radius $x = R/R_0$, where R_0 is the initial radius of the ring, and of dimensionless time $\tau = 12\nu t/R_0^2$ where ν is the viscosity. Taken from Pringle (1981).

decreasing J. Without an external angular momentum sink such as a magnetic field, this can only be achieved by transporting angular momentum outwards. The disc edge thus expands far beyond R_{circ} (see Fig. 1.4). Most of the original angular momentum is carried out to this edge, where it is likely to be returned to the secondary star's orbit through tides.

The agency responsible for both energy dissipation and angular momentum transport is called viscosity, assumed to provide a torque between the shearing Kepler orbits. The physical basis of the viscosity is almost entirely unclear, with for example ordinary kinetic-theory viscosity being much too weak. The strongest candidate of recent years is probably magnetorotational instability (Balbus & Hawley, 1991). Here a comparatively weak magnetic field threading the disc is wound up by the shear, and transports angular momentum outwards. Reconnection limits the field growth and produces dissipation.

1.2.3 Accretion Power and the Eddington Limit

The total power available in the accretion process is simply the rate of conversion of gravitational potential energy when matter falls to the surface of the compact object from large distances[1], i.e.

$$L_{acc} = \frac{GM_1\dot{M}_1}{R_1} \tag{1.11}$$

In the case of a neutron star accretor (with canonical parameters $M_1 \sim 1.4M_\odot$, $R_1 \sim$ 10 km), the power output of the accretion process is then

$$L_{acc} \simeq 8.2 \times 10^{37} \left(\frac{\dot{M}_1}{10^{-7}}\right) \; erg \; s^{-1} \tag{1.12}$$

with $\dot{M}_1$ in units of $10^{-7}M_\odot$ yr^{-1}.

A rough upper limit to the sustainable accretion luminosity may be derived by calculating the luminosity at which radiation pressure due to the accretion process is sufficiently strong to halt further accretion. Photons from the central source undergo Thomson (free-free) scattering off incoming electrons in the accretion flow; electrostatic coupling between protons and electrons thus produces a pressure opposing the infall of matter. The *Eddington Limit* is the value of this luminosity for spherical accretion, and is given by

$$L_{Edd} = 1.3 \times 10^{38} M_1 \quad erg \; s^{-1} \tag{1.13}$$

(or alternatively $\dot{M}_{1,Edd} \simeq 1.5 \times 10^{-8} R_{10} \;\; M_\odot$ yr^{-1}, where R_{10} is the accretor radius in units of 10km).

Einstein observations of seven bright spiral galaxies detected 16 point sources with observed $L_X > 10^{39}$ erg s^{-1} (Fabbiano, 1989). Assuming such emission to be isotropic and Eddington-limited then produces the estimates $M_1 \gtrsim 50 - 100 M_\odot$ and $\dot{M} \gtrsim 10^{-6} M_\odot$ yr^{-1} (King et al., 2001). This is the Intermediate Mass Black Hole (IMBH) model. Observations with ROSAT and ASCA yielded the discovery that these Ultraluminous X-ray (ULX) sources are preferentially, but not exclusively, distributed in star-forming regions (Roberts & Warwick, 2000). This is suggestive of an XRB association and resulted in a considerable resurgence of interest in the nature of these objects (Makishima et al., 2000). The main objection to spherically

[1]This is not entirely true; some energy will be converted to rotational energy, which will likely be advected by black holes. Also, jets and winds may carry away kinetic energy.

symmetric models is the difficulty of forming a large number of intermediate mass black holes in a ~ 1 yr orbit with an evolved companion (King et al., 2001). However, individual objects may still contain IMBH accretors.

There are at least two ways for the accretion flow to sidestep the Eddington limit. One model involves deviation from spherically symmetric accretion, with mild beaming of the emergent radiation enhancing the observed L_X (see e.g. Körding et al., 2002). The high $\dot{M}$ required could be achieved during the thermal-timescale stage of mass transfer inevitable in HMXBs, thus fitting the association with starburst regions.

The second method to overcome our theoretical L_{Edd} is to decrease the efficiency with which the radiation pressure couples with incoming matter. For example, the HMXB X-ray pulsar A0538–66 frequently exhibits episodic outbursts in which $L_X > 10^{39}$ erg s^{-1} (Charles et al., 1983). This may be due to a reduction of the scattering cross-section below the Thomson cross-section at the high magnetic field ($\gtrsim 10^{11}$G) of the neutron star (Boerner & Meszaros, 1979). Thus in the X-ray pulsars we may expect super-Eddington accretion rates to be sustained (see also King et al., 2001).

An important caveat to note is that the Eddington limit applies only to the X-ray emission which interacts with the accretion flow; it is thus irrelevant to X-rays generated in regions *outside* the central object. For example, spectral fits of the neutron star LMXB Sco X–1 during flaring show peak L_X at $\sim 1.1 \times 10^{39}$ erg s^{-1}, well in excess of its Eddington limit (Barnard et al., 2003). The majority of this emission arises in an extended region well beyond the inner accretion flow.

1.3 Emission Regions

In the Newtonian limit, the binding energy of the innermost possible Keplerian orbit of mass m of gas is $\frac{1}{2}(GM_1m)/R_1$. Matter falling from L_1 initially has negligible binding energy, so this must be the energy released by mass m as it spirals inwards through the disc. Therefore, the total power output of this disc in a steady state must be $L_{disc} = \frac{1}{2}(GM_1\dot{M}_1)/R_1$, i.e. $L_{disc} = \frac{1}{2}L_{acc}$. Half the total accretion luminosity is thus released between the inner accretion disc and the surface of the compact object, in an accretion column (for X-ray pulsars) or thin boundary layer.

The location of the X-ray generation in the disc may be estimated for thin discs from the basic parameters of the binary (Pringle, 1981). For a neutron star XRB, the vast majority of the energy dissipation takes place in the inner $\sim 0.01\%$ of the disc

radius. In regions where the disc is optically thick to X-ray emission, in the steady state, disc elements may be expected to radiate as blackbodies. Early X-ray spectra of LMXBs were well-fit with a model including just this component alone (Mitsuda et al., 1984). Recent progress suggests this blackbody emission should be regarded as seed photons for Compton scattering off high-temperature electrons, producing the power-law Compton component that is preferentially observed (Section 1.3.3)[2].

1.3.1 X-ray pulsations

The HMXBs are often discovered as X-ray pulsars, in which the neutron star magnetic field is strong enough to disrupt the inner disc, channelling the accretion flow towards the poles (Fig. 1.5) [3]. The disruption radius r_M at which this occurs (for spherical accretion) is found by balancing the magnetic energy density with the kinetic energy density of infalling matter, resulting in

$$r_M = 1.49 \times 10^8 B_S^{4/7} R_1^{12/7} M_1^{-1/7} \dot{M}_1^{-2/7} \quad m \tag{1.14}$$

with R_1 in units of 10^4m, M_1 in units of $M_\odot$, $\dot{M}_1$ in units of $10^{-7} M_\odot$ yr^{-1} and the surface field strength B_S in units of 10^{12}G. Observed spin periods in the HMXBs are typically $\sim$ 0.1–10s (Liu et al., 2000), suggesting the compact object must be a neutron star from breakup considerations, with a surface field strength $B_S \gtrsim 10^9$G and accretion rate $\dot{M}_1 \sim 10^{-7} M_\odot$ yr^{-1}. X-ray pulsars have been seen with much longer pulse periods $\sim$ 100-1000s (e.g. Corbet et al., 2004).

Depending on its angular momentum about the neutron star, accreting matter causes the spin rate of the pulsar to evolve. The *co-rotation radius* r_C is defined as the radius at which matter in a Keplerian orbit co-rotates with the surface of the neutron star. At the inner disc edge r_M, the magnetosphere forces disc matter to co-rotation. If this process imparts angular momentum to the material (i.e. $r_M > r_C$), accretion cannot occur. Alternatively, if angular momentum is taken from the material (so $r_M < r_C$), accretion occurs with a corresponding spin-up torque on the neutron star. For a 10km, $1.4 M_\odot$ neutron star, accretion will only occur if

$$\frac{r_M}{r_C} \simeq 88.7 B_S^{4/7} \dot{M}_1^{-2/7} P_s^{-2/3} < 1 \tag{1.15}$$

with the pulsar spin period P_s measured in seconds.

[2]Note that so-called 'soft-state' black hole XRBs still fit very well to the Mitsuda model.

[3]figure from http://lheawww.gsfc.nasa.gov/users/white/xrb/xrb.html

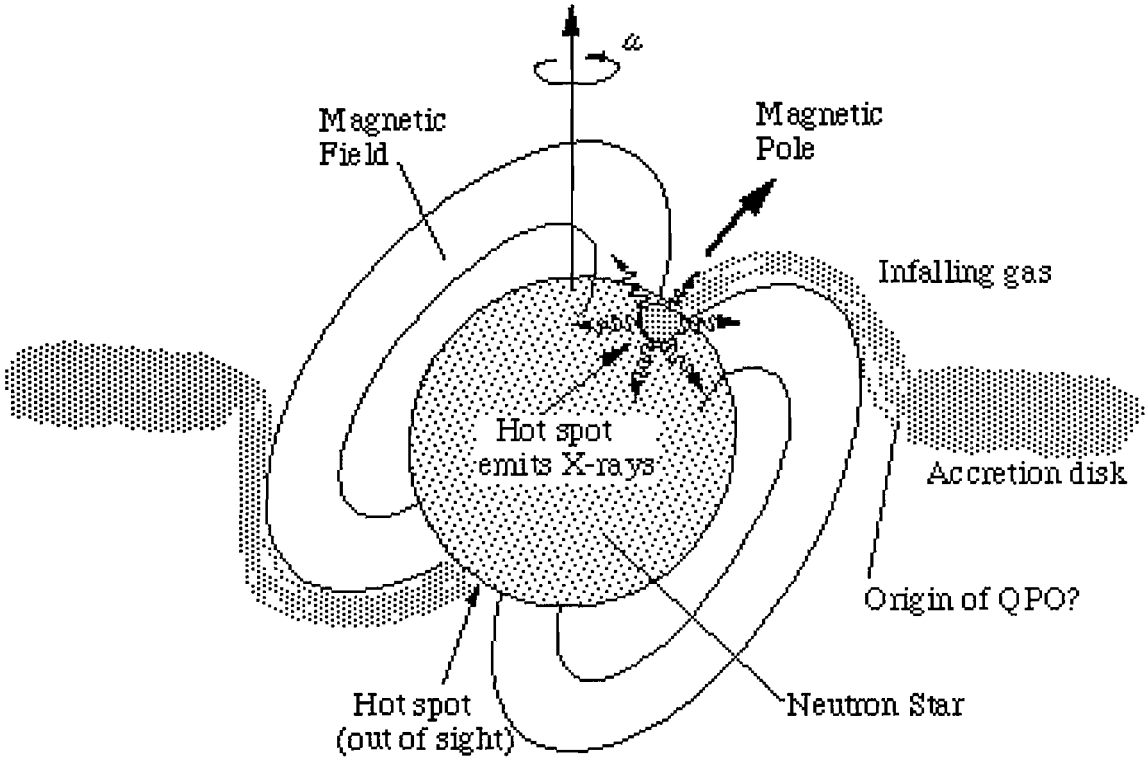

Figure 1.5: Schematic of X-ray pulsar geometry, from NASA/HEASARC

Therefore by regulating $\dot{M}_1$, accretion discs regulate the angular momentum transport onto the neutron star. X-ray pulsars with persistent accretion discs thus show persistent trends in the spin period. SMC X–1, the prototypical disc-fed X-ray pulsar, has been in a state of near-continuous spin-up for as long as it has been observed (Wojdowski et al., 1998). In the disc-fed LMXB pulsar GX1+4, the pulsar spins down at a rate correlated with the X-ray luminosity, suggesting the accretion disc may rotate in the opposite sense to the pulsar (Chakrabarty et al., 1997).

The millisecond *radio* pulsars occur almost exclusively in binaries (80% of the observed sample (Lorimer, 2001) compared to $\lesssim$1% for 'normal' pulsars), suggesting their existence as a separate population from the isolated radio pulsars which generally show monotonic spin-down. These systems are thought to be the result of spin-up in an accreting LMXB, consistent also with lower ($B_S \lesssim 10^8$G) magnetic fields (Frank et al., 1992; Verbunt, 1993). This scenario was confirmed by the RXTE/PCA discovery of millisecond X-ray pulsations from the LMXB SAX J1808.4–3658 (Wijnands & van der Klis, 1998). Only seven millisecond X-ray pulsars are currently known, three of which have $P_{orb} \sim$ 40–80 minutes and three with P_{orb} in the range of 2–4 hours (Psaltis, 2004; Galloway et al., 2005; Kaaret et al., 2006). All such systems are transients, with peak brightness only $\sim 0.01 L_{Edd}$. Millisecond X-ray pulsars make up the majority of observed LMXBs which exhibit X-ray pulsations.

1.3.2 Type I X-ray Bursts

LMXBs are often observed to demonstrate dramatic, rapid increases in X-ray luminosity, with a rise to maximum luminosity $\sim 10^{38}$erg s^{-1} in $\sim$1–10s followed by exponential decay to the quiescent level with a timescale of $\sim$90s (see Lewin et al (1995) and Fig. 1.6). Such *Type I X-ray bursts* are not seen from the HMXB pulsars, but are seen in some of the LMXB millisecond pulsars. They are thought to be due to explosively unstable nuclear processing of accreted material built up on the surface of the compact object. The X-ray spectrum of Type I bursts is that of an isothermal blackbody, allowing the evolution of the blackbody temperature and radius to be charted.

The observed temperatures and the requirement of a surface on which to build up the burning layer suggests the compact object must be a neutron star. All bursters have magnetic fields $\lesssim 10^9$G, as at higher fields explosive fronts cannot propagate. Observations of EXO 0748–673 showed anti-correlation between the persistent luminosity and the average interval between bursts (Gottwald et al., 1986), as well

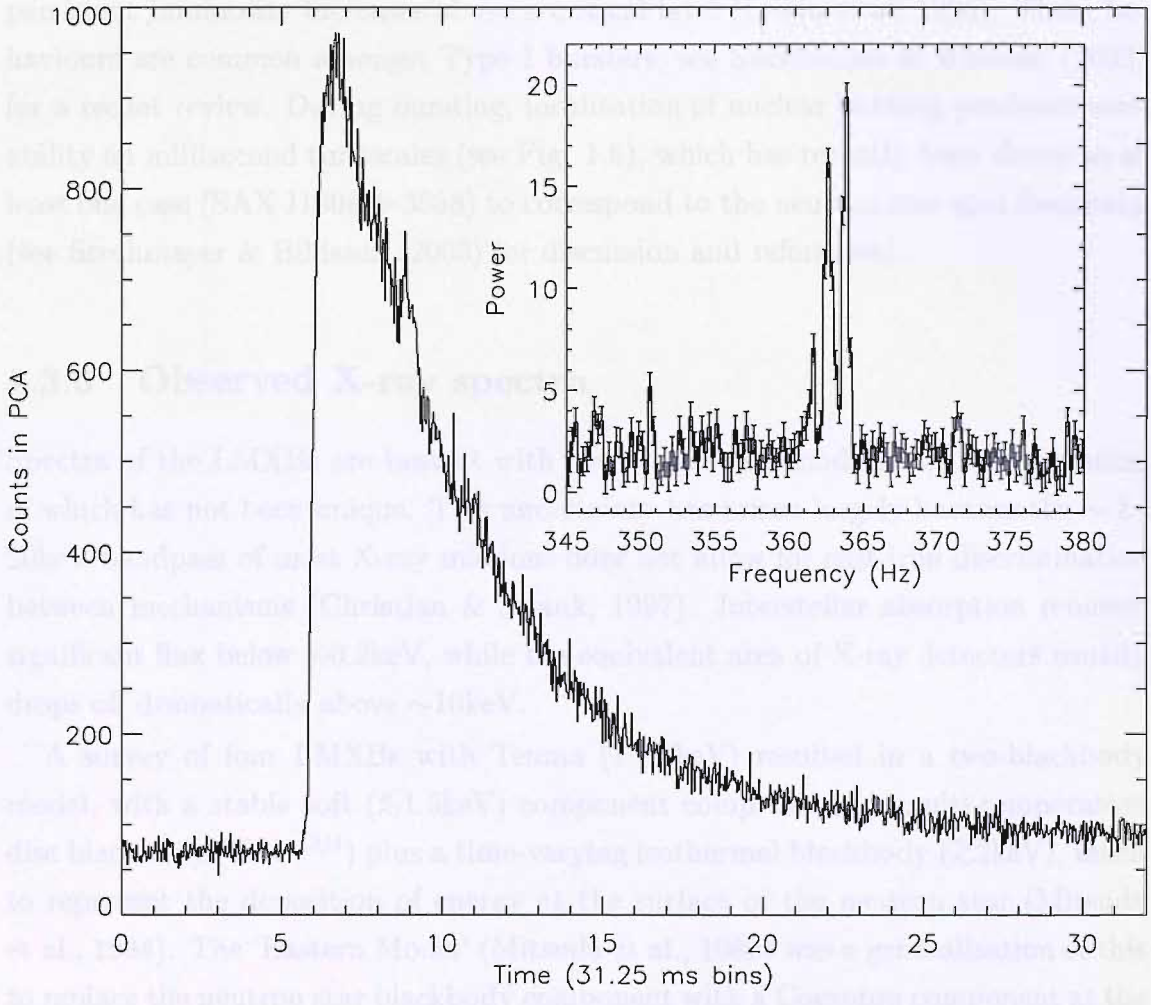

Figure 1.6: RXTE/PCA observation of a typical Type I X-ray burst from 4U 1728–34. The inset panel shows the power spectrum in the vicinity of 363 Hz. From Strohmayer et al. (1996).

as an inverse relation between the peak flux and the persistent luminosity and a strong dependence of the blackbody radius on the peak flux. More recently, RXTE and Chandra studies of the regular 'clockwork burster' X1826–268 show the burst recurrence time $t_{recur} \propto \dot{M}_1^{-1}$; this suggests, remarkably, a constant mass is accumulated between bursts (see Galloway et al. (2004) and Fig. 1.7). In the case of the luminous bursters X1820–303 and GX3+1, bursting ceases altogether when the persistent luminosity increases above a critical level (Lewin et al, 1995). These behaviours are common amongst Type I bursters; see Strohmayer & Bildsten (2003) for a recent review. During bursting, localisation of nuclear burning produces variability on millisecond timescales (see Fig. 1.6), which has recently been shown in at least one case (SAX J1808.4–3658) to correspond to the neutron star spin frequency (see Strohmayer & Bildsten (2003) for discussion and references).

1.3.3 Observed X-ray spectra

Spectra of the LMXBs are best fit with two component models, the interpretation of which has not been unique. This uncertainty has arisen largely because the $\sim$ 1–20keV bandpass of most X-ray missions does not allow for cast-iron discrimination between mechanisms (Christian & Swank, 1997). Interstellar absorption removes significant flux below $\sim$0.2keV, while the equivalent area of X-ray detectors usually drops off dramatically above $\sim$10keV.

A survey of four LMXBs with Tenma (1–37keV) resulted in a two-blackbody model, with a stable soft ($\lesssim$1.5keV) component comprised of a multi-temperature disc blackbody ($T \propto r^{3/4}$) plus a time-varying isothermal blackbody ($\gtrsim$2keV), taken to represent the deposition of energy at the surface of the neutron star (Mitsuda et al., 1984). The 'Eastern Model' (Mitsuda et al., 1989) was a generalisation of this to replace the neutron star blackbody component with a Compton component at the inner disc, with the seed photons taken from the blackbody emission at the surface of the neutron star. The 'Western Model' (White et al., 1988), based initially on EXOSAT observations in the 2–25keV bandpass, replaces the disc blackbody with a single Comptonised component, with the spectrum of seed photons unconstrained. A blackbody component is only required for the highest luminosity sources, when it is identified with the inner disc/neutron star surface boundary layer. Beyond this the geometry of the emission regions is largely unconstrained.

More recently, observations of the dipping LMXBs (see Section 1.4.2) have allowed the geometric extent of the Comptonised and blackbody regions to be uncovered

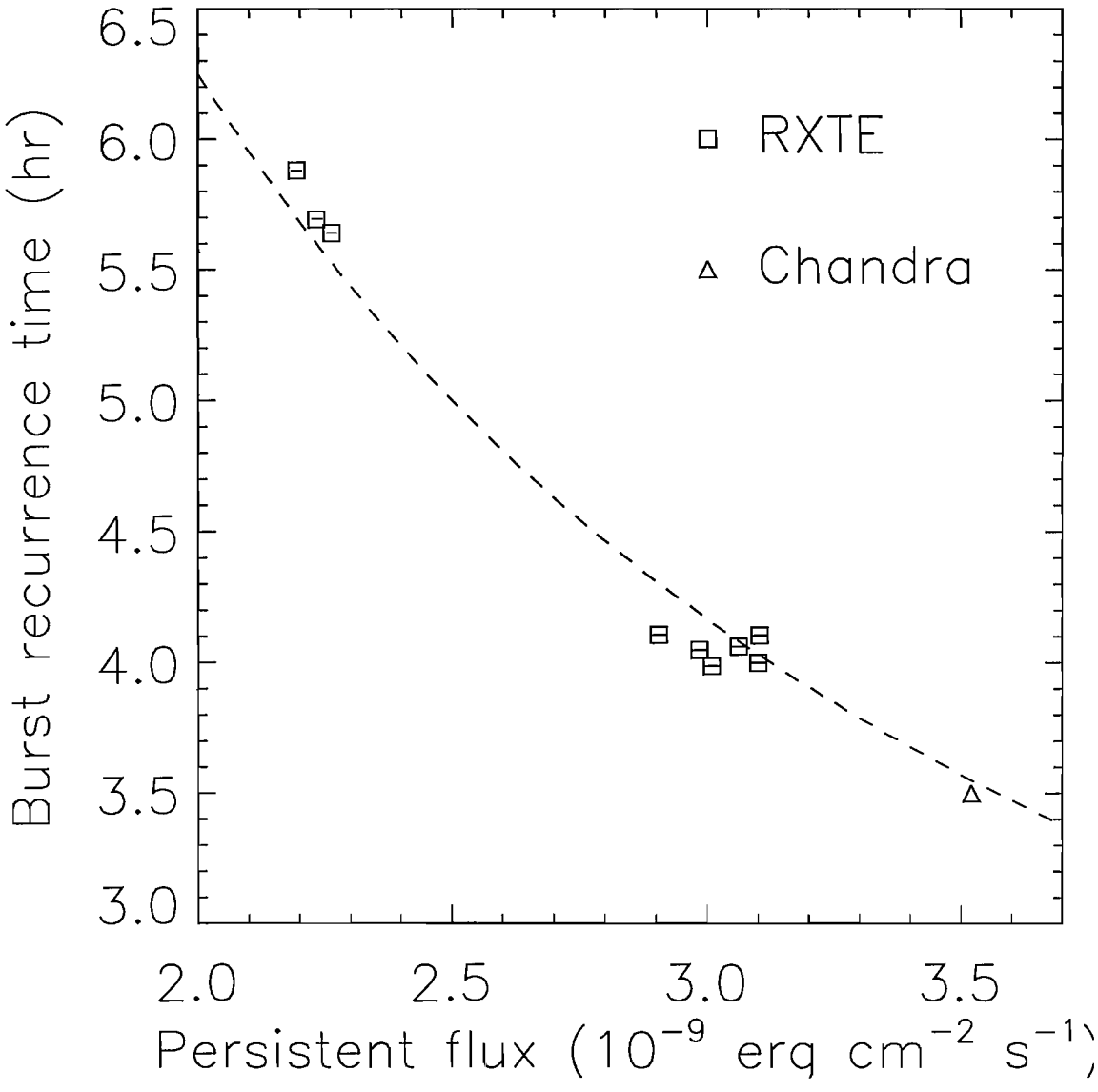

Figure 1.7: Burst recurrence time plotted against persistent flux. The dashed line is the trend expected for constant accumulated mass. From Strohmayer & Bildsten (2003).

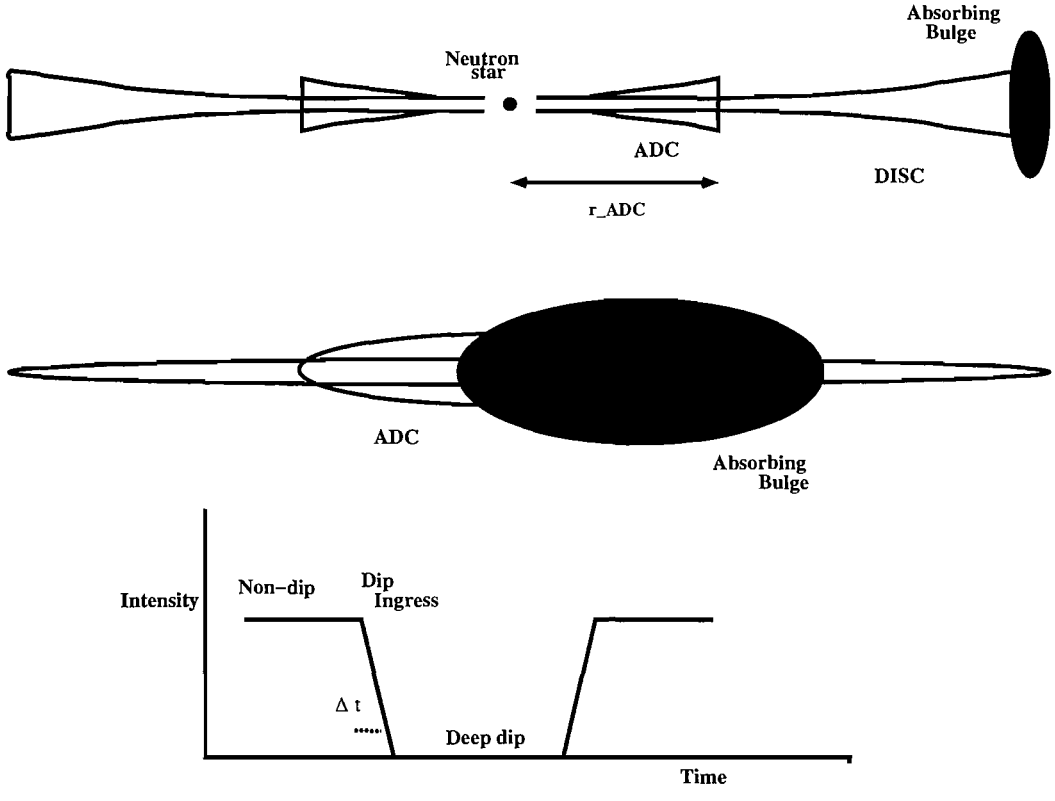

Figure 1.8: Schematic of emission components as suggested by X-ray spectra of the dipping sources. The accretion disc corona (ADC) is confined to a thin region above and below the accretion disc, producing a power-law component in the observed spectrum. From Church & Balucinska-Church (2004).

(Fig. 1.8). During an X-ray dip, flux is removed across all energies as the accretion disc rim blocks the inner disc region from view. Comparison of dip ingress lightcurves with X-ray spectra shows the blackbody component to be rapidly blocked, while the more gradual removal of the Comptonised component suggests it must originate in a region $\gtrsim$ 50,000km (or $\sim$15% of the accretion disc radius) in extent (Church et al., 1997). This accretion disc corona is not spherical but instead has a small height-to-radius ratio (Smale et al., 2001). This model was shown to fit a sample of ten LMXBs observed with ASCA (Church & Balucinska-Church, 2001), and has since been adopted by many authors. In both this two-component model and the Western model, no *direct* X-ray emission is observed from the accretion disc itself, instead the hot thermal plasma of the disc provides the seed photons for the observed Comptonised component (Barret, 2001).

We caution the reader that, while persuasive, this model is not yet accepted by all

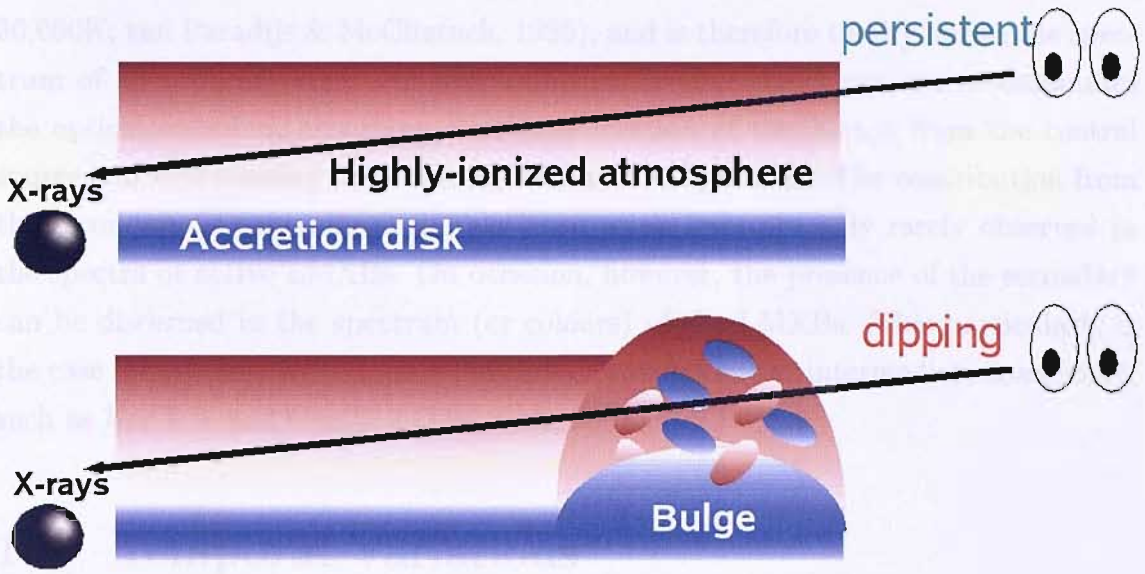

Figure 1.9: Boirin et al. (2005a) suggest that a highly-ionised atmosphere is present above the accretion disc and seen in absorption during persistent segments (top). During dipping (bottom), the bulge passes through the line-of-sight. It is denser, a bit less ionised and probably contains clumps of neutral material.

authors. Traditionally, the X-ray spectral changes during dipping have been modelled by invoking absorption of a point-like emission region by a neutral absorber, together with the progressive and partial covering of an extended emission region by another neutral absorber. Boirin et al. (2005a) proposed a novel explanation by invoking one emission region in addition to a neutral absorber and a photo-ionised absorber (Fig. 1.9). A highly ionised plasma is present above the accretion disc. If the binary is viewed relatively close to edge-on, the ionised plasma lies in our line-of-sight towards the X-rays emitted in the vicinity of the compact object. Signatures of the plasma appear in the spectrum, such as the Fe XXV and Fe XXVI absorption lines in the persistent (i.e. non-dipping) spectrum of 4U 1323–62 (Boirin et al., 2005b). At the azimuth where the stream of material from the companion star impacts the disc, there is material projected at higher altitudes above the disc. This bulge or thickened part of the disc passes through our line-of-sight during dipping. It is denser and less ionised than the plasma seen during persistent intervals, and probably contains lumps of neutral material (Boirin et al., 2005a).

1.3.4 Optical reprocessing

The optical spectrum of an LMXB consists of emission lines (particularly Hα, Hβ, He II λ4686 and C III-N III λ4630–50) superposed on a blue continuum (T_{eff} ~25,000–

30,000K; van Paradijs & McClintock, 1995), and is therefore totally unlike the spectrum of an ordinary star. An accretion disc around the X-ray source dominates the optical emission, absorbing a sizeable fraction of the X-rays from the central source and reprocessing them into optical and UV photons. The contribution from the secondary is generally negligible; absorption lines are only rarely observed in the spectra of active LMXBs. On occasion, however, the presence of the secondary can be discerned in the spectrum (or colours) of the LMXBs. This particularly is the case for systems with donors that are or started out as intermediate mass stars, such as Her X–1 and Cyg X–2 (Liu et al., 2001).

1.4 Temporal Variations

1.4.1 Transient and persistent sources

The Galaxy is populated with ~50 known persistent, bright LMXBs. Persistent sources are defined as those which have maintained an X-ray active state since they were first detected. Transient LMXBs are characterised by episodic periods of outburst at X-ray, optical and radio frequencies, which are separated by long periods of quiescence. The working definition of a transient source is a source which has been observed to vary in X-ray intensity by a factor >100 (with known binary eclipses discounted). There are several types of transient XRBs (e.g. periodic outbursts of HMXBs with eccentric orbits); however, in this section we consider only the soft X-ray Transients (SXTs), a subclass of LMXBs that are sometimes referred to as X-ray Novae.

A SXT outburst is due to a sudden dramatic increase in the rate of mass accretion onto the compact primary. The rise time of the X-ray flux is of the order of days, and its subsequent decline occurs on a time scale of months (White et al., 1984). The optical counterpart can brighten by ΔV ~7 mag, which greatly facilitates its optical identification. During the decline phase, the optical flux always falls much more slowly than the X-ray flux; the relative decay rates can be used to estimate the average temperature of the reprocessing region, with reported values in good agreement with those of the persistent LMXBs (van Paradijs & Verbunt, 1984).

During outburst, SXTs are very similar to persistent LMXBs in their X-ray luminosities, X-ray spectra, frequency of Type I burst behaviour and optical spectra. Thus, it is entirely reasonable to assume that SXTs are a subgroup of LMXBs in which accretion occurs spasmodically. It is believed that the cause of the sudden

increase in mass accretion onto the compact object is either a mass loss instability that arises in the secondary star (Bath, 1975; Hameury et al., 1986) or an instability in the accretion disc (Meyer & Meyer-Hofmeister, 1981; Faulkner et al., 1983; Tuchman et al., 1990).

1.4.2 Inclination Dependent Dipping Behaviour

In many XRB systems, the X-ray flux (and also flux in other wavebands) is periodically cut off at or near to the orbital period. For inclinations $i \gtrsim 60°$, elevated structure in the disc rim occults the compact object, leading to the removal of its flux across all wavebands. In the case of the HMXBs, inclination $\gtrsim 50°$ give rise to sharp eclipses of the compact object by the giant companion, allowing the radial extent and therefore mass of the donor to be estimated and providing a reliable system clock. However, eclipses in LMXBs are more rare; indeed, by 1970, X-ray lightcurves of some 25 sources had been collected, with *none* showing full eclipses (Charles & Seward, 1995), suggesting some mechanism was preventing the observation of eclipses by the donor. No such selection effect is observed in the HMXBs, which as a class possess much smaller accretion discs and more extended donors.

The natural interpretation is that some feature of the accretion disc, probably outer rim structure, extends so far out of the plane that, from the point of view of the point source, it subtends a greater solid angle than the donor (Frank et al., 1987). This indeed appears to be the case; the X-ray lightcurve of EXO 0748–676, the first eclipsing LMXB discovered, shows eclipses lasting just eight minutes out of a total binary period of almost 4 hours (Fig. 1.10), corresponding to a finely-tuned inclination that allows the line of sight to pass through high donor latitudes.

Thus for LMXBs the nature of dipping behaviour is highly inclination dependent; at moderate inclinations ($i \gtrsim 60°$) dipping is due to structure in the mid-outer disc, while for a narrow range of inclinations ($75° \lesssim i \lesssim 80°$) the donor may also eclipse the compact object (Fig. 1.11). At higher inclinations ($\gtrsim 80°$), the outer accretion disc obscures the compact object for most (if not all) of the orbit.

Variation in the height of the disc rim structure can produce eclipses on or near the orbital period, but these eclipses are *partial*, suggesting an extended region is producing the observed emission: the Accretion Disc Corona (ADC). Observations of the prototypical ADC source X 1822–371 provided the first evidence for an extended emission region; the component not removed by the accretion disc rim must be the spatially extended corona (see Fig. 1.10). In the ADC sources, the inner disc and

neutron star are never directly visible, as suggested by the absence of Type I burst behaviour from any ADC source. It is only X-rays scattered into our line of sight from the corona that we manage to observe. ADC sources are thus under-luminous in the X-ray by a factor ~5–50, with X-ray to optical ratio $L_X/L_{opt} \sim 20$ compared to the usual ~100–1000 for LMXBs (White et al., 1995).

1.4.3 Optical lightcurves

Many LMXBs show an orbital modulation of their optical light. This indicates that the distribution of reprocessing material is not axi-symmetric about the X-ray source.

The amplitude, A, of the light curve depends on the orbital inclination i. For low inclinations (no X-ray eclipses or dips, see Section 1.4.2) the light curves are approximately sinusoidal, with A ~0.2–0.3 mag (van Paradijs & McClintock, 1995). At somewhat higher i (i.e. X-ray dips but no eclipses), A ~0.5 mag. For these non-eclipsing systems, minimum light coincides with the superior conjunction of the compact star; this indicates that the optical light curve reflects the X-ray heating of the secondary, insofar as this is not in the X-ray shadow of the disc. The same is likely to be the case for the light curves of the low-inclination systems for which the amplitude of the light curve predominantly reflects the ratio of solid angles (as seen from the X-ray source) of the secondary and the disc.

When X-ray eclipses occur, A reaches ~1.5 mag. The light curves of these systems can be decomposed into the sine wave that is also observed for the low-i systems, and a cusp superposed on the minimum of the sine wave. The cusps are due to the eclipse of the accretion disc.

The dependence of A on i reflects the fact that as i decreases, the relative brightness of the disc increases (larger projection factor, less self-shielding), and the importance of the variable component (eclipses of the disc, X-ray heating of the companion star) decreases.

In HMXBs, and during X-ray off states in LMXBs, the tidal deformation of the donor is sometimes measurable as a variation in the optical brightness of the source on the orbital period, with two maxima and two minima per orbit that occur at quadratures and conjunctions respectively. For a spherical star the projected emitting area is constant, but when the star assumes the shape of its Roche lobe, this projected area becomes a function of orbital phase. Fitting this ellipsoidal variation allows constraints to be placed on the inclination of the system (see e.g.

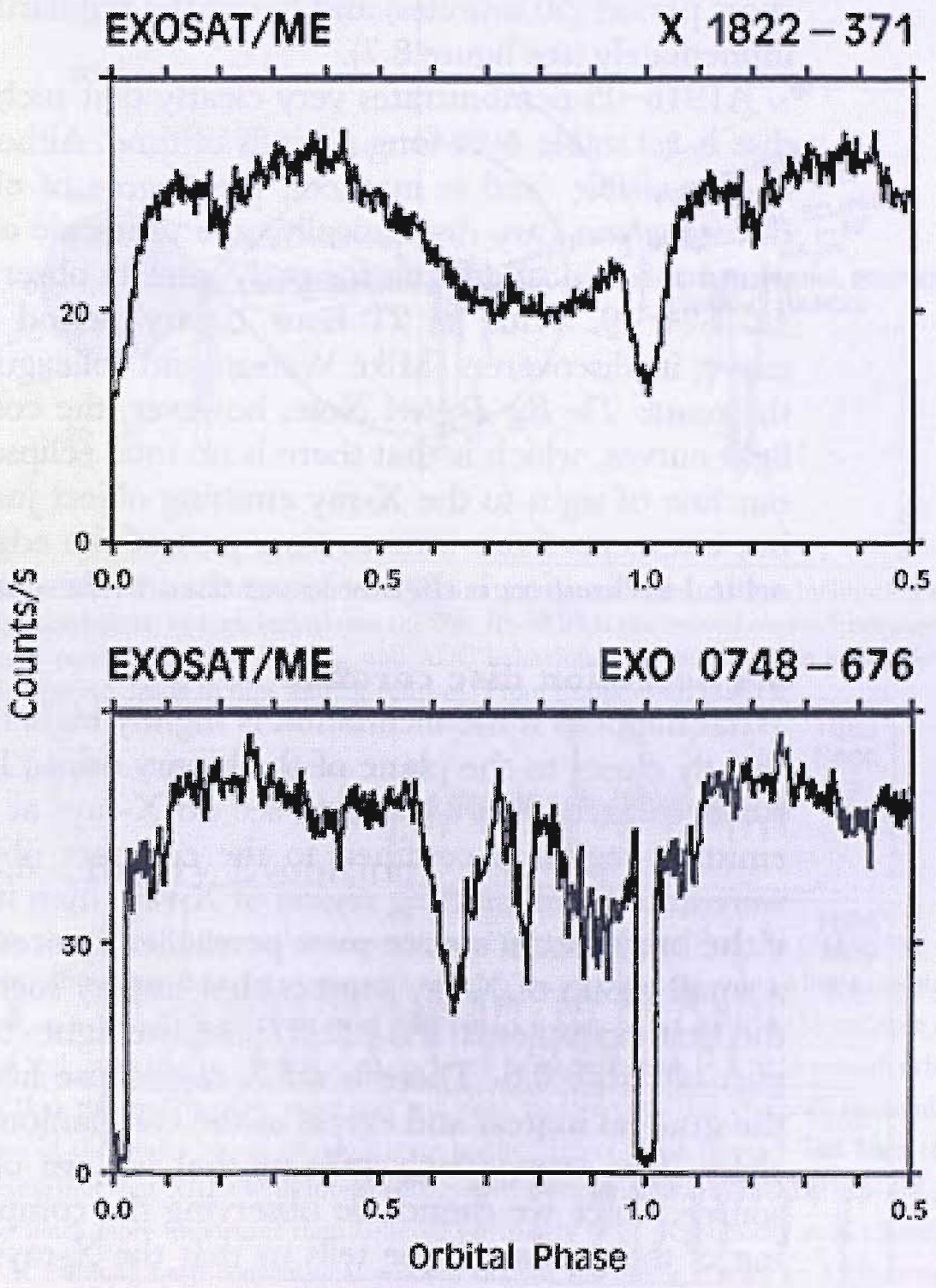

Figure 1.10: EXOSAT lightcurves of the prototypical ADC source X 1822–371 and the prototypical dipper EXO 0748–676. Notice that for X 1822–371 the eclipse is broad and partial, indicating an extended, scattered component. From Charles & Seward (1995).

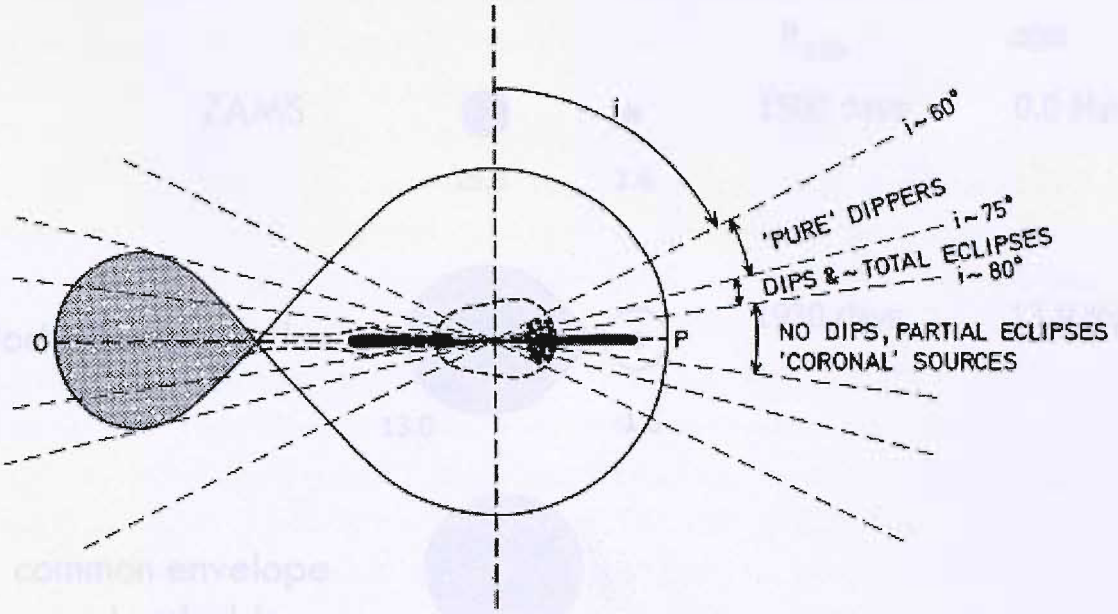

Figure 1.11: The standard model of inclination dependence. At low inclination no dips are visible; at high inclination the disc rim shields the central source from direct sight, producing a low L_X/L_{opt} and ADC behaviour. At intermediate inclinations the disc rim leads to dips and/or eclipses. From Frank et al. (1987).

Kuiper et al., 1988, and Section 2.1.3).

1.5 Binary Evolution

The classic LMXB formation scenario (see Fig. 1.12) argues that the progenitors of these objects are binary systems with extreme mass ratios containing a low mass star and an extremely high mass star. The binary system must survive the collapse of the high mass star to a neutron star or black hole and remain in a tight enough orbit so that the evolving low mass star will shed matter onto this compact remnant[4]. One of the major recent developments in the field of XRB research has been the realisation that XRBs with intermediate-mass companion stars (IMXBs; 1.5–4$M_\odot$) are much more important than believed previously (e.g. Kobulnicky et al., 2006).

It has long been conventional wisdom that, if the donor star in an XRB is significantly higher in mass than the accreting neutron star, mass transfer would be unstable on a dynamical timescale (see Section 1.2.1), and therefore such systems

[4]Note that in globular clusters, with high stellar densities, an XRB may be formed via dynamical interactions between a free neutron star and a stellar object (tidal capture) or partner swapping with another binary system (see Section 1.1.2).

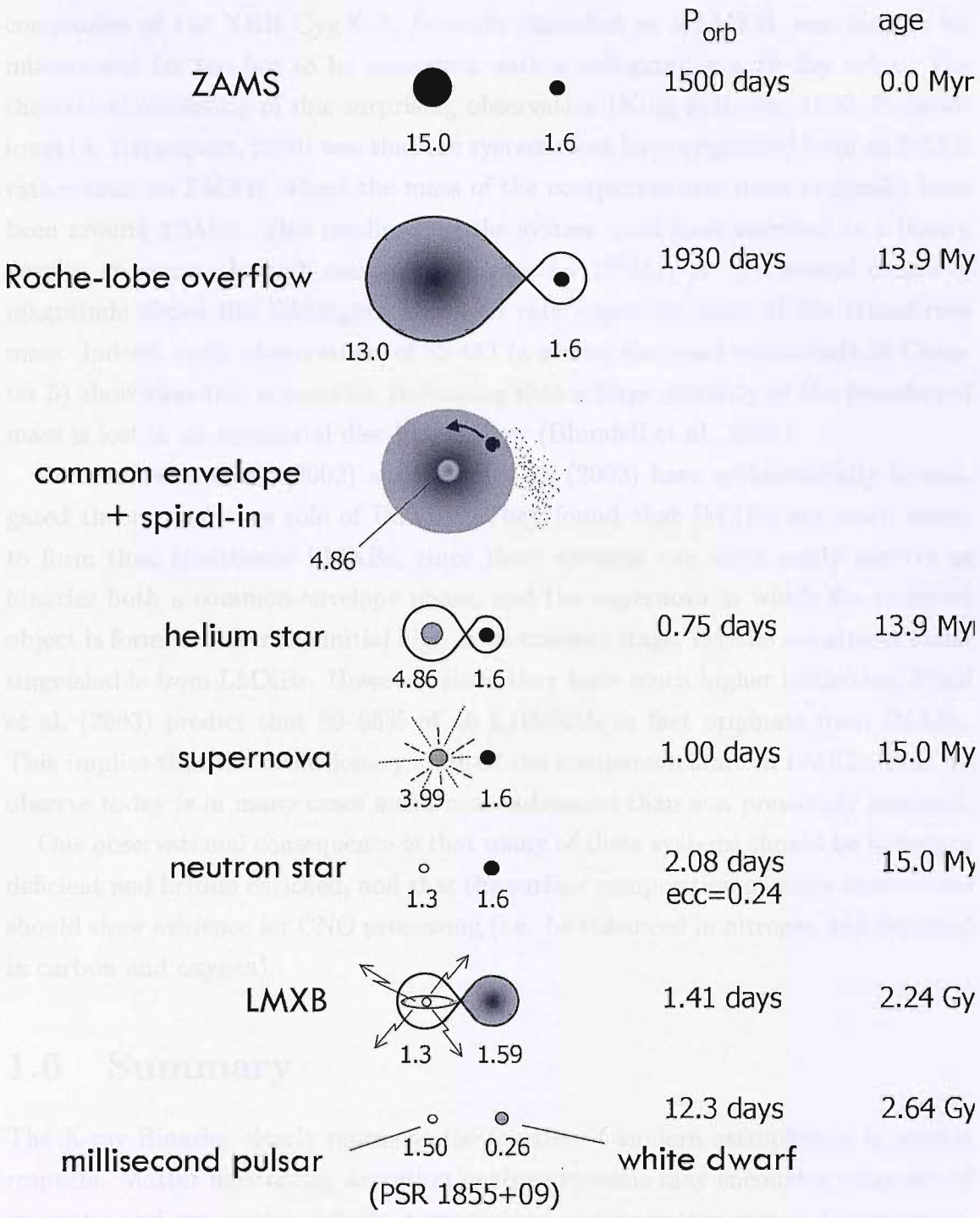

Figure 1.12: Cartoon depicting the evolution of a binary system eventually leading to an LMXB and finally the formation of a binary millisecond pulsar. The parameters given are for a scenario leading to the formation of the observed binary millisecond pulsar PSR 1855+09. The stellar masses given are in solar units. Taken from Tauris & van den Heuvel (2003).

would not survive. However, observations by Casares et al. (1998) showed that the companion of the XRB Cyg X–2, formerly classified as a LMXB, was far too luminous and far too hot to be consistent with a sub-giant in a 10 day orbit. The theoretical resolution of this surprising observation (King & Ritter, 1999; Podsiadlowski & Rappaport, 2000) was that the system must have originated from an IMXB rather than an LMXB, where the mass of the companion star must originally have been around $3.5 M_{\odot}$. This implies that the system must have survived as a binary despite an extremely high mass-transfer rate ($\sim 10^5 M_{\odot}$ yr^{-1}) - several orders of magnitude above the Eddington accretion rate - ejecting most of the transferred mass. Indeed, radio observations of SS 433 (a source discussed extensively in Chapter 5) show that this is possible, indicating that a large quantity of the transferred mass is lost in an equatorial disc-like outflow (Blundell et al., 2001).

Podsiadlowski et al. (2002) and Pfahl et al. (2003) have systematically investigated theoretically the role of IMXBs. They found that IMXBs are much easier to form than traditional LMXBs, since these systems can more easily survive as binaries both a common-envelope phase, and the supernova in which the compact object is formed. After the initial high mass-transfer stage, IMXBs are almost indistinguishable from LMXBs. However, since they have much higher birthrates, Pfahl et al. (2003) predict that 80–95% of all L/IMXBs in fact originate from IMXBs. This implies that the evolutionary state of the companion stars in LMXBs that we observe today is in many cases much more advanced than was previously assumed.

One observational consequence is that many of these systems should be hydrogen deficient and helium enriched, and that the surface composition of many secondaries should show evidence for CNO processing (i.e. be enhanced in nitrogen and depleted in carbon and oxygen).

1.6 Summary

The X-ray Binaries clearly represent the frontier of modern astrophysics in several respects. Matter undergoing accretion in these systems may encounter extremes of magnetic and gravitational fields, temperature and ionisation states. Furthermore, understanding these systems requires the development of new techniques in astronomy, in sensitivity, time resolution and spectral resolution, to provide the necessary information to follow the energetics of such systems fully.

Chapter 2

Extracting the System Parameters of Low Mass X-Ray Binaries

Building up the mass distribution of compact objects is a fundamental experiment in modern astrophysics, and XRBs provide an interesting test bed. Dynamical studies and the mass determination of compact stars in LMXBs can yield new black hole discoveries and, more importantly, probe for the existence of 'massive' neutron stars. The latter, for example, could rule out certain softer equations of state for the nuclear matter which makes up a neutron star (e.g. Brown & Bethe, 1994). However, accurate dynamical information about both components in LMXBs has been very difficult to acquire, yet is essential if accurate masses are to be determined. Hence, evidence for the nature of the compact object in most bright LMXBs is indirect, for example X-ray bursting behaviour indicating the presence of a neutron star.

The majority of detailed LMXB mass constraints are accounted for by the transient systems. In quiescence, SXTs become a valuable resource for research into the nature of LMXBs. Typically their optical brightness has declined by a factor of $\geq$100, with all known SXTs having quiescent $V \sim 16 - 23$, which is now dominated by the companion. With large telescope optical and infra-red spectroscopy it is possible to determine the spectral type, period and radial velocity curve of these objects (see e.g. the Charles & Coe 2003 review for details). Nevertheless, some dynamical information can be derived even during outburst, given spectroscopic data of sufficient resolution. Casares et al. (1995) observed GRO J0422+32 during an X-ray mini-outburst and found intense Balmer and He IIλ4686 emission modulated on what was subsequently found to be P_{orb}. Furthermore, a sharp component within the (highly complex) He II emission profile displayed an S-wave that was likely associated with the accretion hotspot (the point at which the accretion stream and disc

intersect).

Since few LMXBs are X-ray pulsars, remarkably little is known of the fundamental parameters of the persistently X-ray luminous LMXBs. With the exception of a few long period (P_{orb} >1d) systems with evolved donors (e.g. Cyg X–2, X 0921–630), spectroscopic features of the companion stars are perpetually veiled in the glare of the X-ray illuminated accretion disc. Attempts to derive dynamical information from the compact star using emission lines (mainly Balmer or He II λ4686) have proven unreliable because the emission lines are very broad (~500–1000 km s^{-1}) and show a complex, variable, multi-component structure. Indeed, in spite of being the brightest LMXB in the sky (both optically and in X-rays), key parameters of Sco X–1 have only been determined very recently (see Section 2.2.4.1).

2.1 Dynamical Mass Measurements

The *mass function* (see Ostlie & Carroll, 1996, Chapter 7 for a derivation) relates the masses of the compact object M_X, the companion star M_2 (or alternatively the binary mass ratio q) and the binary inclination angle i with two quantities which may be extracted directly from the radial velocity curve of the companion star: the orbital period P_{orb} and the radial velocity semi-amplitude K_2

$$f(M_X) = \frac{K_2^3 P_{orb}}{2\pi G} = \frac{M_X^3 \sin^3 i}{(M_X + M_2)^2} = \frac{M_X \sin^3 i}{(1+q)^2} \tag{2.1}$$

Since $M_2 > 0$ and $0° < i < 90°$ it is straightforward to see that $f(M)$ is a lower limit on M_X. Therefore, a mass function larger than ~$3M_\odot$, i.e. the maximum gravitational mass of a neutron star (Rhoades & Ruffini, 1974), is taken as strong evidence for the existence of a black hole, independently of the actual values of i and q. However, even if both radial velocities are measurable, it is not possible to get exact values for M_X and M_2 without knowledge of the system inclination i and mass ratio q.

2.1.1 Orbital Period

The orbital period is perhaps the most fundamental binary parameter, and may be inferred by extracting periodic signals out of a dataset. This typically involves a combination of photometric and/or spectroscopic measurements.

X-ray observations of X 0748–676 and X 1822–371 display clear, periodic eclipses

(see Fig. 1.10) caused by the donor star passing in front of the compact X-ray source. Courvoisier et al. (1986) observed periodic dips in the X-ray lightcurve of XB 1254–690, and this period is reflected in the optical waveband (Motch et al., 1987). Whilst this can be construed as strong evidence for an orbital period, in the absence of eclipses or radial velocity measurements it is still possible that these variations in the optical and X-ray lightcurves could reflect some alternative, super-orbital period (perhaps the precession of a tidally deformed, elliptical, warped or tilted disc, e.g. SS 433, see Chapter 5; Her X–1, Gerend & Boynton, 1976).

Spectroscopic observations leading to a radial velocity curve of either the primary or donor star can provide a secure detection of a system's orbital period. For example, the period of the SXT GX 339–4 remained indeterminate until Hynes et al. (2003) were able to detect emission lines associated with both the donor star and the compact object (the Bowen blend and the wings of the He II λ4686 line respectively, see Sections 2.1.4 and 2.2.4.2). Fitting the radial velocities of these two lines led to a consistent estimate for the orbital period.

Table 2.1 displays an (incomplete) list of LMXB modulation properties, including information about the modulation period and the nature of the modulation. Note that there are many LMXBs (in particular the persistent sources) in which the periodicity observed has not been confirmed as orbital in origin (such confirmation requiring either eclipses or radial velocity curves).

2.1.2 Mass ratio and rotational broadening

The ratio of the stellar masses in a binary system, q, is related to the observed radial velocity semi-amplitudes K of the two stellar components, independently of the angle of inclination of the system, by

$$q = \frac{M_2}{M_X} = \frac{K_X}{K_2} \tag{2.2}$$

However, it is not always possible to determine the radial velocities of *both* the stellar components in a LMXB system.

In quiescent systems, the mass ratio may be derived by measuring the rotational broadening of the companion spectrum. In short period interacting binaries the secondary is constrained to co-rotate with the primary and must also be filling its Roche lobe (in order for mass transfer to occur). Hence R_2 may be estimated using equation 1.6, and then (Wade & Horne, 1988):

Table 2.1: LMXB Modulation Properties

Source	Period (hrs)	Nature of modulation	X-ray type
X1820-303	0.19	X-ray	Burster, glob.cl.
4U 1850–087	0.34	UV	Burster, glob.cl.
X1626-673	0.7	opt sideband	Burster, Pulsar
X1832-330	0.73	UV	Burster, glob.cl.
X1916-053	0.83	X-ray, opt	Burster, Dipper
J1808.4-3658	2.0	pulsation RV	Burster, Pulsar, Transient
X1323-619	2.9	X-ray dip	Burster, Dipper
X1636-536	3.8	opt	Burster
X0748-676	3.8	eclipsing	Burster, Dipper, Transient
X1254-690	3.9	X-ray dip, opt	Burster, Dipper
X1728-169	4.2	opt	
X1755-338	4.4	X-ray dip	Dipper
X1735-444	4.6	opt	Burster
J0422+32	5.1	opt RV	BH, Transient
X2129+470	5.2	opt	ADC
X1822-371	5.6	eclipsing	ADC
J2123-058	6.0	eclipsing	Burster, Transient
N Vel 93	6.9	opt RV	BH, Transient
X1658-298	7.2	X-ray dip	Burster, Dipper
A0620-00	7.8	opt RV	BH, Transient
G2000+25	8.3	opt RV	BH, Transient
A1742-289	8.4	eclipsing	Burster, Transient
X1957+115	9.3	opt	
N Mus 91	10.4	opt RV	BH, Transient
N Oph 77	12.5	opt RV	BH, Transient
Cen X-4	15.1	opt RV	Burster, Transient
X2127+119	17.1	eclipsing	Burster, ADC, glob.cl.
Aql X-1	19	opt	Burster, Transient
Sco X-1	19.2	opt	Prototype LMXB
X1624-490	21	X-ray dip	Dipper
GX 339–4	42.1	opt RV	BH, Transient
N Sco 94	62.6	opt RV	BH, Transient
V404 Cyg	155.4	opt RV	BH, Transient
2S0921-630	216	eclipsing	ADC
Cyg X-2	235	opt RV	Burster
J1744-28	283	pulsation RV	Burster, Pulsar, Transient

adapted from Charles & Coe (2003)

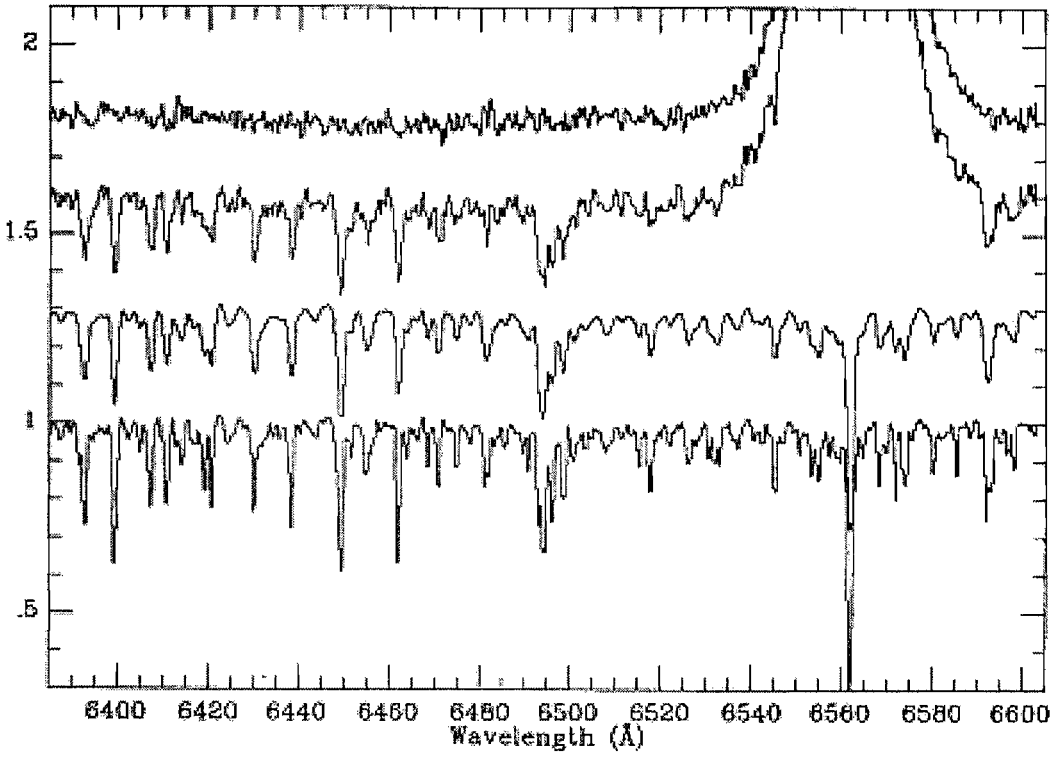

Figure 2.1: Determining the rotational broadening in V404 Cyg. From bottom to top: the K0IV template (HR8857); the same spectrum broadened by 39 km s^{-1}; Doppler corrected sum of V404 Cyg (dominated by disc Hα emission); residual after subtraction of the broadened template. From Casares & Charles (1994).

$$v_{rot} \sin i = \frac{2\pi R_2}{P} \sin i = 0.462 \; K_2 \; q^{1/3}(1+q)^{2/3} \tag{2.3}$$

from which q can be derived if $v_{rot} \sin i$ is measured. Typically $v_{rot} \sim 40$–$100\,\mathrm{km\,s^{-1}}$, which requires high resolution and high signal-to-noise spectra of the secondary.

The method is demonstrated in figure 2.1 for V404 Cyg (Casares & Charles, 1994), based upon techniques developed by Marsh et al. (1994). The Doppler-corrected and summed spectrum of V404 Cyg is dominated by broad Hα emission from the disc, but the cool companion absorption features are visible and clearly broader than those of the template K0IV spectrum. The template is broadened by a range of different velocities by convolution with the rotational profile of Gray (1992), assuming a linearised limb-darkening coefficient. The broadened templates are also multiplied by a variable factor to account for the continuum excess of the accretion disc. The template spectra are subtracted from that of the target and

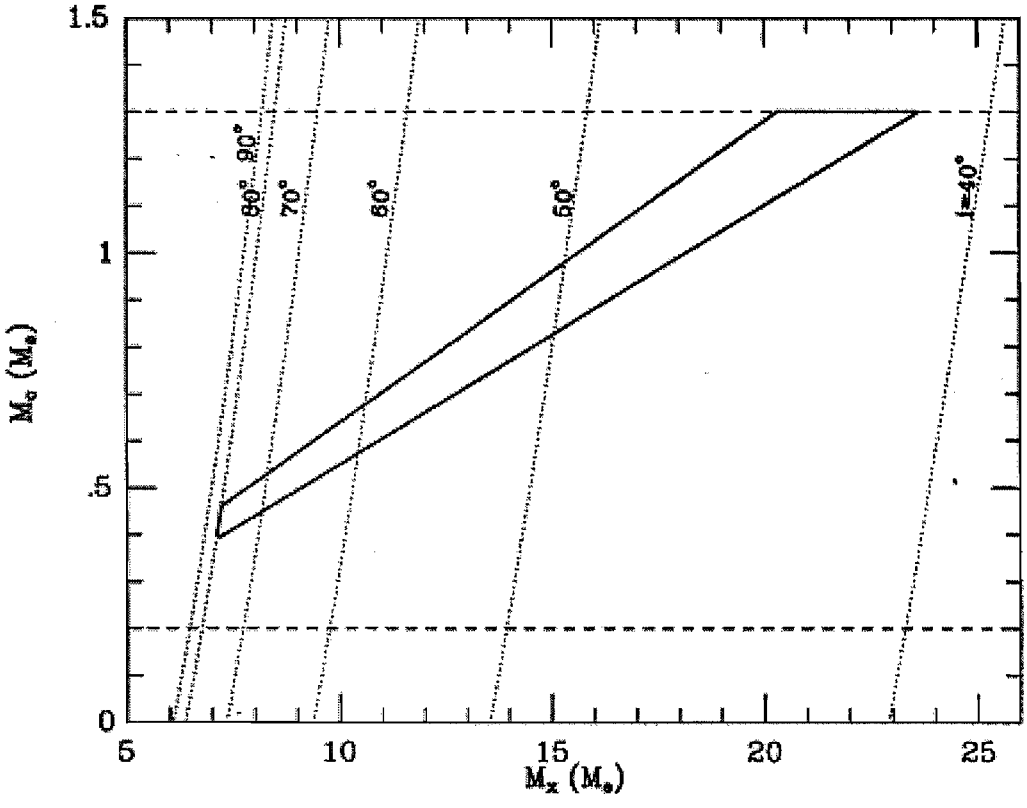

Figure 2.2: Constraints on M_X and M_2 for a range of values of i in V404 Cyg based on the radial velocity curve (giving $f(M)$=6.1$M_\odot$), and determination of q (0.06) from rotational broadening. It is the limited constraint on i (absence of eclipses) that leads to a wide range of M_X. From Casares & Charles (1994).

the residuals χ^2 tested. In the case of V404 Cyg, Casares & Charles (1994) found an optimal broadening of $v_{rot} \sin i = 39 \pm 1$ km s^{-1} and hence were able to derive a mass ratio of $q = 0.06^{+0.004}_{-0.005}$.

The combination of q and $f(M)$ then yields the mass constraints shown in Fig. 2.2), with the only remaining unknown being the inclination i. To date, none of the SXTs is observed to be eclipsing (see Section 1.4.2), and so it is the uncertainty in i that dominates the final mass measurement. Nevertheless there are methods by which i can be estimated.

2.1.3 Estimating the system inclination

The X-ray lightcurves of LMXBs are an excellent way to estimate the inclination of the orbital plane to our line of sight (see Section 1.4.2). In particular, dips and eclipses (both partial and full) caused by material in the accretion disc or

the companion star have provided a good indication regarding the inclination of a number of X-ray bright systems. However, this technique for estimating orbital inclination is necessarily limited to only those systems which lie at a high inclination ($i \gtrsim 60°$) *and* have been caught exhibiting these orbital variations. For example, the well known dipping source XB 1254–690 (see Chapter 3) can pass through many orbital cycles without showing any evidence for dipping (Smale & Wachter, 1999).

Many LMXB systems display evidence of jet emission at radio frequencies (see Fender, 2003, for a review of the jet characteristics of XRBs). Measurement of the jet kinematics, or more specifically the jet's angle to the line of sight, can provide an estimate for the system inclination, under the assumption that the jet is launched perpendicular to the plane of the binary. This is particularly useful for low-inclination, persistent sources such as Sco X–1 (Fomalont et al., 2001). Measurements of the jet kinematics have also provided a very accurate estimate for the system inclination of the intriguing precessing jet source SS 433 (e.g. Eikenberry et al., 2001, see Chapter 5). However, a note of caution must be sounded here since there are at least two jet sources (GRO J1655–40 and V 4641 Sgr) which appear to show significant misalignments from the revolution axis of the orbital plane (Maccarone, 2002, and references therein).

The secondary star in interacting binaries has a peculiarly distorted shape which gives rise to the so-called *ellipsoidal modulation* (see Section 1.4.3) in massive X-ray binaries and quiescent SXTs. This leads to the classical double-humped light curve (Fig.2.3) primarily due to the tidal and rotational distortion of the primary star, and a non-uniform distribution of its surface brightness (gravity darkening). This is well defined by theory, and the observed light curve depends principally on q and i. The technique has been successfully applied to a number of XRBs in order to derive system inclinations to a remarkable level of accuracy, including the SXTs GRO J1655–40 (Orosz & Bailyn, 1997) and XTE J2123–058 (Shahbaz et al., 2003) during quiescent intervals.

In the case of persistent LMXBs, some simple geometrical modelling is possible by considering the X-ray illuminated area of the companion star, the disc radius and opening angle, and the inclination. This can be compared with the observed optical flux and the amplitude of the orbital light curve (see Section 1.4.3) to determine broad constraints on the source inclination. In combination with observations of X-ray dips, Motch et al. (1987) were able to constrain the inclination of XB 1254–690 to $65° - 73°$ in this way (see Chapter 3).

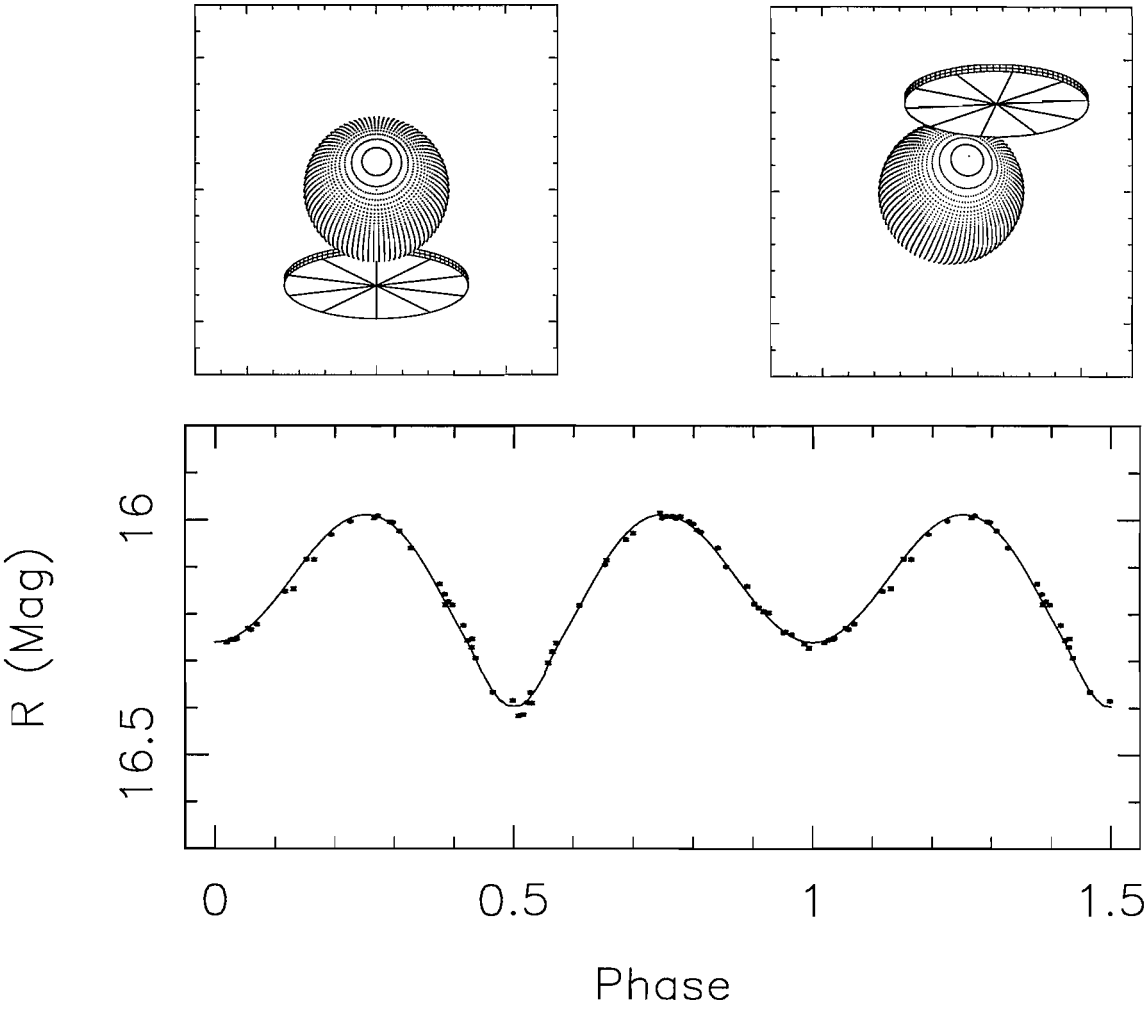

Figure 2.3: R-band light curve of GRO J1655–40 in quiescence (from van der Hooft et al., 1997) together with schematics of the system orientation (taken from Orosz & Bailyn, 1997) which show the grazing eclipses required by fits to the light curve.

2.1.4 Measuring the motion of the compact object

Emission line profiles in LMXBs can be extremely complicated, with a large number of different emission sites (inner accretion disc, accretion disc hot spot, accretion stream, heated inner face of the donor star etc.) contaminating each line. As a result, in the absence of pulsations from the compact object, it is not trivial to determine the radial velocity of the central object. A simple measurement of the orbital variations of an emission line core (either by visual centering or Gaussian fitting) is highly likely to be contaminated by various different sources, and thus will not provide a true trace of the motion of the compact object (see e.g. Orosz et al., 1994).

However, accretion discs possess a Keplerian velocity field, involving circular orbits with velocity v $\propto R^{-0.5}$ (see e.g. Marsh & Horne, 1988). The highest velocity regions are nearest to the disc centre, and thus closely follow the motion of the compact object. By measuring the wings of an emission line, any asymmetries caused by enhanced emission from alternative sites can be bypassed and a truer measure of the compact object radial velocity K_1 can be obtained.

The radial velocity of the inner accretion disc can be extracted by convolving the data with a template consisting of two Gaussian bandpasses, one in each wing of the emission line profile. Specifically, the position of a spectral feature in a spectrum $f(\Lambda)$ is determined by solving the following equation (Schneider & Young, 1980):

$$\int f(\Lambda)K(\lambda - \Lambda)d\Lambda = 0 \tag{2.4}$$

where

$$K(x) = \exp[-(x-a)^2/2\sigma^2] - \exp[-(x+a)^2/2\sigma^2] \tag{2.5}$$

The width (σ) and separation (a) of the Gaussians can be adjusted to measure the velocity at any position in the line profile.

In the majority of cases any asymmetries in the line profile are attributed to contamination by emission from the vicinity of the hot spot. In this case the contamination should be concentrated near a velocity which is representative of the projected Keplerian velocity at the outer rim of the disc. Nevertheless, in some cases the asymmetry may persist well out into the line wings (e.g. the intermittent excess emission in the blue line wings of the Hα emission lines in A 0620–00 and Nova Muscae 1991; Orosz et al., 1994). For obvious reasons, it is desirable to know the magnitude and extent of any such contamination.

A good way to investigate the extent of any phase-dependent line asymmetries which may be present is to measure the lines using a variety of separations for the Gaussians. In this way the line profile may be 'mapped out' in velocity space and any phase-dependent asymmetries may be readily identified. The resulting velocities can then be fitted with sinusoids of the form

$$V(t) = \gamma - K_1 \sin\left(\frac{t - t_0}{P}\right) \tag{2.6}$$

where γ is the systemic velocity, P the orbital period, K_1 the radial velocity semi-amplitude and t_0 the time of conjunction.

It is instructive to plot K_1, γ and t_0 as functions of the Gaussian separation a (see Fig. 2.4). If the line contamination is confined to relatively low velocities, then the solution for K should asymptotically approach the correct value when a becomes sufficiently large. Furthermore, since the phasing of any perturbing component is not generally expected to be in agreement with the orbital motion, any contamination will usually lead to a spurious phasing in the orbital solution. In this case, we expect that the phasing as measured by the value of t_0 from the orbital solution, will be a function of a. For sufficiently large values of a, then, we can expect the $t_0(a)$ curve to flatten out if the perturbing component is confined to low velocities (Shafter, 1985; Shafter et al., 1986).

Selection of the emission line used to trace the motion of the compact object is very important. The low excitation lines (Balmer, He I) can be produced in many different locations in LMXBs, and thus are highly likely to be contaminated by a mélange of different emission sites. He II λ4686 has a much higher excitation temperature than the Balmer and He I lines and is therefore expected to form in a hotter region of the accretion disc. As a result, one would expect the radial velocity variations of the He II emission to reflect the motion of the central compact object with more reliability than the Balmer emission.

Alternatively, K_1 can also be estimated using the technique of Doppler Tomography (see Section 2.3)

2.2 Bowen Fluorescence

Bowen (1934, 1935) first suggested a resonance fluorescence mechanism for the creation of certain intense permitted emission lines of O III and N III in planetary nebulae. The mechanism is the result of a set of chance coincidences between ultraviolet

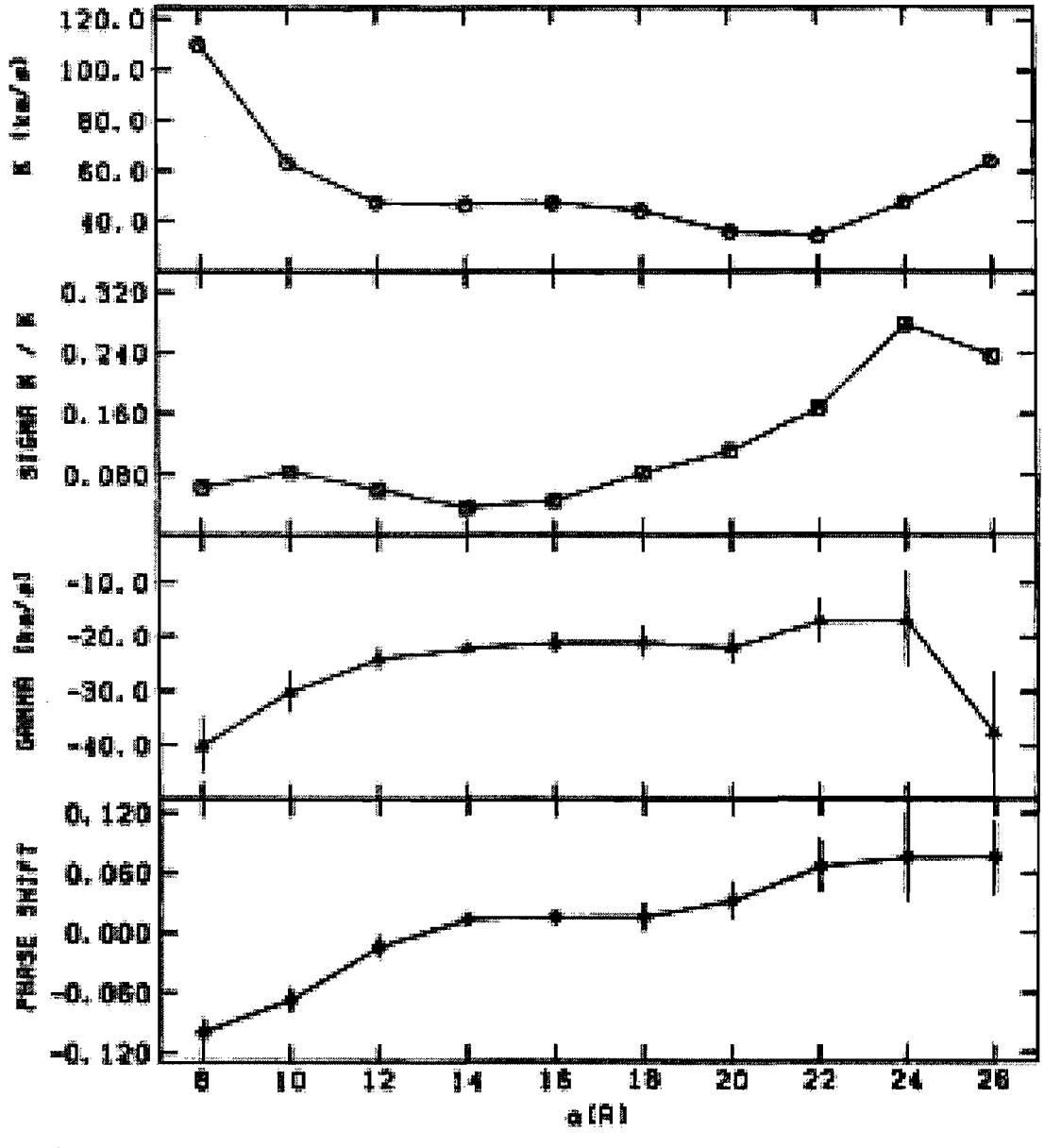

Figure 2.4: The diagnostic diagram for the white dwarf system SW UMa. The K-velocity increases when measurements are made near the line centre. As one measures farther into the line wings the K-velocity converges to a value of 47 km s^{-1}. For values of the Gaussian separation a greater than $\sim$ 16Å the velocity measurements begin to be contaminated by noise in the continuum. Taken from Shafter et al. (1986).

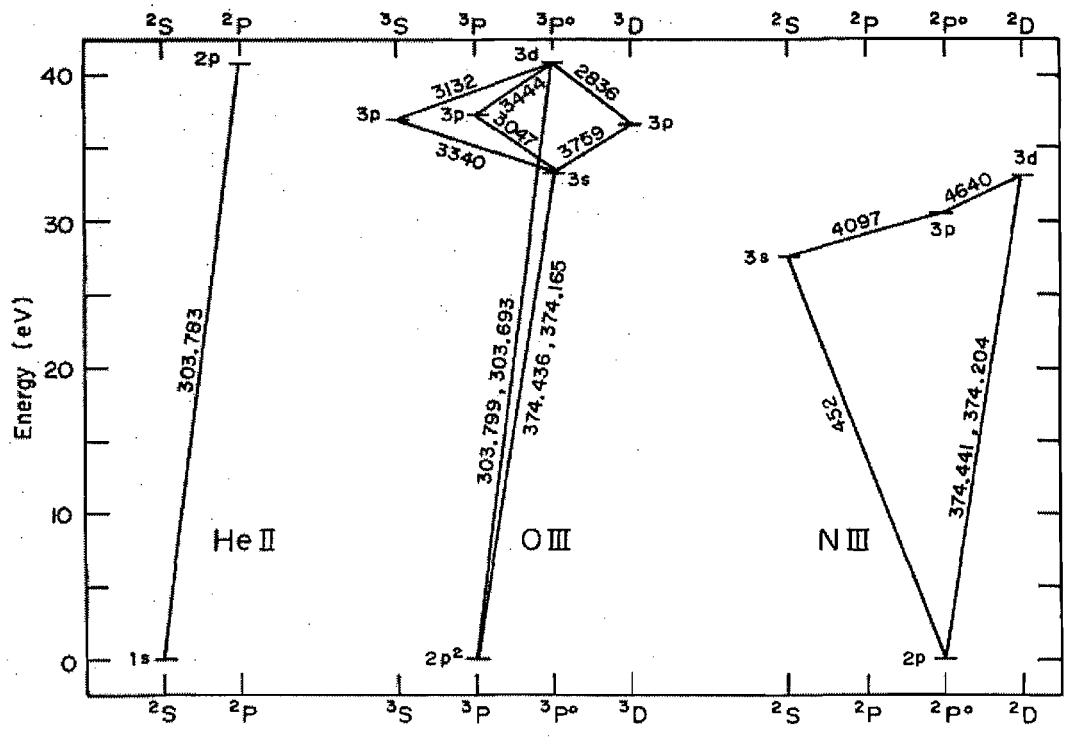

Figure 2.5: Simplified Grotrian diagrams of He II, O III and N III including only the lines which play an important role in the Bowen fluorescence process. Only the wavelengths of the strongest optical lines of O III and N III are given for each multiplet. From McClintock et al. (1975).

resonance lines of He II, O III and N III. The relevant levels and most important transitions of the ions are summarised in Fig. 2.5. The He II Lyα (λ303.783) resonance line coincides almost exactly with the λ303.799 and λ303.693 resonance lines of O III. Usually, the excited O III decays to the ground state by emitting a λ304 photon; however, $\sim$2% of the time the O III emits one or two Bowen lines (λ3133 and λ3444 are the strongest) along with an O III λ374 photon. This in turn may pump the resonance lines of N III $\lambda\lambda$374.441,374.204. Again, re-radiation of the resonant 374 Å photon is the most probable event. In $\sim$1% of the cases, however, the N III will emit one or two Bowen lines from the following multiplets: N III $\lambda\lambda$4634–4642 and N III $\lambda\lambda$4097–4103 (McClintock et al., 1975; van Paradijs & McClintock, 1995).

Although the optical fluorescence efficiencies in a single interaction are small ($\sim$1%), the net efficiency for the generation of optical photons may approach 100%, because in the competing process the reemitted λ304 or λ374 photon is identical to the absorbed photon. However, the λ304 and λ374 photons will not produce O III and N III optical emission if they are destroyed by other non-resonant processes, such as absorption by H I or He I, or the collisional decay of the excited He II ion. The importance of this process is very difficult to estimate (Yada, 1953, 1954).

In the case of planetary nebulae, He II emission is due solely to recombination, and therefore the intensity of He II Lyα is simply proportional to the intensity of He II λ4686; the proportionality constant depends weakly on the temperature in the nebula (Kallman & McCray, 1980). In order to compare theory and observation, one usually computes the yield of the Bowen mechanism. The yield y_B (or y'_B) is defined to be the fraction of the He II Lyα photons that eventually produce O III (or N III) Bowen line emission

$$y_B = \kappa \frac{I(\lambda 3444)}{I(\lambda 4686)}$$

$$y'_B = \frac{2.4 I(\lambda\lambda 4634 - 4642)}{I(\lambda 3444)}$$

where $\kappa \approx 1$ (Kallman & McCray, 1980, and references therein). For a model calculation of a typical planetary nebula, NGC 7027, Kallman & McCray (1980) find mean Bowen yields of $\bar{y}_B = 0.42$ and $\bar{y}'_B = 0.39$. This was found to be in reasonable agreement with the observed mean values and dispersions for a sample of 19 nebulae: $\bar{y}_B = 0.37 \pm 0.04$ and $\bar{y}'_B = 0.61 \pm 0.08$.

2.2.1 Application to LMXBs

McClintock et al. (1975) proposed that one of the dominant emission features in

the optical spectra of LMXBs - a broad blend near λ4640 - is due to the Bowen mechanism and is composed of the N III $\lambda\lambda$4634–4642 Bowen lines plus possible contributions from C III and O II. A strong He II Lyα radiation field and a sufficient supply of O III and N III ions are very likely to be present in X-ray sources. However, a high gas density around the X-ray source may negate the Bowen process by destroying the seed He II photons (Seaton, 1960). Nevertheless, whilst the $\sim \lambda$4100 Bowen blend is difficult to observe due to blending with Hδ, the detection of both the O III λ3444 and N III $\lambda\lambda$4634–4642 Bowen lines in HZ Her (Margon & Cohen, 1978) would appear to support the Bowen fluorescence hypothesis.

A quantitative observational study of Bowen fluorescence in LMXBs was performed by Schachter et al. (1989) on Sco X–1. They observed the two O III Bowen lines that are predicted to be the strongest lines in a static nebula: λ3133 and λ3444. They extracted the intensities of the N III Bowen lines from the blend near λ4640, in addition to the O III Bowen lines and He II λ4686. The intensity ratio $I(\lambda3133)/I(\lambda3444)$ and the observed value of the oxygen Bowen yield ($\bar{y}_B$ ~0.55) are in good agreement with the model calculations of Kallman & McCray (1980). However, the nitrogen Bowen yield was found to be anomalously high ($\bar{y}'_B$ ~3.5). This could be due to the presence of large velocity gradients opening up additional pumping channels; support for this suggestion comes from the possible detection of the O III λ3407 line, which requires a minimum velocity width of ~70km s^{-1} (Deguchi, 1985) within the scattering zone of each λ304 photon.

2.2.2 Alternative emission mechanisms

Kastner & Bhatia (1990, 1991) argue that the λ4640 and λ4100 multiplets of N III emitted by planetary nebulae (and XRBs) are not produced by the Bowen process, though they do agree that the O III lines are pumped by the Bowen process. More recently, Ferland (1992) supplied an alternative model for producing the N III lines in planetary nebulae, based upon continuum fluorescence, though he does concede that the Bowen process must be active at some level.

McClintock et al. (1975) also considered alternative mechanisms for generating the λ4640 emission in X-ray stars, including non-selective emission by C III, N III and O II (found to provide too low a yield, and should produce many more strong emission lines than are observed) and the 'Of star process'. In Of stars, N III $\lambda\lambda$4634–4642 is observed in emission, whilst He II λ4686 may be either in emission or absorption, or be absent. The selective emission at $\lambda\lambda$4634–4642 is primarily a result of di-

electronic recombination from an unusually low-lying auto-ionising state of N III. For incompletely stripped ions, the dominant recombination process is dielectronic capture of a free electron with the simultaneous excitation of the ionic core, yielding one of many possible doubly excited states. Photon emission from the doubly excited intermediate resonance state leads to a stable recombined system and thus completes the dielectronic recombination process. However, the O III emission lines predicted by the Bowen process and present in LMXB systems are not observed in Of stars. It therefore seems unlikely that dielectronic recombination is the most important mechanism active in XRBs, though it could potentially modify the Bowen line intensities.

Charge transfer between O IV and H I can populate excited levels of O III, and thus could potentially affect the Bowen line intensities. In addition to the lines we expect to see from Bowen pumping, charge transfer will result in λ5592 emission. Using this diagnostic, Schachter et al. (1989) found that charge transfer has only a small effect (<4%) on the Bowen emission in Sco X–1.

2.2.3 Metallicity

It is reasonable to assume that the strength of the $\lambda\lambda$4640–4650 blend (heretofore referred to as the 'Bowen blend'), which is composed of the N III Bowen lines and possibly C III and O II, might be positively correlated with metallicity. Observations have shown that the strength of the Bowen blend with respect to that of He II λ4686 varies considerably from one LMXB to another. Motch & Pakull (1989) have made this idea useful by normalising the equivalent width (EW) of the Bowen blend by the EW of He II λ4686 for 18 LMXBs, giving the ratio $R \equiv \mathrm{EW}(\lambda\lambda 4640\text{–}4650)/\mathrm{EW}(\lambda 4686)$. Four systems that are located in low-metallicity environments (LMC X–2, CAL 83 and CAL 87 in the LMC and the globular cluster source X 2127+119 in M 15; Dufour, 1984; Zinn, 1985) have low values of R, ranging from $R < 0.12$ to $R < 0.36$. The values of R for 12 galactic systems are much greater, with $\bar{R} = 0.99 \pm 0.37$. The two remaining LMXBs in the sample, Cyg X–2 and X 0921–63, are possible halo-population systems[1] with low metallicity (Cowley et al., 1982) and display intermediate values of R (0.46 and 0.33 respectively).

The observational evidence is supported by theoretical considerations. For example, photoionisation models of compact X-ray sources show that the He II λ4686

[1]Note that it is possible these systems originated in the Galactic Plane, and simply received a substantial supernova kick at birth, thus causing their potential mis-classification as halo-population sources.

line and the Bowen blend originate approximately in a common region (Kallman & McCray, 1982). Moreover, the intensity of He II λ4686 is intimately tied to the intensity of the N III $\lambda\lambda$4634–42 Bowen blend via the intensity of He II Lyα. It is not too surprising, therefore, that the work of Motch & Pakull (1989) shows a good correlation between the EW variations of He II λ4686 and the Bowen blend. This correlation holds for both orbital and random variations.

2.2.4 Bowen line kinematics

2.2.4.1 Sco X–1

The Bowen blend is produced predominantly in the accretion disc in LMXB systems, which results in the individual emission lines being smeared out into the broad emission blend we typically observe. However, a new avenue for mass determination in LMXBs was opened thanks to the discovery of narrow, high-excitation emission components arising from the irradiated companion in Sco X–1 (Steeghs & Casares, 2002), the most prominent being C III (4647.4/4650.1 Å) and N III (4634.13/4640.64 Å, see Fig. 2.6). These emission lines must arise on the irradiated companion because they are extremely narrow (FWHM $\leq$50 km s^{-1}), and move in anti-phase with the compact star (as traced by the He II λ4686 wings, see Fig. 2.7). Furthermore, the radial velocity curve is sinusoidal indicating a fixed structure in the binary frame (Steeghs & Casares, 2002).

Sco X–1 is the prototype LMXB, consisting of a neutron star accreting matter from a Roche lobe filling companion star. It is the brightest persistent X-ray source in the sky and has been the target of detailed analysis for the last 40 years in all energy bands, from radio to X-rays. Despite intensive efforts, spectroscopic signatures of the companion star remained absent in optical-IR data. This work represented the first detection of the companion star in Sco X–1 and opened up a new window to extract dynamical information on the population of persistent LMXBs with optical counterparts.

2.2.4.2 GX 339–4

The Bowen fluorescence diagnostic is a powerful technique also for transient sources, as was demonstrated by Hynes et al. (2003). GX 339–4 has been a black hole candidate for a number of years, based upon its X-ray properties, but no dynamical proof could be found. It moves regularly between X-ray 'on' and 'off' states, and associated with this the optical counterpart (V 821 Ara) varies between $V < 15$

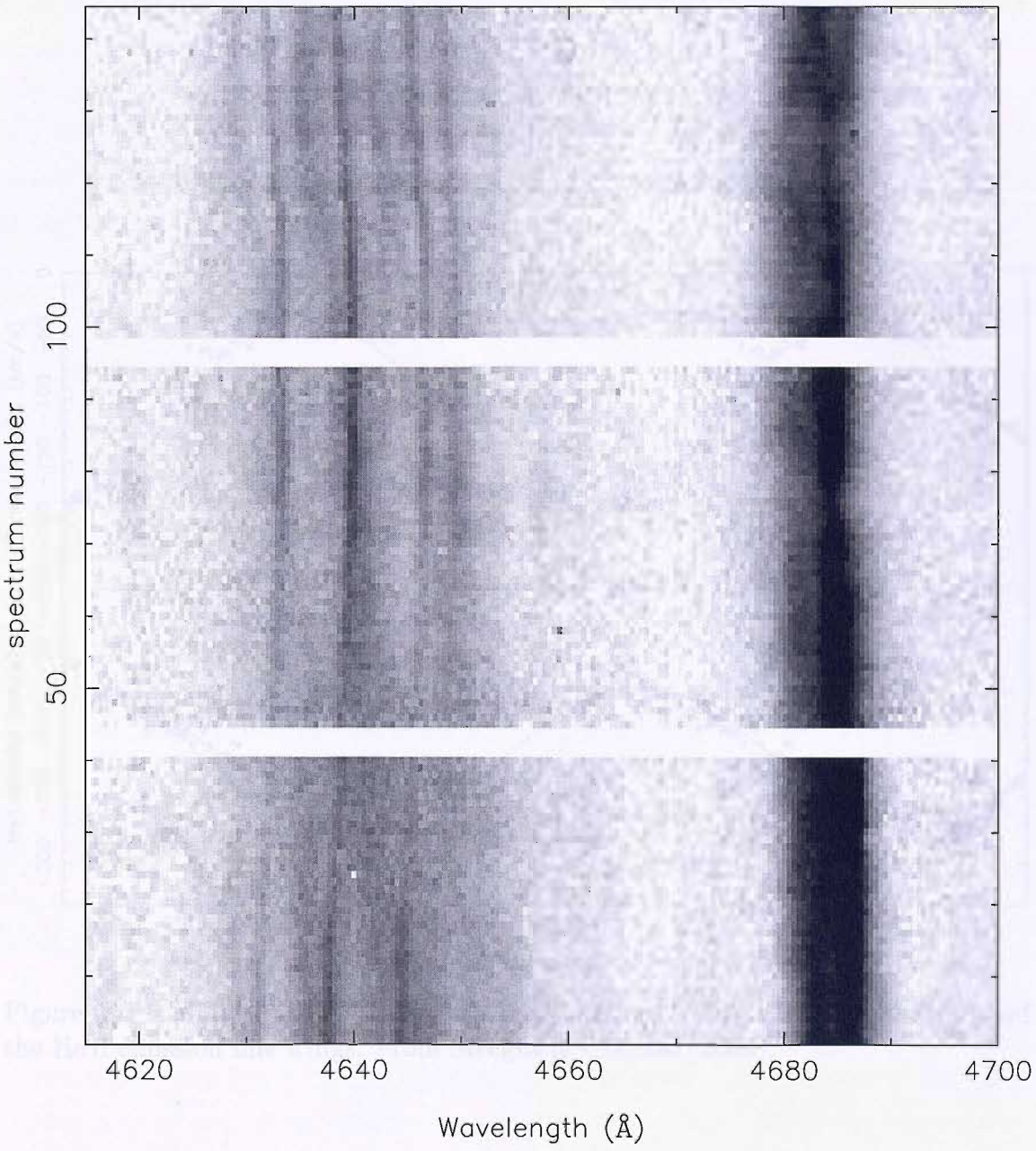

Figure 2.6: Trailed spectrogram of the Bowen blend and He II λ4686 line showing the Doppler shift of the narrow C III and N III components. From Steeghs & Casares (2002).

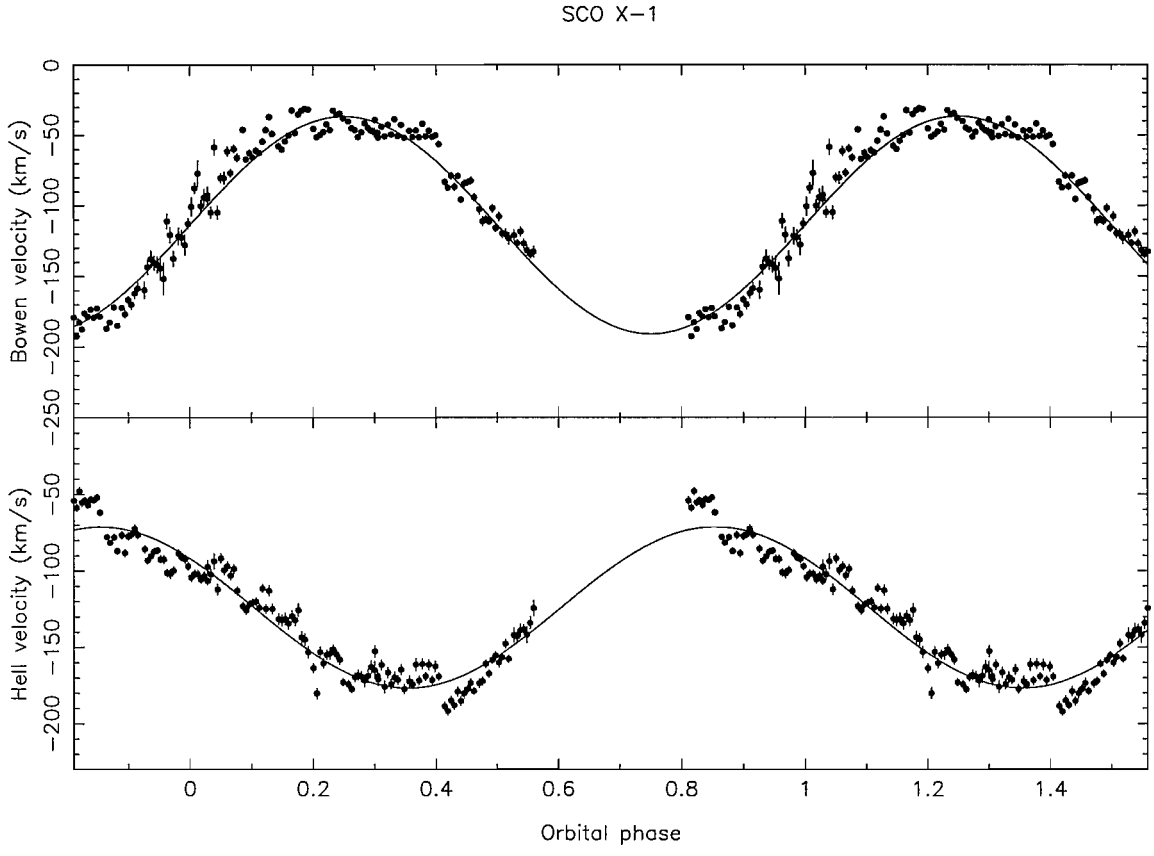

Figure 2.7: Radial velocity curves of the narrow Bowen blend components (top) and the He II emission line wings. From Steeghs & Casares (2002).

at peak to $V > 20$ at minimum. However, even at its faintest, there has been no detection of the (presumed) cool mass donor (Shahbaz et al., 2001). Hynes et al. (2003) used the opportunity of an outburst episode to obtain spectroscopy which revealed narrow N III Bowen components from the companion star. The implied mass function is $5.8 \pm 0.5 M_{\odot}$ and is robust evidence for an accreting black hole. What is curious in this case is the fact that the sharp components are not always visible, suggesting that there are significant intervals during which the face of the donor is effectively shielded from direct illumination. This could arise if the disc is either warped or is elliptical and precesses (Hynes et al., 2003).

2.2.4.3 X 1822–371

The power of imaging the companion stars in LMXBs and outbursting transients using the Bowen fluorescence transitions was confirmed in the studies by Casares et al. (2003). X 1822–371 is the prototypical ADC source (see Section 1.4.2) and detailed modelling of the optical and X-ray lightcurves has provided an extremely accurate determination of the inclination angle i. X 1822–371 is also remarkable thanks to the discovery of X-ray pulses (Jonker & van der Klis, 2001), flagging it as one of the rare precursors to millisecond pulsars. Analysis of the pulse arrival time delay has enabled an extremely precise determination of the orbit of the neutron star. A complete determination of the system parameters therefore only requires the knowledge of the radial velocity curve of the companion star. The faintness of the source, coupled with the high spectral resolution (≤ 70 km s^{-1}) required to resolve the Bowen lines, prevents their detection in individual spectra. However, exploiting Doppler tomography (see Section 2.3, Fig. 2.8), all of the information contained in individually phase-resolved spectra can be combined to reconstruct the emissivity distribution. The N III map displays a compact spot located at the expected velocity and phasing of the donor star, as predicted by the pulsar ephemeris. The centroid of this spot lies at 300 km s^{-1}, establishing a lower limit to the velocity of the companion because the emission arises from the irradiated inner face of the companion. In order to derive the true velocity, one needs to model the displacement between the reprocessing site and the donor's centre of mass, the so-called 'K-correction'.

2.2.5 The 'K-correction' for irradiated emission lines

It is important to note that the centre of light of the Roche lobe filling star does not precisely follow the centre of mass of the star, which will result in a slightly

distorted radial velocity curve. The secondary is not uniformly illuminated by the ionising photons from the central X-ray source; any N III Bowen emission will be excited on the inner hemisphere of the donor and therefore the radial velocity curve of the sharp features traces the motion of the re-processed light centre rather than the true centre of mass of the star. Thus, the radial velocity curve of the narrow Bowen components only provides a lower limit to the true K_2-velocity.

The K-correction for radial velocity curves[2] derived from absorption lines formed on the companion's photosphere was presented by Wade & Horne (1988). In this case, absorption lines are quenched in the heated face, and hence the observed K-velocity provides only an upper limit to the real K_2, i.e. the true velocity of the centre of mass of the companion star. A rough estimate of the size of the necessary K-correction is obtained by assuming that the light centre of the donor, weighted by the strength of the absorption lines, is displaced from the centre of mass of the star in the direction away from the accretor.

In the case of LMXBs, we are interested in the K-correction for irradiation induced spectral lines originating from the heated inner face of the donor star, which is opposite to the case presented by Wade & Horne (1988). This problem was first addressed by Horne & Schneider (1989):

$$K_2 = \frac{K_{\rm em}}{(1 - 0.46 f\, q^{1/3}(1+q)^{2/3})} \tag{2.7}$$

where $K_{\rm em}$ is the velocity semi-amplitude of the site where the irradiation-induced emission is produced, $q{=}M_2/M_X$ and f is the displacement of the reprocessing site compared to the centre of mass of the star, normalised to the radius of the companion star. Thus $f{=}0$ implies uniform emission over the secondary (and thus no correction), while $f{=}1$ places the emission entirely at the L_1 point (see Section 1.2.1). Clearly both of these limits are unrealistic; uniform irradiation-induced emission over the co-rotating donor is impossible, whilst emission only at the L_1 point would be rather surprising since any shielding of the donor from the X-ray source would preferentially affect the mid- rather than upper-latitudes. The difficulty in estimating a reasonable value for f creates a great deal of systematic uncertainty in this method.

Munoz-Darias et al. (2005) were able to compute a general K-correction algorithm as a function of the mass ratio q (i.e. the size of the companion) and disc flaring angle α (height of the disc rim obscuring the heated star), and including the effects of

[2]Note that this is not related to a similar term used in extra-Galactic astronomy.

inclination i. Knowledge of these parameters removes the uncertainty in estimating the form factor f suffered by earlier methods. In particular, the flaring angle α may be estimated by a number of different methods; Hellier & Mason (1989) modelled X-ray and optical eclipses of X 1822–371, from which they found $\alpha \sim 8-9°$. An opening angle of 10° was derived by Gerend & Boynton (1976) for the tilted accretion disc in Her X–1 from a modelling of its optical light curves. Motch et al. (1987) estimated $\alpha \sim 9 - 13°$ based upon optical observations of XB 1254–690, whilst de Jong et al. (1996) derived a mean disc opening angle of $\alpha \sim 12°$ by studying the effects of X-ray reprocessing in LMXBs.

Munoz-Darias et al. (2005) applied their model to the neutron star LMXB X 1822–371, building upon the earlier work of Casares et al. (2003). The previous determination of the system parameters were refined to $1.61M_{\odot} \leq M_X \leq 2.32M_{\odot}$ and $0.44M_{\odot} \leq M_2 \leq 0.56M_{\odot}$ for the two binary components, providing compelling evidence for the presence of a massive neutron star in this system.

2.3 Doppler Tomography

Doppler tomography (Marsh & Horne, 1988) is a method that can be used to optimise observational data to form useful visualisations of line-forming regions in a binary system. The required observational data are velocity profiles at different binary phases. The Doppler-broadened line profile offers a projection of the velocity distribution onto the observer's line of sight, while the rotation of the binary presents the observer with a continuously varying sequence of velocity projections. This combination of Doppler shifting and binary rotation can provide sufficient information for the assembly of 2-dimensional Doppler maps, analogous to the CAT scans used in medical imaging (e.g. Cormack, 1979; Hounsfield, 1979).

Spectral lines yield diagnostics of binary structure because they indicate the kinematics of the production region, and line fluxes reveal obscuration and/or changing optical depths. Emission regions within the system, for example the companion star, stream and disc, have distinct signatures within a Doppler map. Doppler tomography helps in system parameter determination, as it allows for the decomposition of multiple components and the simultaneous exploitation of a large number of individual phase-resolved spectra. For example, we can separate axisymmetric disc emission from distortions such as that due to the stream impact point. The mean motion of this disc emission should follow the motion of the compact object, hence we can measure its radial velocity, K_1, and estimate the mass ratio as was done for

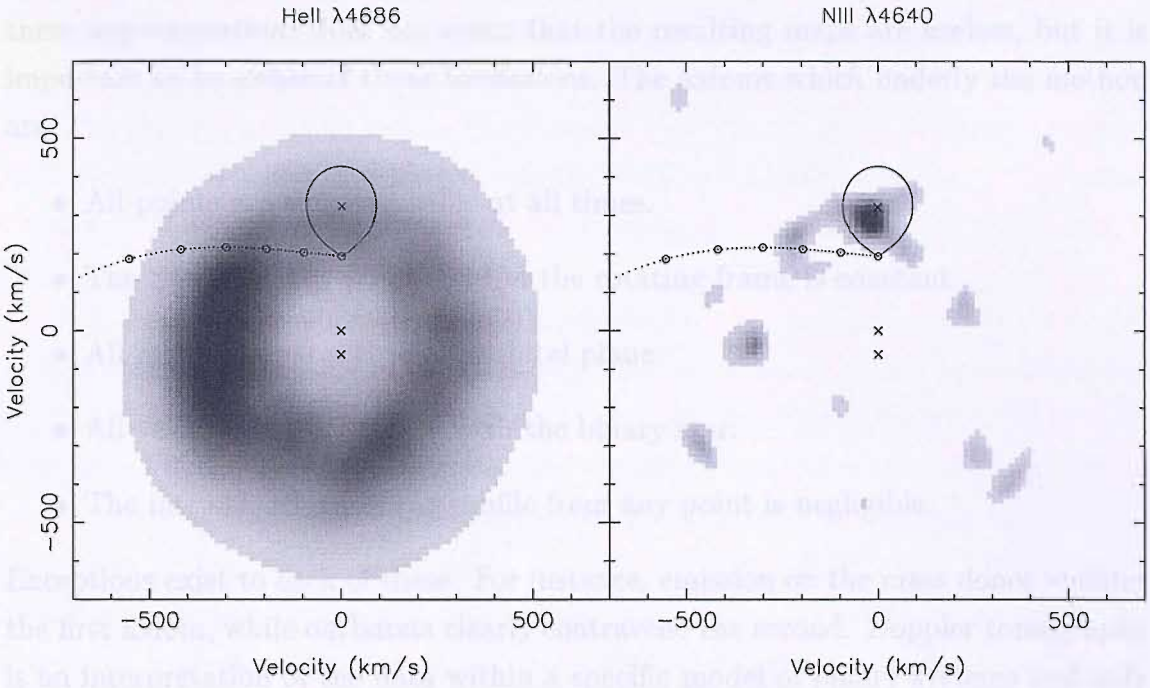

Figure 2.8: Doppler images of He II λ4686 (left, showing the classic accretion disc ring structure) and N III (right) for X 1822–371. The Roche lobe of the donor and gas stream trajectory are over-plotted for a $1.4M_{\odot}$ neutron star. From Casares et al. (2003).

Sco X-1 (Steeghs & Casares, 2002). More importantly, Doppler imaging allows for the detection of very faint emitting components (as was the case in e.g. X 1822–371; see Fig. 2.8) by using the information encoded in *all* the available spectra.

2.3.1 The assumptions of Doppler tomography

With Doppler tomography, a 2D data set consisting of a time series of line profiles is inverted into a 2D Doppler tomogram. Since the dataset provides us with projected radial velocities of the emitting gas, the Doppler tomogram that is reconstructed provides the distribution of the line emission in the binary in a *velocity* coordinate frame. This permits image reconstructions without detailed *a priori* assumptions concerning the nature of the flow that one is mapping. The velocity coordinate frame greatly increases the flexibility of Doppler tomography and significantly simplifies the inversion process compared to image reconstructions in the Cartesian X-Y frame.

Nonetheless, some implicit assumptions are made when performing Doppler tomography, and these must be borne in mind when interpreting reconstructed accretion flow maps (Marsh, 2001; Steeghs, 2003). Doppler tomography rests on certain approximations to reality that are, at best, only partially fulfilled. Violation of

these approximations does not mean that the resulting maps are useless, but it is important to be aware of these limitations. The axioms which underly the method are:

- All points are equally visible at all times.
- The flux from any point fixed in the rotating frame is constant.
- All motion is parallel to the orbital plane.
- All velocity vectors rotate with the binary star.
- The intrinsic width of the profile from any point is negligible.

Exceptions exist to each of these. For instance, emission on the mass donor violates the first axiom, while outbursts clearly contravene the second. Doppler tomography is an interpretation of the data within a specific model of binary systems and only applies inasmuch as the model does itself.

2.3.2 Interpretation of the maps

The rather unfamiliar velocity coordinate frame of Doppler tomograms is the main hurdle to be overcome in order to interpret a Doppler map. In the Doppler tomogram coordinate frame, each line source is characterised by its inertial velocity vector in the orbital plane, $\mathbf{V}=(V_x, V_y)$, where the binary centre of mass is at the origin, the x-axis points from the accretor to the donor and the y-axis points in the direction of motion of the donor, as viewed in the co-rotating frame of the binary. Each source then traces a sinusoidal radial velocity curve as a function of the orbital phase (ϕ) centred on the systemic velocity of the binary (γ);

$$V(\phi) = \gamma - V_x \cos 2\pi\phi + V_y \sin 2\pi\phi.$$

The observed line profiles are the projection of the radial velocities and intensities of all velocity vectors considered;

$$F(v_r, \phi) = \int I(V_x, V_y) \star g(V - v_r)\ dV_x dV_y,$$

with $g(V - v_r)$ describing the local line profile intensity at a Doppler shift of $V - v_r$ and $I(V_x, V_y)$ the image value of the Doppler map at the corresponding velocity grid point. The inversion from data-set to Doppler map can be achieved via either

a Radon transform in the form of filtered back-projection (Horne, 1991) or via regularised fitting using maximum entropy or a similar quantity as the regularising function (Marsh & Horne 1988). The superior handling of noise and image artifacts with maximum entropy mapping, combined with its flexibility and usage of a formal goodness of fit parameter in the form of χ^2 make it the preferable inversion choice in most cases.

Despite the unfamiliar coordinate frame of Doppler tomograms, it is relatively straightforward to identify and resolve prominent emission sites such as the extended accretion disc, the gas stream and its impact on the outer disc (Fig. 2.9), the magnetically channelled flow in polars and emission from and around the mass donor star. Spatial asymmetries in the emissivity of the accretion disc map into similar structures in the inside-out Doppler projection of that disc. Since each of these sites has a completely different position-velocity relation, it would be impossible to reconstruct the equivalent position image without imposing detailed assumptions concerning the (unknown) translation between velocity and position. Therefore it is advisable to compare data with models by presenting models in the velocity coordinate frame if possible, as opposed to trying to reconstruct the data in an XY-frame (e.g. Hynes et al., 2001). It is also important to search for prominent features in a Doppler reconstruction in trailed spectrograms in order to confirm the veracity of their origin and check for any systematic residuals in the map.

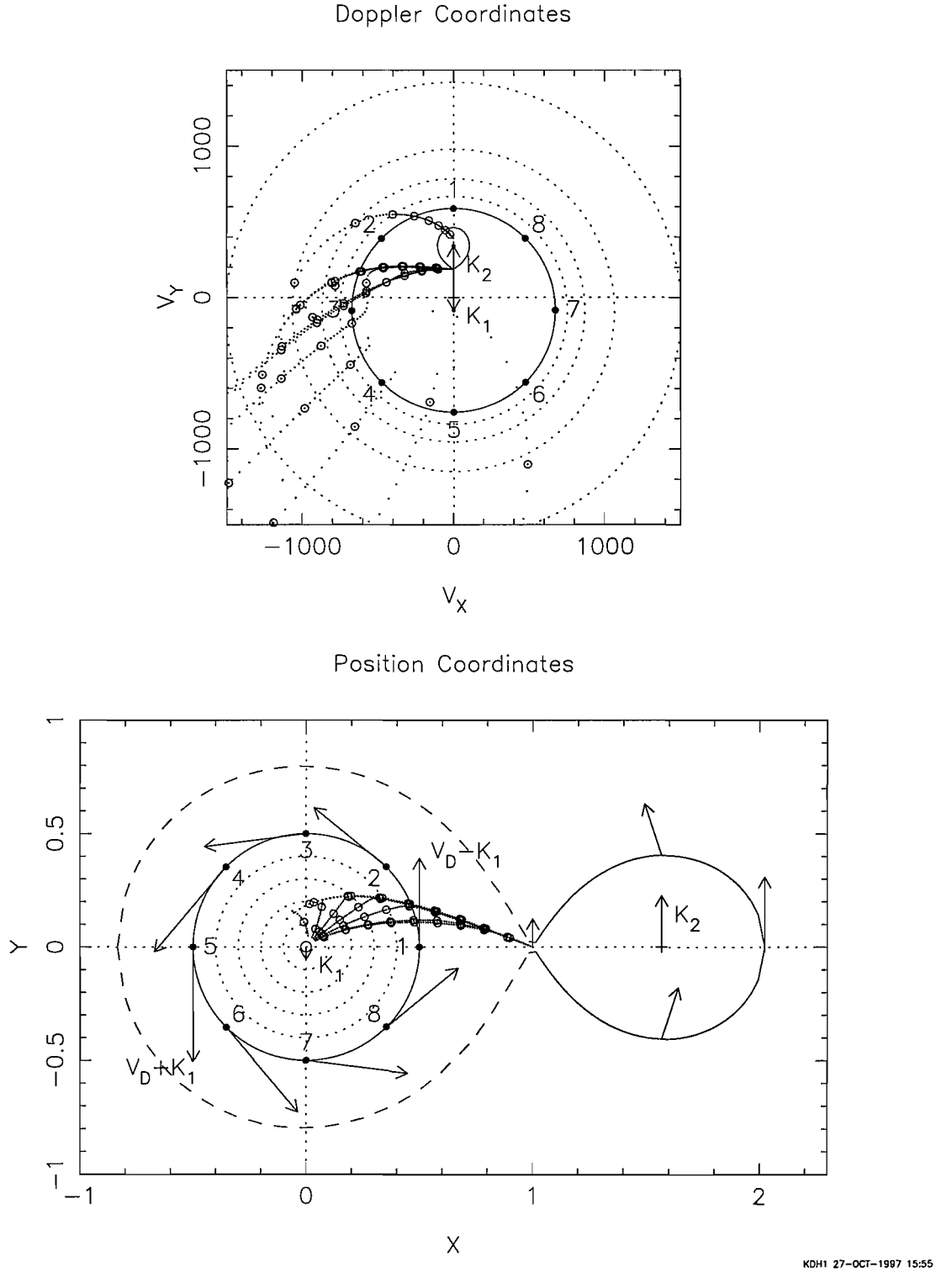

Figure 2.9: Schematic view of an XRB, including the Roche lobe filling companion star, the mass transfer stream, and the accretion disc around the compact object, shown in both spatial coordinates (X, Y) and the corresponding Doppler coordinates (V_X, V_Y). From Horne (1991).

Chapter 3

Kinematical Studies of the Low Mass X-Ray Binary XB 1254–690

In this chapter simultaneous B-band spectroscopy and X-ray data of the X-ray dipping source XB 1254–690 is presented and discussed. The X-ray observations are used to establish a new orbital ephemeris for this source. The optical data includes the first spectroscopic detection of the donor star in this system, using the Doppler Tomography technique with the Bowen fluorescence blend. In combination with an estimate for the orbital parameters of the compact object using the wings of the He II λ4686 emission line, dynamical mass constraints for the individual system components are derived.

3.1 Introduction

XB 1254–690 is a persistently bright, low-mass X-ray binary (LMXB). It was identified with a faint blue star (GR Mus, $V = 19.1$), which exhibited the Bowen blend of N III and C III in emission (Griffiths et al., 1978). The object produced Type I X-ray bursts (Mason et al., 1980; Courvoisier et al., 1986), indicating the presence of a neutron star as the compact object. A Type I X-ray burst is a seconds to minutes long X-ray event caused by a thermonuclear flash in the upper layers of a neutron star that is accreting matter from a nearby, Roche-lobe filling, companion star (see Section 1.3.2).

Dips of up to 95% of the 1–10 keV flux, with a recurrence period of $P_X = 3.88 \pm 0.15$ hr and lasting ~ 0.8 hr per cycle, were discovered in *EXOSAT* data by Courvoisier et al. (1986). The dips are caused by obscuration of the central source by a bulge on the outer edge of the accretion disc and imply a moderately high

inclination (e.g. see Section 1.4.2).

From V-band observations of the optical counterpart, Motch et al. (1987) determined an optical ephemeris of T_{min} = JD 2,445,735.693 (4) + 0.163890 (9) days, equivalent to a period of $P_{opt} = 3.9334 \pm 0.0002$ hr. This broad optical modulation is probably due to the changing visibility of the heated face of the secondary star in the system, with an additional contribution from the X-ray heated bulge, although other explanations such as an asymmetrical disc or occultation of the disc by the companion cannot be definitively ruled out (see Section 2.1.1).

Within the errors, the optical and X-ray period measurements are consistent, with later X-ray observations indicating that the optical modulation provides a more accurate measurement of the orbital period (Smale et al., 2002). A short section of simultaneous X-ray and optical coverage showed that the optical minimum occurs ~ 0.16 in phase after the centre of the X-ray dips (Motch et al., 1987).

Simple geometrical modelling is possible by considering the X-ray illuminated area of the companion star, disc radius, disc opening angle, and inclination at given distances which are compatible with the observed optical flux and the amplitude of the light curve. This leads to constraints on the source inclination of 65°–73°, and on the distance of 8-15 kpc (Motch et al., 1987). Interestingly, this modelling would appear to rule out the possibility of the secondary being a strongly evolved, low-radius star in favour of a larger, main-sequence-like secondary. For a strongly evolved star, the implied distance would become too small, as would the range of possible opening angles for the accretion disc (2–4°, whereas an opening angle of 9–13° is needed in order to explain the observed amplitude of the optical photometric modulation).

The first mass constraints for this system were based upon a unique relation between the orbital period and the mass of the companion, assuming that the companion is a low mass, zero-age main sequence (ZAMS) star filling its Roche lobe (Warner, 1976). The main source of uncertainty is claimed to stem from the efficacy of the chosen stellar models, though a larger uncertainty is undoubtedly whether the assumption of a ZAMS donor is appropriate. Regardless, using this approximation, Courvoisier et al. (1986) estimated the mass of the companion to be in the region of $\sim 0.45 M_{\odot}$.

The first kinematic constraints were proposed by Cowley et al. (1988), who obtained intermediate resolution ($\sim$ 3Å) spectra using the 4m telescope at the Cerro Tololo Inter-American Observatory. The velocity of the He II λ4686 emission line was measured in several ways: by line-profile fitting, by visual centering on the line,

Table 3.1: Log of observations of GR Mus / XB 1254–690

Date	Observatory	Total Int. Time
2004-05-26	VLT	3.75 h
2004-05-26	RXTE	4.75 h
2004-05-27	VLT	4 h
2004-05-27	RXTE	5.25 h
2004-05-28	VLT	2 h

and by cross-correlation against the sum of all the other spectra of the target. The measured velocities were fitted to so-called 'mini-orbits'; very approximate, preliminary orbits tailored to the limited phase coverage of the data. These provided solutions for the semi-amplitude (114 $\pm$ 13 $\mathrm{km\,s^{-1}}$) and the systemic velocity (98 $\pm$ 10 $\mathrm{km\,s^{-1}}$). If the velocities derived from the He II emission line represent the motion of the compact star and not, for example, the streaming of gas between the stars or out of the system (see e.g. Section 2.1.4), then approximate stellar masses can be derived using the mass function. The result is consistent with a low-mass main-sequence star ($M \simeq$ 0.5-0.8 $M_{\odot}$) and a canonical 1.4 $M_{\odot}$ neutron star.

In the remainder of this chapter we will attempt to confirm and better constrain these mass estimates using high-resolution blue optical spectroscopy. We will measure the wings of the He II λ4686 emission line to gain an estimate for the compact object velocity (Section 3.3.3), and use the Bowen Fluorescence technique (Steeghs & Casares, 2002) to measure the donor star velocity (Section 3.3.4).

We also obtained simultaneous X-ray observations (see Section 3.3.1) in order to re-establish the ephemeris of Motch et al. (1987). This cannot be extended to the observations described herein because the propagated uncertainty in phase is now comparable to the orbital period itself.

3.2 Observations

We have obtained simultaneous optical and X-ray data for XB 1254–690. The journal of observations is given in Table 3.1.

3.2.1 Optical data

Phase-resolved spectroscopy of XB 1254–690 was obtained from 26 to 28 May 2004 using the FORS 2 spectrograph mounted on the VLT/UT4 at ESO's Paranal observatory. During each night we observed XB 1254–690 for $\simeq$ one full orbit, resulting in a total of 38 spectra with an integration time of 900s each. We used the 1400V

volume-phased holographic grism, and a slit width of 0.7″, giving a wavelength coverage of $\lambda\lambda$4513-5814 with a resolution of 70 km s^{-1} (FWHM). The seeing during these observations varied between 0.5 and 2.1 arcsec. The slit was orientated at a position angle of 88.15° to include a comparison star in order to calibrate slit losses. We observed the flux standard Feige 110 with the same instrumental set-up in order to correct for the instrumental response. He, Ne, Hg and Cd arc lamp exposures were taken during daytime for the wavelength calibration scale. We de-biased and flat-fielded all of the images and used optimal extraction techniques to maximise the signal-to-noise ratio of the extracted spectra (Horne, 1986). The pixel-to-wavelength scale was derived through polynomial fits to a large number of identified reference lines resulting in a dispersion of 0.64 Å pix^{-1}. Velocity drifts due to instrumental flexure (found to be always <5 km s^{-1}) were corrected by cross-correlation with the sky spectra.

The images were bias corrected and flat-fielded, and the spectra subsequently extracted using conventional optimal extraction techniques in order to optimise the signal-to-noise ratio of the output (Horne, 1986). Frequent observations of comparison arc lamp images were performed in the course of each run and the pixel-to-wavelength scale was derived through polynomial fits to a large number of identified reference lines. The final rms scatter of the fit was always <1/30 of the spectral dispersion.

3.2.2 X-ray data

Simultaneous X-ray data from XB 1254–690 were obtained using the Proportional Counter Array (PCA) on board the *Rossi X-Ray Timing Explorer* (*RXTE*). The Proportional Counter Array (PCA; for a detailed description, see Jahoda et al. (1996)) onboard the *RXTE* satellite consists of an array of 5 co-aligned Proportional Counter Units (PCUs) that are sensitive to photons of energy 2 to 60 keV with a total collecting area of 6500 cm^2. The spectral resolution is 18% full-width at half maximum (FWHM) at 6 keV and the field of view is 1° FWHM. We obtained 36 ks of total coverage during our optical observations. The Standard 2 configuration was used, with a time resolution of 16 seconds.

3.3 Analysis

3.3.1 Determination of Orbital Phase

The ephemeris of Motch et al. (1987) is now out of date because the propagated uncertainty in phase is over a factor of 2 greater than the orbital period [1]. We therefore need to make use of our contemporaneous *RXTE* observations to set a new zero point using the X-ray dips. This is not quite as simple as it would first appear since there are large variations in dip depth and structure that are apparent from observation to observation, as well as cycle to cycle (Courvoisier et al., 1986). Additionally, a note of caution must be sounded since in a number of earlier *RXTE* and *BeppoSAX* observations (Smale & Wachter, 1999; Iaria et al., 2001), X-ray dipping was not observed at all, with an accompanying decrease in the mean optical variability of the source. The combination of these effects suggests that the vertical structure on the accretion disc edge associated with the impact point of the accretion stream had decreased in angular size at the time of these observations. The cause of this intermittent reduction in opening angle is not understood. Perhaps it is fortunate then that our observations included even just one deep dipping episode (Fig. 3.1), co-incident with our first night of optical observations.

XB 1254–690 typically exhibits 'shoulders' of dipping, i.e. regions both before and after the deep dipping in which there is a small decrease of intensity. Each shoulder of the dip lasts ~650–925 seconds, during which the total count rate in the 2-25 keV band drops by ~15% with no strong changes in the hardness ratio. The shoulder is followed by an interval of strongly variable deep dipping lasting ~1100 seconds (Smale et al., 2002), with associated strong changes in the hardness ratio (Fig. 3.2). The hardening of the spectra in the dips is most likely to be due to absorption by cold matter (Uno et al., 1997, see also Section 1.3.3).

Our observation of a dipping episode opens with the system already in the first shoulder phase, the onset of deep dipping occurring approximately 200–250 seconds into the observation (before a brief return of the source intensity to the non-dip level), and then continuing to capture the full egress from deep dipping, into the shoulder and then returning to the continuum level. Note that the return of the source intensity to the non-dip level during this episode is not unusual (Uno et al., 1997), and the light curve can in fact be interpreted as superpositions of small micro-dips (see Fig. 3.3).

[1] $\left(\frac{\sigma_n}{n}\right)^2 = \left(\frac{\sigma_P}{P}\right)^2 + \left(\frac{\sigma_T}{T-T_0}\right)^2 \Rightarrow \sigma_n \approx 2.5$ where n is the orbit number.

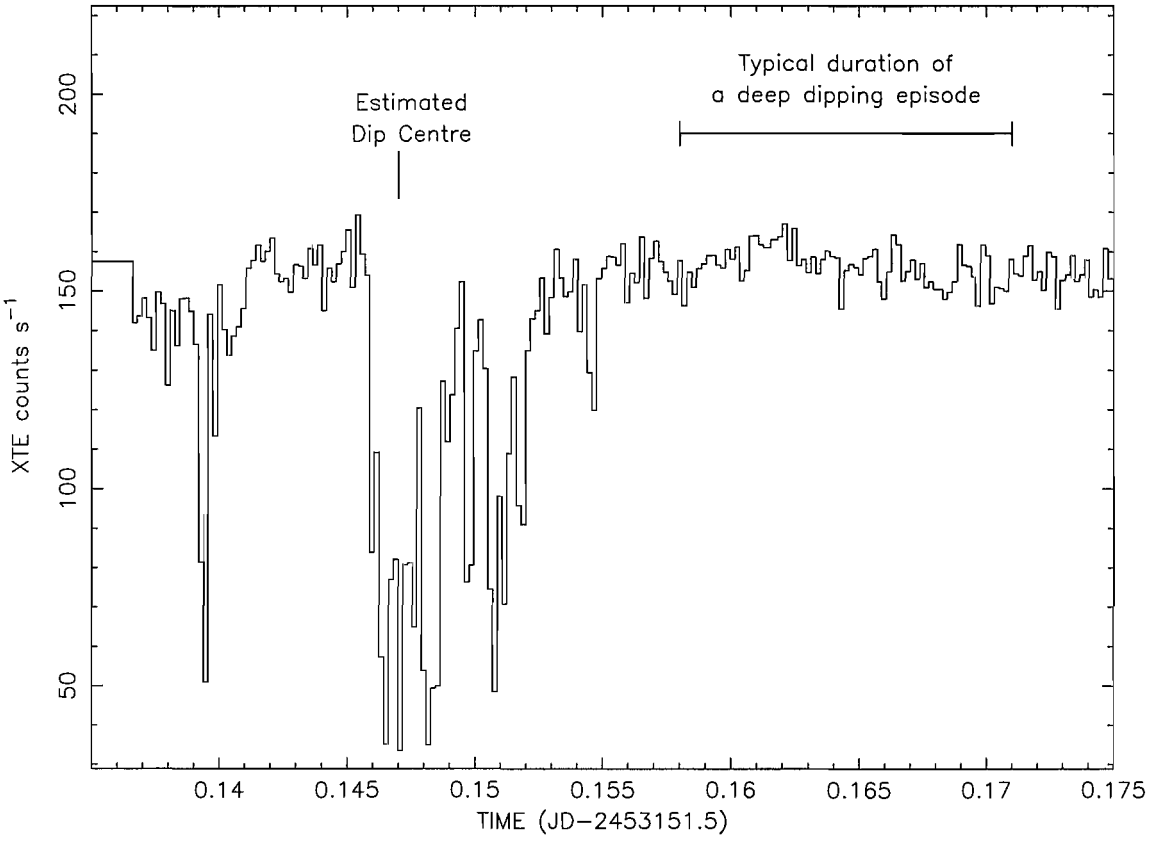

Figure 3.1: 2–20 keV X-ray lightcurve showing the deep dip used to calibrate a new ephemeris for the system. The dipping episode appears to begin shortly before JD 2453151.64, and occurs for the typical dip duration of ∼1100 seconds (Smale et al., 2002).

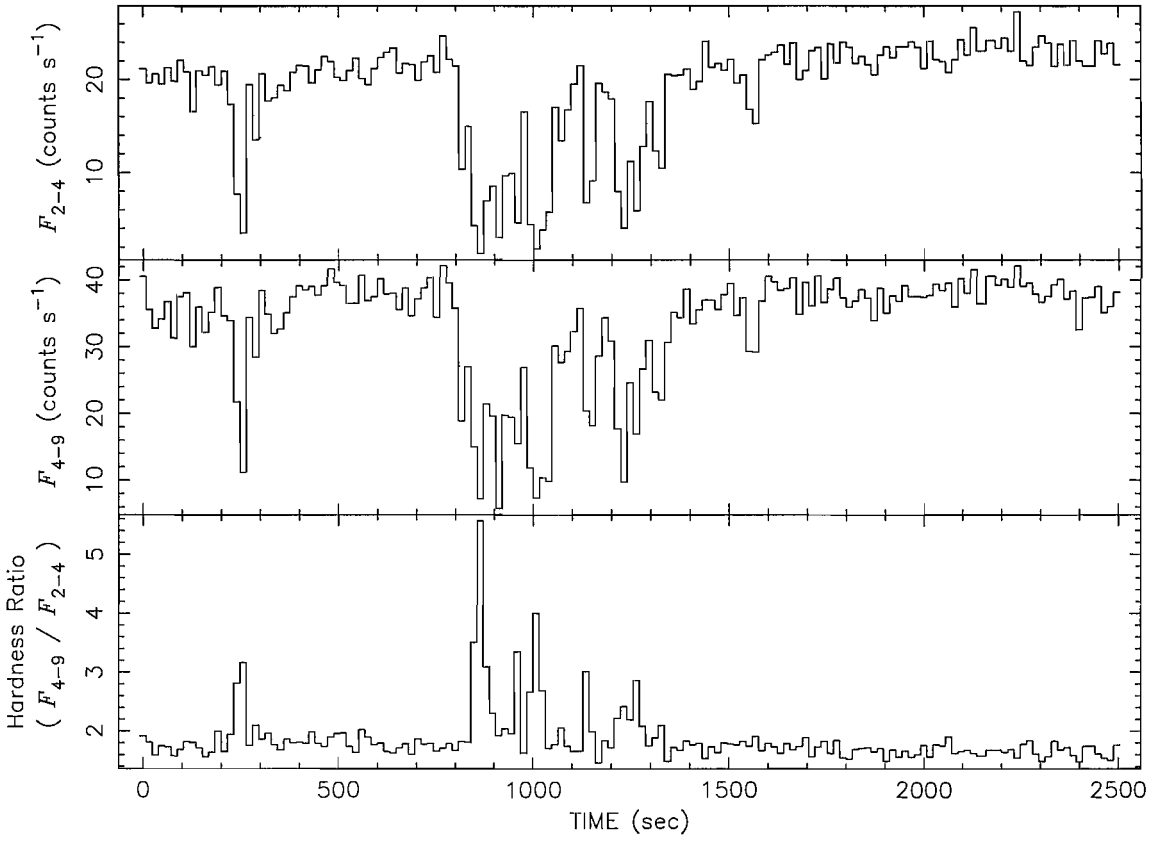

Figure 3.2: 2–4 keV (top) and 4–9 keV (centre) X-ray lightcurves displaying the deep dipping episode. The bottom panel displays hardness as a function of intensity. There is an anti-correlation between intensity and hardness ratio during the deep dipping episode, which begins shortly after 200 seconds on the above scale.

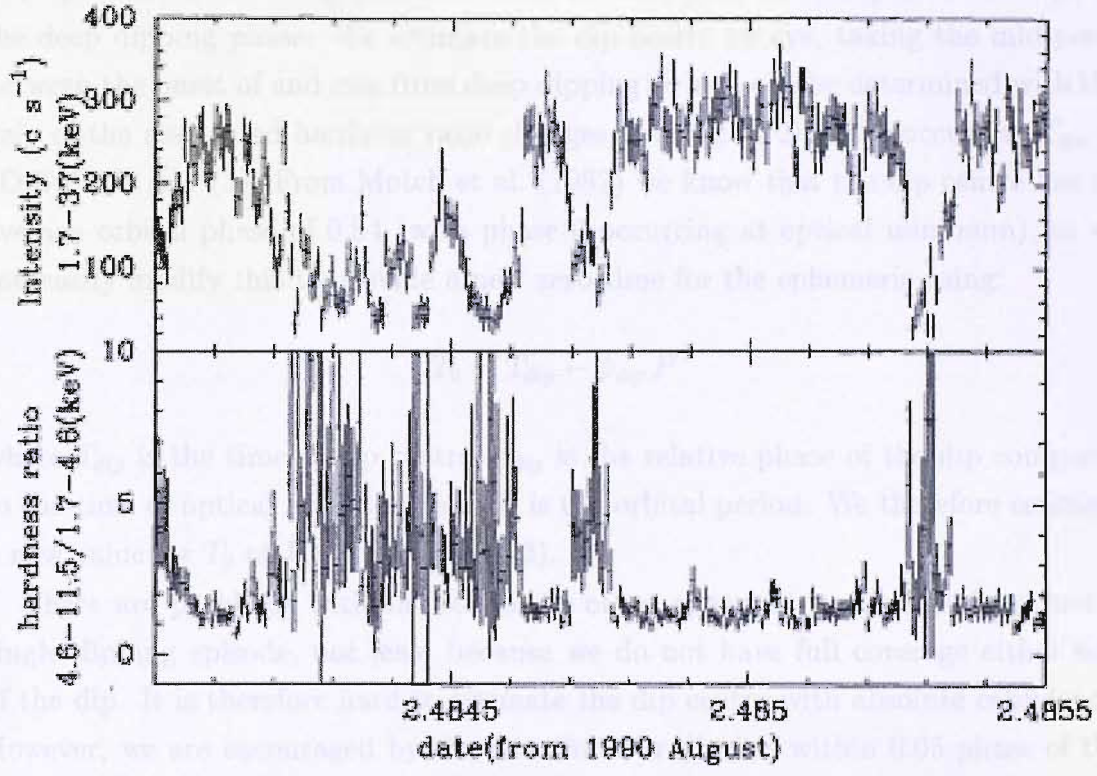

Figure 3.3: Lightcurve and hardness ratio presented by Uno et al. (1997). The intensity varies drastically during the dip and can be divided into small micro-dips. The hardness ratio increases as the intensity decreases.

Unfortunately, the lack of information regarding the full ingress to deep dipping through the preceding shoulder introduces a degree of uncertainty into our estimate of the dip centre. For example we could potentially be observing only a small section of an extended deep dipping episode (e.g. Uno et al., 1997, report dips lasting for ~40 minutes). If this is the case, the absence of the beginning of the dip will cause the estimate for dip centre to be incorrect. Nevertheless, we do have cause for optimism. The deep dipping which we observe is approximately 1100 seconds in length, equivalent to the typical period of a dipping episode in XB 1254–690 (see above). This is a strong indicator that we have full, or nearly-full, coverage of the deep dipping phase. We estimate the dip centre by eye, taking the mid-point between the onset of and exit from deep dipping (which can be determined with the help of the associated hardness ratio changes, see Fig. 3.2). This occurs at T_{dip} = JD 2453151.647 (3). From Motch et al. (1987) we know that the dip centre has an average orbital phase of 0.84 (with phase 0 occurring at optical minimum), so we can easily modify this to provide a new zero-time for the ephemeris using:

$$T_0 = T_{dip} - \phi_{dip} P$$

where T_{dip} is the time of dip centre, ϕ_{dip} is the relative phase of the dip compared to the time of optical minimum, and P is the orbital period. We therefore estimate a new value for T_0 of JD 2453151.509 (3).

There are problems with the reliability of an ephemeris generated from just a single dipping episode, not least because we do not have full coverage either side of the dip. It is therefore hard to estimate the dip centre with absolute confidence. However, we are encouraged by the fact that our dip lies within 0.05 phase of the 1999 dips (the propagated uncertainty from these dips is of the order ~0.6) reported by in't Zand et al. (2003). More importantly, the continuum lightcurve from the resulting ephemeris possesses the same phasing relation reported by Motch et al. (1987) (Fig. 3.4)[2]. In light of this evidence we are confident that we have identified the dip centre correctly.

3.3.2 Optical Emission Spectrum

The average of the 38 individual optical spectra, corresponding to an exposure time of nearly 10 hours, is given in Fig. 3.5. The overall spectrum resembles that

[2]Note that the large intrinsic scatter in the optical continuum lightcurve makes the generation of a new ephemeris solely from a relatively limited dataset such as ours rather difficult.

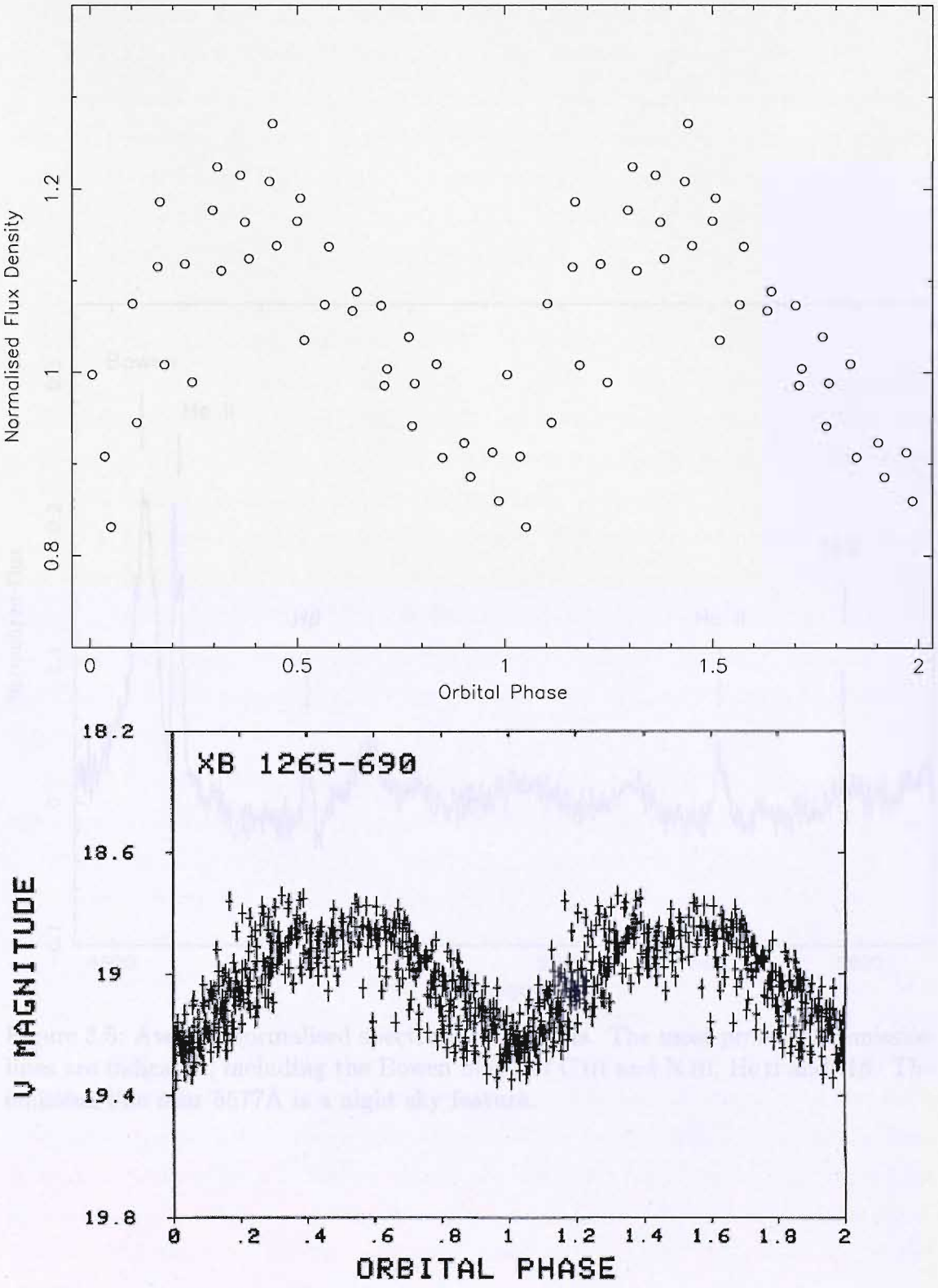

Figure 3.4: Continuum lightcurve of GR Mus, normalised to the first observation (upper panel). Below this is plotted the V-band lightcurve obtained by Motch et al. (1987).

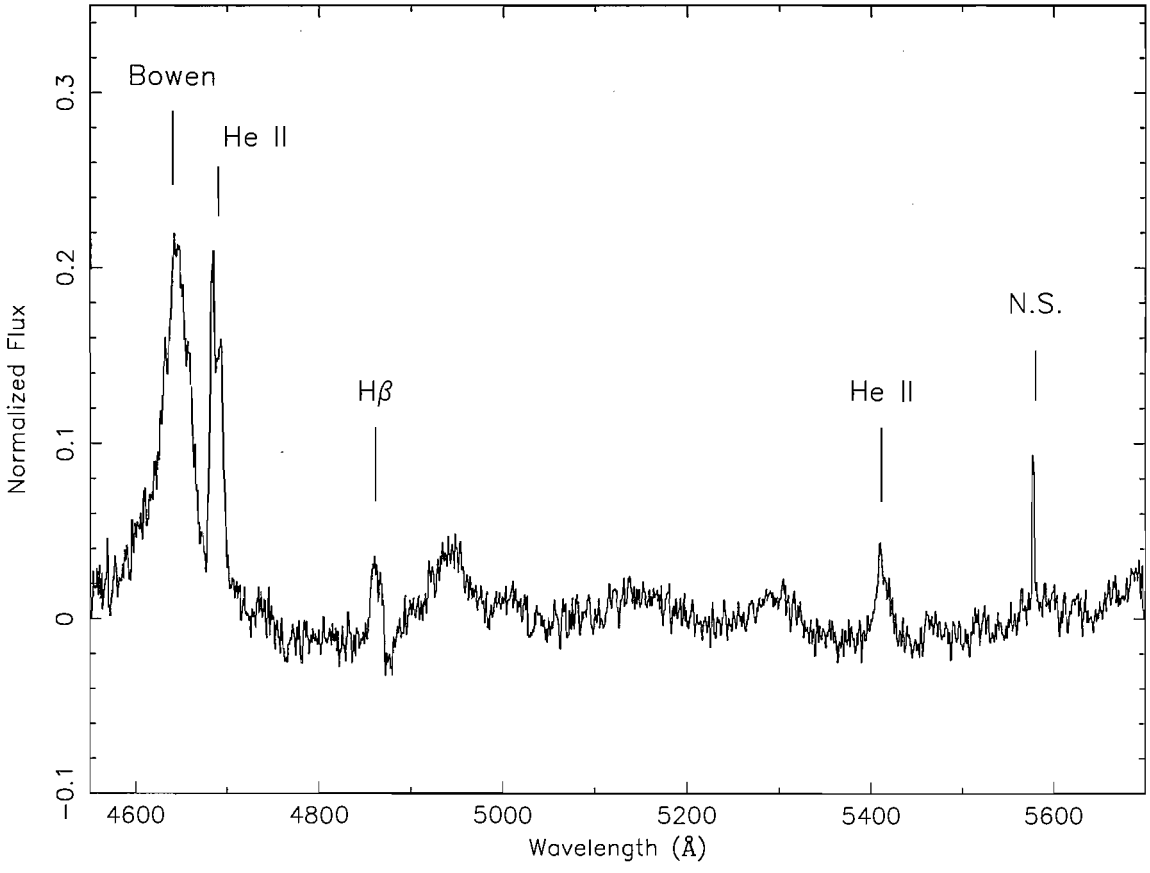

Figure 3.5: Average normalised spectrum of GR Mus. The most prominent emission lines are indicated, including the Bowen blend of C III and N III, He II and Hβ. The emission line near 5577Å is a night sky feature.

of other LMXBs, with high excitation lines superposed on a blue continuum (see Section 1.3.4). This is typical of strongly X-ray heated accretion discs.

The blue end of the optical spectrum in this system is dominated by the Bowen emission blend of C III and N III. He II λ4686 is also seen strongly in emission, in addition to weaker Hβ and He II λ5411. The absorption component longward of Hβ is observed in a few other LMXBs such as X 1822–371 (Casares et al., 2003), XTE J2123–058 (Hynes et al., 2001), GX 339–4 (Buxton & Vennes, 2003) and MM Ser (Hynes et al., 2004).

The narrow emission feature at 5577Å is [O I], a strong night-sky line useful for confirming the veracity of our wavelength calibration. The broad features between 4900–5300Å remain unidentified. We see these 'bumps' in other LMXBs (e.g. GX 9+9, X 1822–371, V801 Ara, V926 Sco) which leads us to believe that they are real, perhaps blends of a number of different weak emission lines. Part of this could be He I λ4922 and λ5016, and also Fe II λ4924, λ5018, λ5169 and λ5297. There are also several O II and O III lines between 4891–5006Å which may explain the large bump at ~4930Å. Note also that the Bowen blend (and to a lesser extent the He II λ4686 emission line) appears to be sitting upon a broad emission 'hump'. This has been noted in other LMXBs (e.g. X 1636–536; Augusteijn et al., 1998), and attributed to a blend of Fe II emission lines (Schachter et al., 1989).

In Fig. 3.6, we display the Bowen blend and He II λ4686 in the form of a trailed spectrogram. All of the individual spectra were first normalised to the continuum using a third-order polynomial fit, and then phase-folded into 15 bins. The spectra were then smoothed using a Gaussian filter with a FWHM of two pixels. We see a clear S-wave structure modulated on the orbital period in the He II λ4686 emission. The blue-to-red crossing phase is ~0.6 and the semi-amplitude ~250 km s^{-1}. This behaviour indicates a close association with the accretion disc or compact object. There is also an additional, weaker, component present. Again, this is modulated on the orbital period, approximately a quarter cycle out of phase with the more prominent component. There also appear to be faint traces of two anti-phased sharp components in the Bowen blend, though the broad underlying component moves in phase with the accretion disc S-wave (maximum blue-shift at phase 0.25). The Hβ line is shown in the right-hand panel in Fig. 3.6, along with the broad emission feature at ~4930Å. The absorption component longward of Hβ is present at all phases, and in common with the emission component and the broad feature at ~4930Å displays an S-wave approximately in phase with the expected motion of the accretion disc. The He II λ5411 emission line is too weak in the individual

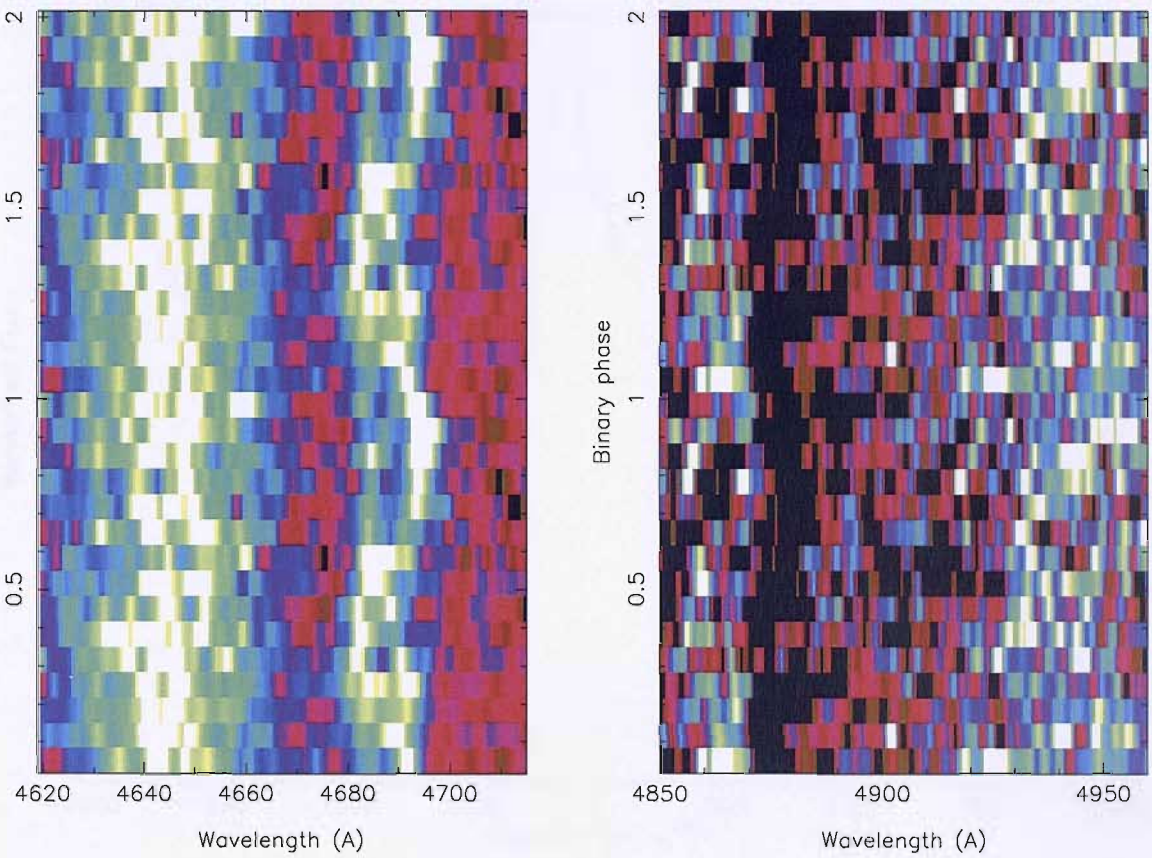

Figure 3.6: Trailed spectra of the Bowen complex and He II λ4686 (left) and the Hβ region (right). The data are plotted twice for clarity. Note that the wavelength scales differ. There are clear S-waves evident in the He II emission line, $\sim$0.25 out of phase with each other, and also in the Bowen complex. The absorption component redwards of Hβ is present at all phases.

spectra to produce a useful trailed spectrogram.

3.3.3 Motion of the compact object

Early attempts to determine any kinematic constraints on this system met with limited success. Motch et al. (1987) noted that the relative weakness of the emission lines in their spectra did not allow for the study of their variation with orbital phase. However, they did exclude the possibility of orbital motion of He II λ4686 (which requires a source of highly ionising radiation, and is typically seen in accretion discs) in excess of 300 km s^{-1}. Later observations by Cowley et al. (1988) did result in a measurement of the same He II line's core velocity, which possessed a semi-amplitude of 114 $\pm$ 13 km s^{-1}. However, this is not a particularly reliable measurement of the compact object velocity. The line core can often be heavily contaminated by

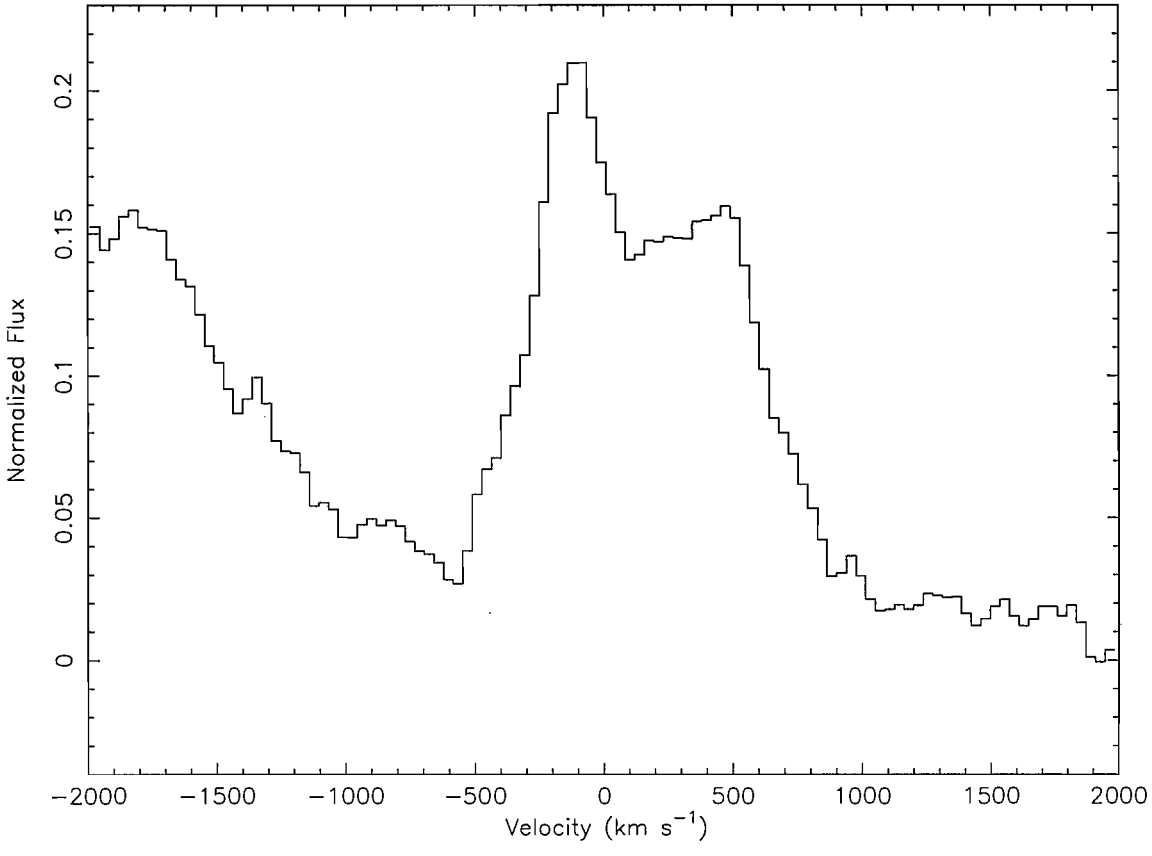

Figure 3.7: Velocity profile of the He II λ4686 emission line displaying a complex core structure. The extreme blue wing is contaminated by the Bowen emission blend.

other emission sites, for example from the accretion stream or 'hot-spots' on the accretion disc itself (see Fig. 3.7). Instead, the compact object velocity can be better estimated by examining the wings of the emission line (see Section 2.1.4). These wings find their origin in the high-velocity gas of the inner accretion disc, very close to the compact object itself. Presumably this gas will closely replicate the motion of the compact object, and it is far less likely that alternative emission sites will provide a strong contaminating effect.

We have followed the double-Gaussian technique (Section 2.1.4) to estimate both the velocity semi-amplitude and the systemic velocity of the compact object K_1 from He II λ4686 (Schneider & Young, 1980). We employed a double Gaussian bandpass with FWHM of 100 km s^{-1} and Gaussian separations of 300–1700 km s^{-1} in steps of 100 km s^{-1}. Radial velocity curves of line sections with separations of 700–1400 km s^{-1} yield consistent results with a median blue-to-red crossing phase of 0.58 $\pm$ 0.03, median velocity semi-amplitude $K_1 = 130 \pm 16$ km s^{-1} and median systemic velocity $\gamma = 173 \pm 12$ km s^{-1} (Fig. 3.8). The errors are conservatively taken from the maximum error obtained from sine wave fits to the results from each individual

line section. Separations below 700 $\mathrm{km\,s^{-1}}$ suffer from contamination by the line core, whilst separations over 1400 $\mathrm{km\,s^{-1}}$ become corrupted by continuum noise and the Bowen emission blend. The small difference in phasing (0.08 orbits) indicates that even the line wings are contaminated to some extent by inhomogeneities in the disc. For example, phase delays of 0.1–0.2 relative to the expected motion of the compact object can be caused by some residual hot spot contamination.

Unfortunately, the He II λ5411 and Hβ emission lines, which are clearly seen in our averaged spectrum (Fig. 3.5), are too weak in the individual spectra for a similar analysis. For example, Fig. 3.8 clearly shows a lack of consistency in the results from different line sections of the He II λ5411 emission line. This indicates that the fitting procedure is dominated by noise.

3.3.4 Doppler Tomography

We can use Doppler tomography (Marsh & Horne, 1988, see Section 2.3) to measure the radial velocity amplitudes of any weak, narrow, emission lines that may be present. By mapping the observed data onto a velocity co-ordinate frame, Doppler tomography makes use of all data at once and can thus be used to search for features that are too weak to be distinguished in each individual spectrum. One effectively resolves the distribution of line emission in the co-rotating frame of the binary system, providing an excellent tool for identifying the origin and kinematics of the various emission components. It also allows us to map the emission line distribution from the broader He II and Hβ lines.

Secondary star emission is readily identifiable in Doppler tomograms since the solid body rotation of the Roche lobe is mapped to a corresponding Roche lobe area along the positive V_y-axis. For reference, in Figs. 3.9–3.13 we overplot the area of the Roche lobe and the centres of mass of the donor star (uppermost cross), full system (map centre) and the compact object (lower cross) assuming a mass ratio of $\sim$0.4 (equivalent to the mass ratio proposed by Cowley et al., 1988) and compact object velocity of 130 $\mathrm{km\,s^{-1}}$. Additionally, we have overplotted the ballistic accretion stream for such a system. The concentric circles, centred upon the compact object and with radii of 200–450 $\mathrm{km\,s^{-1}}$, indicate typical emission regions from a LMXB accretion disc. We employed a maximum entropy implementation of Doppler tomography whereby the data are fitted under the added constraint of maximising the entropy (i.e. image smoothness) of the tomogram (Marsh & Horne, 1988). This reduces the presence of noise artifacts in the recovered tomograms and allows for a

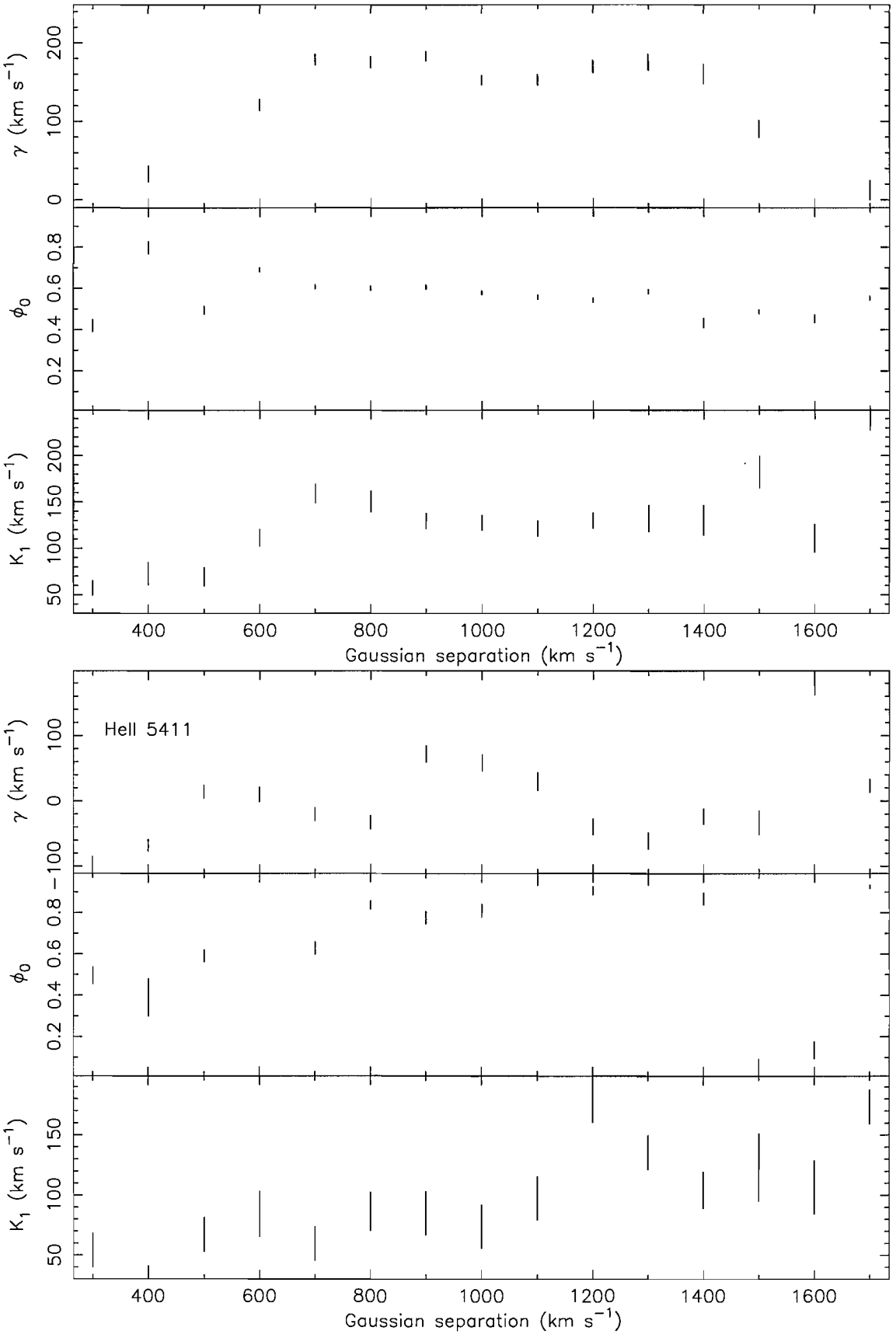

Figure 3.8: Diagnostic diagram for the He II λ4686 (top panel) and He II λ5411 (bottom panel) emission line wings, displaying the systemic velocity γ (top), phasing (centre) and radial velocity K_1 (bottom) in each panel.

simultaneous fit to a number of heavily blended lines.

In Fig. 3.9 we display a tomogram of the He II λ4686 emission line. This displays a clear enhancement in the lower left quadrant and an additional component close to the accretion stream. We do not observe the classic ring-like distribution of the accretion disc, presumably due to the strength of the line core features vastly overwhelming the high velocity inner disc emission. The enhancement in the (lower) left quadrant is also seen in the tomograms of Hβ (Fig. 3.10) and He II λ5411 (Fig. 3.11). Whilst this phenomenon is a common feature in the remarkable SW Sex-type systems (Hellier, 2000), it has also been noted in some other LMXBs, notably XTE J2123–058 (Hynes et al., 2001), GX 9+9 (Cornelisse et al., 2006c) and J 0422+32 (Casares et al., 1995). However, in this case (and in the case of X 1636–536 and X 1735–444, Casares et al 2006; see Fig. 3.12) the emission is not quite so localised in the lower-left quadrant, but is present in a broad band on the left-hand side of the maps. Rather than being an analogue to the highly magnetic SW Sex-type systems, it is likely that this emission is produced in an extended disc bulge. In most LMXBs, the He II emission is predominantly produced in a hotspot where the accretion stream impacts the disc (thus producing a spot in the upper left quadrant of a Doppler map) or is more evenly distributed around the bulk of the accretion disc. If the emitting gas was symmetrically distributed around the primary, the Doppler image would reveal a circular distribution centred on $V_x = 0$, $V_y = -K_1$. This would have been a useful way of confirming the K_1 estimate derived from the wings of the He II λ4686 emission line.

Like He II λ4686, the He II λ5411 tomogram also indicates the presence of some diffuse emission at velocities which partially correspond to the Roche lobe of the donor star. However, as this emission is diffuse in the Doppler map, extending over a broad range of velocities, it is unlikely to be associated with the donor in physical space. Fluorescent emission from the donor in this case should manifest itself as a tightly concentrated spot situated on the positive V_y axis.

In Fig. 3.13 we present a tomogram of the N III λ4640 emission line. The maximum entropy method of producing Doppler tomograms allows us to simultaneously fit a number of different lines to produce one map. However, in this case the N III λ4640 line strongly dominates over any others. We see two regions of enhanced emission. The brighter of the two spots occurs at a combination of phasing and velocity where we would expect the donor star to be fluorescing. The small horizontal offset of $V_x \simeq 35 \pm 30$ km s^{-1} is consistent with the errors in our ephemeris ($\pm$ 0.02 in phase). The second spot occurs at a much lower velocity, and is 1–2 σ weaker

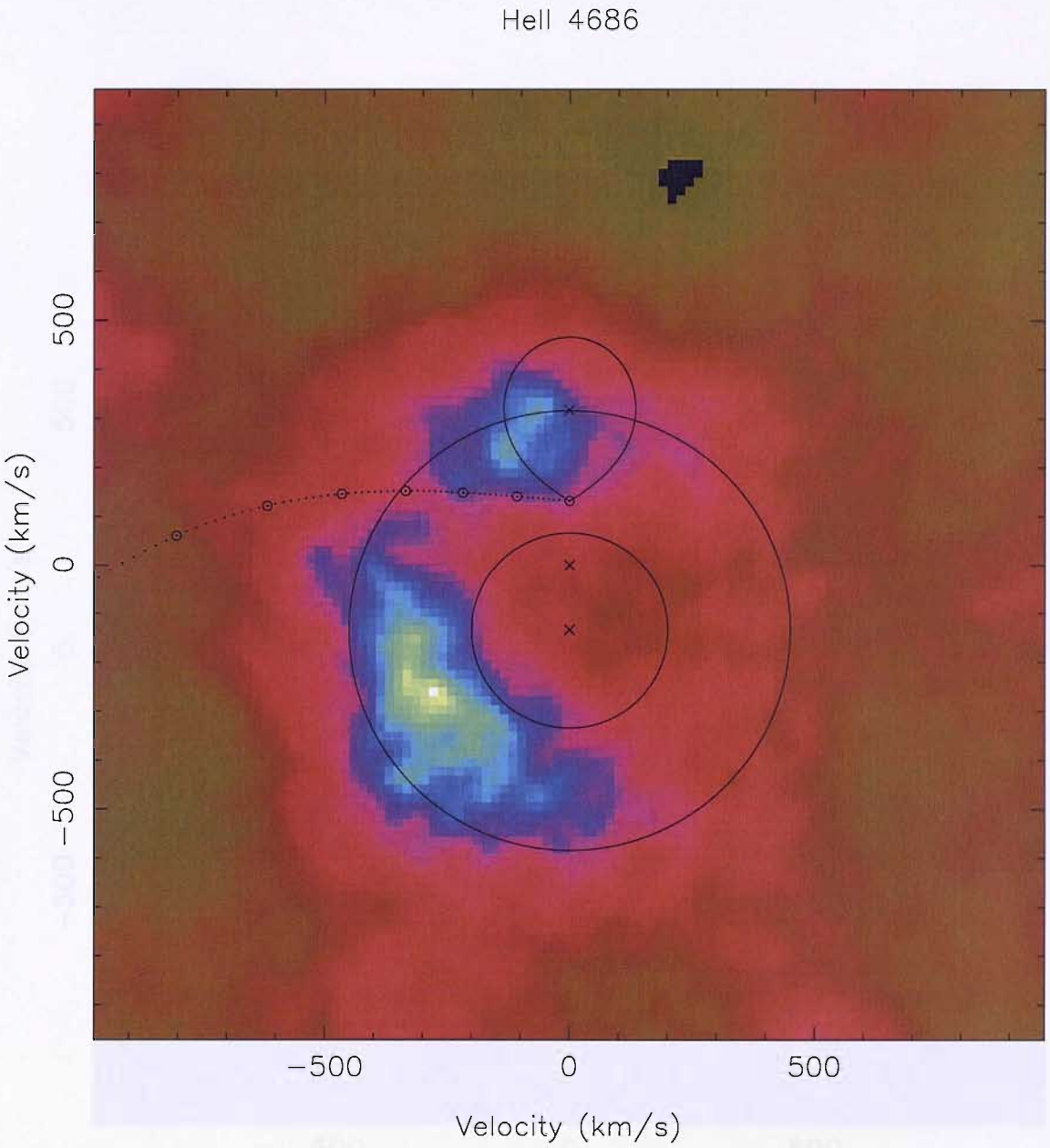

Figure 3.9: Doppler tomogram reconstructed from the He II λ4686 emission line using maximum entropy optimisation. The area of the Roche lobe, the ballistic accretion stream and the centres of mass of the donor star (uppermost cross), system (map centre) and the compact object (lower cross) are plotted assuming a mass ratio of $\sim$0.4 and compact object velocity of 130 km s^{-1}. The concentric circles, centred upon the compact object and with radii of 200–450 km s^{-1}, indicate the typical emission regions from the accretion disc.

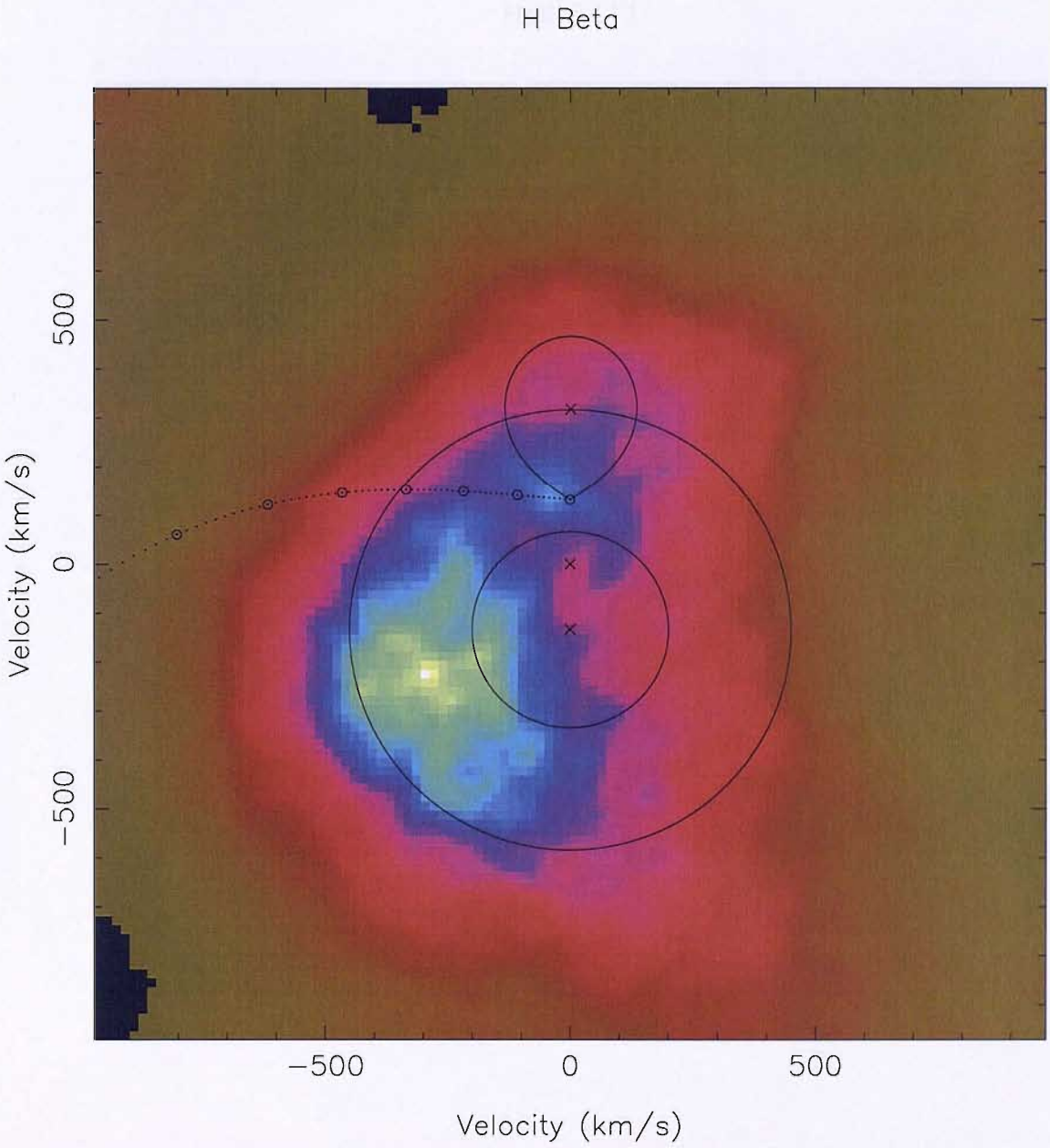

Figure 3.10: Doppler tomogram reconstructed from the Hβ emission line using maximum entropy optimisation. The symbols are as for Fig. 3.9.

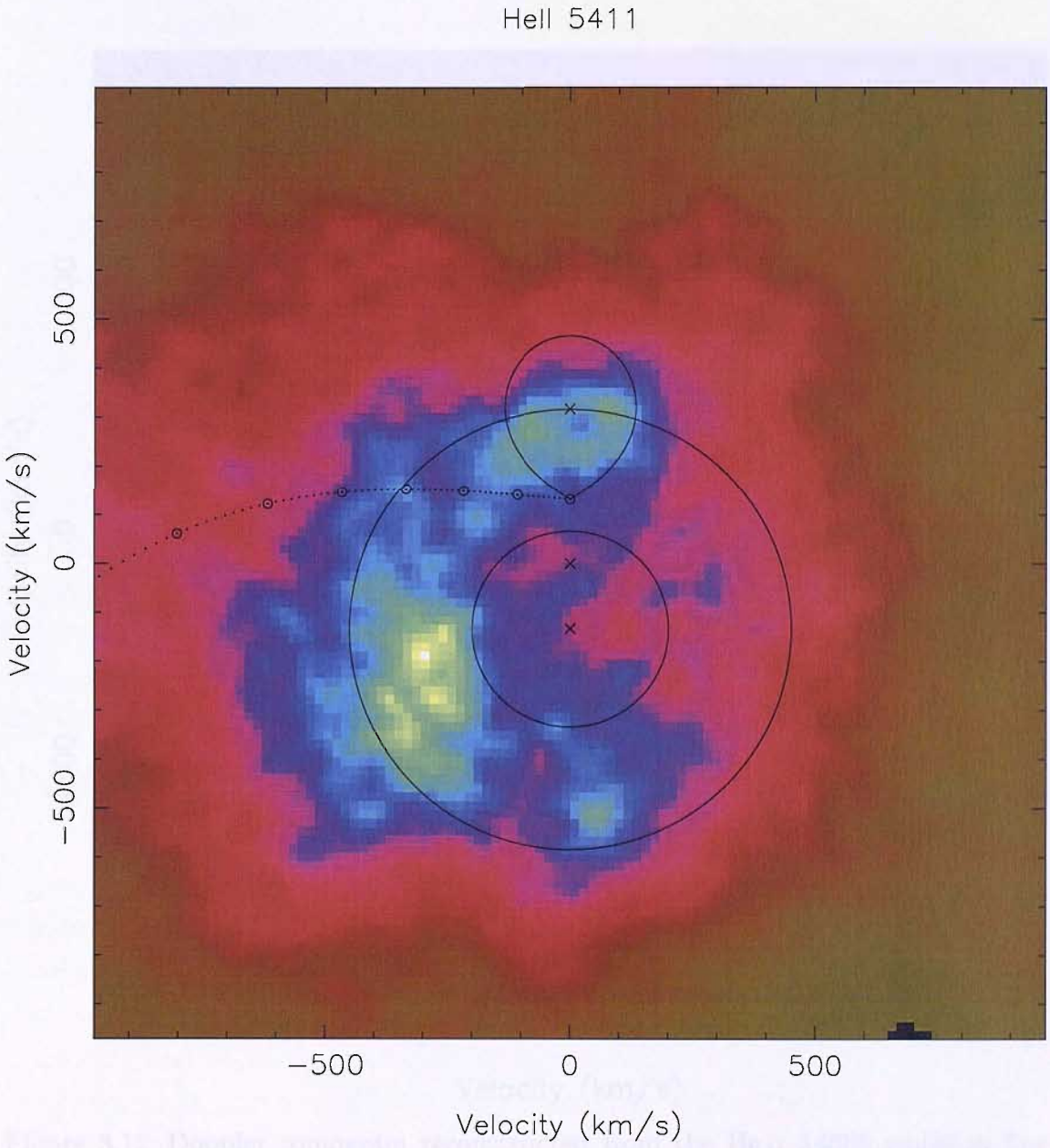

Figure 3.11: Doppler tomogram reconstructed from the He II λ5411 emission line using maximum entropy optimisation. The symbols are as for Fig. 3.9.

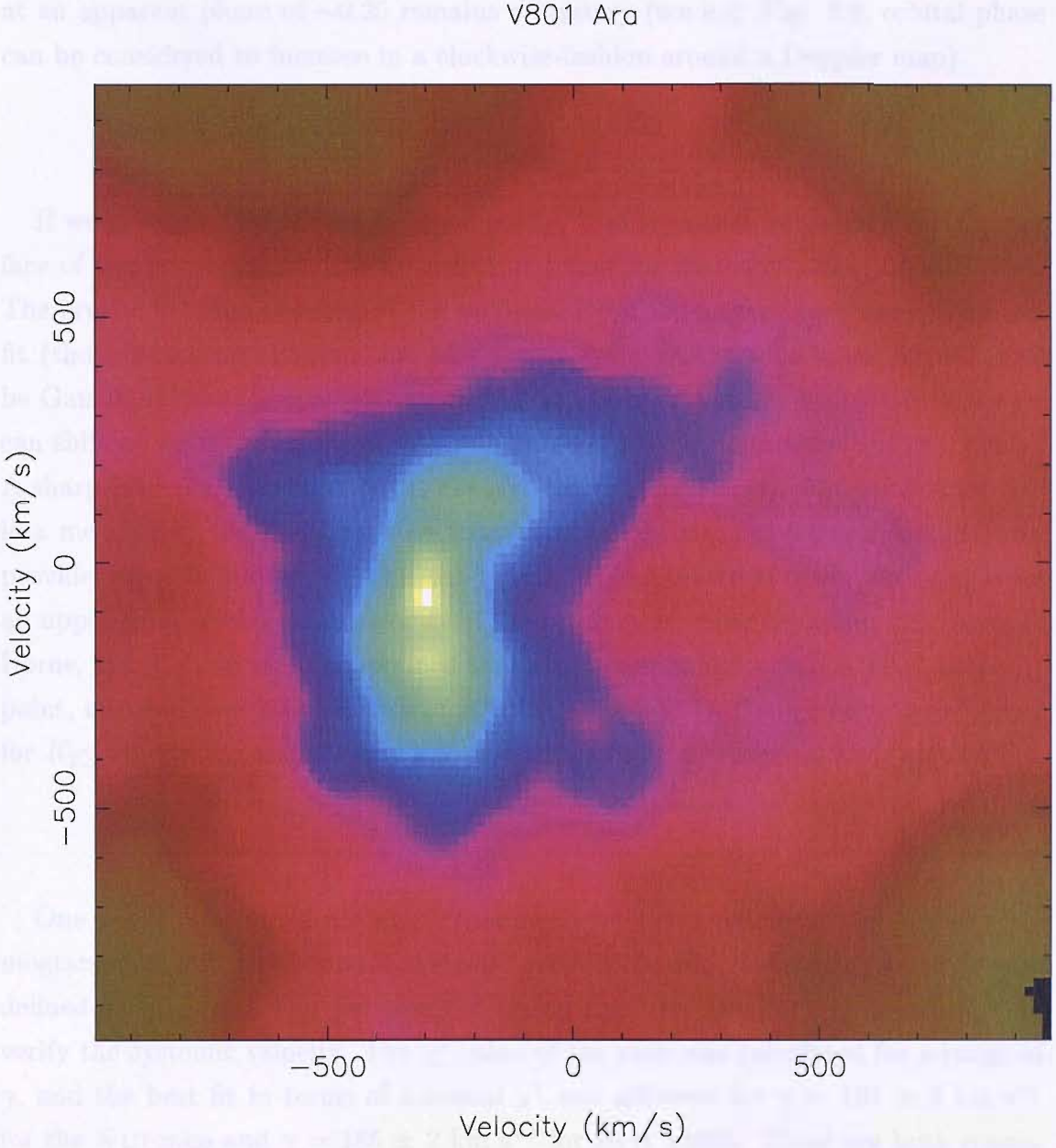

Figure 3.12: Doppler tomogram reconstructed from the He II λ4686 emission line in X 1636–536. This system, like XB 1254–690 and X 1735–444, displays enhanced emission in the left hand side of the Doppler map, possibly from an extended disc bulge.

(relative to the local noise level) than the first. It is difficult to provide a truly satisfactory explanation for its origin. Perhaps it originates from some form of low velocity outflow (e.g. disc wind), though why it should be preferentially observed at an apparent phase of ~0.25 remains a mystery (see e.g. Fig. 2.9, orbital phase can be considered to increase in a clockwise-fashion around a Doppler map).

If we presume that the bright spot in Fig. 3.13 is caused by the irradiated inner face of the donor star, this is an excellent tracer for the kinematics of the system. The precise location of the spot can be measured using a two-dimensional Gaussian fit (though bearing in mind that the actual shape of the spot is not expected to be Gaussian), providing a velocity of $K_{\rm em} = 245 \pm 30$ km s^{-1}. Using this value we can shift all of our spectra into the rest-frame of the (irradiated face of the) donor. A sharp N III λ4640 component is clearly resolved (Fig. 3.14). However, since this is a measure of the motion of the irradiated inner face of the donor star, it only provides us with a lower-limit on the velocity of the centre of mass. We can derive an upper-limit to the radial velocity of the companion using Equation 2.7 (Wade & Horne, 1988). Here we have assumed that the Bowen emission is produced at the L_1 point, i.e. f=1 and at a velocity of $K_{\rm em}^{max}$= 245 km s^{-1}. This gives an upper-limit for $K_2 \leq 446$ km s^{-1} and thereby a mass ratio (Eqn. 2.2) range of $0.26 \leq q \leq 0.68$.

One final piece of information remains to be extracted from the Doppler tomograms; assigning the correct systemic velocity should produce the most sharply defined features in a Doppler map. We used the He II and N III Doppler maps to verify the systemic velocity. The χ^2 value of the map was calculated for a range of γ, and the best fit in terms of minimal χ^2 was achieved for $\gamma = 192 \pm 2$ km s^{-1} for the N III map and $\gamma = 185 \pm 2$ km s^{-1} for He II λ4686. These are both consistent with, if slightly higher than, the results derived from the He II λ4686 wings in Section 3.3.3. The complex, asymmetric core profile of the He II emission line could be contaminating one wing more than the other, leading to this small offset. We heretofore adopt the value for γ derived from the He II λ4686 Doppler map. This should be more reliable than the N III map since only a single, isolated emission line is involved in the fitting process, rather than the more complicated blend of Bowen lines.

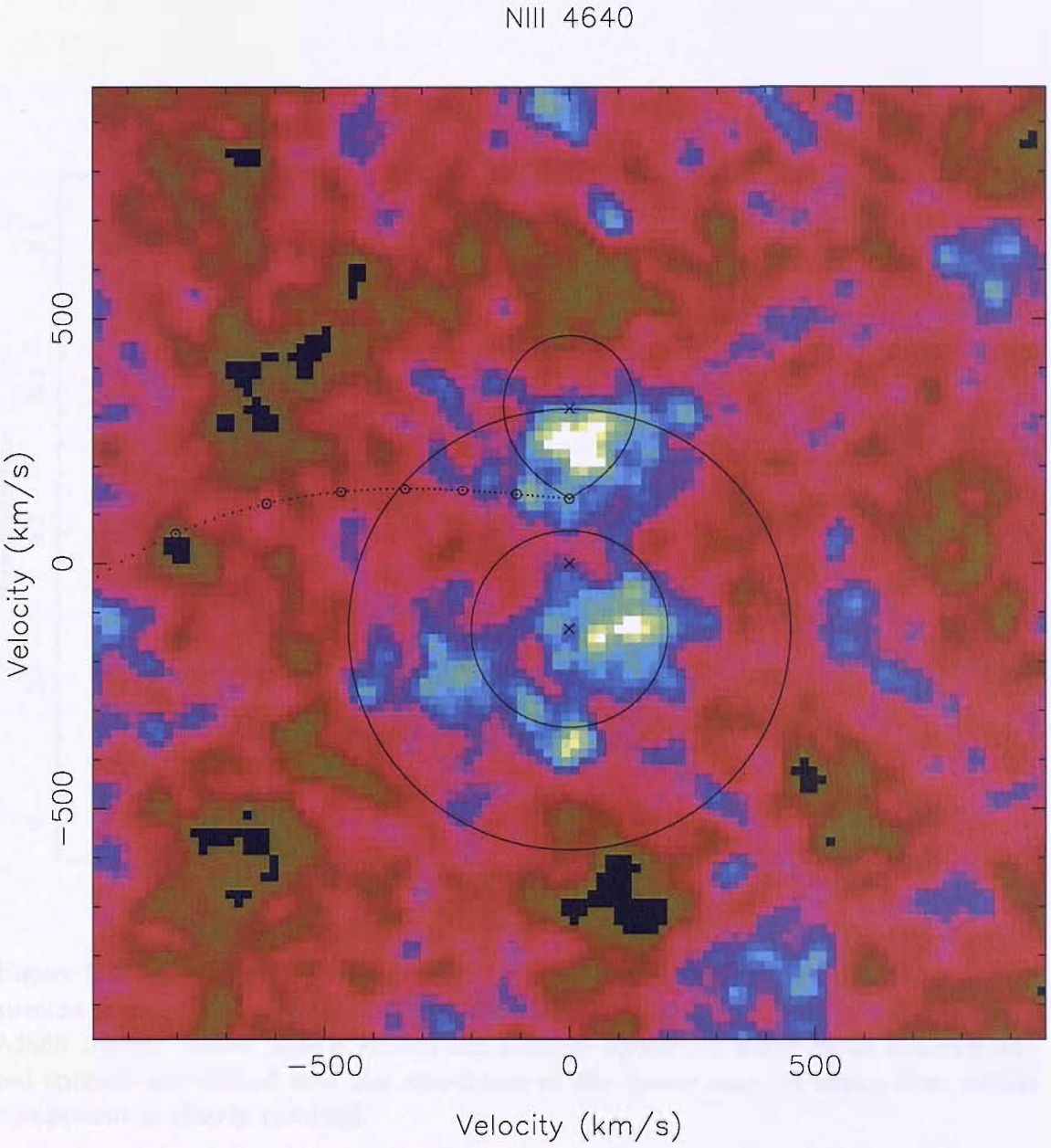

Figure 3.13: Doppler tomogram reconstructed from the N III λ4640 emission line using maximum entropy optimisation. The symbols are as for Fig. 3.9.

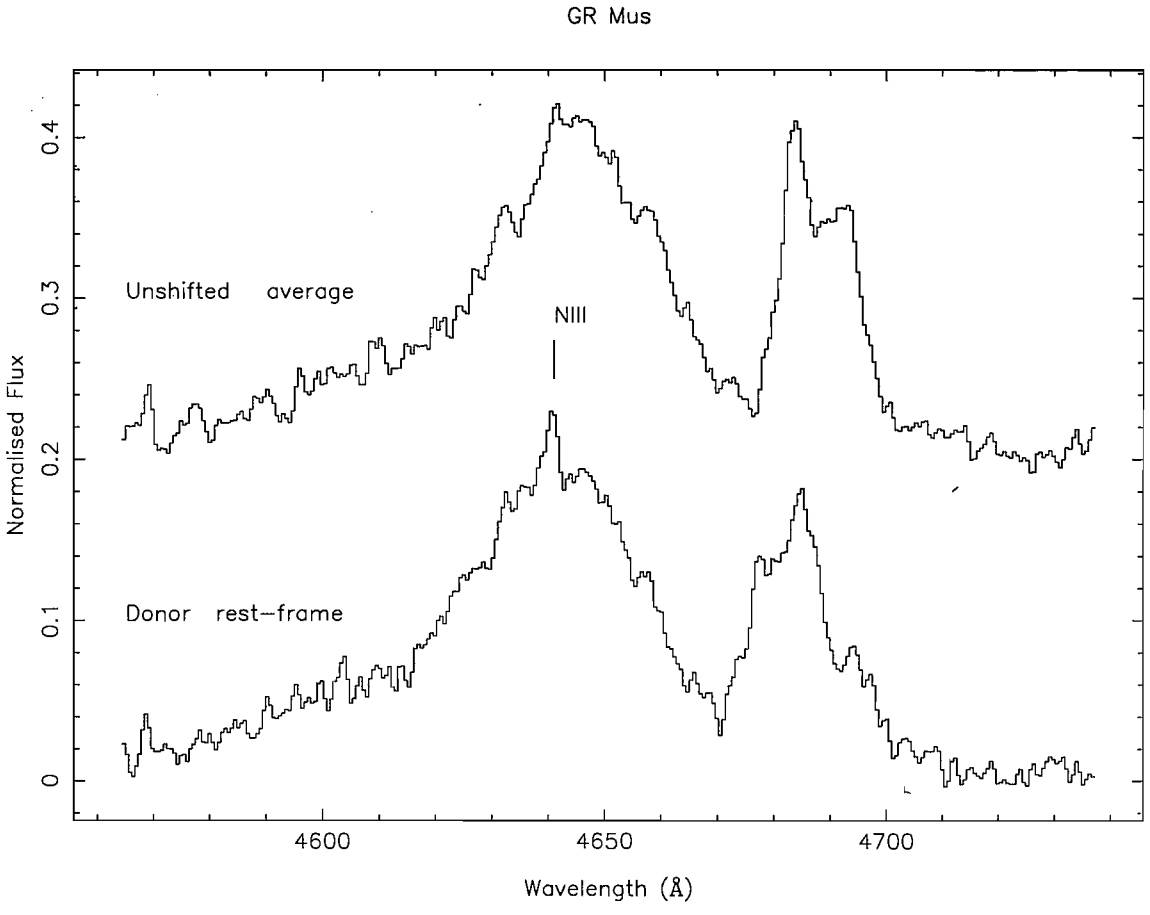

Figure 3.14: Average spectrum created by combining all of the individual unshifted spectra from our observations (top), showing the Bowen emission blend and He II λ4686 region. Below this is shown the average spectrum when all of the individual spectra are shifted into the rest-frame of the donor star. A sharp N III λ4640 component is clearly resolved.

3.4 Discussion

3.4.1 Systemic Velocity

Whilst the systemic velocities inferred from both the wings of the He II λ4686 line and the Doppler tomograms are self-consistent ($\sim$ 185 km s^{-1}), they are considerably higher than the earlier estimate by Cowley et al. (1988) (98 $\pm$ 10 km s^{-1}). This measurement was obtained from rather low quality data, with poor spectral and temporal resolution. Additionally, they based their measurements on the motion of the He II λ4686 line core. There are a number of different emitting regions which contribute to this line, leading to a complex core structure (see e.g. Figs. 3.7, 3.9). A basic measurement of the line centre under the assumption that this will accurately trace the motion of the compact object will therefore be subject to large systematic errors.

In light of this, we believe that our estimate for the systemic velocity will be a better reflection of the true value. Although large, our measurements do seem reasonable in the context of the high galactic latitude (b = -6.42) of XB 1254–690; the neutron star is likely to have received a substantial 'kick' out of the Galactic Plane at birth. A number of statistical studies on pulsar velocities have been carried out. These studies give a mean birth velocity of 100–500 km s^{-1}, with some possessing velocities of $\geq$1000 km s^{-1} (Wang et al., 2006).

3.4.2 Interpretation of the Bowen blend Doppler map

The N III Doppler map (Fig. 3.13) appears to display enhanced emission in the region of and at the phasing where we would expect to see the companion star Roche lobe, in addition to an abundance of noisy structure in the outer regions of the map. A useful way to confirm the validity of the Doppler map is to observe the behaviour of sharp components in our trailed spectrogram (Fig. 3.6). This is not trivial due to the faintness of XB 1254–690 compared to a system such as Sco X-1, which clearly features narrow Bowen lines moving in phase with the donor star (Steeghs & Casares, 2002, see Fig. 2.6).

We can reconstruct an ideal trailed spectrogram from the Doppler tomograms to test for systematic residuals in the maps. As a test, we first apply this technique to the He II λ4686 emission line. The two distinct components we see in the Doppler map (Fig. 3.9) are reproduced clearly in the predicted trailed spectrogram (left hand panel, (Fig. 3.15), and can be easily identified in the observed data.

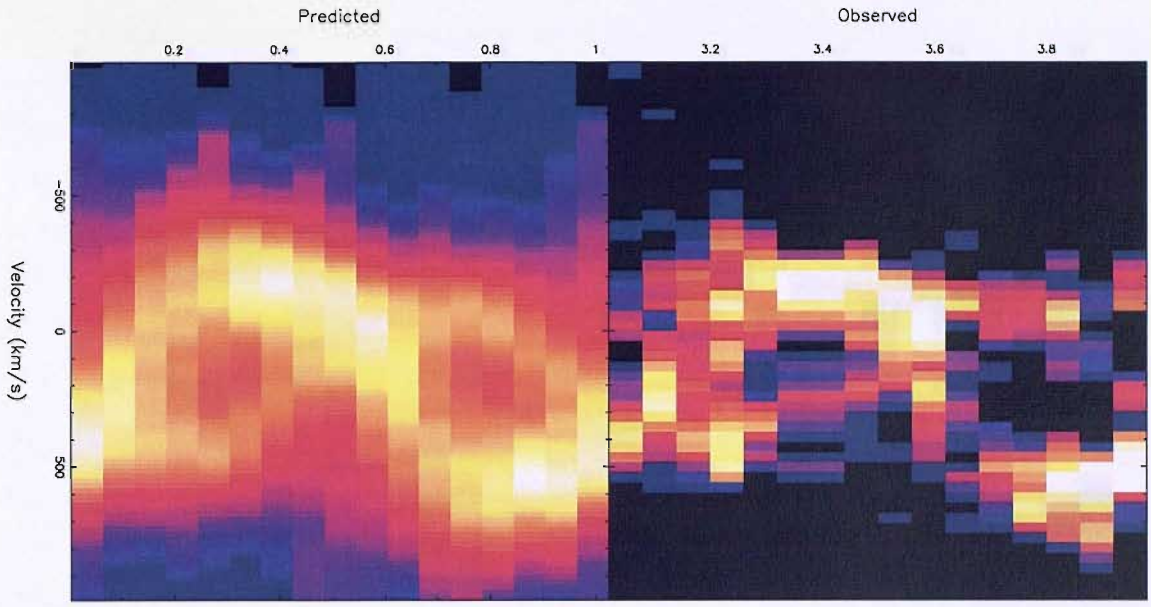

Figure 3.15: The right hand panel displays the observed trailed spectra of the He II λ4686 emission line and the left hand panel shows the ideal trailed spectrogram reconstructed from the Doppler tomogram shown in Fig. 3.9. Orbital phase is plotted along the x-axis.

For the case of the N III λ4640 emission line (Fig. 3.16) we again see two components in the reconstructed spectrogram, though not quite so distinctly as for the case of He II. Comparing this idealised image to the real data it is indeed possible to detect faint traces of these two narrow, approximately anti-phased lines which produce the two distinct spots in Fig. 3.13. The second spot is therefore unlikely to be a systematic residual produced when creating the Doppler map, and its unusual phasing/positioning could perhaps therefore be attributed to a region which violates one of the axioms of Doppler Tomography (Section 2.3.1), for example that all motion should be parallel to the orbital plane. Note that a violation of these axioms does not mean that the map is useless, but it does complicate the successful interpretation of the map.

3.4.3 A simple estimate for the mass of the system components

The mass function (see Section 2.1) provides an extreme lower-limit for the mass of the compact object in this system of $f_{em}(M) = 0.17\ M_{\odot}$, derived using the lower-limit to $K_{\rm em}$ taken from section 3.3.4. Being a dipping source, the inclination is reasonably well known (65°–73°; Motch et al., 1987). As such, we can derive absolute

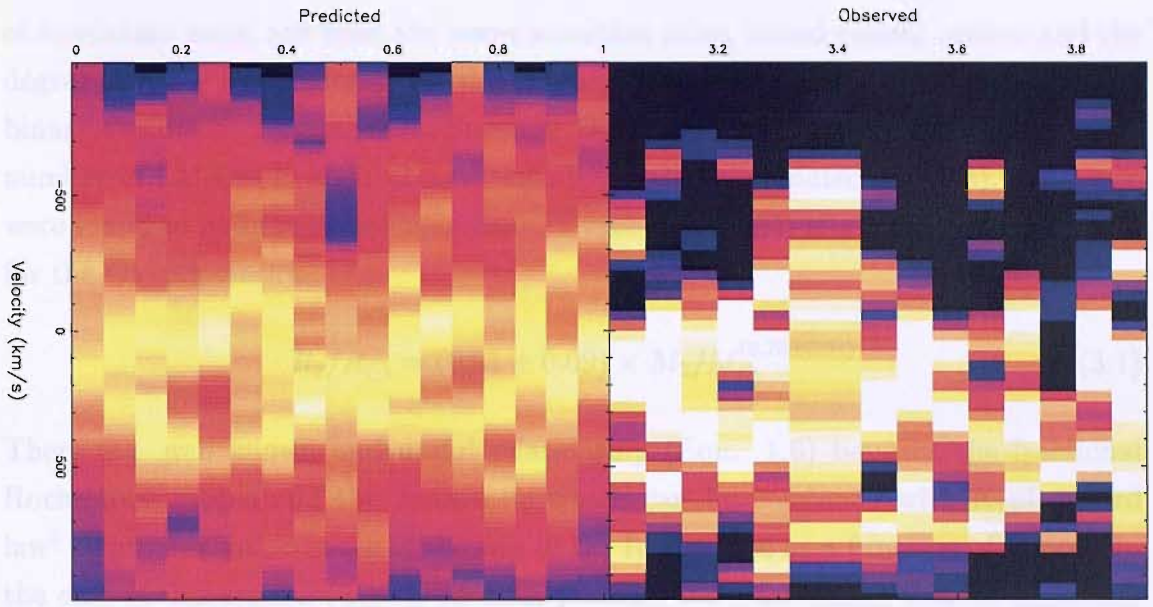

Figure 3.16: The right hand panel displays the observed trailed spectra of the N III λ4640 emission line, part of the Bowen emission complex. Next to this is plotted the ideal trailed spectrogram reconstructed from the Doppler tomogram in Fig. 3.13. Orbital phase is plotted along the x-axis.

mass estimates for the individual system components of $0.535 \leq M_X/M_\odot \leq 3.09$ and $0.321 \leq M_2/M_\odot \leq 1.10$. The lower limits are obtained by assuming no K-correction is necessary (i.e. the light centre of the sharp Bowen fluorescence lines is equivalent to the centre of mass of the donor star) whilst the upper limits emerge from the assumption that the maximum possible K-correction is necessary (i.e. f=1 in Eqn. 2.7).

These rather weak limits derive mainly from the errors incurred in measuring the N III fluorescence line in the Doppler tomogram and then performing the K-correction. There is nothing that can be done to improve the quality of our data, but we can tighten the mass constraints somewhat by applying other considerations (see below and Section 3.4.4).

We know that the companion must be filling its Roche lobe in order to permit persistent accretion. Additionally, previous studies (Motch et al., 1987) favour the presence of a main-sequence-like donor over a highly evolved one. A number of studies have been performed to derive a mass-to-radius (M–R) relationship for the companion star in X-ray active, optically bright systems. Unfortunately for our purposes, the majority of these studies have concentrated on Cataclysmic Variable (CV) systems (which feature a white dwarf as the accreting object, for a comprehensive review see Warner, 2003). These systems differ from LMXBs in a number

of important ways, not least the lower accretion rates, initial system masses and the degree of X-ray irradiation of the donor star, which will all have an impact upon the binary evolution. Nevertheless, Smith & Dhillon (1998) did include a (very) small number of LMXBs in their observations (otherwise dominated by CVs), and these were found to be in reasonable agreement with the (M–R) relationship they derived for the CV population:

$$R_2/R_\odot = (0.91 \pm 0.09) \times M_2/M_\odot^{(0.75\pm0.04)} \tag{3.1}$$

There is a well known and useful relationship (Eqn. 1.6) between the fractional Roche lobe radius and the mass-ratio which can be combined with Kepler's 3rd law[3] to provide an estimate of the size of the Roche lobe as a function of period. In the case of this system (with a 3.9 hour period), the relationship may be expressed as:

$$R_L = 0.58 M_2^{1/3} \tag{3.2}$$

We can combine these relationships to refine our mass limits for the companion star to $0.32 \leq M_2/M_\odot \leq 0.47$ (see Fig. 3.17). In combination with the limits to the mass ratio derived in section 3.3.4 and the earlier estimate for the mass of the compact object, this can further constrain the compact object mass to $0.53 \leq M_X/M_\odot \leq 1.81$.

We must be extremely careful when considering the merits of these refinements however. For example, the M–R relationship we use is dominated by Cataclysmic Variable systems, as it is their proximity that makes such studies possible. Only three short-period LMXBs are used in the dataset of Smith & Dhillon (1998), and it is likely that there are significant evolutionary effects in these systems which will alter their M–R relationship as a population.

3.4.4 Refined mass limits

Recent work by Munoz-Darias et al. (2005) (see Section 2.2.5) allows us to determine a more accurate K-correction. This will take into account the screening of the donor star by the accretion disc, which has the effect of modifying the position of the possible emission sites of any fluorescence lines originating upon the companion star.

[3]defined as $a^3 = \frac{G(M_1+M_2)P^2}{4\pi^2}$

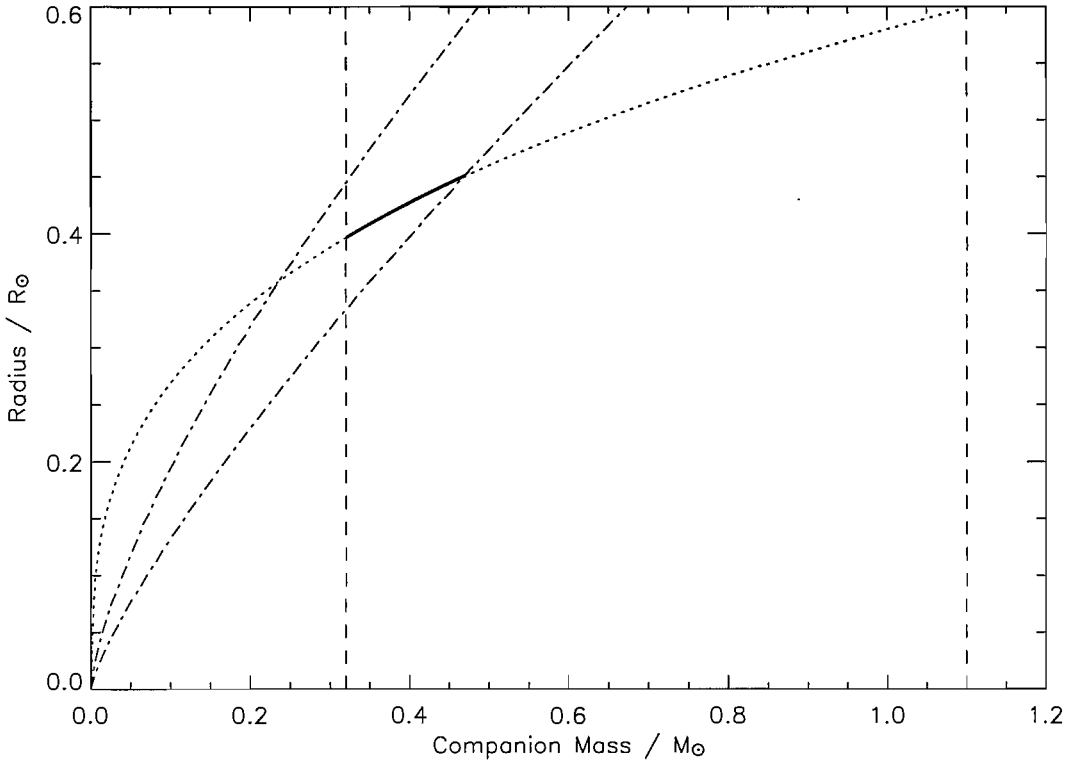

Figure 3.17: Mass versus radius plot for the companion star. The dotted line is the estimated size of the Roche lobe (Eqn. 3.2), the dashed lines indicate the limits determined using the N III λ4640 fluorescence line, dot-dashed lines are the Mass-Radius relationship of a typical companion star in a CV or LMXB system (Eqn 3.1. The solid line indicates the allowed parameter space for the companion star using these constraints.

Table 3.2: Derived system parameters for XB 1254–690

Parameter		Parameter	
T_{dip} (HJD)	2453151.647 (3)	γ (km s^{-1})	185 ± 2
T_0 (HJD)	2453151.509 (3)	q	0.32–0.43
K_1 (km s^{-1})	130 ± 16	$M_X(M_\odot)$	1.20–2.64
K_{em} (km s^{-1})	245 ± 30	$M_2(M_\odot)$	0.45–0.85

de Jong et al. (1996) estimated an opening (semi-) angle for the accretion disc in XB 1254–690 of $\sim 12°$, using a simple geometric model for the reprocessing of X-rays in LMXBs. It is important to note that this value is hostage to the implicit assumptions underlying these models, for example the geometric description of the disc and of the X-ray emitter. This will entail a systematic uncertainty that likely exceeds the internal model accuracy of less than a degree.

Nevertheless, this value agrees well with Motch et al. (1987) who estimated an opening angle of $\sim 9° - 13°$ in order to explain the observed amplitude of the orbital photometric modulation. We can use this information to derive a more accurate mass estimate for the individual components by using the K-correction algorithm developed by Munoz-Darias et al. (2005). This measures the deviation between the reprocessed light centre of the fluorescence emission lines and the centre of mass of a Roche lobe filling star in a persistent LMXB, including the screening effects by a flared accretion disk. Using the fourth order polynomial fits given by Munoz-Darias et al. (2005) for disc opening angles of 8°, 10°, 12° and 14° gives a total mass range for the neutron star of $1.20 \leq M_X/M_\odot \leq 2.64$. Since the neutron star mass and the mass ratio are related by the mass function, we obtain $0.32 \leq q \leq 0.43$, and limits on the companion mass of $0.45 \leq M_2/M_\odot \leq 0.85$.

This correction is most strongly dependent upon the opening angle of the accretion disc, monotonically decreasing with opening angle such that the largest opening angle gives the lowest neutron star mass. Since the largest opening angle we have used exceeds the estimates of both Motch et al. (1987) and Munoz-Darias et al. (2005), this gives a very conservative lower limit to the neutron star mass, and the true value is unlikely to be so low. Equally, the upper limit is derived using an opening angle lower than that suggested by Motch et al. (1987) and as such the neutron star is unlikely to be quite so massive.

Limiting ourselves to a disc opening angle of exactly 12° (de Jong et al., 1996), the mass constraints upon the neutron star tighten up to $1.35 \leq M_X/M_\odot \leq 2.32$, with $0.33 \leq q \leq 0.41$ and $0.49 \leq M_2/M_\odot \leq 0.79$. These limits are not a vast improvement over the ones derived above using a range of opening angles from 8–14°. This indicates that the major source of uncertainty in this case is still incurred

from the measurement of $K_{\rm em}$ and K_1, in addition to the system inclination angle. The choice of disc opening angle (within a reasonable range) has only a small effect in comparison. Nevertheless, we feel it is prudent not to restrict our final mass estimate by the assumption of a disc opening angle of exactly 12°, preferring the more conservative range of 8–14°. The derived parameters for XB 1254–690 are listed in Table 3.2.

Using Eqn. 3.2, we can derive the range of potential Roche lobe radii consistent with the mass range of the companion star that we have derived kinematically. This turns out to be $0.44 \leq R_L \leq 0.55$. Whilst at the lower end of our mass constraints the donor would be consistent with a main-sequence-like object as proposed by Motch et al. (1987), we cannot rule out the possibility that XB 1254–690 harbours an over-massive evolved companion that has been stripped of its outer layers (e.g. King & Schenker, 2002).

3.5 Conclusions

We have used the Bowen emission blend and Doppler tomography to trace for the first time the motion of the donor star in the persistent LMXB XB 1254–690. This has allowed us to derive kinematical mass limits for this system. In combination with estimates for the opening angle of the accretion disc, and new measurements of the He II λ4686 emission line (which traces the motion of the compact object), we have derived new mass constraints of $1.20 \leq M_X/M_\odot \leq 2.64$ for the compact object and $0.45 \leq M_2/M_\odot \leq 0.85$ for the companion star.

We cannot rule out the possibility that XB 1254–690 harbours an over-massive evolved companion star, or more intriguingly an over-massive neutron star. Tighter constraints on the system parameters may therefore have important implications for our knowledge of the equation of state of nuclear matter (e.g. Cook et al., 1994) or indeed on the formation scenarios for typical LMXBs (e.g. Pfahl et al., 2003).

Future investigations should also concentrate on determining the origin of the unusual second spot in the N III Doppler map (Fig. 3.13). This feature is hard to explain, and perhaps could be caused by a violation of the axioms of Doppler Tomography. Related to this point, the broad emission band seen in the left hand side of the Doppler maps for He II and Hβ (in this system and a number of others) is of uncertain origin. We believe this emission to be produced in an extended disc bulge, but physical modelling will be necessary to confirm this.

Chapter 4

An Atlas of the Bowen Blend Features in Low Mass X-Ray Binaries

In this chapter all of the LMXBs thus far studied using the Bowen fluorescence technique are gathered together and discussed as a population. There is strong evidence that the transient systems Aql X–1 and GX 339–4 possess highly evolved, over-massive donors. Furthermore, it is possible that up to 90% of the included sample derive from evolved, intermediate mass systems, in accordance with the recent predictions of Pfahl et al. (2003).

4.1 Introduction

Observations show that the strength of the Bowen blend with respect to that of He II λ4686 varies considerably from one LMXB to another (see e.g. Fig. 4.1). Based upon a comparison between sources in the Galaxy and in the LMC, Motch & Pakull (1989) proposed that the relative strength of the Bowen N III–C III complex could be used as a possible indicator of metallicity in LMXBs (see Section 2.2.3).

The idea that a reduced strength of the Bowen blend could be associated with a low metallicity of the emitting plasma is mainly based upon the comparison of the optical spectra of three identified LMXBs in the Large Magellanic Cloud (LMC) with spectra of similar sources in the Galaxy. Optical and UV observations of H II regions in the LMC have revealed that the present time abundances of nitrogen and oxygen are respectively a factor of 4 and 2 smaller in Magellanic than in Galactic H II

regions (see Dufour, 1984, and references therein). One would therefore expect the progenitors of Magellanic LMXBs to be born from low metallicity matter, whereas Galactic objects are known to display a large scatter in metallicity. Remarkably, each of the Magellanic sources (in addition to a Galactic source located in a known low-metallicity environment; 4U 2127+11/AC 211 located in the globular cluster M15) possess extremely low relative strengths of the Bowen complex ($R < 0.4$, see Section 2.2.3). Based on these results, Motch & Pakull (1989) concluded that the Bowen–He II equivalent width (E.W.) ratio is a qualitative indicator of metallicity, in particular the CNO abundance in the binary system.

Recent work by Pfahl et al. (2003) has resulted in the prediction that between 80–95% of all (current) LMXBs in fact originate from IMXB precursors, rather than evolving from the beginning with a low mass companion. An observational test proposed by Pfahl et al. (2003) in order to distinguish between LMXBs and IMXBs is to look for chemical anomalies. For example, many of the descendants of IMXBs should be helium-rich and show evidence for CNO processing.

The CNO cycle (Bethe, 1939) is an important process in stars of over $\sim$1.5 $M_{\odot}$, with these elements acting as 'catalysts' in the conversion of hydrogen to helium. While the total number of 'catalytic' CNO nuclei is conserved in the cycle, in stellar evolution the relative proportions of the nuclei are altered. When the cycle is run to equilibrium, nitrogen becomes the most abundant element, regardless of initial composition. During the evolution of a star, convective mixing episodes bring material in which the CNO cycle has operated from the stellar interior to the surface, altering the observed composition of the star. The N/C ratio is therefore a potential indicator for the presence of CNO processing.

In this chapter we present a compilation of all the sources which possess derived kinematical system constraints using the Bowen fluorescence technique (see Table 4.1 for a list of the included sources and their properties). Each of these sources feature narrow, moving emission lines of nitrogen and carbon superimposed upon the broad Bowen blend, whose radial velocity behaviour is consistent with emission from the donor star. We can take advantage of this archive of high resolution spectroscopy and build upon the work of Motch & Pakull (1989). In particular, a systematic investigation into the specific N/C ratios of our sample of LMXBs could help to determine the evolutionary history of these systems (see Section 1.5).

Whilst it is extremely difficult to predict theoretically the absolute N/C ratio for a single source, we hope that by comparing the N/C ratios in our sample of ten LMXBs we can distinguish between evolved and unevolved systems. In addition

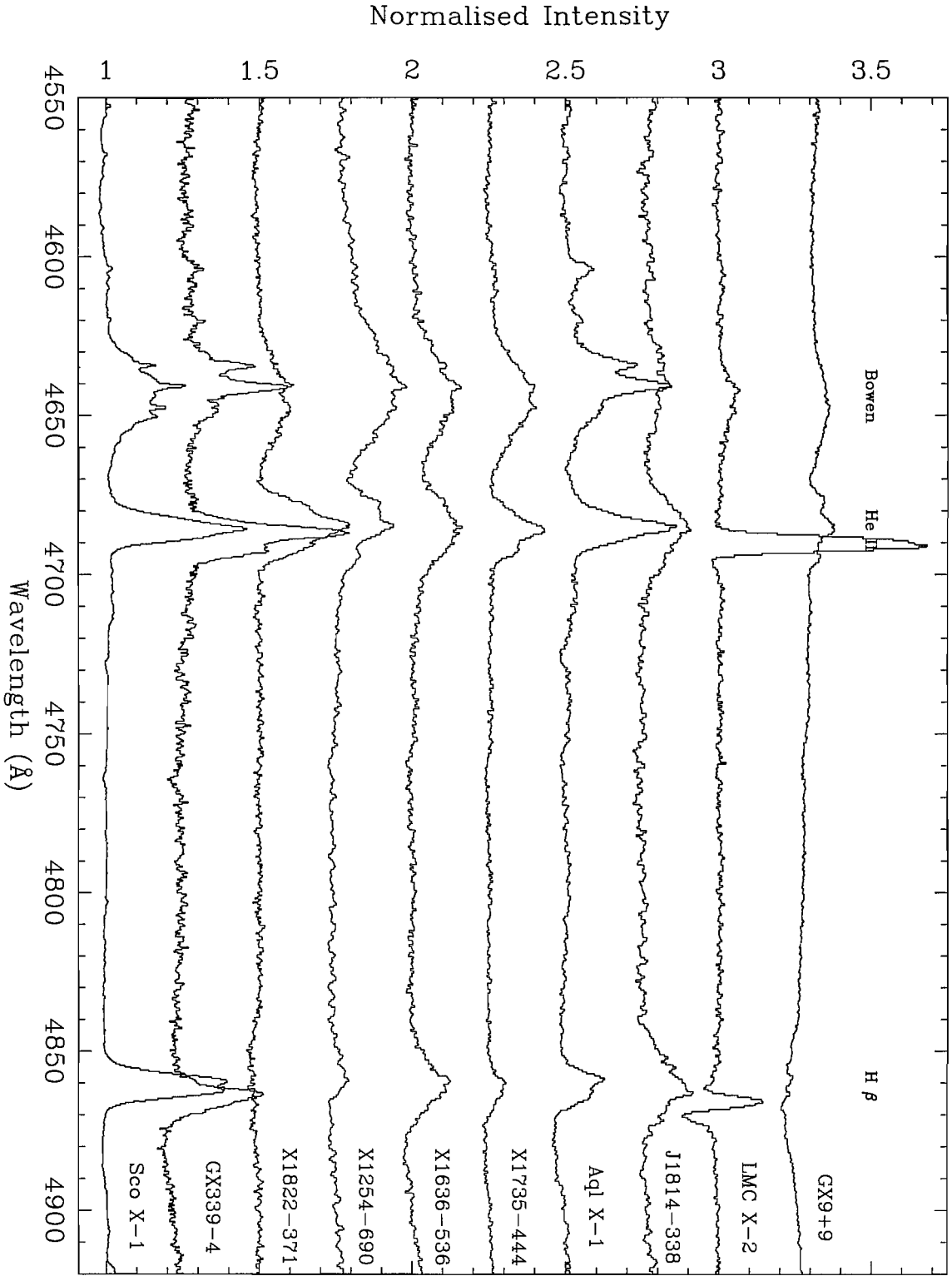

Figure 4.1: Our sample of LMXBs which display the Bowen blend. Note that all spectra have been shifted into the rest-frame of the donor star, with continuum intensity normalised to 1. The Bowen blend is much more prominent in sources such as Sco X–1 and GX 339–4 than GX 9+9 and LMC X–2.

to this we will test to see if there are any relationships between non-spectroscopic parameters (e.g. orbital period) and the apparent degree of nuclear evolution within a system.

4.2 Analysis

With the exception of Sco X–1, GX 339–4 and X 1822–371, all of the spectroscopy presented in this chapter was obtained using the FORS2 instrument on VLT/UT4 at ESO's Paranal observatory. A similar setup and reduction routine to that described in Section 3.2.1 was used in these cases. For more details of the observation and analysis of the aforementioned systems, references to the original work are provided in each section.

All of the spectra have been normalised and then shifted into the rest-frame of the donor star. The various emission components were then modelled using the multiple Gaussian fit routine *mgfit* in MOLLY. The underlying broad Bowen blend, with the narrow emission components masked out, was initially fitted using a single Gaussian. Once a suitable fit was achieved, the parameters for the base Gaussian were fixed and the narrow components (see descriptions below for details of which lines appear in the spectra of each source) were then added to the model. The narrow lines in each spectrum were fitted simultaneously, with the line separations fixed, and the width of each narrow line was set to a single parameter, which along with the height of each line was then allowed to vary freely. A single Gaussian was also fitted to the He II λ4686 emission line.

In addition to modelling the narrow components in the Bowen blend, the equivalent widths (E.W.) of the He II λ4686, Hβ, and overall Bowen blend (i.e.. including both the narrow components and the underlying broad component) were determined. The results of this analysis are listed in Table 4.2.

4.2.1 Sco X–1

Sco X–1 (optical counterpart V 818 Sco) is the prototypical LMXB, composed of a compact object and a donor star that have masses of 1.4 $M_{\odot}$ and 0.42 $M_{\odot}$ respectively (Steeghs & Casares, 2002), and an orbital period of 18.9 hr. Although the mass of the compact object is consistent with that of a neutron star, no Type I X-ray bursts have been reported so far (Mirabel & Rodrigues, 2003).

The optical spectrum of Sco X–1 is dominated by strong and broad emission lines

Table 4.1: Source list and documented parameters

Ref.	Source	P_{orb} (hrs)	d (kpc)	m_V	L_X (10^{37} erg s^{-1})	[a]Type	X-ray Bursts
1	Sco X–1	18.90	2.8	12.2	23	P	N
2	GX 339–4‡	42.14	6-15	15.5	20–100	T	N
3	X 1822–371	5.57	2.5	15.9	2–4	P	N
4	X 1254–690	3.93	8-15	19.1	2.9	P	Y
5	X 1636–536	3.80	6	17.5	0.8	P	Y
6	X 1735–444	4.65	9.1	17.5	4	P	Y
7	Aql X–1‡	18.97	5	14.8	2	T	Y
8	J 1814–338‡	4.27	8	18.4	0.2	T	Y
9	LMC X–2	7.68	55	18.8	6–30	P	N
10	GX 9+9	4.20	5	16.8	2–2.7	P	N

[a] Persistent or Transient (observed in outburst) source.
‡ Apparent magnitude and X-ray luminosity are taken from outburst levels.
1 Bradshaw et al. (1999); Steeghs & Casares (2002), and references therein.
2 Hynes et al. (2003, 2004), and references therein.
3 Mason & Cordova (1982); Jonker & van der Klis (2001); Casares et al. (2003), and references therein.
4 Motch et al. (1987); in't Zand et al. (2003), and references therein.
5 van Paradijs (1996); Galloway et al. (2006), and references therein.
6 van Paradijs (1996); Augusteijn et al. (1998), and references therein.
7 Rodriguez et al. (2006), and references therein.
8 Markwardt et al. (2003); Strohmayer et al. (2003); Krauss et al. (2005), and references therein.
9 McGowan et al. (2003), and references therein.
10 Church & Balucinska-Church (2001); Kong et al. (2006), and references therein.

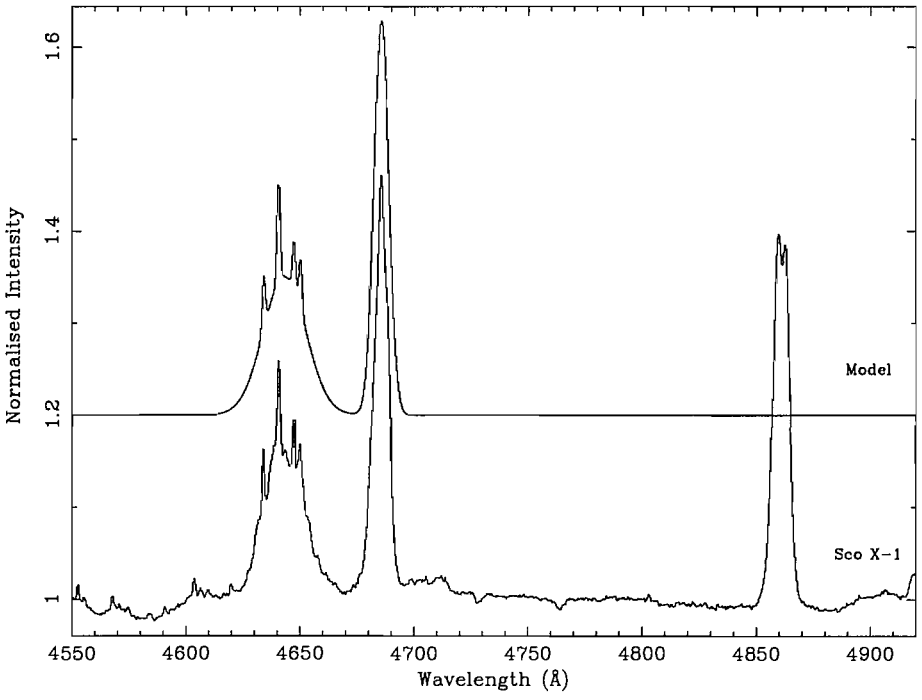

Figure 4.2: Average spectrum of Sco X–1 shifted into the donor rest-frame (bottom) and the accompanying model fit to the Bowen blend and He II λ4686 (top).

from the Balmer series as well as He II and the Bowen blend. Steeghs & Casares (2002) were able to resolve the Bowen blend into an underlying broad component as well as several narrow components from the individual Bowen transitions, representing the first detection of the mass donor in this system (see Section 2.2.4.1). The average normalised spectrum of Sco X–1 (see Steeghs & Casares, 2002, for details of the observations) in the rest-frame of the donor star is shown in Fig. 4.2, clearly displaying the strong He II λ4686 and Hβ emission lines together with the narrow N III λ4634,4640 and C III λ4647,4650 emission components within the Bowen blend.

4.2.2 GX 339–4

GX 339–4 (optical counterpart V 821 Ara) is a transient LMXB, where bright X-ray outbursts are interspersed with long quiescent periods. However, even when the X-rays are at their faintest, absorption lines from the companion star remain undetectable (Shahbaz et al., 2001). Several orbital periods have been proposed on the basis of both photometric and spectroscopic observations, but even this most basic of binary parameters remained in dispute for many years. When GX 339–4 entered a bright X-ray outburst in mid-2002, Hynes et al. (2003) were able to detect the motion of sharp emission components in the Bowen blend, and in the wings of the He II λ4686 line. No previously proposed period was found to be consistent with the periodic behaviour of these lines. However, consistent and sensible solutions were obtained for periods around 1.7 days. For the most likely period, Hynes et al. (2003) estimated a mass function of 5.8 ± 0.5 $M_{\odot}$, thus adding GX 339–4 to the list of dynamical black hole candidates.

Like Sco X–1, the optical spectrum of GX 339–4 in outburst is dominated by strong and broad emission lines from the Balmer series as well as He II and the Bowen blend. The widths of the 'narrow' components are larger than the expected rotational broadening, in particular during later observations obtained near the peak of the outburst. Outflows driven by X-ray irradiation may be one source of additional broadening mechanism. To reduce this effect, the average normalised spectrum of GX 339–4 in the donor rest-frame (Fig. 4.3) was created using only the mid-outburst NTT observations of Hynes et al. (2003). In these observations, the spectrum around 4640Å is dominated by narrow emission components of N III λ4634,4640 and some C III λ4647,4650. The C III emission appears more prominently in a few later observations obtained when the X-ray flux was higher (0.84 Crab compared to 0.46 Crab; Hynes et al., 2003), but these have been excluded from our analysis in favour of the

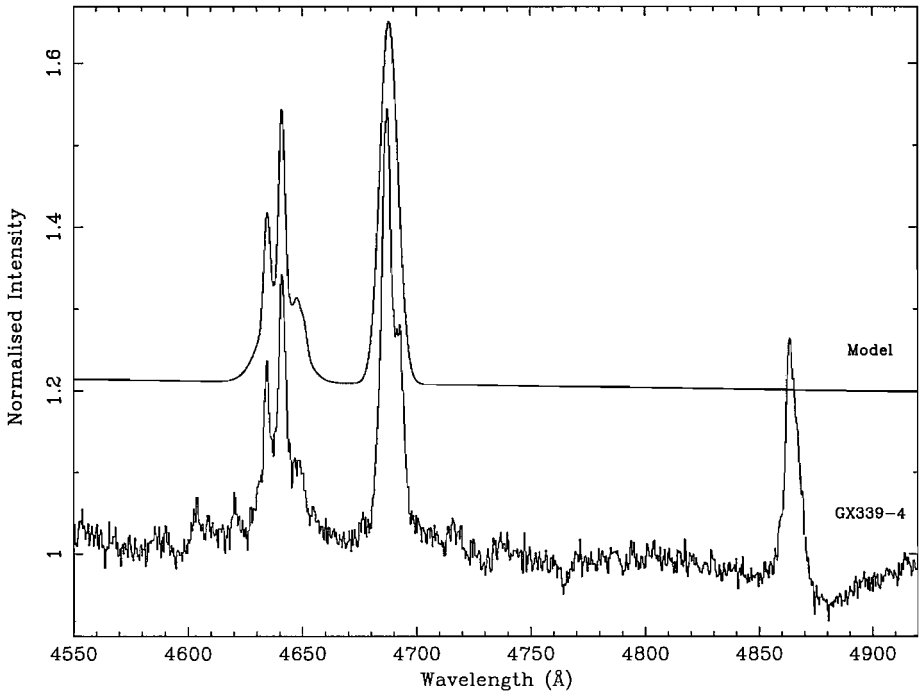

Figure 4.3: Average spectrum of GX 339–4 shifted into the donor rest-frame (bottom) and the accompanying model fit. The 'narrow' components in the Bowen blend are surprisingly broad.

mid-outburst observations which make up the majority of the data.

4.2.3 X 1822–371

X 1822–371 (optical counterpart V 691 CrA) is one of the brightest LMXBs in the optical band, but comparatively weak in X-rays, making it the prototypical accretion disc corona source (see Section 1.4.2). The optical light curve displays regular eclipses of the accretion disc by the donor star on a 5.57 hour orbital period (see e.g. Hellier & Mason, 1989). Detailed modelling of the optical and X-ray light curves has provided an accurate determination of the inclination angle, $i = 82°.5 \pm 1°.5$ (Heinz & Nowak, 2001). This system is also remarkable thanks to the discovery of 0.59 second X-ray pulses (Jonker & van der Klis, 2001), which flags it as a precursor to the millisecond pulsars. Analysis of the pulse arrival time delay has enabled an extremely precise determination of the orbit of the neutron star. A complete determination of the system parameters therefore requires only the knowledge of the radial velocity curve of the companion star. Bowen fluorescence studies by Casares et al. (2003) enabled the first secure detection of the donor star, leading to mass estimates for the binary components of $1.61 \leq M_X/M_\odot \leq 2.32$ for the neutron star

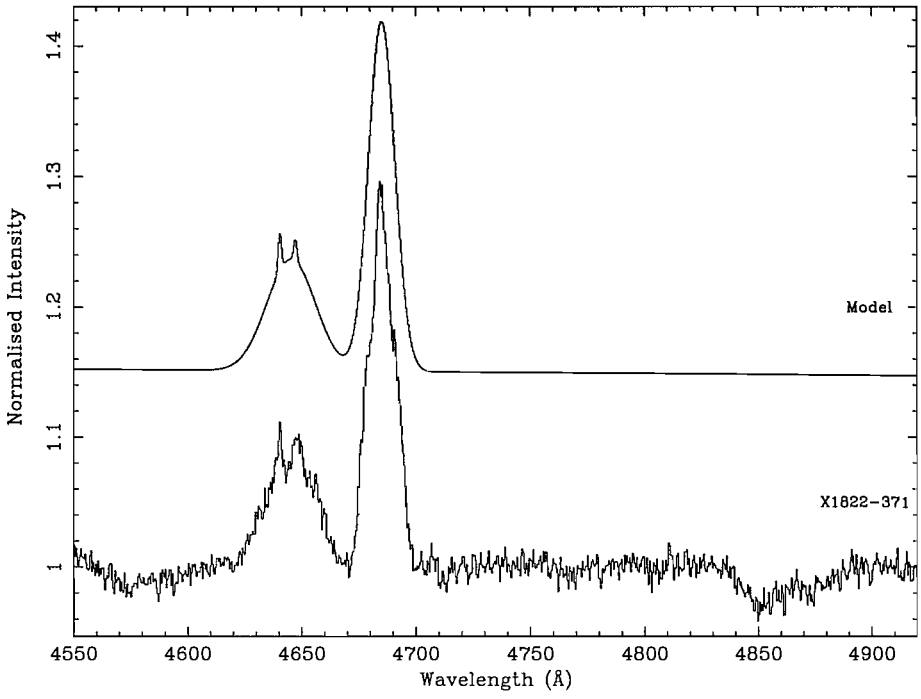

Figure 4.4: Average spectrum of X 1822–371 shifted into the donor rest-frame (bottom) and the accompanying model fit. Hβ is found to be in absorption in this system.

and $0.44 \leq M_2/M_\odot \leq 0.56$ for the companion (Munoz-Darias et al., 2005).

He II λ4686 and the Bowen blend are observed to be strongly in emission in the optical spectrum of X 1822–371 (Fig. 4.4). However, the Balmer lines are dominated by broad absorption troughs, possibly due to obscuration of the accretion disc by vertically extended cool material from the splash region and overflowing stream (Casares et al., 2003). Narrow components of N III λ4640 and C III λ4647 (and perhaps C III λ4650 also) are obvious in the donor rest-frame spectrum, though only the two strongest narrow components were used in the model. See Casares et al. (2003) for details of the observations.

4.2.4 XB 1254–690

XB 1254–690 (optical counterpart GR Mus) is a persistently bright LMXB which exhibits Type I X-ray bursts. The inclination is moderately high, as evidenced by the presence of X-ray dips. This source is discussed in much more detail in Chapter 3.

The average optical spectrum of XB 1254–690 shifted into the donor rest-frame is displayed in Fig. 4.5. The Bowen blend is extremely broad and intense, almost

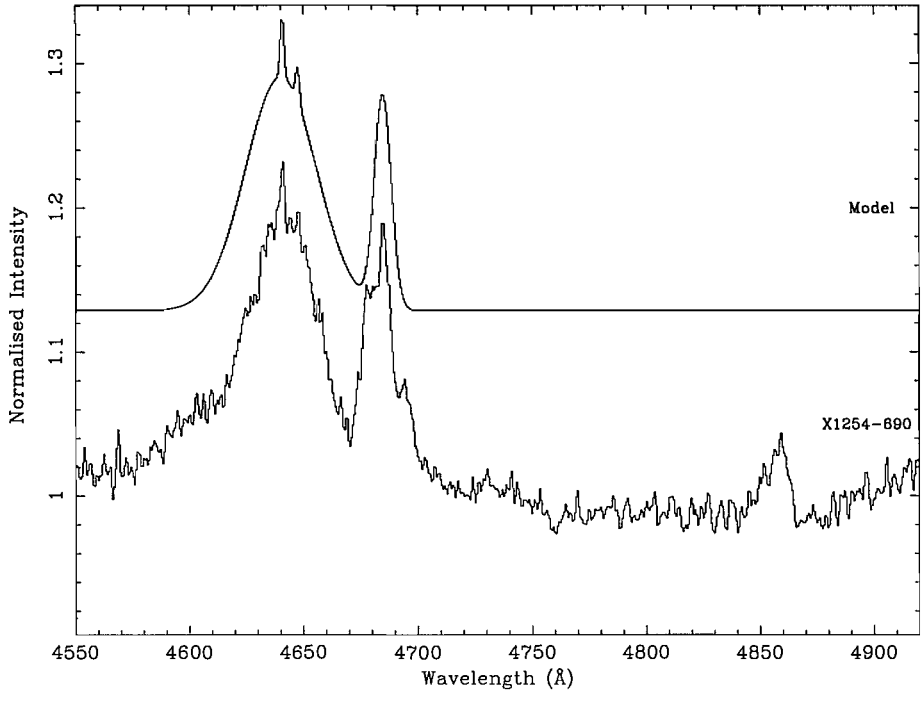

Figure 4.5: Average spectrum of XB 1254–690 shifted into the donor rest-frame (bottom) and the accompanying model fit. The Bowen blend and He II emission line appear to be sitting upon a broad emission 'hump' (see text).

dwarfing the complex, asymmetric He II λ4686 emission line. We also note that the Bowen blend in particular, and to a lesser extent the He II emission line, are themselves sitting upon a large, extended bulge. This has been noted in other LMXBs (e.g. X 1636–536; Augusteijn et al., 1998), and attributed to a blend of Fe II emission lines (Schachter et al., 1989). Importantly, it will lead to an overestimate of the E.W. of the Bowen blend (in particular) which must be taken into account when comparing this source to the others in our sample. Hβ is observed to be weakly in emission. A narrow emission line of N III λ4640 dominates the Bowen blend, with an additional, weaker component of C III λ4647.

4.2.5 X 1636–536

X 1636–536 (optical counterpart V 801 Ara) is a persistent LMXB, consisting of a neutron star in a 3.8 hr orbit. The X-ray source exhibits a variety of rapid time variability, including Type I bursts. Using the Bowen fluorescence technique, Casares et al. (2006) were able to derive the first dynamical mass constraints for this system. The mass function was found to be 0.76 ± 0.47 M$_\odot$, with an additional constraint on the mass ratio of $0.21 \leq q \leq 0.34$.

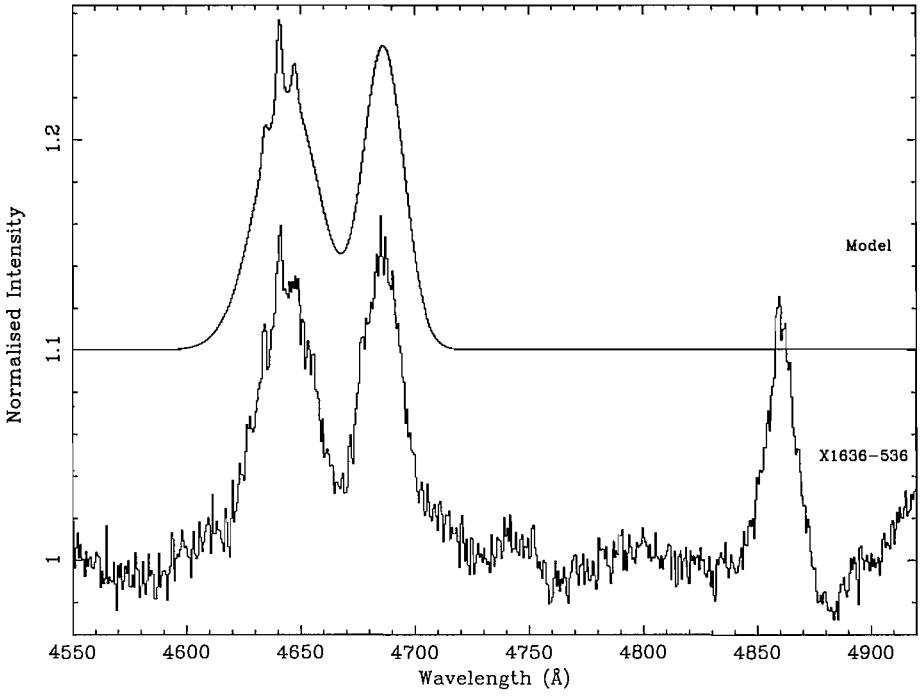

Figure 4.6: Average spectrum of X 1636–536 shifted into the donor rest-frame (bottom) and the accompanying model fit.

X 1636–536 possesses an optical spectrum typical of LMXBs, with prominent emission of N III/C III in the Bowen blend in addition to strong He II λ4686 emission. Like XB 1254–690, there appears to be a broad 'hump' below both the Bowen blend and He II emission line, noted previously by Augusteijn et al. (1998). Hβ is also observed to be strongly in emission. Narrow components of N III λ4634,4640 and C III λ4647 are evident in the donor rest-frame spectrum of this source (Fig. 4.6).

4.2.6 X 1735–444

X 1735–444 (optical counterpart V 926 Sco) is a relatively bright LMXB, similar in many ways to X 1636–536. They possess similar photometric periods (4.65 hr in the case of X 1735–444), are both of similar apparent brightness in the optical and in X-rays, and both exhibit X-ray bursts. Casares et al. (2006) presented the first detection of the donor star in this system, deriving a mass function of 0.53 $\pm$ 0.44 $M_{\odot}$ and mass ratio limits of $0.05 \leq q \leq 0.41$.

As with X 1636–536, X 1735–444 exhibits prominent Bowen and He II emission, typical of all LMXBs. However, this source differs from X 1636–536 in displaying much weaker Hβ emission relative to the He II λ4686 emission line. Narrow com-

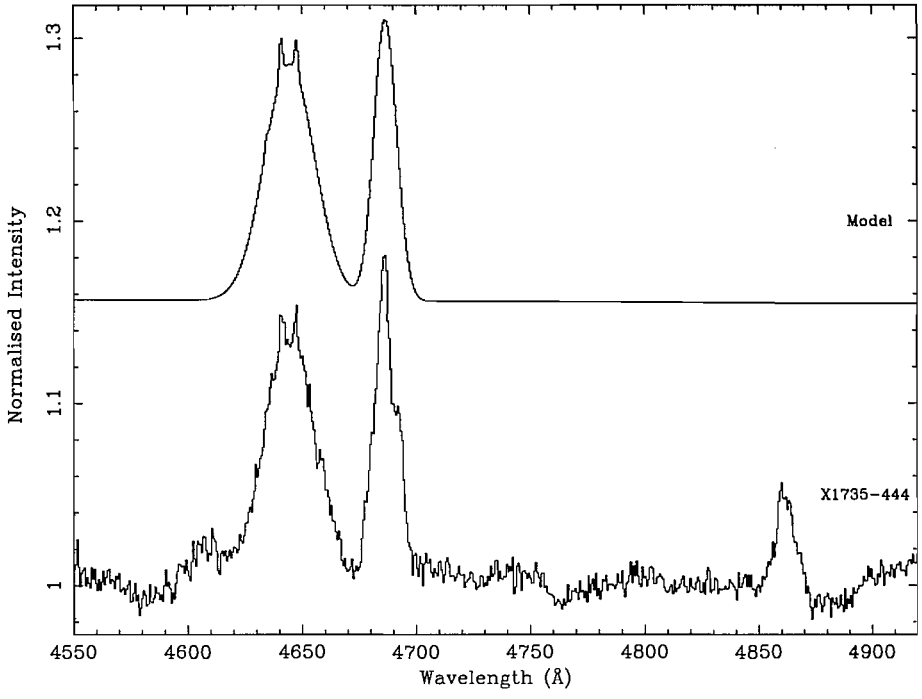

Figure 4.7: Average spectrum of X 1735–444 shifted into the donor rest-frame (bottom) and the accompanying model fit.

ponents of N III λ4634,4640 and C III λ4647 are evident in the donor rest-frame spectrum of this source, though the C III emission is relatively much stronger than that observed in X 1636–536 (Fig. 4.7).

4.2.7 Aql X–1

Aql X–1 (optical counterpart V 1333 Aql) is a transient LMXB (SXT, see Section 1.4.1) which undergoes quasi-periodic outbursts at approximately one year intervals (Priedhorsky & Terell, 1984). During such outbursts it displays Type I X-ray bursts, implying that the compact object is a neutron star. An 18.97 hour periodic optical modulation was observed during an outburst, which was interpreted as the orbital period (Chevalier & Ilovaisky, 1991). In quiescence, the optical counterpart fades to $V \simeq$21.6, but is only 0.46" away from a V=19.26 star, severely hampering kinematical studies of the system in this state. Recent fluorescence studies by Cornelisse et al. (2006b) provided the first strong constraints on the system parameters, deriving a mass function of $f(M_X) > 1.23 \pm 0.03 M_\odot$ with indications that the system could harbour a massive neutron star $\sim$2.2 $\pm$ 0.3 $M_\odot$.

The average mid-outburst optical spectrum of Aql X–1, shifted into the donor

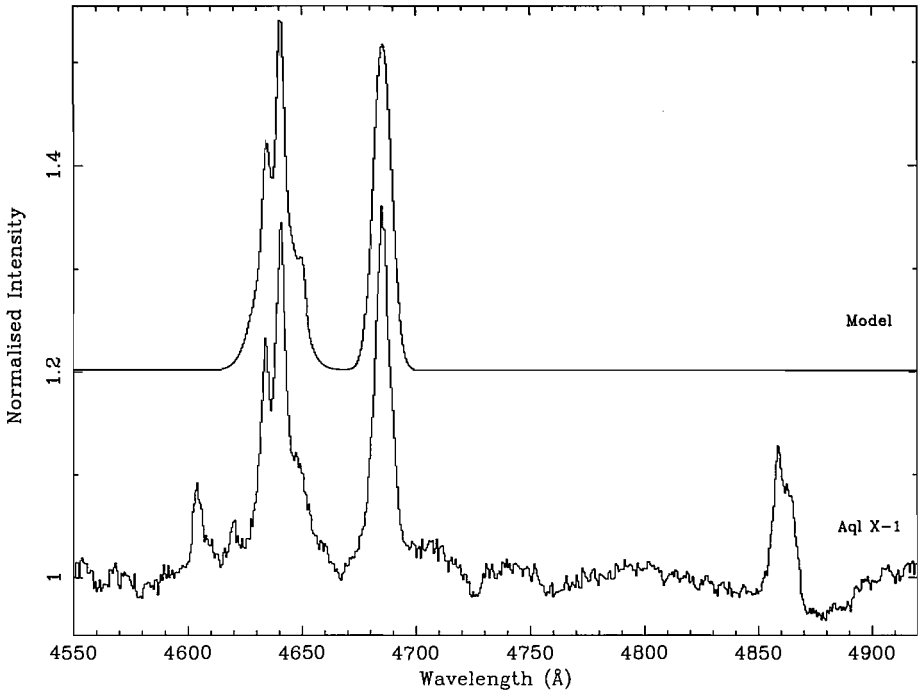

Figure 4.8: Average spectrum of Aql X–1 shifted into the donor rest-frame (bottom) and the accompanying model fit. The N III lines are much stronger than the C III emission in the Bowen blend.

rest-frame, is displayed in Fig. 4.8. This includes only the observations obtained in 2004 May, excluding the later data (2004 June) when the Bowen blend and He II λ4686 emission had significantly reduced in intensity (see Cornelisse et al., 2006b). Intriguingly, at the later epoch the Hβ emission increased significantly in intensity, being observed only weakly in emission in Fig. 4.8. It is possible that this increase in intensity and width of the Hβ emission line is caused by contamination with the He II λ4859 emission line from the Pickering series, which may also be present in the earlier observations. The narrow Bowen components are dominated by N III λ4634,4640, with the C III λ4647,4650 lines being significantly weaker.

4.2.8 XTE J 1814–338

The SXT XTE J 1814–338 was discovered in outburst on 2003 June 5 by *RXTE* (Markwardt & Swank, 2003). The outburst lasted for approximately 55 days, with a peak 2–10keV flux of around 13 mCrab (Krauss et al., 2005). *RXTE* observations also established the source as a 314 Hz (3.2 ms) accretion-powered X-ray pulsar with a 4.27 hour orbital period (Markwardt et al., 2003). Strohmayer et al. (2003) observed over two dozen thermonuclear X-ray bursts during the 2003 June outburst.

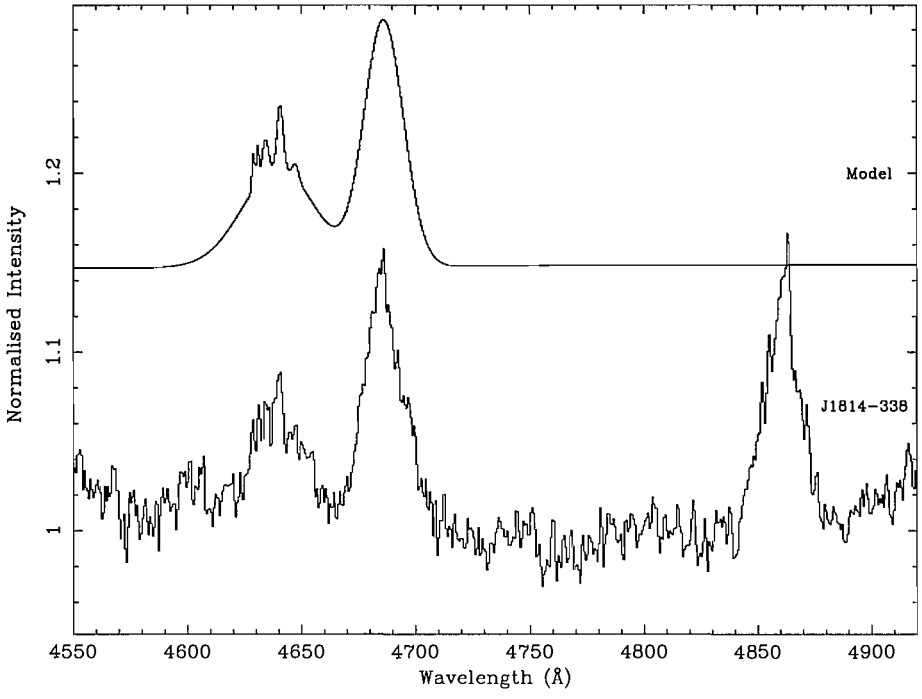

Figure 4.9: Average spectrum of XTE J 1814–338 shifted into the donor rest-frame (bottom) and the accompanying model fit. The Bowen blend features narrow O III and O V emission lines in addition to the more commonly observed N III and C III.

Bowen fluorescence spectroscopy observations during the outburst constrain the masses of the two stars to $M_X = 1.62 \pm 0.82$ M$_\odot$ and $M_2 = 0.26 \pm 0.14$ M$_\odot$ (Jorge Casares, private communication).

The optical spectrum of XTE J 1814–338 is dominated by strong He II λ4686 and Hβ emission, in addition to the Bowen blend. We can identify narrow components of N III λ4634,4640 and C III λ4647 in addition to O III λ4630 and O V λ4628 emission in the Bowen blend (see Fig. 4.9). This is the only source in our sample in which any species of oxygen is apparent in the Bowen blend. It is important to note that there are emission lines of O II at λ4641.8 and λ4649.1. These may be contributing to the presumed C III and N III emission in these spectral regions.

4.2.9 LMC X–2

LMC X–2 is one of the most luminous LMXBs known, and yet little is known about the binary parameters. There is no report of X-ray bursts from this source. In spite of a number of studies, the period of this system remains uncertain; Motch et al. (1985) found evidence for a period of ~6.4 hours, whereas Callanan et al. (1990) found a periodicity of 8.15 hours, and Crampton et al. (1990) suggested a

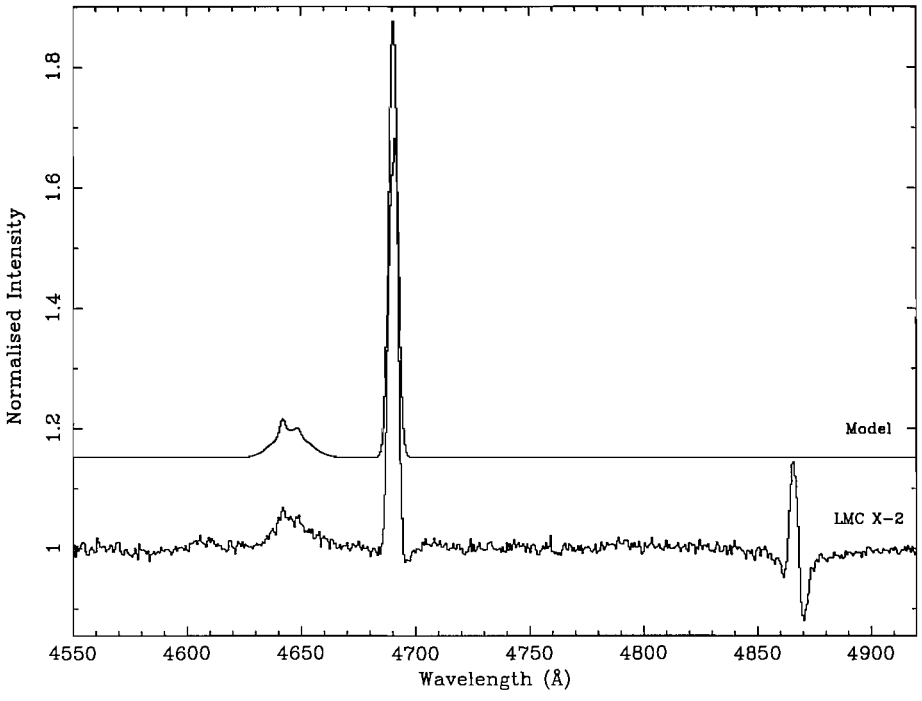

Figure 4.10: Average spectrum of LMC X–2 shifted into the donor rest-frame (bottom) and the accompanying model fit. The He II emission line is extraordinarily powerful compared to the Bowen blend.

much longer period of ~12.5 days. Recent optical photometry (I.C. Shih, private communication) is consistent with a period around 7–10 hours, whilst Bowen fluorescence studies (Remon Cornelisse, private communication) suggest the period is 7.68 hours. This final period was used to create the 'donor rest-frame' average spectrum displayed in Fig. 4.10

The He II λ4686 emission line dominates the optical spectrum of LMC X–2, completely dwarfing the Bowen blend. Hβ is observed weakly in emission, with a significant absorption component in the red wing of the line profile. The apparent weakness of the Bowen blend is often attributed to the much lower metal abundances in the LMC compared to the Galaxy (see e.g. Motch & Pakull, 1989, and references therein). Despite the weakness of the blend, there do appear to be narrow components of both N III (λ4634,4640) and C III (λ4647,4650) apparent in the (assumed) donor rest-frame spectrum.

4.2.10 GX 9+9

GX 9+9 is a persistently bright LMXB located in the Galactic bulge. A 4.2 hour periodic modulation in X-ray flux was detected and interpreted as the orbital mod-

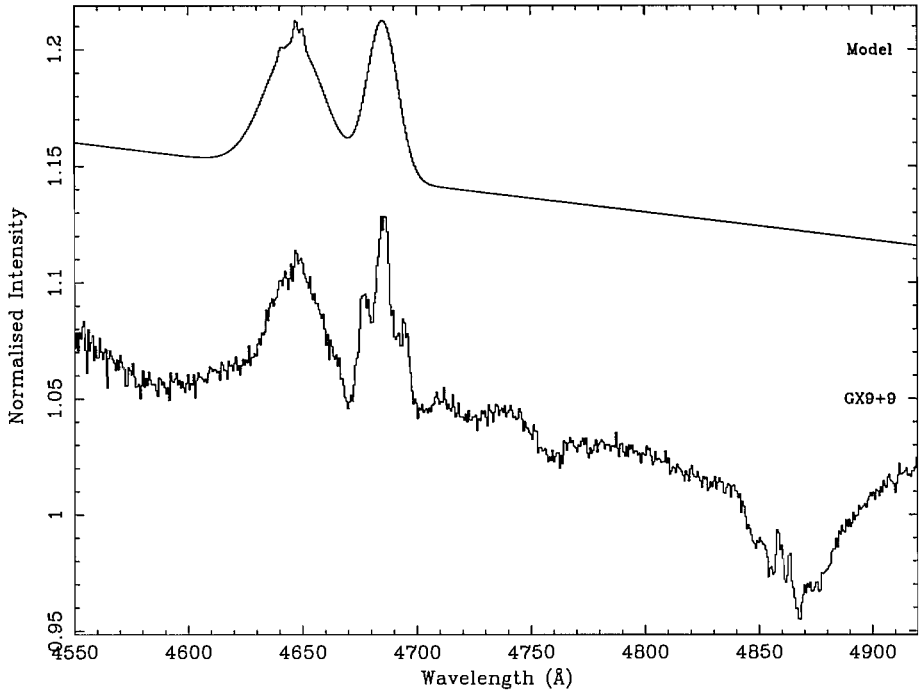

Figure 4.11: Average spectrum of GX 9+9 shifted into the donor rest-frame (bottom) and the accompanying model fit. Hβ is seen as a broad absorption feature, contaminated by a narrow C III emission line (Cornelisse et al., 2006c). C III also dominates the Bowen blend to an extent not seen in other LMXBs.

ulation (Hertz & Wood, 1988), later confirmed in the optical by Schaefer (1990). There is no report of X-ray bursts from this source. Phase-resolved optical spectroscopy has revealed a signature of the donor star, leading to constraints on the mass ratio of $0.39 \leq q \leq 0.52$, and pointing towards a compact object mass around the canonical neutron star value of 1.4 $M_{\odot}$ (Cornelisse et al., 2006c).

The optical spectrum of GX 9+9 features emission from the Bowen blend and He II λ4686, as expected for a LMXB. What is more remarkable is the deep, broad absorption feature with a superposed narrow emission line around Hβ. This emission line is attributed to C III λ4860 (and possibly a He II feature). Another C III emission feature is observed to occur at λ5305, and indeed the donor rest-frame adjusted (see Fig. 4.11) Bowen blend is dominated by C III λ4647,4650, with only a minimal contribution from N III λ4640.

Table 4.2: Derived parameters for the blue optical emission features.

Source	[a]Peak Ratio			[b]E.W. (Å)		
	N/C	C/He	N/He	Bowen	He II	Hβ
Sco X–1	2.03 ± 0.03	0.128 ± 0.001	0.259 ± 0.002	4.2	4.0	3.2
GX 339–4	6.84 ± 1.27	0.065 ± 0.012	0.444 ± 0.014	5.1	5.9	1.1
X 1822–371	1.72 ± 0.57	0.064 ± 0.018	0.110 ± 0.019	2.5	4.1	-0.6
X 1254–690	1.74 ± 0.56	0.161 ± 0.043	0.280 ± 0.049	7.2	3.7	0.6
X 1636–536	2.28 ± 0.48	0.122 ± 0.023	0.278 ± 0.026	4.0	3.4	1.6
X 1735–444	1.20 ± 0.26	0.116 ± 0.019	0.138 ± 0.020	3.8	2.3	0.4
Aql X–1	30.9 ± 12.6	0.018 ± 0.007	0.542 ± 0.009	5.0	3.9	0.4
J 1814–338	4.31 ± 2.42	0.061 ± 0.033	0.262 ± 0.039	2.0	3.0	2.8
LMC X–2	3.02 ± 0.90	0.012 ± 0.003	0.035 ± 0.004	1.1	3.4	-0.5
GX 9+9	0.33 ± 0.14	0.111 ± 0.017	0.036 ± 0.015	2.0	1.5	-1.8

[a] Uncertainties are the 1σ formal errors from the fitting routine.
[b] Formal errors are of the order of ∼0.04. However, there are likely to be larger systematic errors, for example from the continuum and zero-level placement.

4.3 Discussion

As the first ever co-ordinated survey of elemental abundances in LMXBs, there are many interesting conclusions which may be drawn from this work. However, before expanding upon the results of this survey, it is important to be aware of some of the implicit limitations. For example, our sample is clearly limited by small number statistics and sample incompleteness (10 out of ∼150 LMXBs in the Galactic neighbourhood).

A number of observational selection effects need to be borne in mind, including the optical brightness of the sources and spatial separation from other objects in the same field of view. Clearly only those LMXBs with an identified optical counterpart can be studied using the Bowen fluorescence technique. Additionally, our sample is dominated by persistent LMXBs (with only 3 transient systems, observed in outburst; GX 339–4, Aql X–1 and J 1814–338). The requirement to observe fluorescence lines upon the donor star (in order to trace its orbital motion) means that only X-ray active systems may be observed. We include only one source from a readily identified low metallicity environment (LMC X–2; see Motch & Pakull, 1989). The minimal Bowen blend observed in the other low metallicity sources identified by Motch & Pakull (1989) has thus far prevented them from being included as a potential source for kinematical studies using the Bowen blend.

The sample includes both X-ray burst and non-burst sources, and also both short (P_{orb} ∼hours) and long period (P_{orb} ∼days) systems[1]. There are no globular cluster sources in our sample, despite their surprising relative over-abundance (∼10% of

[1]There are no ultra-compact systems (P_{orb} ∼minutes) in our sample. The small, degenerate donor stars in these systems are likely to be well shielded by the outer accretion disc, making donor fluorescence unlikely. In addition, optical faintness in combination with short orbital periods prevents a reasonable balance between SNR and phase-resolution being obtained.

known XRBs lie in globular clusters, even though the clusters only contain about 10^{-4} of the number of stars in the Galaxy; Verbunt & van den Heuvel, 1995). Globular cluster LMXBs are likely to be formed via different evolutionary channels to LMXBs in the Galactic disc (tidal capture/partner swapping/direct impact - the binary system does not need to survive a supernova event intact; see Sections 1.1.2 & 1.5) due to the enormous stellar densities found in a cluster. Considering the different formation scenarios, the chemistry of the donor stars in globular cluster systems is therefore likely to differ somewhat from systems found in the field.

The broadening of the narrow lines in the Bowen blend of our sample is in some cases greater than would be expected from rotational broadening only. There could be additional effects such as orbital smearing in short period or faint systems, irradiation induced winds as suggested for the case of GX 339–4 (Hynes et al., 2003), or simply inaccuracies in the designation of the donor rest-frame. Also, the N III λ4640.64 line can be blended with N III λ4641.85 which gives an additional broadening effect. This is a more serious problem than those metioned earlier, since it affects only the nitrogen line whereas the aforementioned broadening mechanisms will affect both carbon and nitrogen equally. This problem could potentially be side-stepped by using a different nitrogen emission line within the Bowen blend, such as N III λ4634. However, this line is weaker than N III λ4640 and cannot be identified in some of our sources. Therefore, given the complexity of the Bowen region and in particular the many potential broadening mechanisms, we believe that the peak flux rather than the equivalent width is likely to give the best description of the narrow carbon and nitrogen lines.

4.3.1 The Bowen blend as a possible indicator of metallicity and CNO processing

We have presented our sample of LMXBs in a diagram similar to that presented by Motch & Pakull (1989). This displays the relationship between X-ray luminosity (L_X) and the ratio of the Bowen blend and He II λ4686 equivalent widths (in the donor rest-frame in our case) (Fig. 4.12). The result is largely similar. Motch & Pakull (1989) found that the 4 sources in their sample associated with low metallicity environments all clustered towards the left hand side of the diagram, denoting a weak Bowen blend compared to He II. However, there was no apparent dependence upon X-ray luminosity. Our own sample contains only one source from an identified low metallicity region (LMC X–2) so we cannot test for any variation with L_X. However,

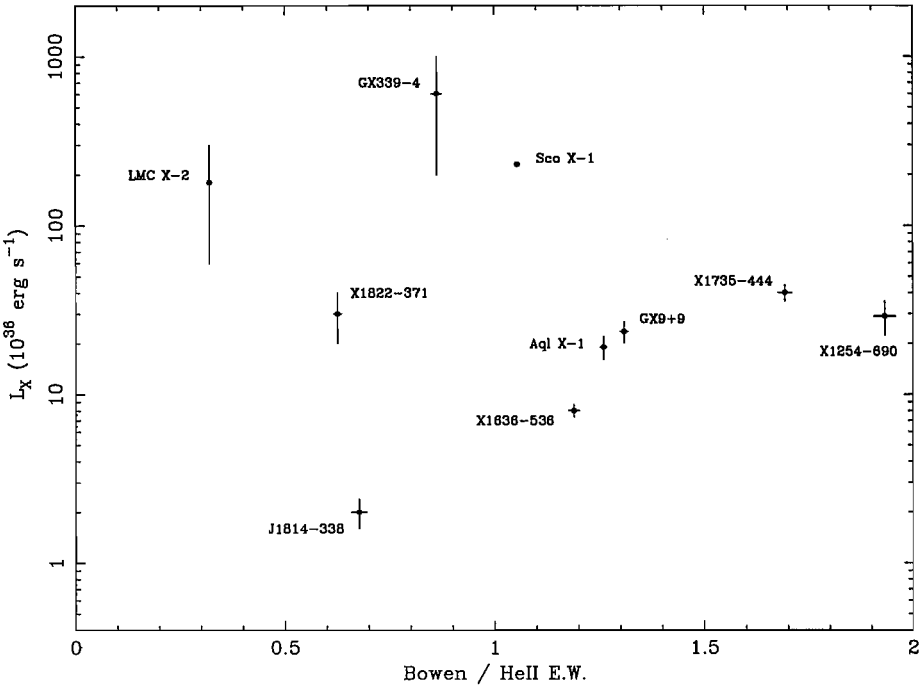

Figure 4.12: The Bowen/He II λ4686 E.W. ratio versus X-ray luminosity for our sample of active LMXBs.

it is notable that LMC X–2 possesses an extremely weak Bowen blend in comparison to He II (see e.g. Fig. 4.1), with an E.W. ratio of Bowen/He II less than half that of any other source in our sample. This is in accordance with the presumed low metallicity of the donor star in LMC X–2. The range of E.W. ratios observed in the remainder of our (Galactic) sources could reflect to some extent the intrinsic scatter in age and birth metallicity of the progenitors.

Interestingly, Motch & Pakull (1989) also made the tentative prediction that X-ray burst sources, when plotted in a diagram such as Fig. 4.12, tend to cluster in a region of intermediate X-ray luminosity and high Bowen/He II E.W. ratio. Whilst all of the X-ray bursters in our sample do occur at intermediate X-ray luminosities, there is a large scatter in the Bowen/He II E.W. ratio (ranging from $\sim$0.7 for J 1814–338 to $\sim$1.7 for X 1735–444; note that the E.W. of the Bowen blend in the bursting source X 1254–690 is likely to be significantly overestimated due to underlying emission).

The lack of low L_X bursters could be attributed to an obvious observational bias against the detection of X-ray burst activity at low luminosities, whilst bursting activity can be inhibited at high luminosities (and hence high mass accretion rates). The large scatter in Bowen/He II E.W. ratios amongst the bursting sources

could imply that X-ray bursting behaviour has little dependency upon metallicity. Theoretically, this should not be the case. The main ingredient of thermonuclear runaway is helium which burns explosively through the strongly temperature dependent triple-α reaction. In the physical conditions prevailing in X-ray bursters, theory predicts that hydrogen can participate in the helium flash but is unlikely to trigger the X-ray burst (Lewin et al, 1995); a thermonuclear runaway occurs when a critical concentration and mass of helium is reached in some layer. Hydrogen steady shell burning through the CNO cycle is the main mechanism leading to helium enrichment and plays a critical role in the onset of thermonuclear runaway. Therefore we can expect that X-ray bursting behaviour will depend upon CNO abundances in the accreted matter. Whilst the Bowen/He II E.W. ratio has successfully identified (a limited number of) low metallicity sources, it does not appear (from our small sample, and with no *a priori* evolutionary information) to be a useful parameter in determining the evolutionary state of the accreting matter in LMXBs, or more particularly the level of CNO processing.

4.3.2 Simple spectroscopic parameters as an indicator of evolutionary status

4.3.2.1 Comparisons with the broad Bowen blend

We can investigate what the broad Bowen blend can tell us about the evolutionary status of a system by comparing it with other parameters which might be expected to indicate the level of nuclear processing within the system; hydrogen and helium, carbon and nitrogen. We have obtained measurements of these emission (and in some cases absorption) lines in our donor rest-frame shifted spectra. A process of fitting multiple Gaussian components to the Bowen blend has allowed for the estimation of the relative intensities of nitrogen and carbon within the system, elements which play an important role in stellar evolution. The Bowen fluorescence process itself is initiated by He II Lyα photons, the intensity of which is simply proportional to the intensity of the He IIλ4686 emission line (see Section 2.2). The proximity of this line to the Bowen blend makes it a particularly useful parameter to measure. These high excitation emission lines are all produced under similar physical conditions, and in similar physical regions within the LMXB system. It therefore seems acceptable to compare them directly.

Another common LMXB feature in the spectral region of the Bowen blend is the Balmer line Hβ. However, this is a low excitation line and as such is formed

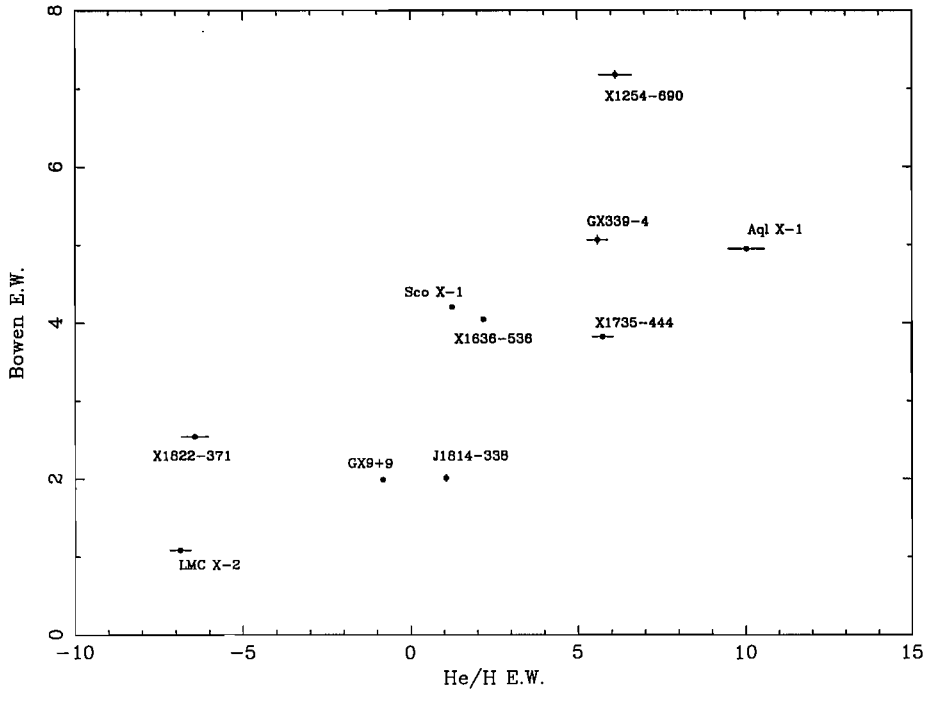

Figure 4.13: Plot showing the E.W. of He II λ4686 normalised by the E.W. of Hβ versus the E.W. of the overall Bowen blend. The Bowen E.W. in X 1254–690 is likely to be a substantial over-estimate.

under different physical conditions to the Bowen blend and He II; whilst the He II originates in the inner disc, all hydrogen in this high temperature environment is likely to be ionised. Instead, the profile and strength of the Hβ line is influenced by the properties of the outer disc, and hence the material that has just been transferred from the donor. The conversion of hydrogen to helium is a fundamental process in stellar evolution, and as such the abundance of hydrogen could be a very instructive parameter when considering the evolutionary status of a stellar object. Always considering the different production sites, it is therefore interesting to compare the Hβ feature with the higher excitation emission lines.

In Fig. 4.13 we compare the helium-to-hydrogen equivalent width ratio with the equivalent width of the Bowen blend. There appears to be a strong linear correlation between these two parameters[2], and a least squares fit to the points in Fig. 4.13 gives the relation E.W.(Bowen) $\simeq 3.5 + 0.25$ E.W.(He/H). X 1254–690 is an obvious outlier; however, this is not unexpected since the Bowen emission line sits upon a broad emission 'hump' of heavier elements (see Section 4.2.4). The equivalent width of the Bowen line is therefore likely to be heavily overestimated.

[2]Linear Pearson correlation coefficient $\sim$0.8.

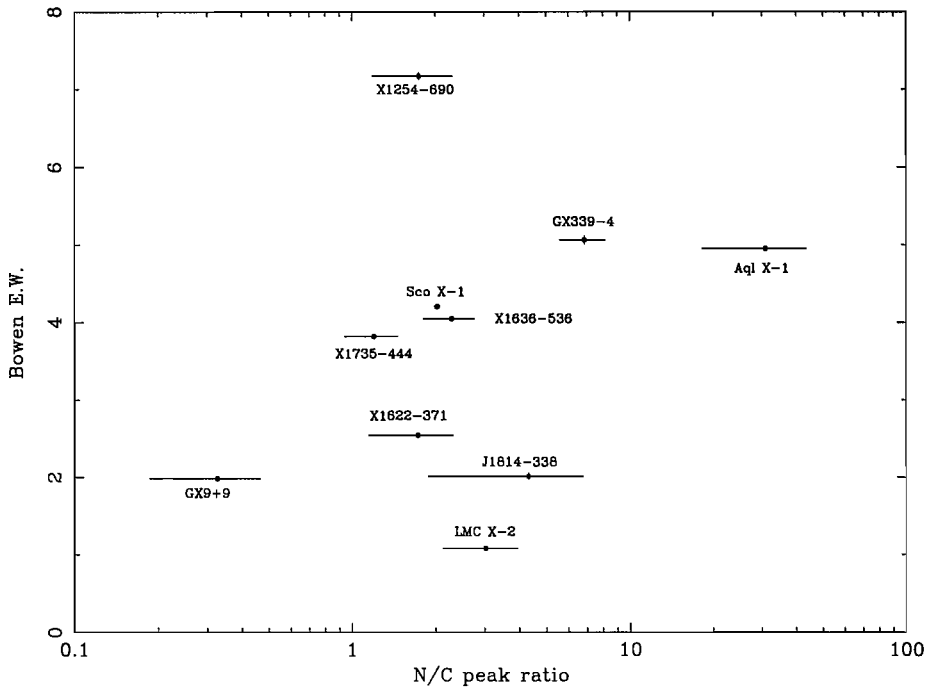

Figure 4.14: Plot showing the peak ratios of nitrogen to carbon from the multiple Gaussian fits against the E.W. of the overall Bowen blend. The Bowen E.W. in X 1254–690 is likely to be a substantial over-estimate.

Those sources which feature Hβ in absorption all display weak Bowen emission. They are joined by the millisecond pulsar J 1814–338, which also possesses rather weak Bowen emission, though Hβ in this source is seen to be *strongly* in emission. The sources with relatively weak Hβ emission (as opposed to absorption) tend to possess a more powerful Bowen blend. It is difficult to explain this trend physically. Naïvely it might be expected that a higher He/H ratio indicates a more highly evolved star. Why this should be related to the Bowen blend however is unclear; the Bowen blend encapsulates each of the elements carbon, nitrogen and potentially oxygen, and since CNO processing should not alter the total abundances of these elements (though it will alter their relative abundances), a more highly evolved star should not necessarily possess a more powerful Bowen blend.

Further complication arises when considering that hydrogen is seen in both emission and absorption. Thus, although systems such as X 1822–371 and LMC X–2 feature low He/H equivalent width ratios, this is due purely to the fact that Hβ is seen in absorption and does not therefore accurately reflect the absolute power of the line. These two systems both possess powerful absorption features, indicative of significant levels of hydrogen. Plotting instead the *modulus* of the He/H ratio (per-

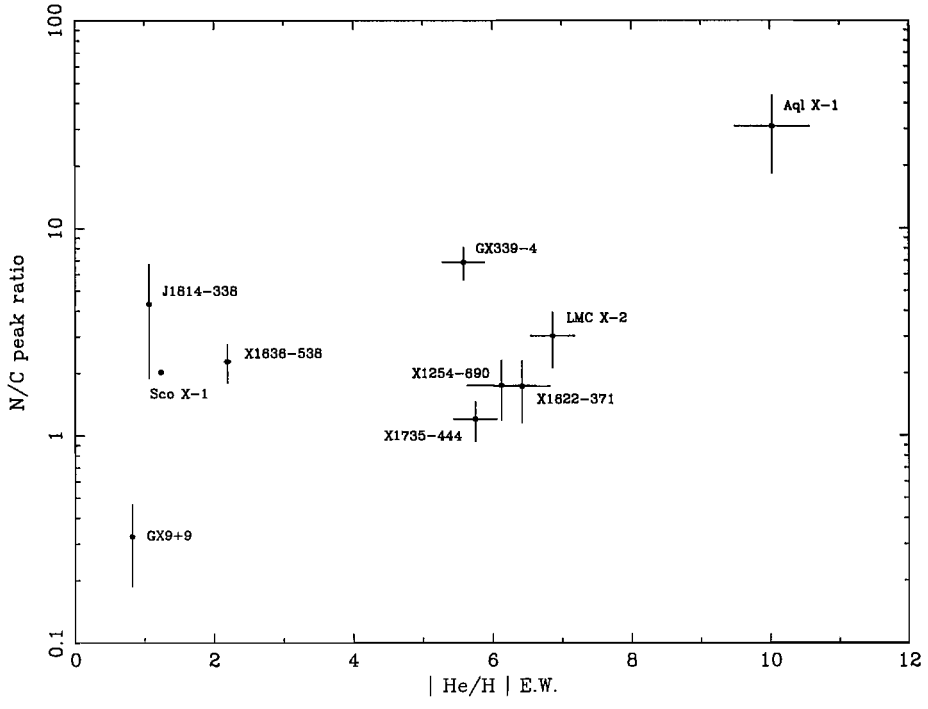

Figure 4.15: The relationship between the E.W. of He II λ4686 normalised by the absolute E.W. of Hβ versus the peak ratios of the nitrogen and carbon lines in the Bowen blend.

haps more indicative of the actual abundances) produces no correlation with the strength of the Bowen blend. Similarly, comparing the overall Bowen blend with the ratios of the individual nitrogen and carbon lines (Fig. 4.14) provides no apparent correlation. It seems likely that a simple measurement of the overall Bowen blend will reveal little about the evolutionary status of a LMXB. More important factors determining the strength of the blend are likely to be the metallicity of the birth environment of the system (LMC X–2) or perhaps in the case of X 1822–371 (an ADC source; see Section 1.4.2) the system inclination.

4.3.2.2 Comparisons with the nitrogen-to-carbon ratio

Next we compare the ratio of equivalent widths of the helium and hydrogen lines with the peak ratios of nitrogen and carbon within the Bowen blend. Looking at Fig. 4.15, we can divide our sources into different groups. Firstly, considering only the N/C ratio, 8 of the sources cluster in the intermediate range of $\sim$1–7. GX9+9 possesses an unusually low ratio of $\sim$0.3, whilst Aql X–1 features an extraordinary apparent overabundance of nitrogen, with a N/C ratio two orders of magnitude higher than that of GX9+9.

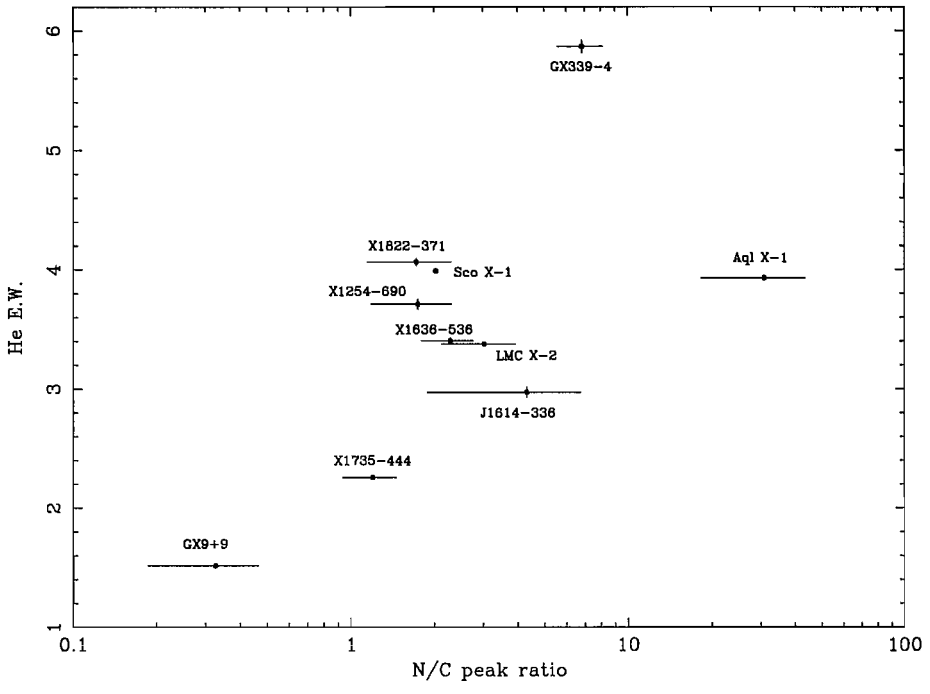

Figure 4.16: The relationship between the peak ratios of the nitrogen and carbon lines in the Bowen blend and the equivalent width of the He IIλ4686 emission line.

The horizontal scatter is a result of the relative strength of Hβ compared to He II. The sources featuring weak Hβ on the whole (excluding Aql X–1) tend to cluster in a single region with a He/H E.W. ratio of ~5–7. The four sources with a relatively strong Hβ feature (Sco X–1, J 1814–338, GX9+9 and X 1636–536) all appear on the left hand side of Fig. 4.15. With the exception of GX9+9, this difference in the strength of Hβ is not reflected in the N/C ratio. If both the N/C and He II/Hβ ratios were sound measures of abundances, one would expect to observe a correlation between the two. In particular, more evolved systems can be expected to display higher ratios of both N/C and He/H as a result of greater levels of nuclear processing. The absence of an obvious correlation between these two parameters implies that at least one of the He II/Hβ or N/C ratios is not linked to elemental abundances or the degree of evolution. This is most likely to be the relative strengths of the He II λ4686 emission line and Hβ. Vastly different physical processes are responsible for the production of these two lines, and the differences in the helium and hydrogen equivalent widths are likely to reflect the efficiency of production mechanisms in individual sources rather than actual elemental abundances.

In Fig. 4.16 we show the relationship between the peak ratios of the nitrogen and carbon emission lines in the Bowen blend and the equivalent width of the

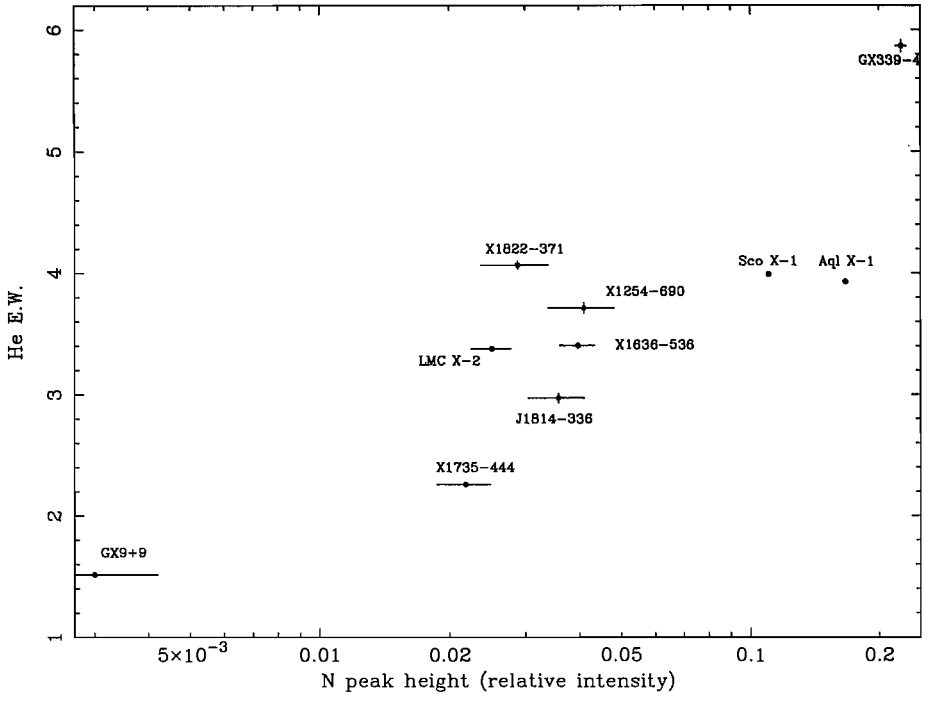

Figure 4.17: The peak intensity of the N IIIλ4640 emission line, relative to the normalised continuum, plotted against the equivalent width of the He IIλ4686 emission line.

He II λ4686 emission line. These parameters appear to divide our sample into three distinct groups, with a higher ratio of nitrogen to carbon appearing to be linked to a higher value for the equivalent width of helium. This is slightly worrying, since the N/C ratio may not actually be giving us information about elemental abundances and thus the presence of CNO processed material. Instead, the higher nitrogen intensities may simply be a result of greater levels of helium photons seeding the Bowen fluorescence mechanism. Alternatively, since the CNO cycle converts hydrogen into helium, greater intensities of both nitrogen and helium could simply imply that the material has undergone a greater level of nuclear processing.

Figure 4.17 displays the relationship between the absolute peak height of the N III λ4640 emission line and the equivalent width of He II λ4686. As with Fig. 4.16, there is an increasing trend between the peak height of the nitrogen line and the power of the helium emission. There are also three distinct groups, with GX9+9 again in the bottom left hand corner and Aql X–1 and GX 339–4 in the top right. The central group displays a great deal of vertical scatter in both Figs. 4.16 & 4.17. It is possible that this is linked to the orbital inclinations of the systems, or perhaps the flaring angle of the accretion disc. Certainly the systems possessing the

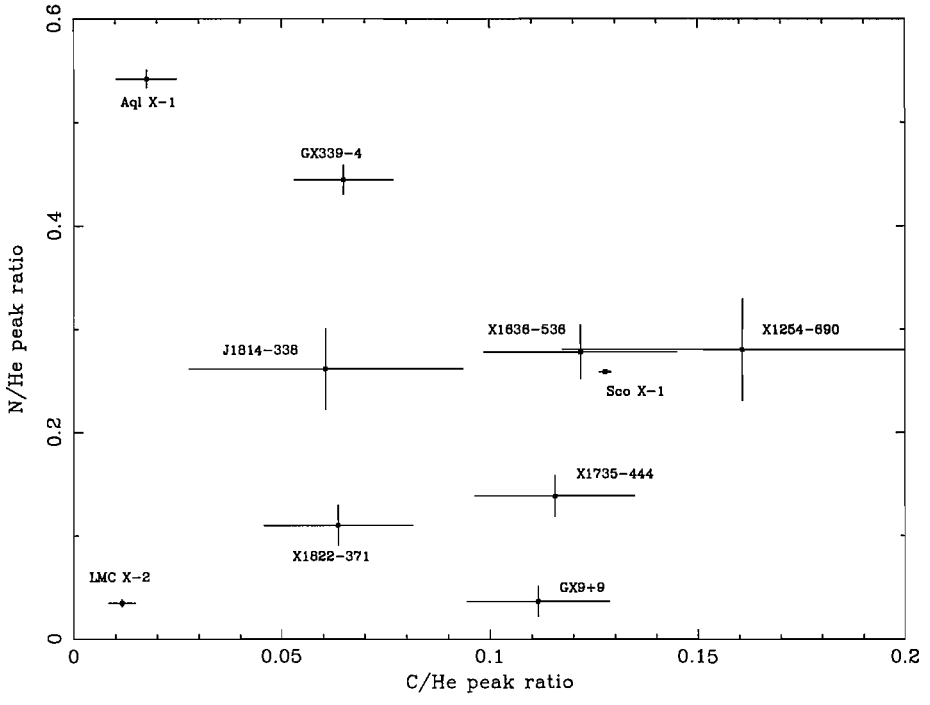

Figure 4.18: The peak intensity ratios of N/He and C/He taken from the Gaussian fitting routines.

highest inclinations (the ADC source X 1822–371 and the dipper X 1254–690) sit at the top of the group. Also, it is noticeable that X 1636–536 lies higher than X 1735–444; it has previously been suggested that the former source is observed at a higher inclination than the latter (Casares et al., 2006). However, the reason why a high inclination source should possess more powerful helium emission remains unclear.

If the nitrogen and carbon intensities within the Bowen blend are influenced mainly by the efficiency of the emission mechanism (as opposed to elemental abundances), then one would expect to see a clear relationship with the intensity of the seed photons. The nitrogen emission is the result of a resonant relationship seeded by helium (see Section 2.2), whilst carbon emission is simply the result of photoionisation. Therefore, carbon should not be strongly related to the intensity of helium emission, whilst the nitrogen intensity could potentially be dominated by the level of helium emission. This can be tested by plotting the peak intensity ratio of carbon and helium against the same ratio for nitrogen. A large degree of scatter is to be expected in the value of C/He whilst (if the nitrogen intensity is dominated by the level of helium emission) the N/He ratio should tend towards a single value. In Fig. 4.18 we can see that this is clearly not the case, from which we can take confidence that the N/C ratio is a reasonable measure of elemental abundances rather than

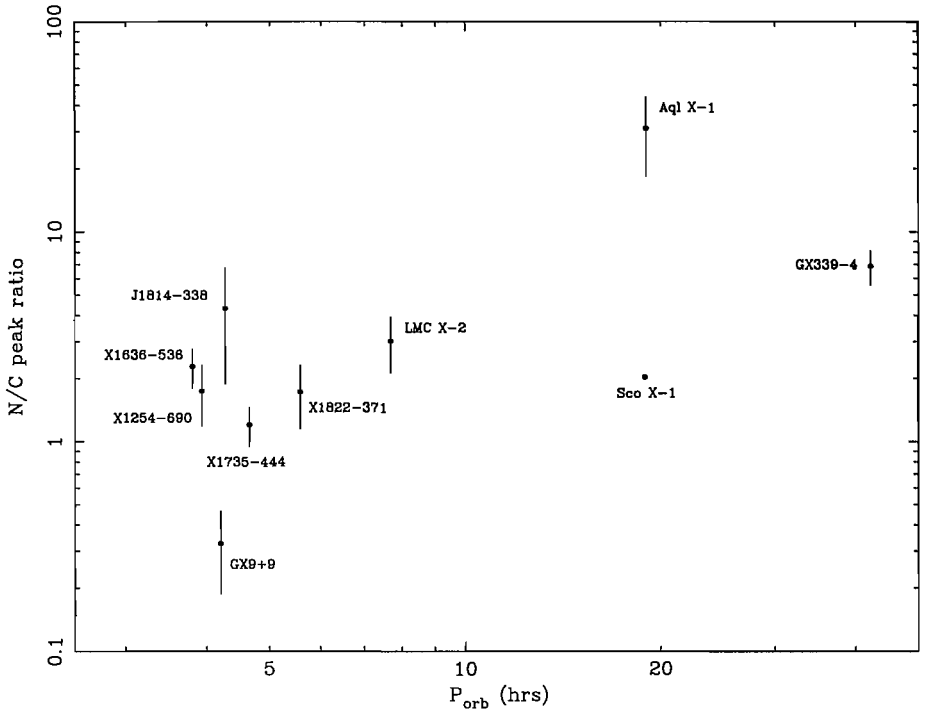

Figure 4.19: The relationship between orbital period and the N/C ratio in our sample of LMXBs, plotted on a log-log scale.

relative efficiencies.

4.3.3 Potential non-spectroscopic indicators of evolutionary status

The orbital period is one of the most fundamental binary parameters. As a binary system evolves, spiralling in and exchanging/losing mass, the orbital period is a variable (e.g. see Fig. 1.12), being related to the binary separation and total system mass (Eqn. 1.2). As such, the orbital period when a system enters the active LMXB stage might perhaps be expected to reflect the initial system parameters, and more specifically the degree of evolution of the accreting matter.

However, there are no obvious differences in the nitrogen-to-carbon ratios (which can indicate evidence for CNO processing) between the short and long orbital period systems in our sample of LMXBs (see Fig. 4.19). Eight of these sources possess a N/C ratio in the range of $\sim$1–7, including the systems with the shortest and the longest orbital periods. Potentially, this could imply similar levels of nuclear processing in each of these systems (see Section 4.3.4). Whilst the systems with unusual N/C ratios (GX9+9 and Aql X–1) occur at opposite ends of the period spectrum, it

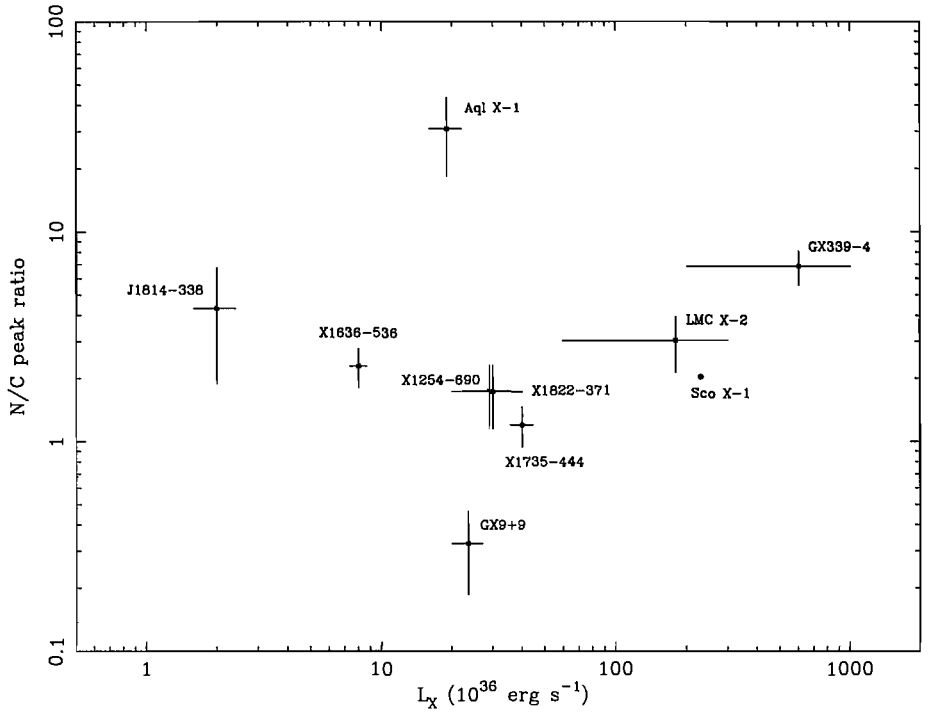

Figure 4.20: The relationship between X-ray luminosity and the N/C ratio in our sample of LMXBs.

is impossible with the current dataset to proscribe any sort of relationship between orbital period and the abundances of nitrogen and carbon in the accreting matter[3]. Nor does there appear to be any simple correlation between the orbital period and the equivalent widths of the Bowen blend, Hβ or He II λ4686. This is unsurprising considering the large scatter that is likely in the initial metallicities of these sources.

Another factor which may affect the evolution of the donor star in a LMXB is the degree of irradiation of the donor by the central X-ray source and accretion disc. Interception of radiation by the donor may cause it to expand and accelerate mass transfer. It may also evaporate mass from the donor surface. If this matter leaves the binary with sufficient angular momentum, this will also accelerate mass transfer. Evaporation of the outer layers will also affect the chemical balance of the system.

We have plotted the X-ray (Fig. 4.20) and optical luminosities (Fig. 4.21) of our sample of LMXBs against the N/C peak ratio. The values for L_X are taken from the published literature (see Table 4.1), whilst the absolute V-band magnitudes are calculated (to a first order approximation) by simply combining the apparent magnitude with the estimated source distance (see Table 4.1). Effects such as reddening

[3]A simple linear fit to the data results in a χ^2 of ~50 (9 degrees of freedom), whilst fitting the data with a constant also produces an unacceptably high value for χ^2.

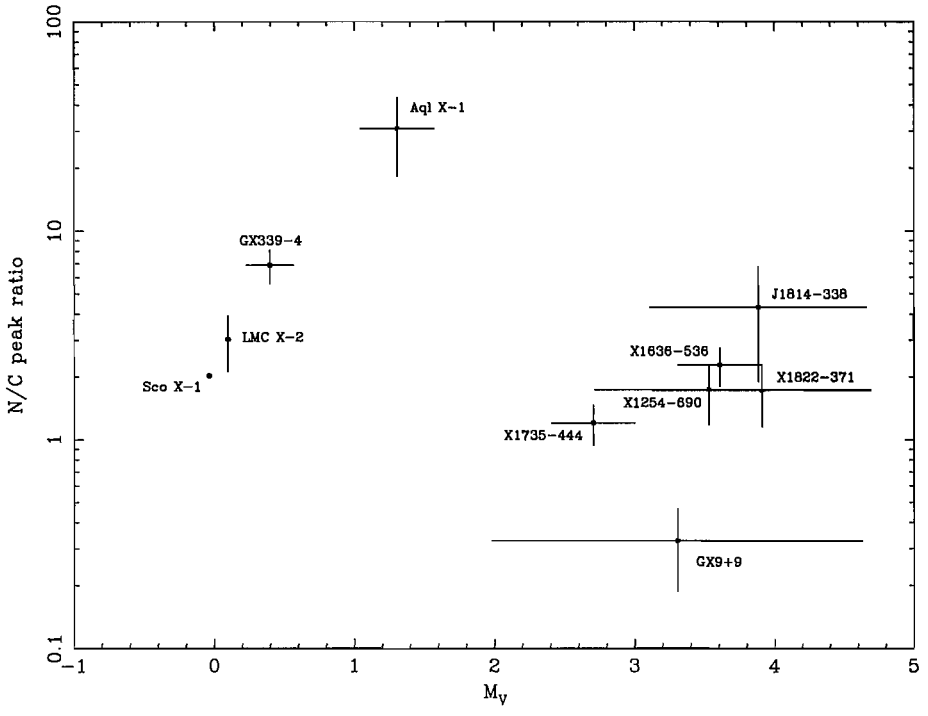

Figure 4.21: The relationship between absolute magnitude and the N/C ratio in our sample of LMXBs. Note that reddening has not been included when calculating magnitudes.

are ignored for this basic comparison of blue-end optical spectra.

As for the case of the orbital period, we observe no correlation between the source luminosity (in either X-ray or optical wavebands) and the N/C ratio. Nor is there any simple correlation with the equivalent widths of the Bowen blend, Hβ or He II λ4686. One striking feature of Fig. 4.21 (and to a lesser extent Fig. 4.20) however is the bimodal distribution of the short period and longer period systems. This is a result of the larger accretion discs in the long period systems, resulting in a much brighter system.

4.3.4 Application to individual sources

What can we learn from the N/C ratios for each individual source? There are a number of common features in each of the figures presented in this section. For example, despite the low metallicity environment in which it was formed, and thus the overall weakness of the Bowen blend, the N/C ratio in LMC X–2 ($\sim$3) falls in line with the majority of our sources. One explanation for this common trend is that each of these systems is observed at a similar evolutionary epoch, following a period of

CNO processing in one of the stellar components. This could be either the donor star itself, which would therefore imply it is a descendant of an intermediate (or higher) mass star, or it could have been the compact object pre-supernova (from which the donor star inherits the observed nitrogen and carbon abundances; Israelian et al., 1999).

Another notable feature is the enhanced N/C ratio found in the transient systems Aql X–1 in particular, and perhaps also GX 339–4 (see e.g. Fig. 4.16). The only other transient source in our sample (J 1814–338) intriguingly also possesses the next greatest N/C ratio, though Figures 4.16 and 4.17 in particular suggest that this millisecond pulsar sits more comfortably in the intermediate group. Considering our extremely limited sample, it would be imprudent to suggest that all transient LMXBs will display enhanced N/C ratios. Instead, we note that GX 339–4 is the only black hole candidate in our sample (Hynes et al., 2003), and that dynamical information obtained for Aql X–1 is very suggestive for the presence of a massive neutron star $\sim$2.2 $M_{\odot}$ (Cornelisse et al., 2006b). With the combination of high mass compact objects and the unusually enhanced N/C ratios (suggestive of high levels of CNO processing), we suggest that these two sources in particular are strong candidates for systems which, though in the current epoch are observed as LMXBs, are in fact descended from intermediate mass systems (see e.g. Podsiadlowski et al., 2002).

GX9+9 is unusual in displaying a significantly lower N/C ratio than any of the other sources in our sample. It is in fact the only system which features more prominent carbon than nitrogen emission in the Bowen blend. The low N/C ratio implies that this is a system which has not undergone any significant levels of CNO processing, and thus that the donor is descended from a rather low mass, main-sequence star. Alternatively, it could merely indicate that the donor star is more heavily carbon-enriched than those in the intermediate group of N/C ratios, either from the supernova event which formed the compact object or perhaps simply from the initial environmental conditions of the stellar nursery in which it was formed.

Returning finally to the remainder of our sample, which lies in the intermediate range of N/C ratio values, more information is needed in order to justify speculation regarding their evolutionary history. Whilst the observations of Sco X–1 by Steeghs & Casares (2002) strongly suggest the presence of a significantly evolved subgiant in order for the low-mass companion to fill its Roche lobe, such compelling evidence for the case of the shorter period systems is not yet available. Improved mass constraints for the individual system components could potentially provide

irrefutable evidence for the presence of an over-massive, evolved donor star which has been stripped of its outer layers in the short period systems. Alternatively (or additionally), rigorous theoretical modelling of the evolution of these systems with particular attention to elemental abundances which can be directly compared to the observations presented here would be extremely useful. It is otherwise impossible to comment with absolute authority upon whether these systems display N/C values expected for low mass or intermediate mass systems. However, the similarity in these ratios for the majority of our sample of short and long period systems (see Fig. 4.19) does suggest (through analogy to Sco X–1) the presence of evolved donors. If they really are all descendants of intermediate mass progenitors, then our sample is in good accord with the predictions of Pfahl et al. (2003) (that 80–95% of current LMXBs are descended from intermediate mass systems).

4.4 Conclusions

We have collated a sample of LMXBs which display the Bowen blend and possess dynamical mass constraints from application of the Bowen fluorescence technique (Steeghs & Casares, 2002). By tracing the orbital motion of the donor star, our high-resolution spectra may be shifted into the donor rest-frame, thus unveiling in tremendous clarity the narrow nitrogen and carbon emission lines produced on the irradiated inner face of the donor. Previous non-dynamical studies of the broad, smeared-out Bowen blend have provided evidence for a link between the strength of the overall blend and the metallicity of the source (Motch & Pakull, 1989). However, using our donor rest-frame shifted spectra to measure the intensities of individual nitrogen and carbon emission lines within the blend, we can find no link between the strength of the overall Bowen blend and the degree of evolution (in the form of CNO processing) present in the system. Equally, we find no link between simple non-spectroscopic parameters such as the orbital period or X-ray and optical luminosities to the ratios of nitrogen and carbon observed within the system.

Indeed, the majority of sources appear to possess a N/C ratio between ∼2–4, irrespective of luminosity, period, the presence of X-ray bursts or the equivalent width of the Bowen complex. Aql X–1 and GX 339–4 are unusual in this respect, displaying extremely enhanced N/C ratios up to ∼30. This is indicative of high levels of CNO processing at some point in the history of the system, making them excellent candidates for systems which possess evolved donor stars.

At the other end of the spectrum, GX9+9 alone amongst our sample possesses

a N/C ratio of <1. This nitrogen depletion/carbon enrichment compared to the majority of our sample could simply be a result of the initial conditions in which the binary system was formed, or alternatively it could be evidence for the absence of significant levels of CNO processing within the donor star (i.e. the donor was formed as a low-mass star).

Theoretical modelling by Pfahl et al. (2003) of the Galactic population of low- and intermediate-mass X-ray binaries has suggested that the importance of the standard formation scenario for LMXBs is overstated, with intermediate mass systems being much more common than previously believed. Indeed, they calculate that 80–95% of the LMXBs observed in the current epoch are in fact descended from intermediate mass progenitors. In this picture, we can expect that our sample of ten LMXBs should contain only 1–2 'standard' systems, with 8–9 displaying evidence of descendancy from IMXBs (i.e. they are more evolved, showing evidence for CNO processing). This prediction complements our sample very well under the assumption that those sources displaying intermediate values of the N/C ratio are indeed displaying evidence of CNO processing, leaving a ratio of 9:1 of IMXBs compared to LMXBs. However, the current body of evidence is not enough to unilaterally declare this result, and further observations are necessary in order to more closely associate this group with the apparently highly evolved systems such as Aql X–1 and GX 339–4, or with the substantially less evolved GX9+9. Refined mass constraints could distinguish between a low mass, main-sequence or an over-massive, evolved donor star in these systems. Alternatively, observations of globular cluster sources (with different formation mechanisms to those found in the Galactic field) could be useful in truly distinguishing low mass from intermediate mass systems.

Chapter 5

On the Origin of the Absorption Features in SS 433

We present high-resolution B- and I-band spectroscopy of the X-ray binary system SS 433, obtained over a wide range of orbital phases. The spectra display numerous weak absorption features, including the clearest example seen to date of features resembling a mid-A type supergiant spectrum. These absorption features have previously been associated with the donor star. However, the new data precludes this hypothesis, indicating that there may be an alternative region within the system producing an A supergiant-like spectrum, probably an accretion disc wind. Indeed, whilst we cannot confirm the possibility that the companion star is visible at certain phase combinations, it is possible that all supergiant-like features observed thus far are produced solely in a wind. We conclude that great care must be taken when interpreting the behaviour of these weak features. Some of the work presented in this chapter has been published in Barnes et al. (2006).

5.1 Introduction

5.1.1 The Discovery of SS 433

The bizarre object SS 433 is a Galactic X-ray binary at the centre of the supernova remnant W 50, and is sometimes ascribed to be the prototypical microquasar (though in reality it is very different to most other microquasars). It was first identified in a survey of stars exhibiting Hα emission by Stephenson & Sanduleak (1977), the 433rd of 455 objects included from the Galactic plane. The prominent radio emission from the star was independently discovered (Clark et al., 1975), but ini-

tially without an optical identification, as was also the case for the X-ray emission from the object (Seward et al., 1976; Forman et al., 1978). The realisation that all these sources of radiation originated from the same object was reached independently by several authors, with Clark & Murdin (1978) in particular drawing attention to the triple co-incidence of the radio, optical and X-ray sources. An excellent introduction to this system may be found in the major review by Margon (1984).

The first spectroscopic observations of this object revealed bright and variable lines whose origin was unclear. In addition to very strong and broad Balmer and He I emission lines, the optical spectrum contains a number of prominent broad emission features at unfamiliar wavelengths (Margon et al., 1979a). These latter emissions were identified with two sets of Doppler-shifted Balmer and He I lines (Liebert et al., 1979; Margon et al., 1979b), one with a large redshift and the other with a huge blue-shift. The Doppler-shifted features are seen to change in wavelength and move through the spectrum on a timescale of days as the velocity of the two shifted systems changes smoothly (Fig. 5.1), with the mean velocity of the two systems remaining approximately constant at the astonishing value of $\sim$ 12,000 km s^{-1}.

Fabian & Rees (1979) and Milgrom (1979) both proposed collimated, oppositely ejected jets as a possible explanation of the simultaneous redshifts and blue-shifts. A periodic precession of the jet axis was proposed to explain the observed velocity modulations. Abell & Margon (1979) considerably elaborated upon this model, making the advance prediction that the 'moving' emission line systems would cross through each other (with the redshift system acquiring a blue-shift and vice versa) for a part of the cycle (Fig. 5.2).

The 'Kinematic Model' hypothesises that matter is ejected in two opposing jets that are collimated and oppositely aligned to within a few degrees. The time variable aspect of the jets with respect to the observer explains the observed modulation of the redshifts and blue-shifts. The near-relativistic ejection velocity of the jets creates a substantial and directly observable transverse Doppler shift. The observed jet ejection velocity (v $\sim$ 0.26c) corresponds to a Lorentz factor of 1.035, leading to a 'time dilation' redshift in the velocity data as a zero point offset regardless of the geometric phase of the jet axis. This explains the 12,000 km s^{-1} symmetry value for the Doppler shifts. Both radio (Hjellming & Johnston, 1981a,b) and X-ray (Seward et al., 1980) imaging observations provide strong support for the jet model (Fig. 5.3). SS 433 remains the only known Galactic relativistic jet source to

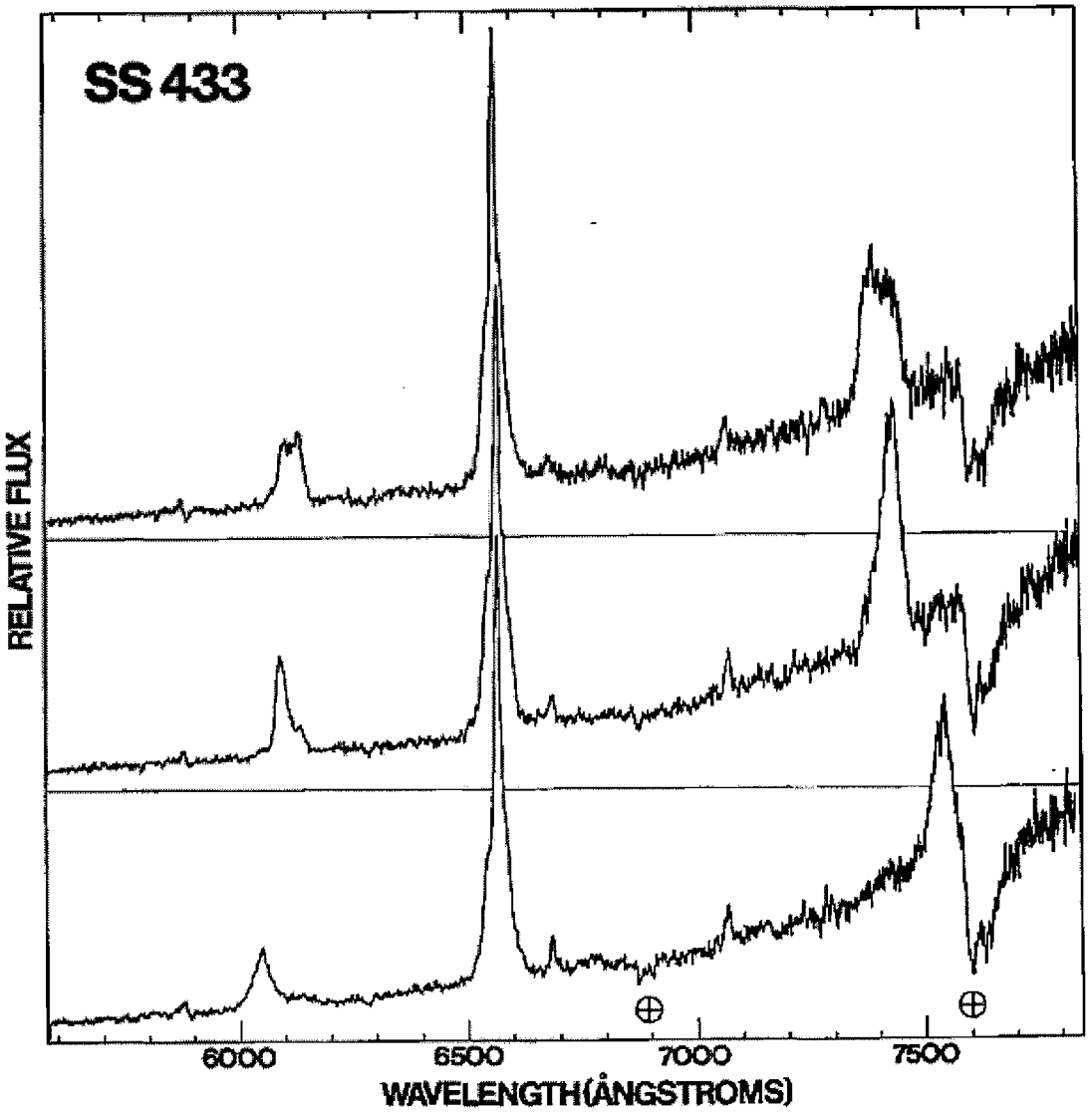

Figure 5.1: The spectra that started it all: 3 spectra obtained by Rem Stone with the 0.6m Lick reflector on 1978 October 23 (upper), 24 (centre) and 26 (lower, see Margon et al. 1979a). The 'unidentified' prominent emission features flanking Hα to the red and blue are readily apparent, and are seen to drastically change wavelengths on a timescale of days. These prove to be Doppler-shifted Hα from the relativistic jets.

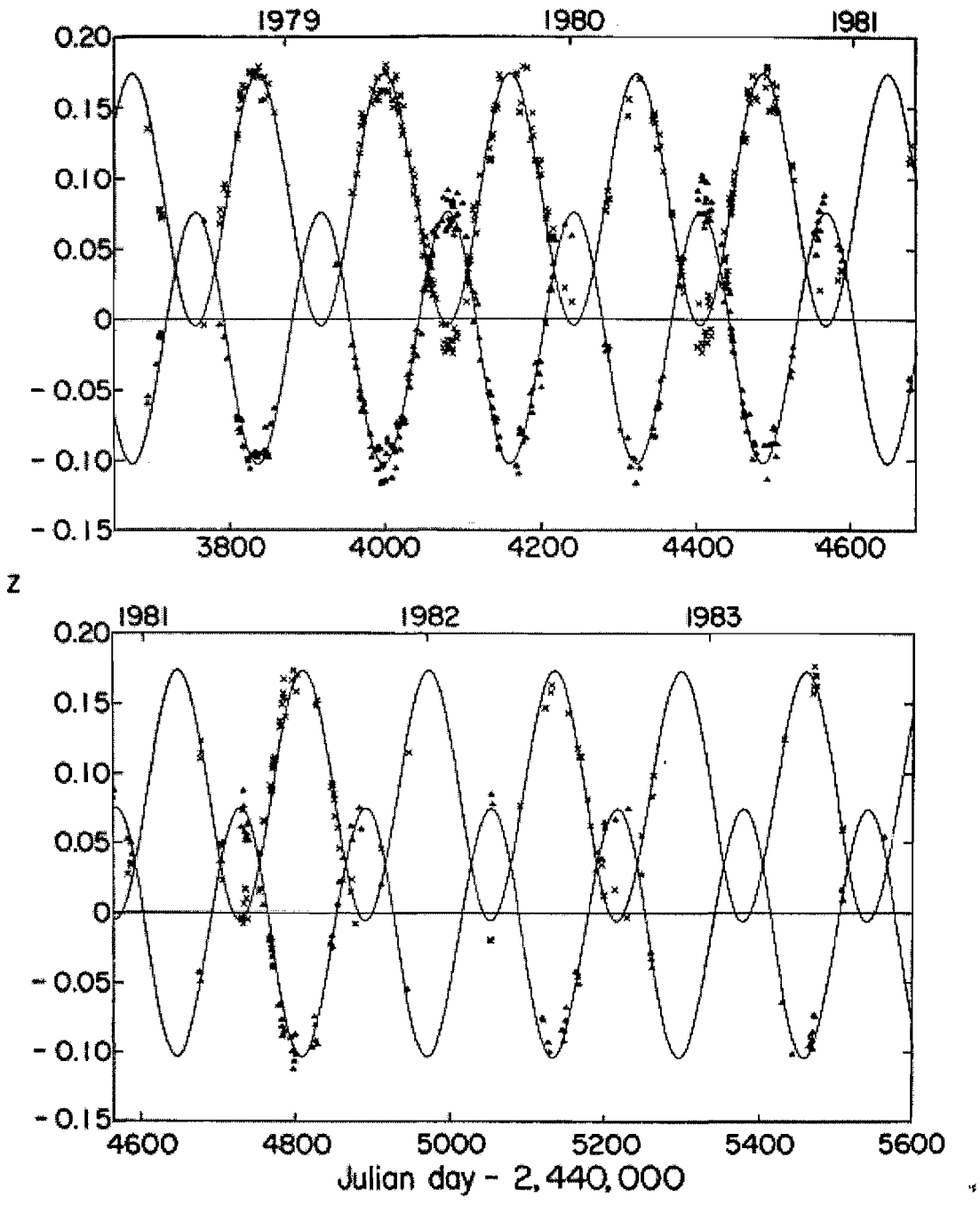

Figure 5.2: Doppler shifts of SS 433 on 450 nights in the period 1978-1983 (taken from Margon 1984). The solid curve is a least-squares best fit to the kinematic model.

reveal the presence of baryonic matter in the jets (in the form of both optical and X-ray emission lines from thermal gas) in spite of now numerous instances of highly energetic, likely relativistic, jets in microquasars (e.g. Fender, 2003).

The kinetic luminosity in the jets is estimated to be at the astonishing level of $\sim 10^{39}$–10^{41}erg s^{-1} (Safi-Harb & Kotani, 2003). Although the origin of the jet energy is still a matter of debate, unless the compact object is extremely massive ($\geq$10 $M_{\odot}$) the Eddington limit must be exceeded in order to power the jets[1]. A high mass-transfer rate is indicated by the mass-loss rate of $\sim 10^{-6}$ $M_{\odot}$ yr^{-1} in the precessing jets (Begelman et al., 1980). King et al. (2000) considered possible evolutionary models for SS 433 and predicted mass loss rates between 7 x 10^{-6} $M_{\odot}$ yr^{-1} and 4 x 10^{-4} $M_{\odot}$ yr^{-1}. This estimate agrees well with measurements of the 2–12 μm continuum emission, corresponding to optically thin and partially optically thick free-free emission. From this, Fuchs et al. (2006) calculated an extremely high mass loss rate of 2–3 x 10^{-4} $M_{\odot}$ yr^{-1} if the wind is homogeneous, and a third of these values if it is clumped.

This supercritical accretion regime provides a strong link to the ultraluminous X-ray sources (ULX) and the newly discovered INTEGRAL sources in our own galaxy. It was suggested originally by Katz (1987) that if SS 433 were observed close to the jet axis, it would be an extremely bright X-ray source. Indeed, the idea that SS 433 itself might be a ULX viewed 'from the side' provides a natural explanation of its otherwise puzzlingly feeble X-ray emission.

Whilst in many aspects of its character SS 433 appears to be unique within the Galaxy, the X-ray behaviour of, for example, XTE J1716–389 (Cornelisse et al., 2006a) is remarkably similar not only to SS 433, but also to the new class of obscured X-ray binaries detected by INTEGRAL. This suggests that they may all be members of the same population. This has already been proposed by Revnivtsev et al. (2003) for the case of IGR J16318–4848. The idea of an HMXB transferring material via Roche lobe overflow on to a compact object, and thereby producing a Compton thick cloud is exactly the model suggested for SS 433. Furthermore, the mass transfer in these systems should be unstable, leading to supercritical accretion rates, just like SS 433. This would suggest that SS 433 is currently the best-known member of a much wider population of X-ray binaries that are only now being discovered by INTEGRAL. The exact nature of each system depends upon the inclination at which we view the system, akin to the unification scenario for active galaxies (see

[1]It should be noted here however that the Eddington limit applies to radiation, not kinetic power.

e.g. Madau et al., 1994).

The Kinematic Model is a convenient and simple device which is still useful for predicting the kinematics of the ejected jets. However, it leaves unspecified almost all of the interesting physical aspects of the system, in particular the nature of the underlying stars. Mass determinations for the stellar components are particularly important for a system whose properties link it to both the microquasars and ULX systems. However, in spite of many studies over the last two decades, SS 433 has steadfastly refused to reveal these details.

5.1.2 System Parameters

SS 433 is observed as a weak ($\sim 10^{36}$erg s^{-1}) X-ray source (X1909+048), which combined with the high orbital inclination ($i \sim 78°$, Eikenberry et al., 2001) and low L_X/L_{opt} ratio ($L_X \sim L_{opt} \sim 10^{36}$erg s^{-1}, e.g. Margon, 1984) suggests that it may be an accretion disc corona source (see Section 1.4.2). Observations of the radio emitting material ejected in the relativistic jets lead to a distance estimate of 5.5 $\pm$ 0.2 kpc (Blundell & Bowler, 2004). In addition to the pair of jets, recent radio observations have detected extended emission in a direction that is perpendicular to the main jet outflow (Paragi et al., 1999; Blundell et al., 2001). This provides evidence for some form of circumbinary outflow such as a disc-like outflow of matter from the outer parts of the accretion disc (Zwitter et al., 1991). The overall system geometry suggested by these recent studies is illustrated in Fig. 5.4*a*, a schematic that we will use extensively throughout this chapter.

The system displays two key periodicities, a $\sim$ 162d precession period of its jets and a $\sim$ 13d orbital period. The precession of the jets is revealed in the radial velocity curves of the strong, blue- and red-shifted 'moving' Balmer emission lines (Margon, 1984). This 162d modulation is also present in the optical flux, a result of the changing orientation of the precessing accretion disc. The orbital period was first discovered through the radial velocity variations of the 'stationary' Balmer and He I emission lines (Crampton et al., 1980), which reach maximum velocity at superior conjunction of the X-ray source. However, the He II λ4686 has a different radial velocity curve, with a velocity maximum occurring when the compact object is receding (Crampton & Hutchings, 1981; Fabrika & Bychkova, 1990). This may indicate an origin in or around the accretion disc/compact object.

Due to the strong and broad emission lines, the detection of any spectroscopic signatures of the donor star has proved rather more difficult, and the suggestions

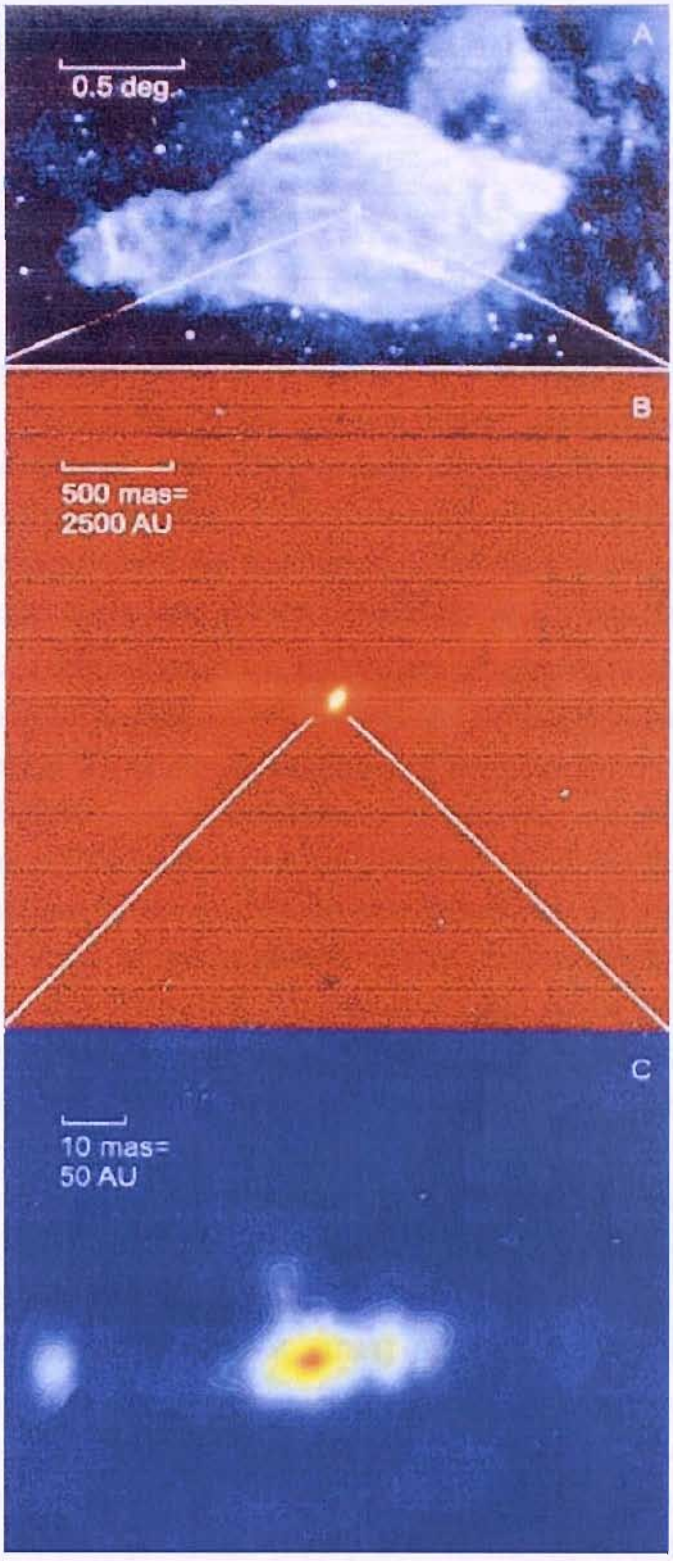

Figure 5.3: Radio images of SS 433 on various angular scales, taken from Paragi et al. (2000). (a) The W50 nebula depicted as a mosaic of VLA images at 1.4 GHz (Dubner et al., 1998) (b) the precessing radio jets at 1.6 GHz, (c) the inner jets at 1.6 GHz. The radio brightening zone about 50 mas along the jet and the weak radio emission approximately perpendicular to the jets are both visible.

Table 5.1: Historical mass estimates for the stellar components of SS 433.

M_X $M_\odot$	M_{donor} $M_\odot$	Technique	Author
62	52	V-band lightcurves	Antokhina & Cherepashchuk (1985)
0.8 ± 0.1	3.2 ± 0.4	optical emission lines, X-ray eclipse	d'Odorico et al. (1991)
11 ± 5	19 ± 7	optical absorption lines	Gies et al. (2002b)
2.9 ± 0.7	10.9 ± 3.1	optical absorption lines	Hillwig et al. (2004)
9	30	X-ray eclipse, optical absorption lines	Cherepashchuk et al. (2005)
20 ± 5	35 ± 7	X-ray spectra	Lopez et al. (2006)

for its spectral type range from OB (Crampton & Hutchings, 1981) to Wolf-Rayet (van den Heuvel et al., 1979; Hut & van den Heuvel, 1981), including a massive Main Sequence star (Lopez et al., 2006) or both hot (Murdin et al., 1980) and cool supergiants (e.g. King et al., 2000). Since the interpretation of the radial velocity curves requires assumptions about the nature of the mass donor, estimates for the mass of the compact object have ranged remarkably widely (see Table 5.1).

d'Odorico et al. (1991) obtained a limited set of spectroscopic observations of the He II λ4686 line to provide an estimate of the orbital motion of the compact object. To disentangle the values of the masses of the binary components, the mass ratio was inferred from X-ray observations of the primary eclipse. In contrast to many contributions to the optical emission, most of the X-ray flux comes from a small region at the base of the relativistic jets. When it is eclipsed by the normal star, the duration of the eclipse is related to the relative size of the normal star and in turn to the mass ratio (the normal star is assumed to fill its Roche lobe). These estimates suggested a mass ratio of $q = M_X \,/\, M_{donor} \simeq 0.245$ if the X-ray jets are partly obscured by the accretion disc and normal star. The corresponding masses of the compact object and companion star were derived to be 0.8 $M_\odot$ and 3.2 $M_\odot$ respectively. However, a somewhat higher mass ratio could be inferred by considering a moderate flattening of the secondary, or a wind-type mass flow that obscures the X-rays for a small fraction of the eclipse.

Whilst the studies of d'Odorico et al. (1991) imply the presence of a neutron star (and a low mass one at that!) rather than a black hole as the central engine, other estimates have disagreed strongly. By modelling the observed V-band lightcurves of the system, and assuming a thick accretion disc due to the supercritical accretion rates, Antokhina & Cherepashchuk (1985) derived an estimate for the compact object mass of 62 $M_\odot$ and the companion of 52 $M_\odot$. If correct, these would make SS 433 dramatically different to any other Galactic XRB.

The best way to resolve these issues is to observe the companion star itself directly. Unfortunately, our attempts to utilise Bowen fluorescence lines to trace the

motion of the donor proved unsuccessful. Making use of a number of archival observations (from the WHT, AAT and Calar Alto) from a variety of orbital and precessional phases, we were unable to confirm the presence of any sharp features in the strong, broad Bowen blend exhibited by SS 433. Our data possessed insufficient phase coverage to make Doppler Tomography viable. Attempting to fit a model comprising two sets of Gaussian lines, corresponding to the strongest N III and C III lines in the Bowen blend region (c.f. Hynes et al., 2003), produced extremely inconsistent results (likely caused by the measurement of random noise rather than real physical features). The apparent lack of observable sharp Bowen features in this system could perhaps be due to the high gas density (e.g. jets, circumbinary outflow) around the X-ray source, which may negate the Bowen process by destroying the seed He II Lyα photons (see Section 2.2.1).

A simple measurement of the spectral type of the donor can provide constraints for the system parameters or, even better, phase-resolved kinematical studies of any photospheric features produced by the donor can lead to an estimate for the mass function (see Section 2.1). Gies et al. (2002b) and Hillwig et al. (2004) suggested that the optimal time to detect a spectral signature of the donor star is during the X-ray eclipse ($\phi_{orb} \sim 0$), at a precessional phase when the disc is most open to the observer ($\Psi_{prec} \sim 0$, Fig. 5.4*b*). During this configuration of phases, light from the donor should be least 'obscured' by any extended circumbinary disc or disc wind. Based on observations taken during this combination of phases, Hillwig et al. (2004) discovered features (between ~4500–4600Å) corresponding to a mid-A supergiant (A3–7 I) and suggested that these could originate upon the donor star. This constrained the binary system to be a low mass black hole ($2.9 \pm 0.7 M_{\odot}$) with a $10.9 \pm 3.1 M_{\odot}$ companion, consistent with the predictions of King et al. (2000).

Cherepashchuk et al. (2005) confirmed the presence of mid-A supergiant features (at a shorter wavelength, ~4200–4340Å), including low-ionisation Fe I lines, at the phase combination used by Hillwig et al. (2004). However, their measurement of these features (which at their low resolution of ~3Å appear as complex blends) produced a completely different radial velocity amplitude, leading to mass estimates of 18 $M_{\odot}$ and 24 $M_{\odot}$ for the compact object and companion respectively. Dissatisfied with these values, the authors were able to re-interpret their data based upon models of the X-ray eclipse lightcurve. The modified values of 9 $M_{\odot}$ and 30 $M_{\odot}$ still disagree with any previous mass estimate. Cherepashchuk et al. (2005) believe that the cross-correlation measurements of Hillwig et al. (2004) were contaminated by strong Fe II absorption lines which are produced in a circumbinary outflow. In con-

trast, their own measurements which include low excitation Fe I lines, are claimed to be less likely to suffer from contamination by alternative sources.

Historically, the calculations using 'donor star' features are based upon very limited orbital phase coverage. In this chapter we will test the possibility of observing the supergiant features over a much broader range of phases. We look to confirm their origin and hopefully provide a more secure estimate of the system parameters. Next, we give an overview of the observations. In Section 5.3 we will begin with a general description of all our B-band spectra, then discuss the three best spectra in more detail (Sections 5.3.1-5.3.3), and finish by presenting the radial velocities in Sections 5.3.4-5.3.5. The I-band data will be presented in Section 5.4. We will begin Section 5.5 with a discussion of the consequences of the model proposed by Gies et al. (2002b) and then present our own findings.

5.2 Observations

SS 433 was observed using three different telescopes and instruments in the blue spectral range ($\lambda\lambda$4000-5000) between 2000 and 2004. Four high-resolution spectra of SS 433 were obtained with the TWIN spectrograph mounted on the 3.5 m telescope at Calar Alto Observatory. A 1200 lines mm^{-1} grating together with a 1.5″ long slit covered $\lambda\lambda$3700-4800 at 0.51 Å pix^{-1}, yielding a spectral resolution of 67 km s^{-1} (FWHM) at 4550Å. Two intermediate resolution spectra (0.63 Å pix^{-1}) were obtained using the Intermediate Dispersion Spectrograph (IDS) attached to the 2.5 m Isaac Newton Telescope (INT) at the Observatorio del Roque de Los Muchachos on the nights of 15-16 August 2002. We used the R900V grating in combination with the 235 mm camera and a 1.2″ slit to provide a spectral resolution of 83 km s^{-1} (FWHM) at 4550Å.

SS 433 was observed on nine separate nights, in addition to an A4 Iab comparison star (HD 9233), using both the red and blue arms of the ISIS spectrograph with the 4.2 m William Herschel Telescope (WHT) at the Observatorio del Roque de Los Muchachos in June/July 2004. The R1200B grating was used with a central wavelength setting of 4550 Å and a 0.93″ slit, giving a spectral resolution of 29 km s^{-1} (FWHM) 4550Å. The R1200R grating was used with three different central wavelength settings of 7300, 7900 and 8500 Å and a 0.93″ slit, giving spectral resolutions of 19 km s^{-1} (FWHM) at 7300Å, 17 km s^{-1} (FWHM) at 7900Åand 16 km s^{-1} (FWHM) at 8500Å. A complete log of the blue observations is presented in Table 5.2, and the red arm ISIS observations are presented in Table 5.3. Orbital phases

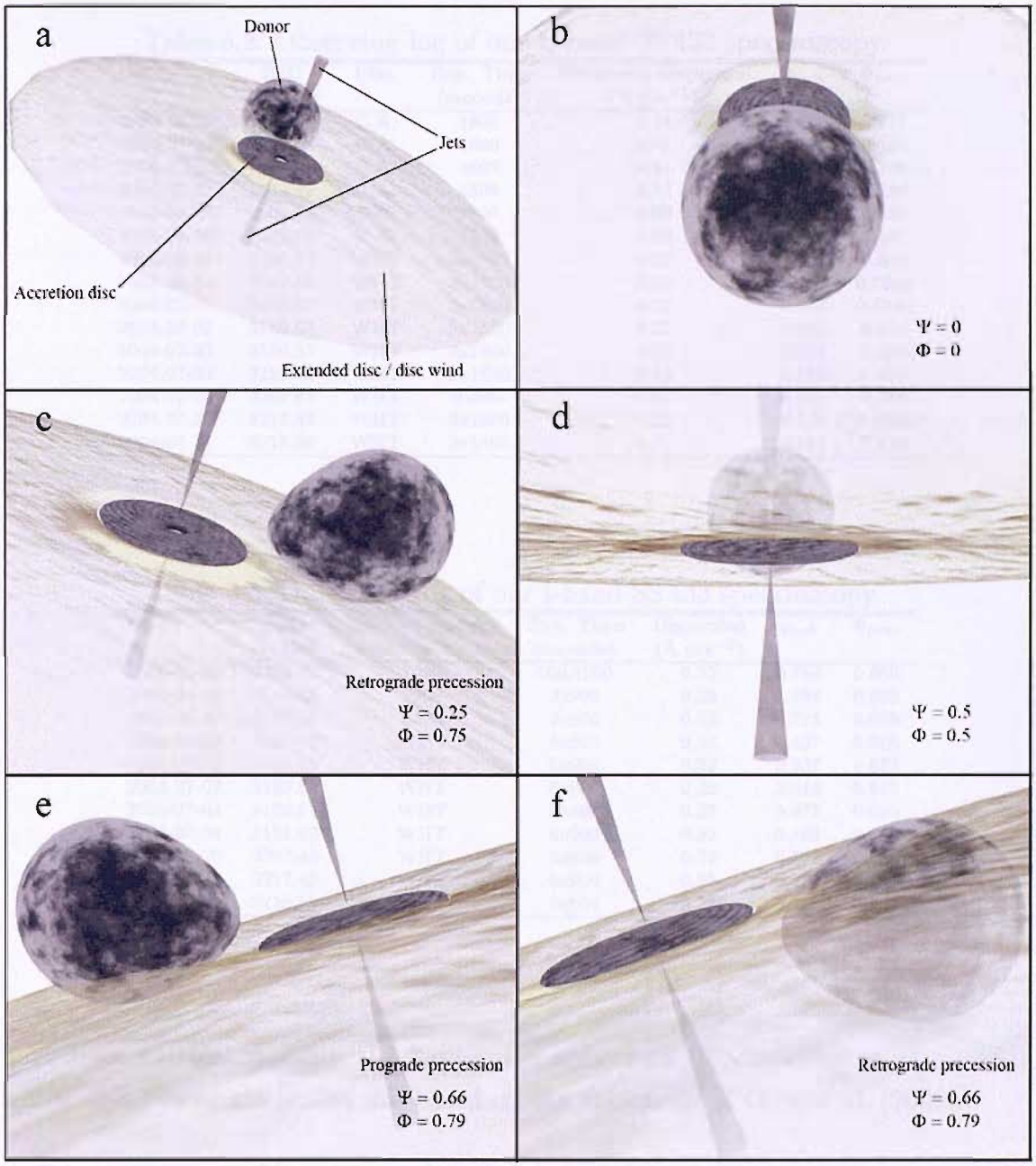

Figure 5.4: Cartoon picture of the SS 433 system featuring an equatorially expanding extended disc, from the point of view of an observer on earth. In all panels the sense of precession is represented as being anti-clockwise, with orbital motion clockwise in the retrograde case and anti-clockwise in the prograde case. *a*) Overview. Note the extended disc is arbitrarily cut-off in the radial direction, and its opening angle is rather narrow. *b*) Preferred phase combination of Hillwig et al. (2004). Donor could still be visible above the extended disc from $\phi_{orb} \sim 0.75$–0.25. *c*) Later Ψ_{prec}, but the donor could still be visible above the extended disc at this combination of phases. *d*) Donor star becomes fully masked behind the extended disc, but will become partially visible *below* the disc from $\phi_{orb} \sim 0.75$–0.25. *e*) & *f*) The system alignment on 2004 June 29. Here the donor is mostly visible assuming prograde precession, and masked in the case of retrograde (the preferred model).

Table 5.2: Observing log of our B-band SS 433 spectroscopy.

Date	HJD -2450000	Obs.	Exp. Time (seconds)	Reciprocal Dispersion (Å pix^{-1})	ϕ_{orb}	Ψ_{prec}
2000-07-20	1746.38	C.A.	1800	0.51	0.687	0.777
2000-07-21	1747.43	C.A.	1800	0.51	0.768	0.784
2000-07-22	1748.36	C.A.	1800	0.51	0.839	0.789
2000-07-23	1749.42	C.A.	1800	0.51	0.920	0.796
2002-08-15	2501.64	INT	1800	0.63	0.420	0.435
2002-08-16	2502.55	INT	1800	0.63	0.490	0.441
2004-06-29	3186.67	WHT	3x1800	0.22	0.784	0.660
2004-06-30	3187.63	WHT	3x1800	0.22	0.857	0.6668
2004-07-01	3188.67	WHT	3x1800	0.22	0.937	0.6723
2004-07-02	3189.68	WHT	3x1600	0.22	0.014	0.678
2004-07-03	3190.51	WHT	3x1800	0.22	0.077	0.683
2004-07-04	3191.63	WHT	3x1800	0.22	0.163	0.690
2004-07-20	3207.43	WHT	6x600	0.22	0.371	0.788
2004-07-30	3217.43	WHT	3x1800	0.22	0.135	0.8495
2004-07-31	3218.50	WHT	3x1800	0.22	0.217	0.856

Table 5.3: Observing log of our I-band SS 433 spectroscopy.

Date	HJD -245000	Cen. wavelength Å	Exp. Time (seconds)	Dispersion (Å pix^{-1})	ϕ_{orb}	Ψ_{prec}
2004-06-29	3186.67	7300	600,1200	0.23	0.784	0.660
2004-06-29	3186.67	7900	2x900	0.23	0.784	0.660
2004-06-29	3186.67	8500	2x900	0.23	0.784	0.660
2004-06-30	3187.63	WHT	6x900	0.22	0.857	0.666
2004-07-01	3188.67	WHT	6x900	0.22	0.937	0.672
2004-07-02	3189.68	WHT	6x800	0.22	0.014	0.678
2004-07-03	3190.51	WHT	6x900	0.22	0.077	0.683
2004-07-04	3191.63	WHT	6x900	0.22	0.163	0.690
2004-07-20	3207.43	WHT	6x600	0.22	0.371	0.788
2004-07-30	3217.43	WHT	6x900	0.22	0.135	0.849
2004-07-31	3218.50	WHT	6x900	0.22	0.217	0.856

have been calculated using the light-curve ephemeris of Goranskii et al. (1998), whilst disk precession phases are based on the ephemeris of Gies et al. (2002a).

The images were bias corrected and flat-fielded, and the spectra subsequently extracted using conventional optimal extraction techniques in order to optimise the signal-to-noise ratio of the output (Horne, 1986). Frequent observations of comparison arc lamp images were performed in the course of each run and the pixel-to-wavelength scale was derived through polynomial fits to a large number of identified reference lines. The final rms scatter of the fit was always $<1/30$ of the spectral dispersion. Finally, the B-band spectra have been rectified using a high-pass filter to remove any low-order variations (0.001–0.08 cycles/Å) caused by the broad jet lines, and then the data were combined to produce an average spectrum for each night.

5.3 Analysis of the B-band spectra

We analysed a portion of the continuum that is free of stationary emission lines and rich in absorption features. The best available region encompasses the range between ~4500 – 4630 Å, which is bracketed by emission from He I λ4471 and the N III/C III complex ~4640-4650 Å.

Spectra from twelve of the fifteen separate nights, covering a broad range of orbital phases, display photospheric features that appear to be similar to that of an A supergiant (Fig. 5.5). Whilst the strongest Fe II absorption lines (λ4549 & λ4584 Å) are present in each of these spectra, the morphology of these features, and indeed the presence of other weaker features, is highly variable, a fact which seems difficult to reconcile with the donor star being the only system component producing these lines.

We have extracted velocity measurements from each of the spectra which display clear A supergiant-like photospheric features by cross-correlating with an optimally broadened comparison star (HD 9233). The systemic velocity of the comparison star was first removed (γ = -34 $\pm$ 2 km s^{-1}, Hillwig et al. 2004) and then the data were re-binned into velocity space and cross-correlated with the optimally broadened spectrum of HD 9233 across the range ~ 4500 – 4630 Å. The comparison star was smoothed to the resolution of the spectra for the Calar Alto and INT runs using a Gaussian smoothing algorithm. We present these results in Section 5.3.4, after a more detailed description and comparison of three of these spectra which display the clearest absorption lines.

For each nightly average spectrum, we broadened (see Section 2.1.2) our supergiant template from 39 to 99 km s^{-1} in steps of 2 km s^{-1}, taking into account that the template star HD 9233 already possesses an intrinsic rotational broadening of 39 km s^{-1} (Hillwig et al., 2004). A spherical rotational profile (Gray, 1992) was applied, with a linear limb-darkening law of coefficient ϵ = 0.62, interpolated for λ = 4500 Å and $T_{eff} \simeq$ 8350 K (Kudritzki et al., 2003; Al-Naimy, 1978). The broadened versions of the template star were multiplied by fractions $f < 1$, to account for the fractional contribution to the total light, and subsequently subtracted from the nightly average spectra for SS 433. Minimising χ^2 yields an optimal value for f and $v \sin i$ in each case (see Table 5.4).

Table 5.4: Derived velocity parameters of the λ4500–4600 Å absorption features.

HJD -2450000	ϕ_{orb}	Ψ_{prec}	†Radial Velocity (km s^{-1})	°f	‡$v \sin i$ (km s^{-1})
1746.38	0.687	0.777	-54 ± 15	0.80 ± 0.09	97 ± 30
1747.43	0.768	0.784	-91 ± 16	1.03 ± 0.10	110 ± 20
1748.36	0.839	0.789	-20 ± 22	1.04 ± 0.05	108 ± 15
1749.42	0.920	0.796	-	-	-
2501.64	0.420	0.435	-120 ± 5	0.51 ± 0.05	80 ± 8
2502.55	0.490	0.441	-115 ± 12	0.29 ± 0.07	77 ± 10
3186.67	0.784	0.660	6 ± 2	0.77 ± 0.04	84 ± 5
3187.63	0.857	0.666	-5 ± 8	0.46 ± 0.08	98 ± 17
3188.67	0.937	0.672	4 ± 13	0.65 ± 0.05	39 ± 4
3189.68	0.014	0.678	-	-	-
3190.51	0.077	0.683	-12 ± 13	0.30 ± 0.06	53 ± 8
3191.63	0.163	0.690	-	-	-
3207.43	0.371	0.788	-78 ± 8	0.10 ± 0.06	73 ± 20
3217.43	0.135	0.849	-1 ± 5	0.59 ± 0.04	49 ± 4
3218.50	0.217	0.856	-35 ± 4	1.05 ± 0.08	117 ± 10*

* Measurement of the combined features in the double-lined spectrum (see Sect. 5.3.3)
† obtained via cross-correlation fitting with HD 9233
° estimated scaling factor of the absorption lines compared to HD 9233
‡ optimal broadening applied to the comparison star (see Sect. 5.3)
- do not display clear A supergiant-like features

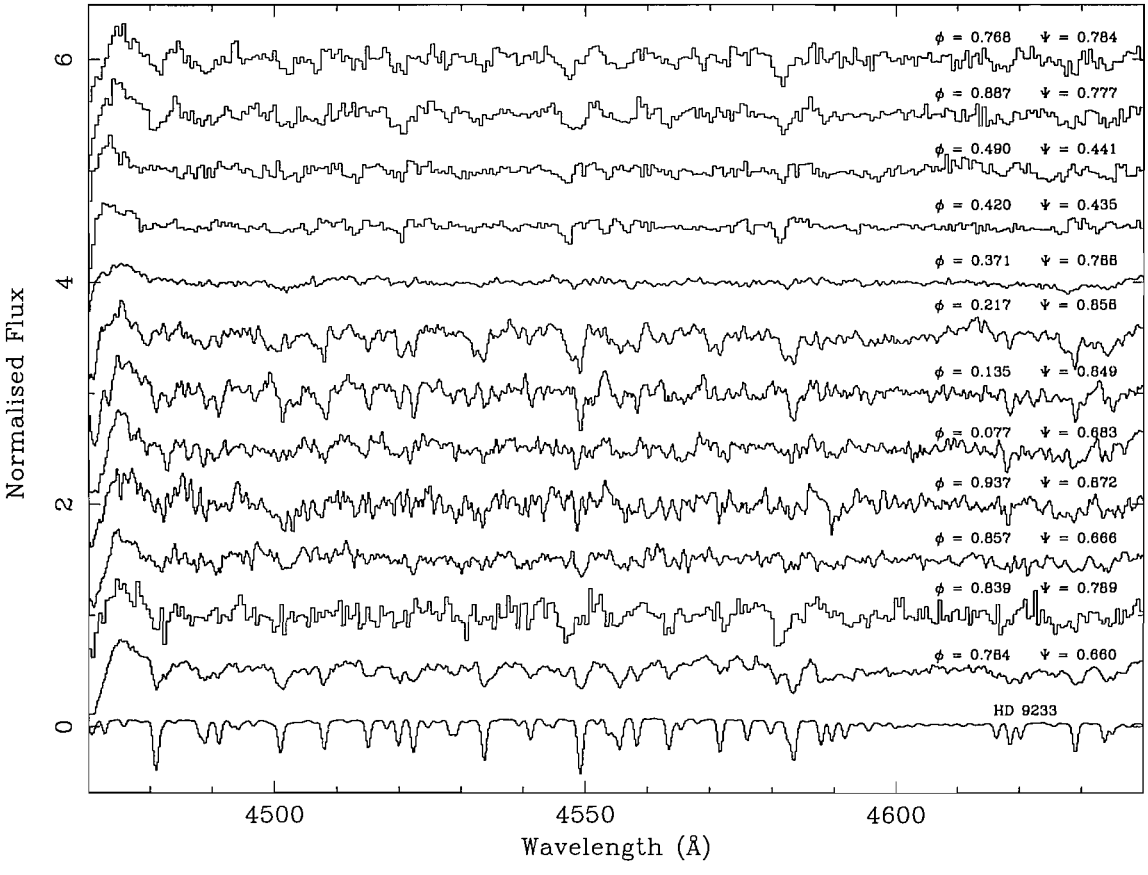

Figure 5.5: All of the nightly averaged spectra which display key A supergiant-like features arranged in orbital phase order beginning with the spectrum discussed in Section 5.3.1 (second from bottom). The template star HD 9233 is shown at the bottom. Line identifications have been omitted here for clarity, see Figs. 5.6, 5.7, 5.8 for this information.

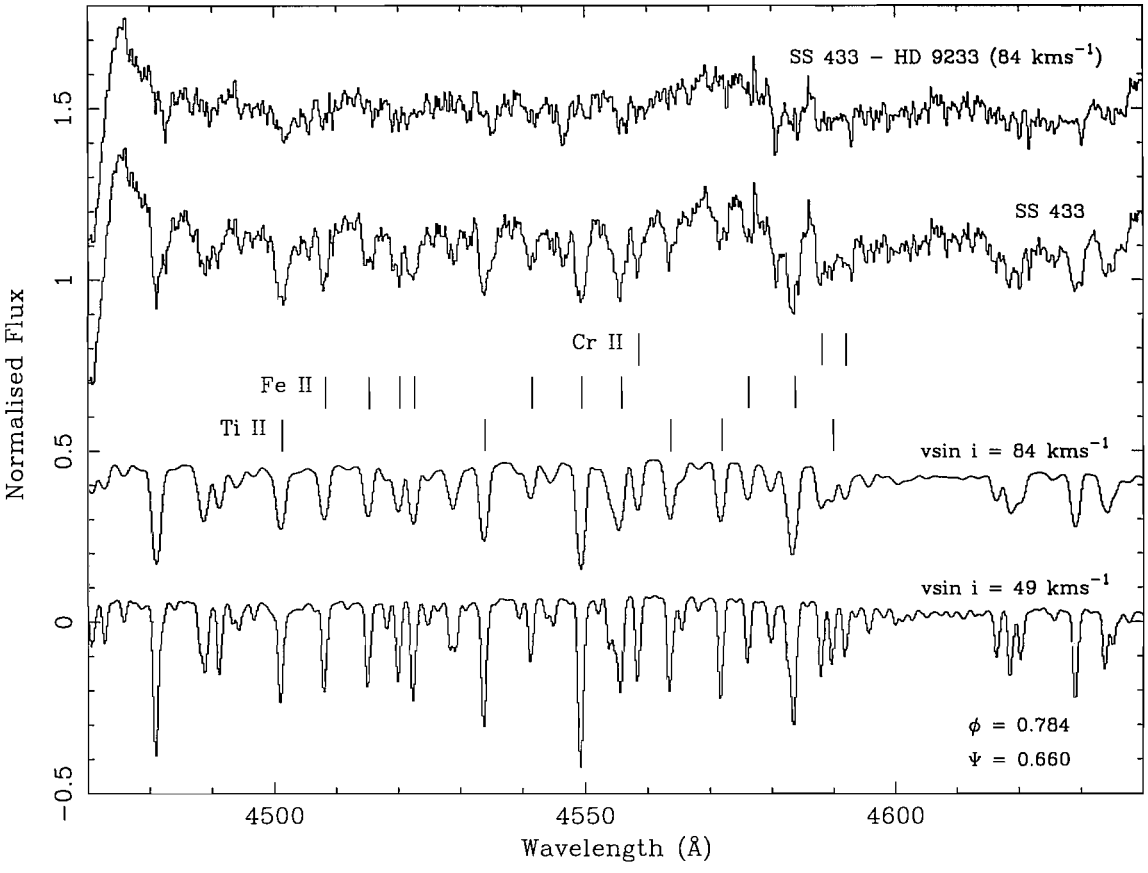

Figure 5.6: Average spectrum of SS 433 from 2004 June 29 ($\Psi_{prec} \sim 0.66$, $\phi_{orb} \sim 0.78$), together with the template star HD 9233 broadened by different amounts (below), and the residual of SS 433 - optimally broadened template (top).

5.3.1 Presence of an early-type spectrum in SS 433?

As can be seen in Fig. 5.6 ($\Psi_{prec} \sim 0.66$, $\phi_{orb} \sim 0.78$), we have a remarkable match between the SS 433 spectrum and the A4 Iab comparison star. All of the key absorption lines present in this region of the comparison star also manifest themselves in our spectrum of SS 433, though broader and somewhat shallower, as might be expected due to the continuum emission of the accretion disc. A χ^2 test on the residuals yields $v \sin i = 84 \pm 5$ km s^{-1}, whilst the depth of the lines are equivalent to an optimal scaling factor of 0.77 ± 0.04. Cross-correlating with the comparison star HD 9233 results in a velocity shift measurement of 6 ± 2 km s^{-1}.

Subtracting the optimally broadened template star from the average spectrum of SS 433 provides a remarkably clean residual spectrum (Fig. 5.6, top), with the only unusual features in the region of interest being the He I λ4471 P Cyg profile, and a blue-shifted jet line bump (He I λ4713) which has not been fully eliminated during the high-pass filtering process.

5.3.2 Narrow Absorption Lines

The spectrum displayed in Fig. 5.7 ($\Psi_{prec} \sim 0.85$, $\phi_{orb} \sim 0.14$) is also very rich in the A supergiant-like features identified by Hillwig et al. (2004), including many Fe II, Cr II and Ti II lines. However, it is immediately apparent even by eye that these absorption lines possess a much narrower and sharper profile (49 ± 4 km s^{-1} compared to 84 km s^{-1}) than those from the observation in Section 5.3.1.

The fractional contribution of 0.59 ± 0.04 is somewhat lower too, indicating that a large proportion of the light in this spectral region, at this particular time, may be produced elsewhere in the system, e.g. the accretion disc.

The family of absorption lines are slightly blue-shifted compared to the observation discussed in Section 5.3.1, with a velocity of -1 $\pm$ 5 km s^{-1}. If these lines are coming from the donor star then this is not the expected behaviour, which should have been close to its maximum blue-shift in the earlier observation, and approaching maximum red-shift at this orbital phase.

5.3.3 Double Absorption Lines

Even more anomalously, the spectrum from the following night ($\Psi_{prec} \sim 0.86$, $\phi_{orb} \sim 0.22$, Fig. 5.8) appears to possess absorption lines which are doubled (Fe II and Ti II), with a narrower red component blended with a broader, shallower blue. This feature is evident in each of the individual spectra from the night, and is not therefore the signature of some systematic error introduced when producing the average spectrum for the night.

Cross-correlating the data from this night against the A supergiant comparison star gives a velocity of -35 $\pm$ 4 km s^{-1}. This is again much bluer than expected, with the observation coinciding with the expected maximal red-shift of the donor star. However, the cross-correlation technique in this case fails to fit either of the apparent absorption components in this spectrum, instead picking out an average velocity of the two. Gaussians fitted individually to the red and blue features indicate velocities of -10 $\pm$ 10 and -100 $\pm$ 15 km s^{-1}. Neither component therefore possesses a velocity commensurate with the predicted behaviour of the donor star.

5.3.4 Absorption Line Velocities

Our data cover a broad range of orbital phases, and are displayed in Fig. 5.9 as diamonds. The three spectra discussed in Sections 5.3.1–5.3.3 are marked with

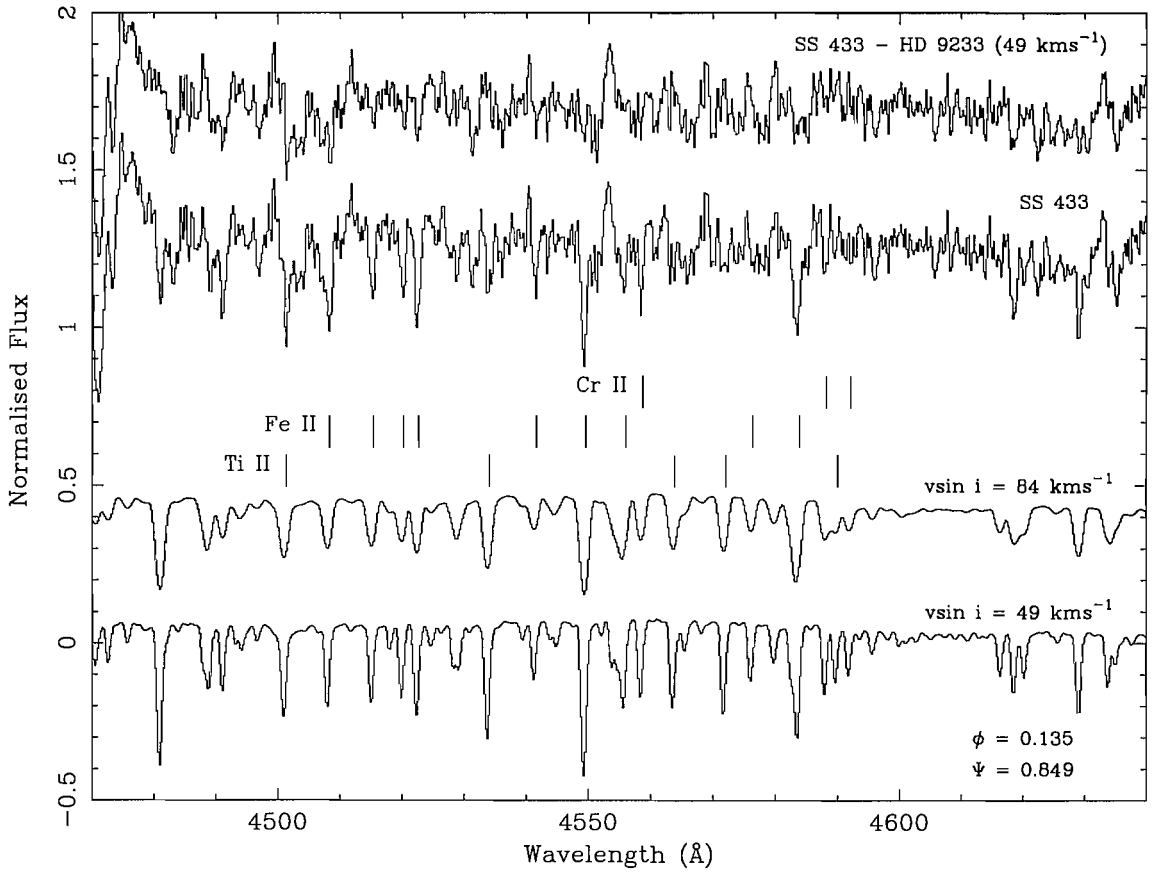

Figure 5.7: Average spectrum of SS 433 from 2004 July 30 ($\Psi_{prec} \sim 0.85$, $\phi_{orb} \sim 0.14$). The template star HD 9233 is shown below for comparison, broadened by different amounts, and the residual of SS 433 - optimally broadened template (top). The emission feature at $\sim$ 4475 Å is a component of the He I λ4471 P Cyg profile (see text).

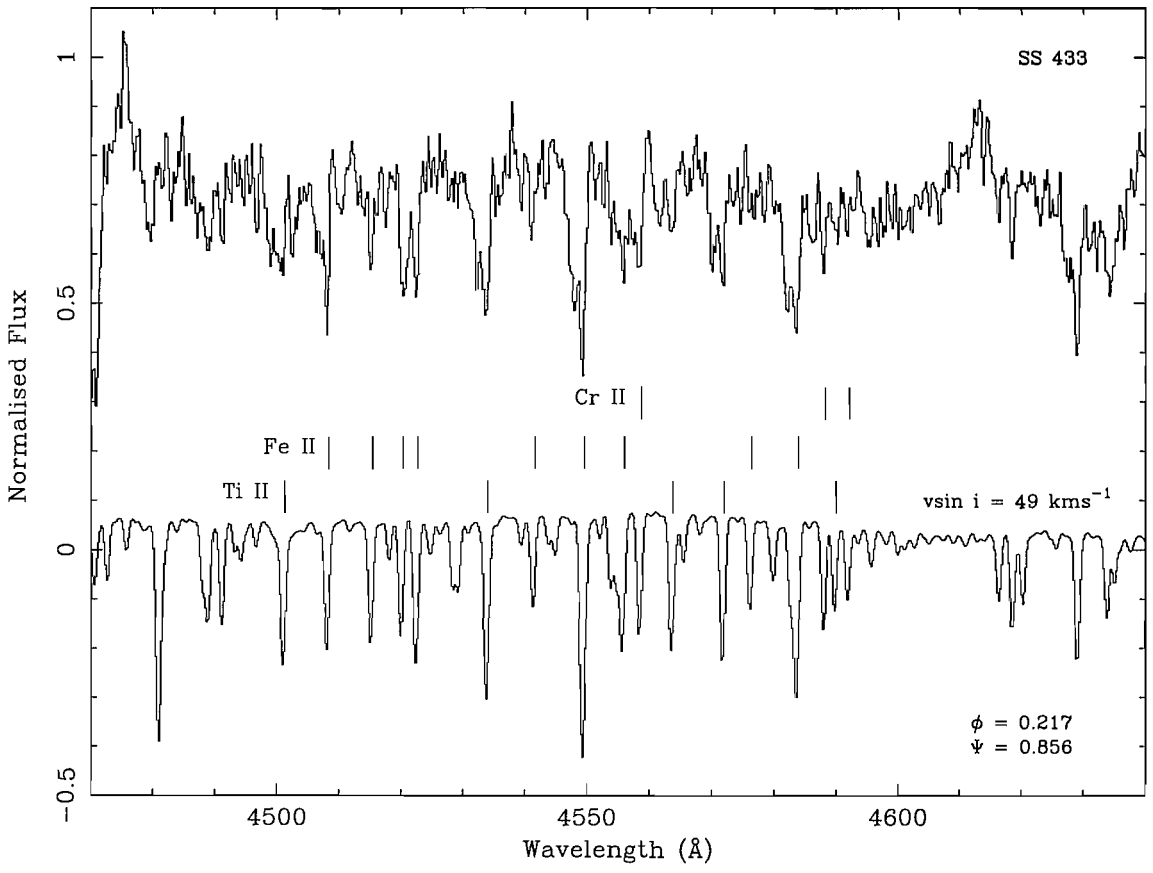

Figure 5.8: Average spectrum of SS 433 from 2004 July 31 ($\Psi_{prec} \sim 0.86$, $\phi_{orb} \sim 0.22$). Note in particular the doubled absorption lines of Fe II and Ti II. Again, the template star HD 9233 is shown for comparison below, broadened to the optimal value from the observations of the preceeding night.

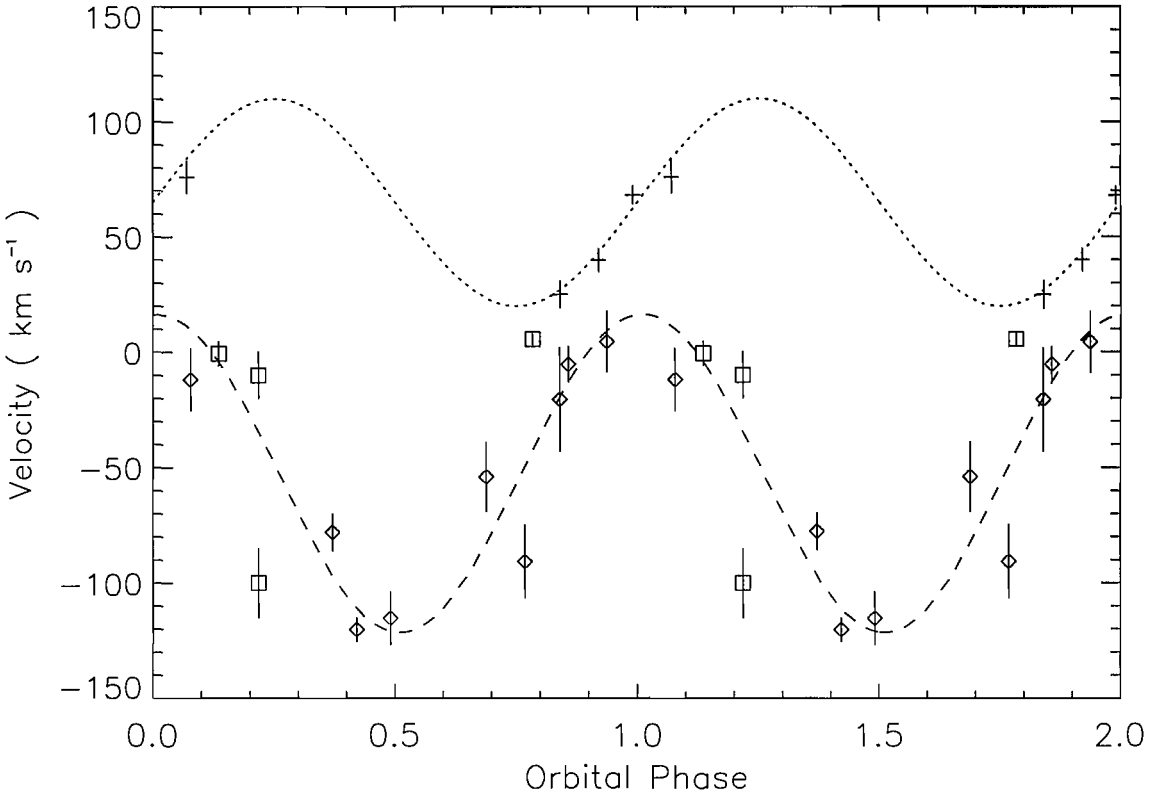

Figure 5.9: The radial velocities obtained via cross-correlation fitting in the λ4500–4600 Å region. The results obtained by Hillwig et al. (2004) are shown marked by pluses, together with their best-fitting sine curve (dotted line). The remaining points are the results of our own campaign, with those marked by squares representing the spectra selected for discussion in Section 5.3.1–5.3.3. The dashed line represents the best-fitting sine curve to these data. Note that two orbits have been plotted for clarity.

Table 5.5: Derived velocities of the Fe I absorption feature.

HJD -2450000	ϕ_{orb}	Ψ_{prec}	Velocity (km s^{-1})
3186.67	0.784	0.660	-27 ± 28
3187.63	0.857	0.666	-6 ± 28
3188.67	0.937	0.672	43 ± 28
3189.68	0.014	0.678	29 ± 28
3190.51	0.077	0.683	-62 ± 56
3191.63	0.163	0.690	-
3207.43	0.371	0.788	-
3217.43	0.135	0.849	-94 ± 60
3218.50	0.217	0.856	-48 ± 28

squares. Note that all the velocities used in this analysis were the result of cross-correlation with a comparison star, with the exception of the individual line fits discussed in Section 5.3.3. The results reported by Hillwig et al. (2004) are indicated by pluses, with the dotted line representing their best-fitting sine curve to these data. The best-fitting sine curve to our data is marked by a dashed line, with semi-amplitude K = 69 ± 4 km s^{-1}, systemic velocity γ = -53 ± 3 km s^{-1} and with velocity maxima occurring at orbital conjunction, 0.26 ± 0.01 out of phase with the motion of the accretion disc (Fabrika & Bychkova, 1990). This inconsistency is discussed in Section 5.4.

5.3.5 Low ionisation absorption lines

Cherepashchuk et al. (2005) suggest that observations in the λ4500–4600 Å region may result in false detections of the donor star due to contamination by the circumbinary outflow. Instead, low excitation lines such as Fe I should be better indicators, and this is what they used (in the λ4200–4340 Å region) for their own measurements. Unfortunately, there is a real paucity of clean, unblended, low excitation Fe I absorption lines in this region. For example, the Fe I λ4325 line features strongly in a large number of our spectra (and in our comparison star HD 9233), but there are Fe II features closely blended with it which make a measurement of the true Fe I line kinematics impossible. Using the spectral atlas of Deneb (Albayrak et al, 2003), spectral class A2 Iae, we were able to identify a suitable Fe I feature at λ4271. Whereas the low resolution spectrographs used by Cherepashchuk et al. (2005) were unable to resolve this line from the Cr II and Fe II features either side of it, this line appears cleanly in seven of the nine nights of data obtained from the WHT (see e.g. Fig. 5.10). The Calar Alto and INT observations, however, do not display this feature clearly.

Due to the need to disentangle the velocity of the low excitation Fe I line from the

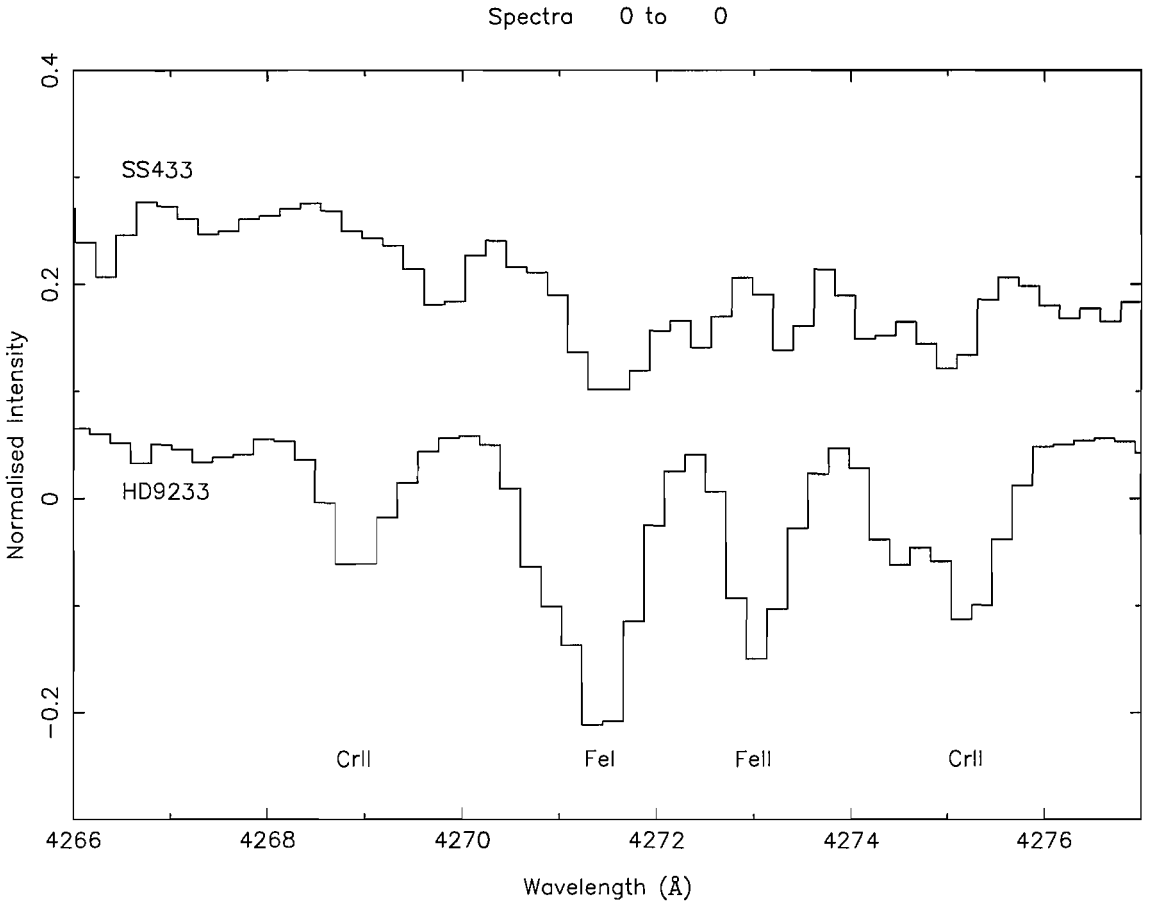

Figure 5.10: Spectra displaying the Fe I λ4271 absorption line in our comparison star HD 9233 (bottom) and in SS 433 (top). Also labelled are neighbouring absorption lines of the higher ionisation species Cr II and Fe II. The spectrum of SS 433 is taken from the night of 2004 June 29.

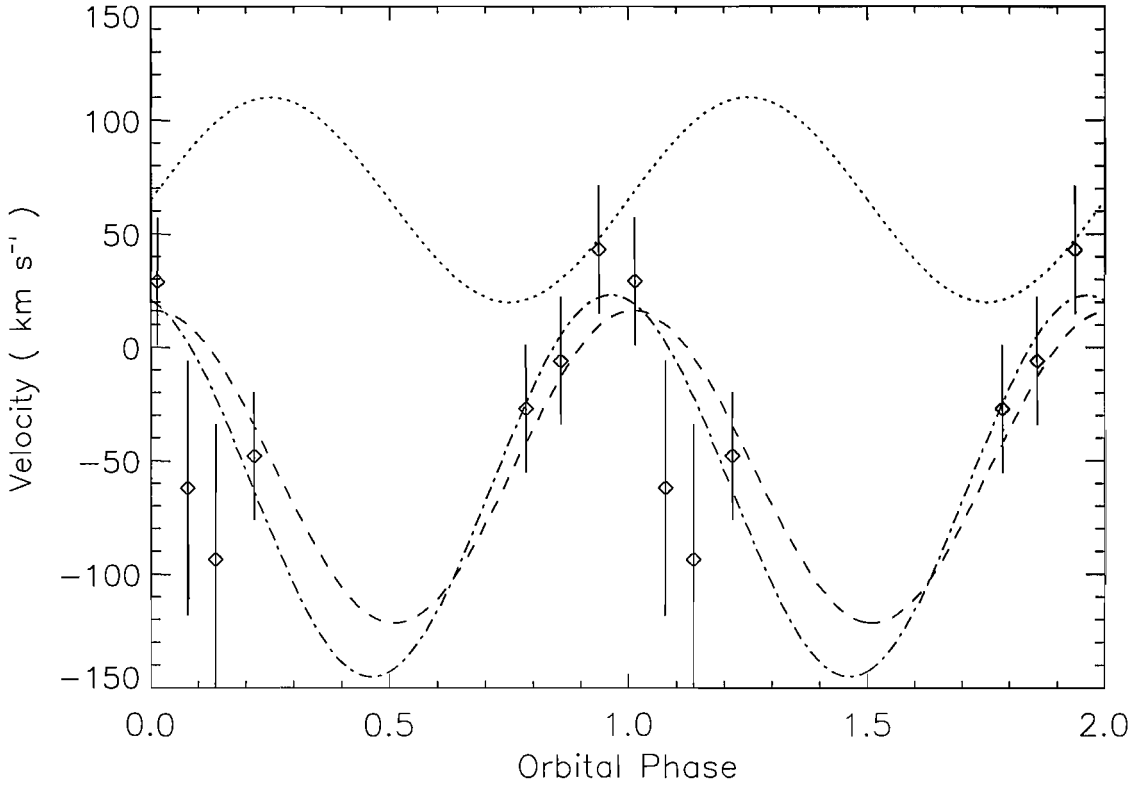

Figure 5.11: The radial velocities obtained from the Fe I λ4271 absorption line, together with the best-fitting sine curve to these data (dot-dashed line). The best-fitting sine curve obtained by Hillwig et al. (2004) is shown by the dotted line. The dashed line represents the best-fitting sine curve to our cross-correlated data from the λ4500–4600 Å region. Note that two orbits have been plotted for clarity.

higher excitation Fe II and Cr II lines, a simple cross-correlation with our comparison A supergiant spectrum is unsuitable. The weakness of these features precludes line profile fitting, and hence we have extracted velocity measurements by visual centering on the line, and comparing this with HD 9233. The errors are conservatively taken from our ability to define the line centre in each case. The results are shown in Table 5.5 and Fig. 5.11. The best-fitting sine curve to the Fe I absorption velocities is marked by the dot-dashed line, with semi-amplitude K = 84 $\pm$ 41 km s^{-1}, γ = -61 $\pm$ 30 km s^{-1} and with a phase offset = 0.287 $\pm$ 0.05. As for the λ4500–4600 Å region absorption line velocities (marked in Fig. 5.11 by a dashed line), the peak red-shifted velocity occurs close to orbital conjunction.

5.4 Analysis of the I-band spectra

In Fig. 5.12 we present spectra from ~8400-8900Å which have been ordered by time with both orbital and precessional phases indicated. A combination of low signal-to-noise ratio, contamination by telluric features and blending of Paschen series emission features precludes the useful interpretation of data shortwards of this spectral range. For brevity we omit presentations of the remaining spectral regions, noting that prominent emission was seen in both the O I 7774Å triplet (the blend of these lines precluding the extraction of any useful kinematic information) and He I 7065Å features, preventing the use of O I 7774Å as a spectral classification tool. Both transitions demonstrate pronounced P Cygni profiles during the course of the observations, with maximum blue shifted velocities for the emission and absorption components of He I 7065Å reaching -500 & -300 kms^{-1} respectively.

Previous lower signal-to-noise ratio and spectral resolution ~8-9000Å observations of SS433 by Filippenko et al. (1988) and Vermeulen et al. (1993) revealed a rich I-band emission spectrum, with contributions from both 'stationary' and moving emission lines. However, these spectra were of too low a S/N to detect the weak metallic absorption features expected for an A SG. Our spectra are superficially similar, showing strong emission in the H I Paschen series and O I 8446Å lines. However, we find differences in emission line profiles, while detecting weak metallic absorption lines for the first time.

5.4.1 The emission components

As seen at shorter wavelengths, the I-band spectrum of SS433 is found to be variable on a nightly basis. The presence of a broad jet emission feature - previously identified by Filippenko et al. (1988) - is suggested by the nightly variations in the 'continuum' longwards of ~8650Å. Subtraction of the respective spectra of SS 433 and the A4 Ia comparison star HD 9233 taken on the first night from the second night clearly indicates the variability is intrinsic to SS 433 (Fig. 5.12; lower 'panel').

The residuals for SS 433 also confirm the presence of night-to-night variability in the stationary lines of SS 433. The Paschen series lines demonstrate P Cygni profiles, rather than the double peaked profiles found by Filippenko et al. (1988). Pa13, 15 & 16 are potentially contaminated by adjacent Ca II transitions; their presence in both absorption and (P Cygni) emission are clearly revealed in the spectra obtained at ϕ=0.077, ψ=0.683 and ϕ=0.135, ψ=0.849 (note the doubled emission peak in the Pa13, 15 & 16 lines, indicating a blending with a P Cygni

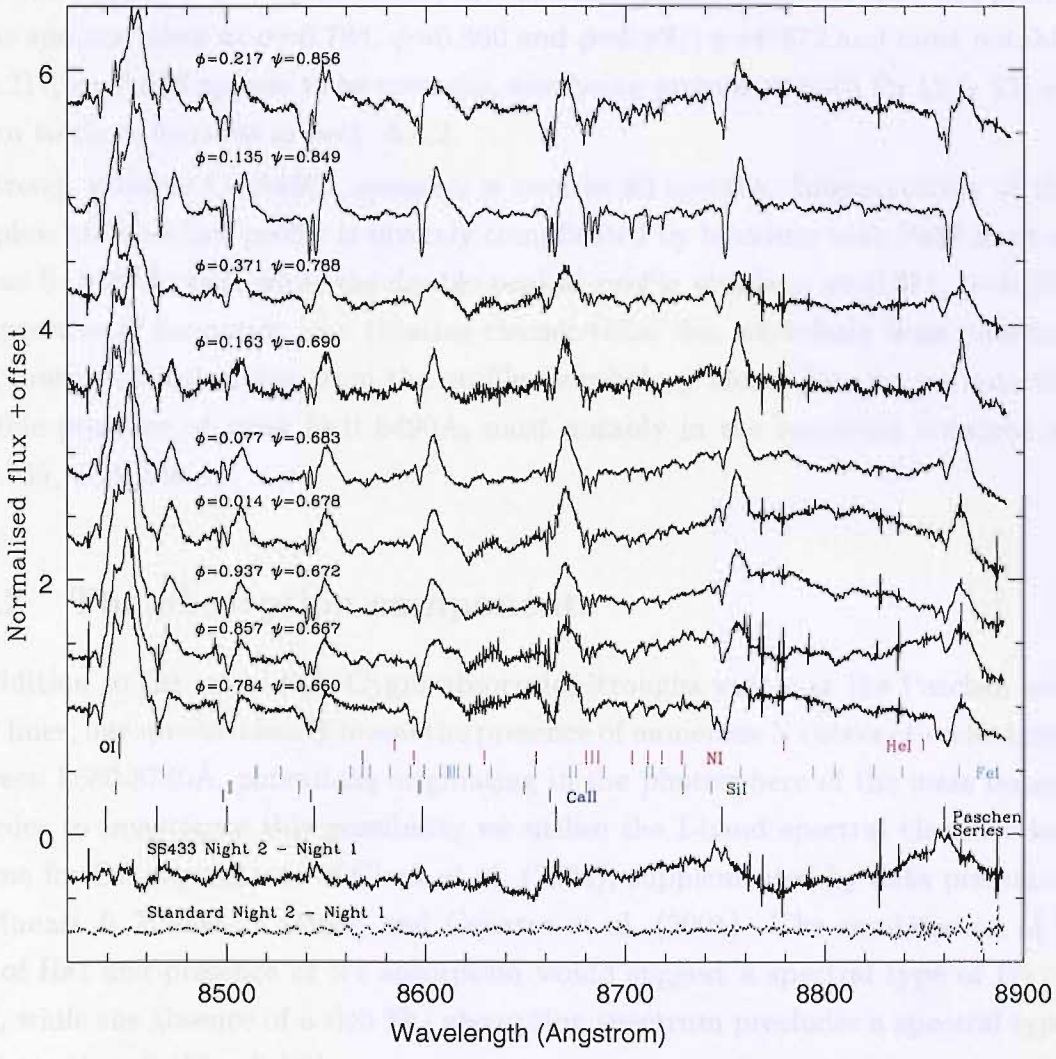

Figure 5.12: Plot of the ~8420-8900Å spectra of SS433 ordered by time, with the orbital and precessional phases indicated. The first six spectra were obtained on consecutive days, with 14, 10 and 1 day separating the final three spectra. Also presented are the residuals obtained after subtracting spectra of SS433 and the A4Ia template star HD9233 obtained on the first and second nights from each other (lower 'panel').

Ca II line profile), respectively. Furthermore, Pa 17 & 18 are blended with the broad O I 8446Å and the profiles of Pa 12 & 13 potentially suffer contamination from the broad jet feature. Consequently Pa 14 appears to be the most suitable transition for the extraction of kinematic information, although we note the presence of a weak N I transition at 8594Å. Nevertheless, the 'double troughs' visible in the Pa14 profile in the spectra taken at ϕ=0.784, ψ=0.660 and ϕ=0.937, ψ=0.672 and most notably ϕ=0.217, ψ=0.856 appear to be intrinsic, also being present in both Pa 12 & 13; we return to these features in Sect. 5.4.2.

Strong, variable O I 8446Å emission is seen in all spectra. Interpretation of the complex, variable line profile is severely complicated by blending with Pa17 & 18 as well as S I 8451Å; thus while the double peaked profile visible at ϕ=0.371, ψ=0.788 is suggestive of formation in a rotating circumstellar disc we refrain from inferring the presence of such a disc from the profile morphology alone. Finally, we note the possible presence of weak Fe II 8490Å, most notably in the spectrum obtained at ϕ=0.135, ψ=0.849.

5.4.2 The absorption components

In addition to the variable P Cygni absorption troughs visible in the Paschen and Ca II lines, our spectra clearly reveal the presence of numerous N I absorption features between 8680-8740Å, *potentially* originating in the photosphere of the mass donor. In order to investigate this possibility we utilise the I-band spectral classification scheme for OB supergiants of Clark et al. (2005), supplemented by data presented by Munari & Tomasella (1999) and Cenarro et al. (2001). The combination of a lack of He I and presence of N I absorption would suggest a spectral type of B5 or later, while the absence of a rich Fe I absorption spectrum precludes a spectral type any later than F (Fig. 5.4.2).

Sub-classification of A supergiants may in principle be accomplished via the (increasing) ratio of Ca II to Paschen series line intensity with decreasing temperature (Fig. 5.4.2), as well as a corresponding increase in strength of the N I absorption features from mid B to mid A spectral types. However, the Ca II and Paschen series in SS 433 are clearly subject to contamination from emission, while the N I lines are variable in intensity. Consequently, if the absorption lines were indeed photospheric in origin, we would be limited to a classification of ~B5-A5 supergiant - the low temperature limit provided by comparison of the maximum strength of the N I lines compared to Fe I) in the standard spectra (Fig. 5.4.2).

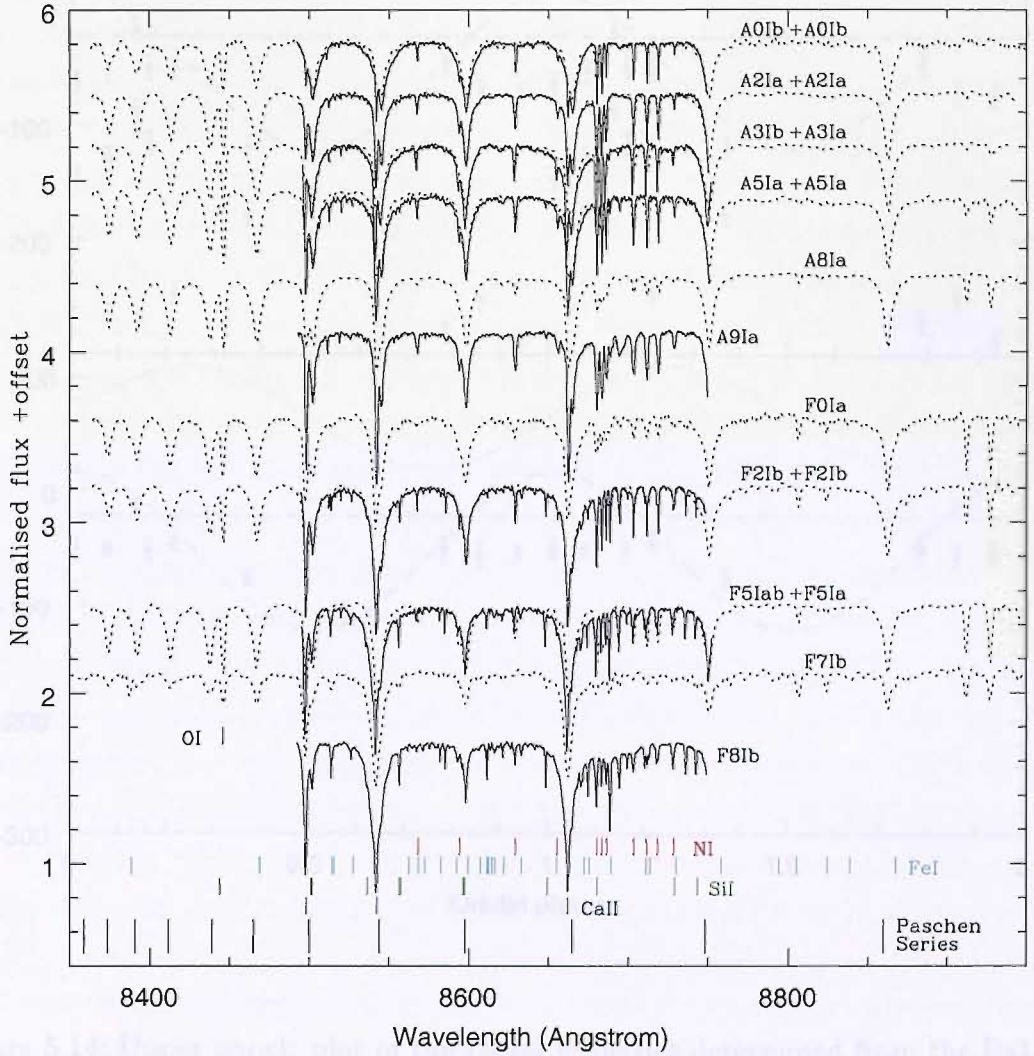

Figure 5.13: Montage of the A & F supergiant spectra presented by Munari & Tomasella (1999) and Cenarro et al. (2001).

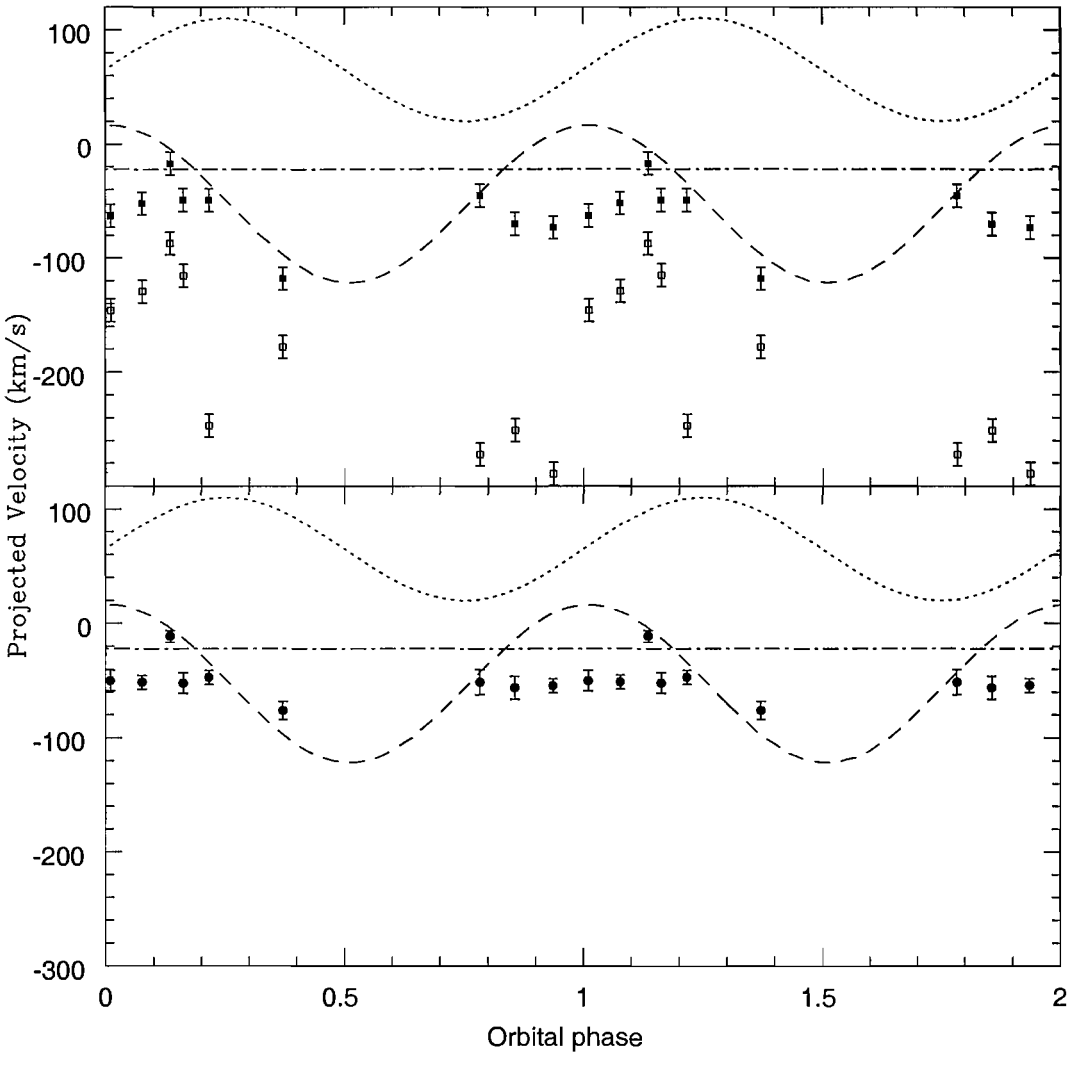

Figure 5.14: Upper panel: plot of the radial velocities determined from the Pa14 P Cygni profile against orbital phase, with the filled and open squares representing the wavelength of the central minimum and blue edge of the absorption profile respectively. The dotted and dashed sinusoids are the best fits to the radial velocities inferred from the ~4500-4600Å absorption features as presented by Hillwig et al. (2004) and Barnes et al. (2006), respectively. Finally, the dot-dashed line represents the systemic velocity of the SS 433 system determined from the He II line (Fabrika & Bychkova, 1990). Bottom panel: similar plot, with the radial velocity determined from the narrow N I absorption features between 8670-8620Å.

Moreover, if arising in the photosphere of the mass donor, we would expect to detect orbital modulation in their positions. In order to investigate this, the radial velocities of the N I features were determined via cross correlation with the spectrum of the A4 Ia star HD 9233 (c.f. Section 5.3) and plotted against orbital phase (Fig. 5.4.2). Physical interpretation of the Pa14 P Cygni profile is less straightforward, given that such profiles are the result of both large scale and turbulent motions. For unsaturated P Cygni profiles in OB stars Prinja et al. (1990) recommend determining the terminal velocity of the outflow by measuring the velocity asymptotically approached by the transient narrow absorption features due to wind substructure.

While we see evidence for additional absorption components (e.g the double troughed profiles at ϕ=0.784, ψ=0.660 and ϕ=0.217, ψ=0.856) and hence may infer substructure in the outflow, a lack of temporal resolution precludes such an approach for SS 433. Consequently, we chose to measure the central velocity of the absorption component(s) and the extreme violet edge of the profile (plotted against orbital phase in Fig. 5.4.2), noting that Prinja et al. (1990) find that the latter value overestimates the terminal velocity by ~20-25%.

It is apparent from Fig. 5.4.2 that there is no obvious orbital modulation of the radial velocities inferred from either the N I or Pa14 line profiles. Furthermore, we find that the velocities inferred from both species are blue-shifted with respect to the systemic velocities inferred for the compact object (from He II; Fabrika & Bychkova, 1990)) or the putative mass donor as determined by Hillwig et al. (2004).

We therefore conclude that these profiles arise in a dense, structured outflow and are not photospheric in origin. There is a strong similarity in absorption line profiles between the I- and B-band datasets, e.g. the double troughed absorption profiles visible in the Paschen and N II lines as well as the Fe II and Ti II lines in the blue (Section 5.3.3). However we note that orbital modulation is apparent in the weak metallic lines between ~4500-4600Å (Section 5.3.4); we are currently unable to explain this discrepancy.

5.5 Discussion

5.5.1 A model for SS 433

Gies et al. (2002b) and Hillwig et al. (2004) provide two constraints to increase the chances of observing the companion star. They state that the mass donor is ideally observed near the primary eclipse, when the accretion disc has precessed to its most

face-on position ($\Psi_{prec} \sim \phi_{orb} \sim 0$). The donor star would then have the highest chance of being positioned above and between any extended disc and an observer (Fig. 5.4*b*). Extending this idea, it should also be possible to detect the donor star at certain other combinations of phases when the donor is positioned between the extended disc and Earth. In Fig. 5.4*c* we show an example, with the companion being positioned clearly above the extended disc, whilst in Fig. 5.4*d* we have the inverse situation, with the companion star being totally obscured behind the extended disc. However, at this Ψ_{prec} the companion could become partially visible *below* the extended disc as it progresses through its orbit from $\phi_{orb} \sim 0.75$– 0.25. The extent to which we may be able to observe the companion will be determined by the opening angle and radial size of the extended disc, parameters which are currently not well constrained, in addition to the degree of irradiation of the inner face of the donor star from the accretion disc (Cherepashchuk et al., 2005).

If this scenario is correct, then observations of the companion star could provide direct information about the precession evident in the system. Many different mechanisms to drive the precession have been proposed over the years. In the 'slaved disc' model, the disc precession is slaved to the precession of the mass-losing star which has a spin axis that is misaligned with respect to the orbital axis. Alternatively, Lense-Thirring precession (Lense & Thirring, 1918) is a purely geometrical effect involving the rotation of local inertial frames relative to those of an observer at infinity. The slaved disc model predicts retrograde precession, whilst the Lense-Thirring effect would lead to a prograde sense of precession (Katz, 1981). More information about these models can be found in Leibowitz (1984) and Sarazin et al. (1980). Radiation-driven warping (Wijers & Pringle, 1999; Begelman et al., 2006) can be either prograde or retrograde depending upon whether the mass transfer stream feeds into the inner or outer disc. Confirming whether the precession is prograde or retrograde with respect to the donor could perhaps cast further light upon the physics driving the precession. Figs. 5.4 *e* & *f* represent the system alignment of the spectrum discussed in Section 5.3.1. It becomes clear that the companion star could only be visible above the disc at this combination of phases if the precession were prograde in nature. The extended disc would mask the donor in the case of retrograde precession.

The presence of the same supergiant-like features reported by Hillwig et al. (2004) in many of our spectra, at a range of different orbital and precessional phases, would at first glance seem to indicate that our data support this scheme. In particular, the observation discussed in Section 5.3.1 (where the accretion disc is close to edge-on,

$\Psi_{prec} \sim 0.66$, $\phi_{orb} \sim 0.78$) provides a hitherto unsurpassed match between an early-type comparison spectrum and SS 433 (Fig. 5.6). If these features really do originate upon the donor star, then the depth and strength of the lines are equivalent to a scaling factor of 0.77 ± 0.04. This would indicate a surprisingly high contribution to the total light at this combination of phases, compared to observations with the disc face-on, where Hillwig et al. (2004) find a fractional contribution of 0.36 ± 0.07.

We can compare our estimated scaling factor with that expected from observed light curves of SS 433 in a similar manner to Hillwig et al. (2004).

$$\frac{F_*}{F_{\phi,\Psi}} = \frac{F_{0.25,0} - F_{0.5,0}}{F_{\phi,\Psi}}$$

Here F_* is the total flux contributed by the unobstructed mass donor and $F_{\phi,\Psi}$ denotes the total observed flux from the system at orbital phase ϕ, precessional phase Ψ. The key assumption required is that the donor star is totally eclipsed by the disc at $\Psi_{prec} = 0$ and $\phi_{orb} = 0.5$, and at all other times both the donor and the accretion disc are contributing to the total light. The maximum donor contribution is assumed to occur at orbital phases $\phi = 0.25, 0.75$ when the donor will present its maximum geometrical area (see Section 1.4.3). We have used the V-band orbital light-curves of Zwitter et al. (1991), which cover a wide range of precessional phases. Higher quality orbital light curves have been published, but these do not cover the precessional phases in which we are interested. For example, the data of Goranskii et al. (1998) is limited to Ψ_{prec} ~0.85–0.15. The Zwitter et al. (1991) results imply a potential fractional contribution for the donor star of roughly 0.70 ± 0.15 at $\Psi_{prec} \sim 0.66$, $\phi_{orb} \sim 0.78$. Whilst this prediction appears to be consistent with our observational data, we must note that there is a large degree of scatter evident in the observed precessional light curves, introducing a degree of systematic error into these calculations. The calculations may also be affected by colour changes during the primary eclipse, the totality or otherwise of the donor eclipse by the accretion disc, and also by irradiation and distortion effects which may be observed at intermediate phases. Indeed, if we use the same method to predict the donor contribution at phase combination $\Psi_{prec} \sim \phi_{orb} \sim 0$ from the Zwitter et al. (1991) light curves, the resulting estimate proves to be higher by a factor of three than when using the Goranskii et al. (1998) data.

If we presume the absorption features noted in Section 5.3.1 to be a signature of the donor star, then retrograde precession may be immediately ruled out. However, the same features also occur in the spectra discussed in Sections 5.3.2–5.3.3. These

observations were performed at a phase combination where the donor should be obscured assuming prograde precession, and visible in the retrograde case. In addition to this apparent conflict, we must also account for the unusual velocity behaviour of these weak absorption features.

5.5.2 A disc wind origin for the B-band absorption lines?

Cross-correlating our B-band spectra of SS 433 with the A4 Iab spectrum produces a velocity curve (Fig. 5.9, γ = -53 $\pm$ 3 km s^{-1}) which is far removed in terms of systemic velocity from the value of 65 $\pm$ 3 km s^{-1} reported by Hillwig et al. (2004). It is, however, close to the result of Gies et al. (2002b), who reported a value of γ = -44 $\pm$ 9 km s^{-1}. Additionally, our best fitting sine curve is almost exactly a quarter out of phase with the Fabrika & Bychkova (1990) He II curve (where γ = -22 $\pm$ 14 km s^{-1}) which is presumed to trace the motion of the compact object. The behaviour of the absorption lines between λ4500–4600 Å is replicated by the low excitation Fe I λ4271 absorption line, one of a number of lines claimed by Cherepashchuk et al. (2005) to be an excellent tracer of the companion star.

The occurrence of a velocity maximum at orbital conjunction essentially precludes the possibility that these features were produced in the photosphere of the companion. A hotspot in the disc or the accretion stream itself could potentially generate some of the features observed in our spectra with a similar phasing. However, assuming a mass ratio of 0.2–0.3 (Cherepashchuk et al., 2005), and a disc that is near maximum radius, the gas stream–disc impact point would occur at a phase of around 0.06. In order to generate a spot at a phase of 0.25, the accretion stream would have to penetrate the disc to within a factor of many less than the tidal radius (Fig. 5.15). Considering the enormously high mass transfer rate in this system, this might well be possible. However, assuming the mass determinations of Hillwig et al. (2004) have some faint basis in reality, we calculate that the disc would possess a Keplerian velocity at this point of over 600 km s^{-1}. This is an order of magnitude higher than is observed in the absorption lines, and we therefore consider it extremely unlikely that these features are produced in a hotspot.

Whilst it is extremely difficult to pin down a particular region within the system which could produce this velocity signature, it is interesting to note that this behaviour has been reported before. Gies et al. (2002a) find the 'stationary' He I and Hα emission lines display a remarkably similar semi-amplitude and phasing to the A supergiant-like features investigated here. This is attributed to a clumpy wind out-

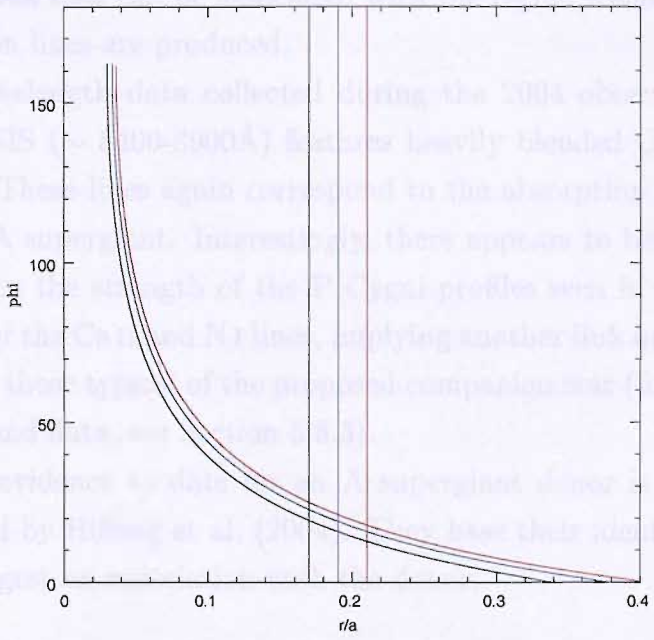

Figure 5.15: The ballistic stream trajectory for three different mass ratios that should bracket the true one: M_X/M_{donor} = 0.2 (black), 0.3 (blue), 0.4 (red). The x-ordinate is the distance (in units of binary separation) of the test particle from the accretor, the y-axis is the angle between the line of centres and the line connecting the accretor and the test particle. The vertical lines are estimates of the tidal radii for these mass ratios as obtained from Paczynski (1977). If the disk had near maximum radius, the stream–disk impact would occur around phi = 20 degrees (i.e. phase = 0.06) for all mass ratios.

flow from the accretion disc rather than the disc itself or to a gas stream (Goranskii et al., 1997; Gies et al., 2002a). Although there is a large disparity in line widths between the stationary emission lines and our narrow absorption lines, if what we observe in SS 433 is a structured outflow then we would expect to see narrow absorption components from localised density enhancements in the wind. This would appear to indicate that for at least some combinations of orbital and precessional phases the A supergiant 'photospheric' features arise not from the donor but instead from a localised area that can be associated with the region where the He I and Hα stationary emission lines are produced.

The longer wavelength data collected during the 2004 observing campaign in La Palma with ISIS ($\sim$ 8400-8900Å) features heavily blended Ca II and weak N I absorption lines. These lines again correspond to the absorption features expected for an early-mid A supergiant. Interestingly, there appears to be a strong positive correlation between the strength of the P Cygni profiles seen in the Paschen lines and the strength of the Ca II and N I lines, implying another link between traditional wind features and those typical of the proposed companion star (for more discussion regarding the I-band data, see Section 5.5.3).

The strongest evidence to date for an A supergiant donor is considered to be the data presented by Hillwig et al. (2004). They base their identification on three criteria which suggest an association with the donor:

- the radial velocity curve characteristics
- the absorption line depths
- the absorption line width

However, their data do not cover the key phases when there should be a turnover in velocity space ($\phi_{orb} \sim 0.25, 0.75$), which would unambiguously associate the lines with the donor. Interestingly, a number of our own spectra which can be clearly associated with an outflow also meet at least two of the above criteria (see Table 5.2), with only the velocity curve excluding an association with the donor.

The systemic velocity of 65 $\pm$ 3 km s^{-1} reported by Hillwig et al. (2004) is troubling, being far removed from the value found by Fabrika & Bychkova (1990) for the He II λ4686 emission line (-22 $\pm$ 14 km s^{-1}). This feature is widely presumed to originate in the inner regions of the accretion disc, and hence should presumably possess a similar systemic velocity to the companion star. Hillwig et al. (2004) attempt to explain this anomaly by claiming that the He II could be produced far

away from the centre of the system, although if this were true then it would be invalid to use it as a tracer of the compact object and thus for calculating the individual object masses.

Furthermore, we note that gas filaments on either side of the associated supernova remnant W 50 are found to possess a systemic velocity of 67 $\pm$ 6 km s^{-1} (Mazeh et al., 1983). Considering the substantial mean birth velocity of pulsars, perhaps as high as $\sim$ 500 km s^{-1} (Lorimer et al., 1997), it seems rather unlikely (although not impossible) that such an allegedly low mass compact object ($\sim 3M_{\odot}$, Hillwig et al., 2004) would have received no kick during the supernova. However, recent work has highlighted a dichotomous distribution in neutron star kick velocities, with one population possessing a much lower mean kick velocity of $\sim$ 30 km s^{-1} (Podsiadlowski et al., 2004). Whilst this value is still substantially larger than the offset noted by Hillwig et al. (2004) between W 50 and SS 433, it is impossible to definitively rule out the possibility of a low kick velocity in this case.

The large offset between the systemic velocity detected by Hillwig et al. (2004) and in our data could be a potential problem for a purely circumbinary outflow origin for the absorption lines. However, this velocity offset could be explained by a considerable cycle-to-cycle variation in the semi-amplitude of the 'stationary' emission lines originating in the accretion disc wind (Gies et al., 2002a). Another problem could be the doubled absorption lines shown in Fig. 5.8. This could perhaps be indicative of two entirely separate regions with identical spectral signatures, though neither component corresponds to a possible donor star origin. It seems more likely that two different components of a clumpy wind outflow could concurrently pass through the line-of-sight, as proposed by Gies et al. (2002a) and Lépine et al. (2000).

5.5.3 What can the I-band data tell us?

A synthesis of multiwavelength observations shows the circumstellar environment of SS 433 to be highly complex, supporting emission and absorption from atomic species with a wide range of excitations in numerous physically distinct regions (accretion disc, relativistic jet and accretion driven outflow). Unfortunately, due to the presence of multiple ionising sources and - as we argue below - aspherical mass outflow we are unable to quantitatively determine the mass loss rate of SS 433 via a non-Local Thermodynamic Equilibrium (non-LTE) model atmosphere code, and instead must proceed in part by analogy to other systems.

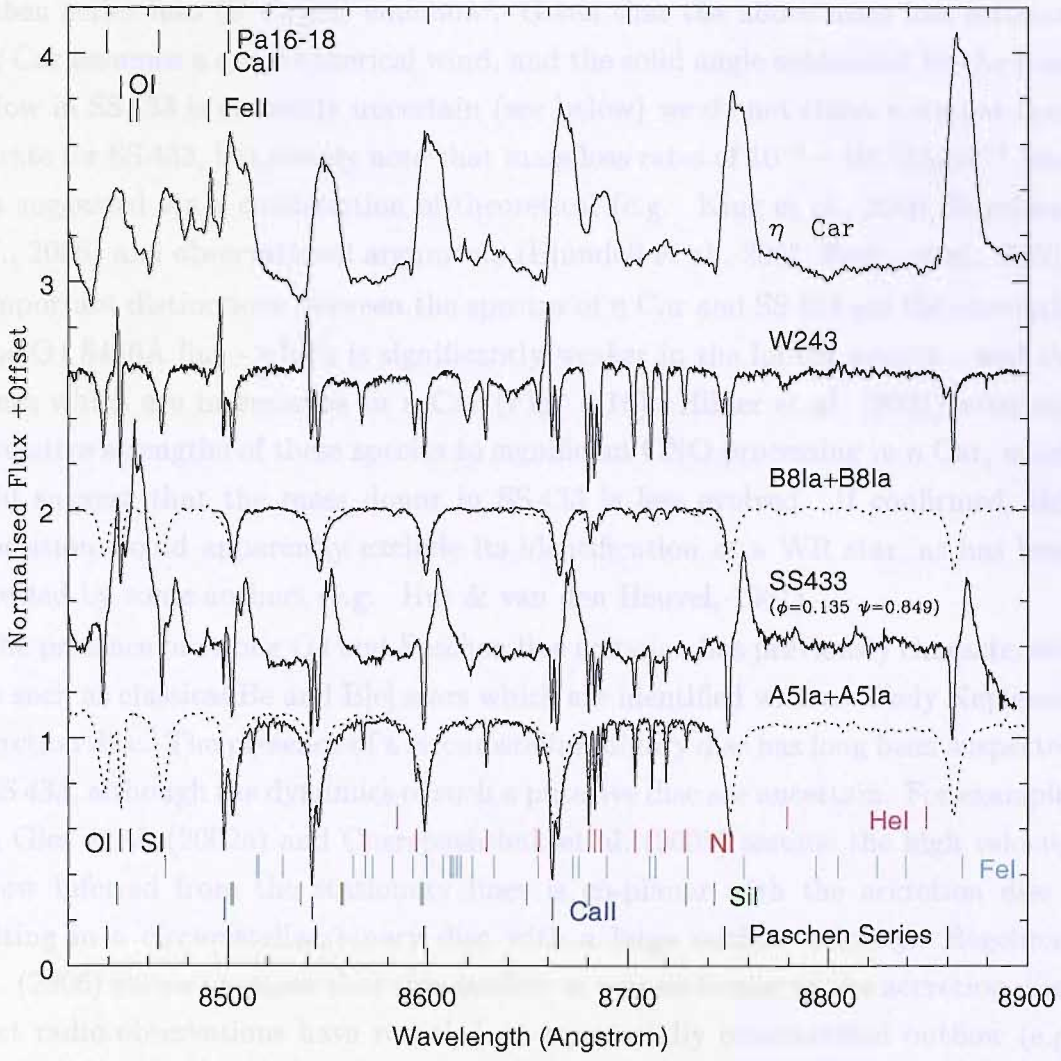

Figure 5.16: Comparison of a representative spectrum of SS 433 against B8 Ia and A5 Ia spectroscopic standards spectra and the LBVs W 243 and η Carinae.

Following previous studies, the presence of P Cygni emission profiles in the Paschen series and Ca II lines indicate significant mass loss from the system. To the best of our knowledge the only other stellar source which demonstrates such line profiles is the Luminous Blue Variable (LBV) η Carinae (Fig. 5.16), which is characterised by a uniquely high mass loss rate ($\sim 10^{-3} M_{\odot} yr^{-1}$; Hillier et al., 2001); presumably mass loss rates for other LBVs such as W 243 are insufficient to drive the Paschen series into (P Cygni) emission[2]. Given that the above mass loss estimate for η Car assumes a quasi-spherical wind, and the solid angle subtended by the mass outflow in SS 433 is currently uncertain (see below) we do not claim a similar mass loss rate for SS 433, but simply note that mass loss rates of $10^{-4} - 10^{-3} M_{\odot} yr^{-1}$ have been suggested via a combination of theoretical (e.g. King et al., 2000; Begelman et al., 2006) and observational arguments (Blundell et al., 2001; Fuchs et al., 2006).

Important distinctions between the spectra of η Car and SS 433 are the strengths of the O I 8446Å line - which is significantly weaker in the former system - and the N lines which are in emission in η Car (Fig. 5.16). Hillier et al. (2001) attribute the relative strengths of these species to significant CNO processing in η Car, which would suggest that the mass donor in SS 433 is less evolved. If confirmed, this supposition would apparently exclude its identification as a WR star, as has been suggested by some authors (e.g. Hut & van den Heuvel, 1981).

The presence of strong O I and Paschen line emission has previously characterised stars such as classical Be and B[e] stars which are identified with a - likely Keplerian - excretion disc. The presence of a circumstellar/binary disc has long been suspected for SS 433, although the dynamics of such a putative disc are uncertain. For example, both Gies et al. (2002a) and Cherepashchuk et al. (2005) assume the high velocity outflow inferred from the stationary lines is co-planar with the accretion disc - resulting in a circumstellar/binary disc with a large outflow velocity. Begelman et al. (2006) instead assume that this outflow is perpendicular to the accretion disc. Direct radio observations have revealed an equatorially concentrated outflow (e.g. Blundell et al., 2001)), albeit at large ($>10^2$ AU) distances from the binary and with outflow velocities (5-10,000kms^{-1}; Mioduszewski et al., 2004) significantly in excess of those inferred from the stationary emission lines of SS 433.

While the presence of a double peaked O I 8446Å line profile in several spectra (e.g. ϕ=0.371, ψ=0.788) is suggestive of a rotating disc, we caution against such a

[2]Emission in the Paschen series is observed in classical Be stars; however this is thought to arise in quasi Keplerian discs and hence does not yield a P Cygni profile. Likewise emission is observed for H-rich WNL stars although current observations are of insufficient resolution to resolve the line profile (e.g. Vreux et al., 1989).

conclusion based solely on the current dataset. This is due to both the significant short- and long-term variability seen in the line profile (e.g. the departure from a double peaked profile reported by Filippenko et al., 1988) and the possibility that the central depression may result from absorption by intervening material along the line of sight. Instead we confine ourselves to the conclusion that the O I emission arises from a cooler, highly structured region that is kinematically distinct from that responsible for the stationary emission lines of H I and C II.

However, in light of the above, the discovery of an IR excess due to dust associated with SS 433 (Fuchs et al., 2006) is of considerable interest. Dust production in hot, UV rich circumstellar environments is particularly difficult; indeed to the best of our knowledge no single massive OB star *with a quasi spherical stellar wind* has been observed to form dust. This is because the two criteria for dust formation - a gas temperature lower than the dust sublimation temperature (~2000K) and a sufficiently high density of the growth species (c.f. Porter, 2003) - are difficult to satisfy simultaneously in a radially accelerating stellar wind. To date the sole examples of dust formation in the outflow of a single massive star are the supergiant B[e] stars which are characterised by the presence of a high density equatorial disc, and we therefore suspect that the dust in SS 433 resides in some form of circumbinary disc.

In support of this hypothesis, we note that dusty circumbinary discs appear to be associated with post-AGB stars in binary systems (De Ruyter et al., 2006), while the massive overcontact binary RY Scuti is associated with a cool (~400K) dusty circumbinary disc/torus (Gehrz et al., 2001), which Smith et al. (2002) suggest was formed by mass loss through the outer Lagrangian points. The dynamics of such a putative circumbinary disc around SS 433 are uncertain but, by analogy to the discs associated with post-AGB stars, we might expect dust in a quasi-Keplerian disc to show evidence of processing (where the molecular structure of the dust has changed e.g. it has melted and then resolidified) and/or dust grain growth; thus further IR-mm observations may enable the kinematics to be determined[3]. The high velocity inferred for the radio 'ruff' might be thought to exclude the possibility of a quasi-Keplerian disc. However, we note that the radio outflow is observed at much larger distances than such a putative disc.

[3]In a steady Keplerian disc, the dust grains will have the opportunity to merge, forming larger grains/molecules. These larger grains will effectively emit as a blackbody. In a constant outflow, the grains possess a much lower interaction cross-section, and thus the grains do not have the opportunity to grow. Emission from these smaller grains will be apparent in IR-mm observations.

5.6 Conclusions

Our series of high-resolution B-band (~4000-5000Å) spectra of SS 433 clearly display numerous typical A supergiant photospheric features , the presence of which have been reported by several authors and attributed to a putative mass donor. Indeed, these spectra are the best evidence yet for anything like normal stellar photospheric features in SS 433. However, the velocities of these features do not correspond to the expected motion of the mass donor, but rather to the Hα and He I 'stationary' emission lines noted by Gies et al. (2002a) and assumed to originate in a clumpy, accretion-driven outflow.

We have also obtained high spectral resolution and S/N I-band (8200-8800Å) observations of SS 433 in order to search for any photospheric signatures of the mass donor. While we have detected weak N I absorption features, which are characteristic of supergiants of spectral type B5 or later, we find no evidence of systematic variability in their radial velocities that would characterise orbital motion. By analogy to the B-band features, we assume these arise in an accretion driven outflow. Strong, variable P Cygni emission profiles are observed in the Paschen series, suggestive of a highly structured outflow. O I emission is observed, the difference in line profile suggesting that it arises in an outflow that is kinematically distinct from that responsible for the Paschen series.

Comparison of the spectra to other mass losing stars implies an extremely high mass loss rate for SS 433, suggesting that continuum rather than line opacity is responsible for driving the outflow (e.g. Owocki et al., 2004, however such a mechanism will not generate the $\sim 10^4 \mathrm{kms}^{-1}$ implied for the radio emitting equatorial 'ruff'). We note that while neither the emission nor the absorption features in our spectra appear to be associated with the mass donor, the strong O I emission apparently excludes the presence of a Wolf-Rayet mass donor since we should expect significant oxygen depletion due to CNO burning (and subsequent H depletion in more evolved stars).

By analogy to both low- and high-mass binaries, the presence of a mid-IR excess detected by Fuchs et al. (2006) suggests the possibility of a cool circumbinary disc within which dust may form. If present, the inter-relationship of the different emission regions - accretion disc, accretion driven outflow(s), circumbinary disc and high velocity equatorially concentrated outflow - is unclear, although we might hope to infer the kinematics (radial outflow versus quasi-Keplerian rotation) from the dust properties.

Returning to the putative nature of the mass donor in this system, although the extremely limited observations of Hillwig et al. (2004) are suggestive of an A supergiant-like donor, we cannot exclude the possibility that these features originate from the same highly variable accretion-driven wind which produces the B-band absorption features noted in this chapter. If these lines are consistent over a number of observations at $\Psi_{prec} \sim \phi_{orb} \sim 0$ then it would seem likely that they are indeed a true signature of the donor. In this case the large off-set in systemic velocity between the Hillwig et al. (2004) data and ours could be due to the velocity of the outflow towards our line of sight. However, if the lines originate exclusively in some form of outflow, then we would expect them to be rather variable in terms of width, depth, shape and velocity. It is certainly intriguing that past observations of similar A supergiant-like features have led to such an extraordinarily broad range of mass estimates (Gies et al., 2002b; Hillwig et al., 2004; Cherepashchuk et al., 2005, see Table 5.1). In any case, considerable care must be taken to correctly interpret these features and thus determine the nature of the stellar components within the SS 433 system.

Chapter 6

Conclusions and Future Work

This thesis illustrates the value of high-resolution, phase-resolved optical spectroscopy to the study of X-ray binaries. Chapter 3 has utilised such observations of the Bowen fluorescence blend ($\sim \lambda\lambda$4630–50) in combination with the technique of Doppler Tomography to trace for the first time the motion of the donor star within the low mass X-ray binary system (LMXB) XB 1254–690. In combination with measurements tracing the motion of the compact object, true dynamical mass constraints for both the compact object and the donor star have been derived.

High-resolution spectroscopy of the Bowen blend in a number of other LMXBs has also proved successful in unveiling the kinematics of these systems. The ten systems studied thus far are presented together for the first time in Chapter 4. With our knowledge of the kinematics of these systems, it is simple to shift the high-resolution spectra of these systems into the rest-frame of the donor star. This allows for the measurement of the abundances of carbon and nitrogen in the outer layers of the donor star in each system. The ratio of these two elements is a powerful indicator for the evolutionary status of the system, in particular the level of nuclear processing which has occurred in the donor star.

We find evidence suggesting that two systems in particular, Aql X–1 and GX 339–4, are highly evolved. On the other hand, GX 9+9 is exceptional in possessing a nitrogen-to-carbon ratio of less than one. The remainder of the sample cluster around similar, intermediate ratios of carbon and nitrogen, regardless of their birth environment. This suggests a common level of evolution in these systems. However, there is currently not enough evidence to determine whether these systems are descended from intermediate- or low-mass progenitors. If they do eventually prove to be the descendants of intermediate-mass progenitors, then this small sample of LMXBs will be in remarkable agreement with the theoretical Galactic population

predictions of Pfahl et al. (2003).

One system for which studies of the Bowen blend have proven unfruitful in the detection of the donor star is SS 433. However, recent phase-limited B-band observations of this source by several different authors have provided tantalising glimpses of absorption features reminiscent of the photosphere of a mid-A type supergiant star. Furthermore, these features appeared to move in phase with the expected motion of the donor star, prompting speculation that this was the first glimpse of the normal stellar component in this mysterious object.

In Chapter 5 we present a series of high-resolution B-band spectra across a broad range of orbital phases. These spectra are the best evidence yet for anything approaching normal stellar photospheric features in SS 433. However, the velocities of these features do not correspond to the expected motion of the mass donor, but rather to a set of emission lines which are assumed to originate in a clumpy, accretion-driven outflow. Absorption features common to early type supergiants are also observed in I-band spectra, but as with the B-band features cannot be associated with the donor star on account of their radial velocity variations. Significant O I emission in the I-band should rule out the possibility of a Wolf-Rayet mass donor however.

6.1 Future potential

For each of the scientific chapters, the next obvious steps in the work have been suggested at the end of the chapter. For example, the Doppler maps presented in Chapter 3 possess some unusual and unexplained features. Some of these features have also been noted in the Doppler maps of other LMXBs, and rigorous theoretical modelling is required to indicate which physical region is producing this emission. This may have interesting implications for our knowledge of the accretion process and disc formation.

The mass constraints applied to XB 1254–690 in Chapter 3 are somewhat broad, such that we may not differentiate between the presence of a main sequence-like or over-massive, evolved donor star. This is a result of pushing the limits of currently achievable signal-to-noise ratios in high-resolution spectroscopy whilst retaining suitable levels of temporal resolution. As technology improves, further observations of the same source should drastically improve these constraints. This will have particular relevance to the results of Chapter 4. Here, we can see that a number of systems including XB 1254–690 possess an intermediate value for the nitrogen-to-

carbon ratio of a little over unity. However, using only the current dataset does not provide sufficient information to indicate whether this ratio implies the presence of an evolved or main sequence-like donor star. Tighter mass constraints should solve this puzzle and help to improve our understanding of the formation and evolution of LMXBs as a population.

An alternative approach would be to obtain observations of globular cluster sources (for example AC 211 in M 15) using the Bowen fluorescence technique. These LMXBs are believed to evolve differently to those found in the Galactic field, and as a result could be very useful in distinguishing low mass from intermediate mass systems.

The focus of Chapter 5, SS 433, remains as one of the most mysterious objects within the Galaxy and interest in it is unlikely to fade at any time in the near future. Indeed, a series of high-resolution blue spectroscopy using the SALT facility in South Africa, and covering *all* combinations of orbital and precessional phases is planned for the next few years. In particular, these new observations should finally resolve the question of whether or not the donor star rather than a circumbinary outflow can indeed be detected at a particular, limited combination of orbital and precessional phases. Another important question is the nature, or more specifically the kinematics, of the circumbinary material which obscures the donor at most (if not all) phases. It is hoped that mid-IR observations will provide the answer, allowing a radial outflow to be distinguished from a quasi-Keplerian disc.

Bibliography

Abell G.O., Margon B., 1979, *Nature*, 279, 701

Albayrak B., Gulliver A.F., Adelman S.J., et al., 2003, A&A, 400, 1043

Al-Naimy, H. M. 1978, Ap&SS, 53, 181

Antokhina E.A., Cherepashchuk A.M., 1985, SvAL, 11, 4A

Augusteijn T., van der Hooft F., de Jong J.A., et al., 1998, A&A, 332, 561

Balbus S.A., Hawley J.F., 1991, ApJ, 376, 214

Barnard R., Church M.J., Balucinska-Church M., 2003, A&A, 405, 237

Barnes, A. D., Caseres, J., Charles, P. A., Clark, J. S., Cornelisse, R., Knigge, C., Steeghs, D., 2006, MNRAS, 365, 296

Barret D., 2001, Advances in Space Research, 28, 307

Barziv O., Kaper L., van Kerkwijk M.H., et al., 2001, A&A, 377, 925

Bath G.T., 1975, MNRAS, 171, 311

Begelman M.C., Hatchett S.P., McKee C.F., et al., 1980, ApJ, 238, 722

Begelman M.C., King A.R., Pringle J.E., 2006, MNRAS, 370, 399

Bethe H.A., 1939, Phys. Rev., 55, 434

Binney J., Tremaine S., *Galactic Dynamics*, Princeton University Press, 1987

Blundell K.M., Mioduszewski A.J., Muxlow T.W.B., Podsiadlowski P., Rupen M.P., 2001, ApJ, 562, L79

Blundell K.M., Bowler M.G., 2004, ApJ, 616, L159

Boerner G., Meszaros P., 1979, A&A, 77, 178

Boirin L., Diaz Trigo M., Mendez M., Parmar A.N., Kaastra J.S., 2005a, to appear in the proceedings of 'The X-ray Universe 2005', San Lorenzo de El Escorial (Spain), 26-30 September 2005, astro-ph/0511191

Boirin L., Mendez M., Diaz Trigo M., Parmar A.N., Kaastra J.S., 2005b, A&A, 436, 195

Bolton C.T., 1972, *Nature*, 240, 124

Bowen I., 1934, PASP, 46, 146

Bowen I., 1935, ApJ, 81, 1

Bradshaw C.F., Fomalont E.B., Geldzahler B.J., 1999, ApJ, 512, L121

Bradt H.V.D., McClintock J.E., 1983, ARA&A, 21, 13

Brown G.E., Bethe H.A., 1994, ApJ, 423, 659

Buxton M., Vennes S., 2003, MNRAS, 342, 105

Callanan P.J., Charles P.A., van Paradijs J., et al., 1990, A&A, 240, 346

Casares J., Charles P.A., 1994, MNRAS, 271, L5

Casares J., Marsh T.R., Charles P.A., et al., 1995, MNRAS, 274, 565

Casares J., Charles P.A., Kuulkers E., 1998, ApJ, 493, L39

Casares J., Steeghs D., Hynes R.I., Charles P.A., O'Brien K., 2003, ApJ, 590, 1041

Casares J., Cornelisse R., Steeghs D., et al., 2006, MNRAS, submitted

Cenarro, A. J., Cardiel, N., Gorga, J., et al., 2001, MNRAS, 326, 959

Chakrabarty D., Bildsten L., Finger M.H., et al., 1997, ApJ, 481, L101

Charles P.A., Booth L., Densham R.H., et al., 1983, MNRAS, 202, 657

Charles, P.A. & Seward, F.D., *Exploring the X-Ray Universe*, Cambridge University Press, 1995

Charles P.A., Coe M.J., 2003, To appear in *Compact Stellar X-Ray Sources*, eds. W.H.G. Lewin and M. van der Klis, Cambridge University Press, astro-ph/0308020

Cherepashchuk A.M., Aslanov A.A., Kornilov V.G., 1982, Sov. Astron., 26, 697

Cherepashchuk A.M., Sunyaev R.A., Fabrika S.N. et al., 2005, A&A, 437, 561

Chevalier C., Iloviasky S.A., 1991, A&A, 251, L11

Christian D.J., Swank J.H., 1997, ApJS, 109, 177

Church M.J., Dotani T., Balucinska-Church M., et al., 1997, ApJ, 491, 388

Church M.J., Balucinska-Church M., 2001, A&A, 369, 915

Church M.J., Balucinska-Church M., 2004, MNRAS, 348, 955

Clark D.H., Green A.J., Caswell J.L., 1975, *Aust. J. Phys. Astrophys. Suppl.*, 37, 75

Clark D.H., Murdin P., 1978, *Nature* 276, 45

Clark, J. S., Negueruela, I., Crowther, P. A., Goodwin, S. P., 2005, A&A, 434, 949

Conti P.S., 1978, A&A, 63, 225

Cook G.B., Shapiro S.L., Teukolsky S.A., 1994, ApJ, 424, 823

Corbet R.H.D., Laycock S., Coe M.J., Marshall F.E., Markwardt C.B., 2004, AIPC, 714, 337

Cormack A.M., 1979, from Nobel Lectures, Physiology or Medicine 1971-1980, Ed. Jan Lindsten, World Scientific Publishing Co., Singapore, 1992

Cornelisse R., Charles P. A., Robertson C., 2006a, MNRAS, 366, 918

Cornelisse R., Steeghs D., Casares J., Barnes A.D., Charles P.A., et al., 2006b, submitted to MNRAS

Cornelisse R., Steeghs D., Casares J., Charles P.A., Barnes A.D., et al., 2006c, submitted to MNRAS

Courvoisier T.J.L., Parmar A.N., Peacock A., Pakull M., 1986, ApJ, 309, 265

Cowley A.P., Crampton D., Hutchings J.B., 1982, ApJ, 256, 605

Cowley A.P., Hutchings J.B., Crampton D., 1988, ApJ, 333, 906

Crampton D., Cowley A.P., Hutchings J.B., 1980, ApJ, 235, L131

Crampton D., Hutchings J.B., 1981, ApJ, 251, 604

Crampton D., Cowley A.P., Hutchings J.B., et al., 1990, ApJ, 355, 496

Cumming A., 2003, ApJ, 595, 1077

D'Odorico S., Oosterloo T., Zwitter T., Calvani M., 1991, Nature, 353, 329

de Jong J., van Paradijs J., Augusteijn T., 1996, A&A, 314, 484

Deguchi S., 1985, ApJ, 291, 492

De Ruyter, S., Van Winckel H., Maas T., Lloyd Evans T., Waters, L. B. F. M., Dejonghe, H., 2006, A&A, 448, 641

Dolan J.F., Boyd P.T., Fabrika S., et al., 1997, A&A, 327, 648

Dubner G.M., Holdaway M., Goss W.M., Mirabel I.F. 1998, AJ, 116, 1842

Dufour R.J., in 'Structure and Evolution of the Magellanic Clouds', edited by S. van den Bergh and K.S. de Boer, p353

Eikenberry S.S., Cameron P.B., Fierce B.W., et al., 2001, ApJ, 561, 1027

Eggleton P.P., 1983, ApJ, 268, 368

Fabian A.C., Pringle J.E., Rees M.J., 1975, MNRAS, 172, 15

Fabian A.C., Rees M.J., 1979, MNRAS, 187, 13

Fabbiano G., 1989, ARA&A, 25, 565

Fabrika S.N., Bychkova L.V., 1990, A&A, 240, L5

Fabrika S.N., 1997, Ap&SS, 252, 439

Faulkner J., Lin D.N.C., Papaloizou J., 1983, MNRAS, 205, 359

Fender R., 2003, To appear in *Compact Stellar X-Ray Sources*, eds. W.H.G. Lewin and M. van der Klis, Cambridge University Press, astro-ph/0303339

Ferland G.J., 1992, ApJ, 389, L63

Filippenko, A. V., Romani, R. W., Sargent, W. L. W., Blandford, R. D., 1988, AJ, 96, 242

Fomalont E.B., Geldzahler B.J., Bradshaw C.F., 2001, ApJ, 558, 283

Forman W., Jones C., Cominsky L., et al., 1978, ApJSuppl., 38, 357

Frank J., King A.R., Lasota J.P., 1987, A&A, 178, 137

Frank J., King A.R., Lasota J., 1992, ApJ, 385, L45

Frank J., King A.R., Raine D.J., *Accretion Power in Astrophysics* 3rd Ed., Cambridge University Press, 2002

Fuchs Y., Koch Miramond L., Abraham P., 2006, A&A, 445, 1041

Galloway D.K., Cumming A., Kuulkers E., et al., 2004, ApJ, 601, 466

Galloway D.K., Markwardt C.B., Morgan E.H., Chakrabarty D., Strohmayer T.E., 2005, ApJ, 622, L45

Galloway D.K., Psaltis D., Muno M.P., Chakrabarty D., 2006, ApJ, 639, 1033

Gardiner L.T., Sawa T., Fujimoto M., 1994, MNRAS, 266, 567

Gerend D., Boynton P.E., 1976, ApJ, 209, 562

Gehrz, R. D., Smith, N., Jones, B., Puetter, R., Yahil, A., 2001, ApJ, 559, 395

Giacconi R., Gursky H., Paolini F.R., Rossi B.B., 1962, Phys. Rev. Lett., 9, 49

Giacconi R., Gursky H., Kellogg E., et al., 1971, ApJ, 167, L67

Gies D.R., McSwain M.V., Riddle, R.L., Wang Z., Wiita P.J., Wingert D.W., 2002a, ApJ, 566, 1069

Gies D.R., Huang W., McSwain M.V., 2002b, ApJ, 578, L67

Goranskii V.P., Fabrika S.N., Rakhimov V.Yu., Panferov A.A., Belov A.N., Bychkova L.V., 1997, Astron. Rep., 41, 656

Goranskii V.P., Esipov V.F., Cherepashchuk A.M., 1998, Astron. Rep., 42, 209

Gottlieb E.W., Wright E.L., Liller W., 1975, ApJ, 195, L33

Gottwald M., Haberl F., Parmar A.N., White N.E., 1986, ApJ, 308, 213

Gray, D. F. 1992, The Observation and Analysis of Stellar Photospheres (2nd ed.; Cambridge: Cambridge Univ. Press)

Griffiths R.E., Gursky H., Schwartz D.A., Schwartz J., Bradt H., Doxsey R.E., Charles P.A., Thorstensen J.R., 1978, Nature, 276, 247

Grimm H.J., Gilfanov M., Sunyaev R., 2002, A&A, 391, 923

Grindlay J., Gursky H., Schnopper H., et al., 1976, ApJ, 205, L127

Gursky H., Giacconi R., Gorenstein P, et al., 1966, ApJ, 146, 310

Haberl F., Pietsch W., 1999, A&AS, 139, 277

Haberl F., Filipovic M.D., Pietsch W., Kahabka P., 2000, A&AS, 142, 41

Hameury J.M., King A.R., Lasota J.P., 1986, A&A, 162, 71

Hayakawa S., Matsuoka M., 1963, in Composition, Origin and Prehistory Proceedings from the 8th International Cosmic Ray Conference, Vol. 3, p. 213

Heinz S., Nowak M.A., 2001, MNRAS, 320, 249

Hellier C., Mason K.O., 1989, MNRAS, 239, 715

Hellier C., 2000, NewAR, 44, 131

Hertz P., Wood K.S., 1988, ApJ, 331, 764

Hillier, D. J., Davidson, K., Ishibashi, K., Gull, T., 2001, ApJ, 553, 837

Hillwig T.C., Gies D.R., Huang W., McSwain M.V., Stark M.A., van der Meer A., Kaper L., 2004, ApJ, 615, 422

Hjellming R.M., Johnston K.J., 1981, *Nature*, 290, 100

Hjellming R.M., Johnston K.J., 1981, ApJ, 246, L141

Horne K., 1985, MNRAS, 213, 129

Horne K., 1986, PASP, 98, 609

Horne K., Schneider D.P., 1989, ApJ, 343, 888

Horne K., 1991, Invited review in 'Fundamental Properties of Cataclysmic Variable Stars: 12th North American Workshop on Cataclysmic Variables and Low Mass X-ray Binaries', San Diego, 3-5 Jan 1991. ed. A.Shafter, San Diego State University Publications

Hounsfield G.N., 1979, from Nobel Lectures, Physiology or Medicine 1971-1980, Ed. Jan Lindsten, World Scientific Publishing Co., Singapore, 1992

Hut, P., van den Heuvel, E. P. J., 1981, A&A, 94, 327

Hut P., McMillan S., Goodman J., et al., 1992, PASP, 104, 981

Hynes R.I., Charles P.A., Haswell C.A., et al., 2001, MNRAS, 324, 180

Hynes R.I., Steeghs D., Casares J., Charles P.A., O'Brien K., 2003, ApJ, 583, L95

Hynes R.I., Steeghs D., Casares J., Charles P.A., O'Brien K., 2004, ApJ, 609, 317

Hynes R.I., Charles P.A., van Zyl L., Barnes A.D., et al., 2004, MNRAS, 348, 100

Iaria R., DiSalvo T., Burderi L., Rossa N.R., 2001, ApJ, 548, 883

Israelian G., Rebolo R., Basri G., et al., 1999, *Nature*, 401, 142

Jahoda K., Swank J.H., Stark M.J., et al. 1996, Proc. SPIE, 2808, 59

Jonker P.G., van der Klis M., 2001, ApJ, 553, L43

Kaaret P., Morgan E.H., Vanderspek R., Tomsick J.A., 2006, ApJ, 638, 963

Kahabka P., 2002, A&A, 388, 100

Kallman T., McCray R., 1980, ApJ, 242, 615

Kallman T., McCray R., 1982, ApJS, 50, 263

Kastner S.O., Bhatia A.K., 1990, ApJ, 362, 745

Kastner S.O., Bhatia A.K., 1991, ApJ, 381, L59

Katz J.I., 1981, A&A, 95, L15

Katz J.I., 1987, ApJ, 317, 264

King A.R., Ritter H., 1999, MNRAS, 309, 253

King A.R., Taam R.E., Begelman M.C., 2000, ApJ, 530, L25

King A.R., Davies M.B., Ward M.J., Fabbiano G., Elvis M., 2001, ApJ, 552, L109

King A.R., Schenker K., 2002, in 'The Physics of Cataclysmic Variables and Related Objects', ASP Conference Proceedings, Vol. 261. Edited by B. T. Gnsicke, K. Beuermann, and K. Reinsch., San Francisco: Astronomical Society of the Pacific, p.233

Kobulnicky H.A., Fryer C.L., Kiminki D.C., 2006, astro-ph/0605069

Kong A.K.H., Charles P.A., Homer L., et al., 2006, MNRAS, 368, 781

Körding E., Falcke H., Markoff S., 2002, A&A, 382, L13

Krauss M.I., Wang Z., Dullighan A., et al., 2005, ApJ, 627, 910

Kudritzki R.P., Bresolin F., Przybilla N., 2003, ApJ, 582, L83

Kuiper L., van Paradijs J., van der Klis M., 1988, A&A, 203, 79

Leibowitz E. M., 1984, MNRAS, 210, 279

Lense J., Thirring H., 1918, Phys Z., 19, 156

Lewin W.H.G., van Paradijs J., Taam R.E., 1995, X-ray Bursts (X-Ray Binaries, Cambridge University Press, edited by Lewin, W.H.G., van Paradijs, J. & van der Heuvel, P.J.)

Lewin, W.H.G., van Paradijs, J. & van der Heuvel, P.J. (editors), *X-Ray Binaries*, Cambridge University Press, 1995

Lépine S., Moffat A.F.J., St-Louis N. et al., 2000, AJ, 120, 3201

Liebert J., Angel J.R.P., Hege E.K., et al., 1979, *Nature*, 279, 384

Liu Q.Z., van Paradijs J., van den Heuvel E.P.J., 2000, A&AS, 147, 25

Liu Q.Z., van Paradijs J., van den Heuvel E.P.J., 2001, A&A, 368, 1021

Lopez L.A., Marshall H.L., Canizares C.R., et al., 2006, accepted to ApJ, astro-ph/0605574

Lorimer D.R., Bailes M., Harrison P.A., 1997, MNRAS, 289, 592

Lorimer D.R., 2001, Living Reviews in Relativity, 4, 5

Maccarone T.J., 2002, MNRAS, 336, 1371

Madau P., Ghisellini G., Fabian A.C., 1994, MNRAS, 270, L17

Makishima K., Kubota A., Mizuno T., et al., 2000, ApJ, 535, 632

Margon B., Cohen J.G., 1978, ApJ, 222, L33

Margon B., Stone R.P.S., Klemola A., et al., 1979, ApJ, 230, 41

Margon B., Ford H.C., Grandi S.A., Stone R.P.S., 1979, ApJ, 233, 63

Margon B., 1984, ARA&A, 22, 507

Markwardt C.B., Strohmayer T.E., Swank J.H., 2003, ATel, 164, 1

Markwardt C.B., Swank J.H., 2003, IAU Circular, 8144, 1

Martayan C., Fremat Y., Hubert A.-M., et al., 2006, A&A, 452, 273

Marsh T.R., Horne K. 1988, MNRAS, 235, 269

Marsh T.R., Robinson E.L., Wood J.H., 1994, MNRAS, 266, 137

Marsh T.R., 2001, LNP, 573, 1

Mason K.O., Middleditch J., Nelson J.E., White N.E., 1980, Nature, 287, 516

Mason K.O., Cordova F.A., 1982, ApJ, 262, 253

Mazeh T., Aguilar L.A., Treffers R.R., Königl A., Sparke L.S., 1983, ApJ, 265, 235

McClintock J.E., Canizares C.R., Tarter C.B., 1975, ApJ, 198, 641

McClintock J.E., Remillard R.A., 1986, ApJ, 308, 110

McGowan K.E., Charles P.A., O'Donoghue D., Smale A.P., 2003, MNRAS, 345, 1039

Meyer F., Meyer-Hofmeister E., 1981, A&A, 104, L10

Milgrom M., 1979, A&A, 76, L3

Mioduszewski, A. J., Rupen M .P., Walker, R. C., Schillemat, K. M., Taylor, G. B., 2004, BAAS, 36, 967

Mirabel I.F., Rodriguez L.F., 1994, *Nature*, 371, 46

Mirabel I.F., Rodriguez I., 2003, A&A, 398, L25

Mitsuda K., Inoue H., Koyama K., et al., 1984, PASJ, 36, 741

Mitsuda K., Inoue H., Nakamura N., Tanaka Y., 1989, PASJ, 41, 97

Motch C., Chevalier C., Ilovaisky S.A., et al., 1985, Space Sci. Rev., 40, 239

Motch C., Pedersen H., Beuermann K., Pakull M.W., Courvoisier T.J.L., 1987, ApJ, 313, 792

Motch C., Pakull M.W., 1989, A&A, 214, L1

Munari, U., Tomasella, L., 1999, A&AS, 137, 521

Munoz-Darias T., Casares J., Martinez-Pais I.G., 2005, ApJ, 635, 502

Murdin, P., Clark, D. H., Martin, P. G., 1980, MNRAS, 193, 135

Newsom G.H., Collins G.W., 1982, ApJ, 262, 714

Orosz J.A., Bailyn C.D., Remillard R.A., et al., 1994, ApJ, 436, 848

Orosz J.A., Bailyn C.D., 1997, ApJ, 477, 876

Ostlie D.A., Carroll B.W., *An* Introduction to Modern Stellar Astrophysics, Addison-Wesley Publishing, 1996

Owocki, S. P., Gayley, K. G., Shaviv, N. J., 2004, ApJ, 616, 525

Paczynski B., 1971, ARA&A, 9, 183

Paczynski B., 1977, ApJ, 216, 822

Paragi Z., Vermeulen R.C., Fejes I., et al., 1999, A&A, 348, 910

Paragi Z., Fejes I., Vermeulen R.C., et al., 2000, *"Galaxies and their Constituents at the Highest Angular Resolution"*. IAU Symp. N 205, R.T. Schilizzi (ed.), Manchester, United Kingdom, p.266.

Petterson J.A., 1978, ApJ, 224, 625

Pfahl E., Rappaport S., Podsiadlowski Ph., 2003, ApJ, 597, 1036

Podsiadlowski Ph., Rappaport S., 2000, ApJ, 529, 946

Podsiadlowski Ph., Rappaport S., Pfahl E., 2002, ApJ, 565, 1107

Podsiadlowski Ph., Langer N., Poelarends A.J.T. et al., 2004, ApJ, 612, 1044

Porter, J. M., 2003, A&A, 398, 631

Priedhorsky W.C., Terell J., 1984, ApJ, 280, 661

Pringle J.E., 1981, ARA&A, 19, 137

Prinja, R. K., Barlow, M. J., Howarth, I. D., 1990, ApJ, 361, 607

Psaltis D., 2004, To appear in *Compact Stellar X-Ray Sources*, eds. W.H.G. Lewin and M. van der Klis, Cambridge University Press, astro-ph/0410536

Revnivtsev M.G., Savonov S.Yu, Gilfanov M.R., Sunyaev R.A., 2003, Ast. Lett., 29, 587

Rhoades C.E., Ruffini R., 1974, Phys. Rev. Lett., 32, 324

Roberts T.P., Warwick R.S., 2000, MNRAS, 315, 98

Rodriguez J., Shaw S.E., Corbel S., 2006, A&A, 451, 1045

Safi-Harb S., Kotani T., 2003, in 'Proceedings of the 4th Microquasar Workshop', eds. Ph. Durouchoux, Y. Fuchs and J. Rodriguez, published by the Center for Space Physics: Kolkata

Salpeter E.E., 1964, ApJ, 140, 409

Sandage A., Osmer P., Giacconi R., et al., 1966, ApJ, 146, 316

Sarazin C.L., Begelman M.C., Hatchett S.P., 1980, ApJ, 238, L129

Schachter J., Filippenko A.V., Kahn S.M., 1989, ApJ, 340, 1049

Schaefer B.E., 1990, ApJ, 354, 720

Schneider D.P., Young P., 1980, ApJ, 238, 946

Seaton M., 1960, Rept. Progr. Phys., 23, 313

Seward F.D., Page C.G., Turner M.J., Pounds K.A., 1976, MNRAS, 175, 39

Seward F.D., Grindlay J., Seaquist E., Gilmore W., 1980, *Nature*, 287, 806

Shafter A.W., 1985, in 'Cataclysmic variables and low-mass X-ray binaries', ed. D.Q. Lamb and J. Patterson (Dordrecht:Reidel), p.355

Shafter A.W., Szkody P., Thorstensen J.R., 1986, ApJ, 308, 765

Shahbaz T., Fender R., Charles P.A., 2001, A&A, 376, L17

Shahbaz T., Zurita C., Casares J., et al., 2003, ApJ, 585, 443

Smale A.P., Wachter S., 1999, ApJ, 527, 341

Smale A.P., Church M.J., Balucinska-Church M., 2001, ApJ, 550, 962

Smale A.P., Church M.J., Balucinska-Church M., 2002, ApJ, 581, 1286

Smith D.A., Dhillon V.S., 1998, MNRAS, 301, 767

Smith, N., Gehrz, R. D., Stahl, O., Balick, B., Kaufer, A., 2002, ApJ, 578, 464

Steeghs D., Casares J., 2002, ApJ, 568, 273

Steeghs D., 2003, MNRAS, 344, 448

Stephenson C.B., Sanduleak N., 1977, *Astrophys. J. Suppl. Ser.* 33, 459

Strohmayer T.E., Zhang W., Swank J.H., et al., 1996, ApJ, 496, L9

Strohmayer T.E., Markwardt C.B., Swank J.H., in't Zand J., 2003, ApJ, 596, L67

Strohmayer T.E., Bildsten L., 2003, To appear in *Compact Stellar X-Ray Sources*, eds. W.H.G. Lewin and M. van der Klis, Cambridge University Press, astro-ph/0301544

Taam R.E., Sandquist E.L., 2000, ARA&A, 38, 113

Tauris T.M., van den Heuvel E.P.J., 2003, To appear in *Compact Stellar X-Ray Sources*, eds. W.H.G. Lewin and M. van der Klis, Cambridge University Press, astro-ph/0303456

Tuchman Y., Mineshige S., Wheeler J.C., 1990, ApJ, 359, 164

Uno S., Mitsuda K., Aoki T., Makino F., 1997, PASJ, 49, 353

van den Heuvel E.P.J., Ostriker J.P., Petterson J.A., 1979, A&A, 81, L7

van der Hooft F., Groot P.J., Shahbaz T., et al., 1997, MNRAS, 286, L43

van Paradijs J., Verbunt F., 1984, in High Energy Transients in Astrophysics, edited by S.E. Woosley, New York, AIP, 49

van Paradijs J., McClintock J.E., 1995, Optical and ultraviolet properties of X-ray binaries (X-Ray Binaries, Cambridge University Press, edited by Lewin, W.H.G., van Paradijs, J. & van der Heuvel, P.J.)

van Paradijs J., 1996, ApJ, 464, L139

Verbunt F., Hut P., 1987, IAUS, 125, 187

Verbunt F., 1993, ARA&A, 31, 93

Verbunt F., van den Heuvel E.P.J, 1995, Formation and evolution of neutron stars and black holes in binaries (X-Ray Binaries, Cambridge University Press, edited by Lewin, W.H.G., van Paradijs, J. & van der Heuvel, P.J.)

Vermeulen, R. C., Murdin, P. M., van den Heuvel, E. P. J., et al., 1993, A&A, 270, 204

Vreux, J. M., Dennefeld, M., Andrillat, Y., Rochowicz, K., 1989, A&AS, 81, 353

Wade R.A., Horne K., 1988, ApJ, 324, 411

Wang C., Lai D., Han J.L., 2006, ApJ, 639, 1007

Warner B., 1976, in *IAU Symposium 73, Structure and Evolution of Close Binary Systems*, ed. Eggleton P., Mitton S., Whelan J., (Dordrecht:Reidel), p. 85

Warner B., 2003, 'Cataclysmic Variable Stars', Cambridge University Press, Cambridge.

Webster B.L., Murdin P., 1972, *Nature*, 235, 37

White N.E., Kaluzienski J.L., Swank J.H., 1984, in High Energy Transients in Astrophysics, edited by S.E. Woosley, New York, AIP, 31

White N.E., Stella L., Parmar A.N., 1988, ApJ, 324, 363

White N.E., Nagase F., Parmar A.N, 1995, The Properties of X-ray Binaries (X-Ray Binaries, Cambridge University Press, edited by Lewin, W.H.G., van Paradijs, J. & van der Heuvel, P.J.)

Wijers R.A.M.J., Pringle J.E., 1999, MNRAS, 308, 207

Wijnands R., van der Klis M., 1998, *Nature*, 394, 344

Wojdowski P., Clark G.W., Levine A.M., Woo J.W., Zhang S.N., 1998, ApJ, 502, 253

Yada B., 1953, PASP, 5, 128

Yada B., 1954, PASP, 6, 76

in't Zand J.J.M., Kuulkers E., Verbunt F., Heise J., Cornelisse R., 2003, A&A, 411, L487

Zel'Dovich Ya.B., 1964, Sov. Phys. Dokl., 9, 246

Zinn R., 1985, ApJ, 293, 424

Zwitter T., Calvani M., D'Odorico S., 1991, A&A, 251, 92